# PORE CHARACTERIZATION OF ULTRALOW-$k$ DIELECTRIC THIN FILMS USING POSITRONIUM ANNIHILATION SPECTROSCOPY

by

**Ming Liu**

A dissertation submitted in partial fulfillment
of the requirements for the degree of
Doctor of Philosophy
(Physics)
in The University of Michigan
2008

Doctoral Committee:

Professor David W. Gidley, Chair
Professor Mark M. Banaszak Holl
Professor Bradford G. Orr
Professor Leonard M. Sander
Associate Professor Cagliyan Kurdak

“他山之石，可以攻玉”
– 诗经 • 小雅 • 鹤鸣

“The stones of those hills, may be used to polish gems.”
—SHI JING · Minor Odes of The Kingdom · He Ming

To my parents Liu Wenlong, Wang Suying
and my wife Liu Xiangyi

## ACKNOWLEDGEMENTS

My experience as a graduate student in the University of Michigan positron group will definitely be one of the most cherished times in my life and it is difficult for me to express my gratitude enough to all the help and support from my colleagues, friends, and families.

I am honored to be a graduate student of my thesis advisor, Professor David Gidley. He has always been an invaluable source of expertise and patient guidance throughout the course of my research. Dave has not only provided me the priceless academic supervision and mentoring, but also created a free and spontaneous research atmosphere that I deeply appreciate. I can never express my sincere gratitude enough for all the things he has offered me.

Dr. Richard Vallery has provided me tremendous help and encouragement that I will never forget. From computer technical issues and experimental apparatus to research problems, Rich has always showed his expertise and been willing to help. Dr. Huagen Peng had always been my resort of support when I first entered the group. I have learned a lot from him and had the good fortune to work with him. I am also very thankful to Dr. William Frieze for his dedicated support on technical issues and he taught me many things in instrumental physics. Sadly, I must acknowledge posthumously Dr. Mark Skalsey. He had not only given me inspiration and encouragement during my research, but also acted now and then as an English teacher. I could not agree more with what Dave has written in his obituary: "Mark

cultivated a gruff exterior to hide the teddy-bear inside and his students universally developed a friendship and admiration for their mentor." I am also thankful to Prof. Jens Zorn, Prof. Bill Ford, and Prof. Craig Davis for the helpful discussions about the simulation work during the time we still had the Cranium.

The research could not have been possible without the contributions of many collaborators, who provided a variety of samples, although not all of the results have been included in this thesis. In particular, I would like to thank Dr. Jin-Heong Yim of Samsung Advanced Institute of Technology (SAIT), Dr. Geraud Dubois, Dr. Willi Volksen, and Dr. Robert Miller of IBM, and Prof. Toh-Ming Lu of Rensselaer Polytechnic Institute (RPI). I am thankful for the valuable information they provided and the intriguing discussions we had which contributed significantly to this thesis. I would also like to thank Prof. Jamie Kruzic and Dr. Maximilien Launey of Oregon State University for their support in the bulk metallic glass work, Dr. Christopher Soles and Dr. Hyun Wook Ro of National Institute of Standards and Technology (NIST) for the collaboration in nanoimprint lithography, Dr. Jeff Wetzel and Hideki Takeuchi of Advanced Technology Development Facility (ATDF) for their support in the exploratory work in high-$k$ gate materials, Prof. Brown Terence of Michigan State University for the collaborative work in synthetic diamond, Prof. Sanat Kumar of Columbia University for the support in the PNC and nanocomposite studies, Martyn Folan of Boston Scientific Corporation, Mark O'Neill of Air Products and Chemicals, Inc., as well as Prof. Do Y. Yoon of Seoul National University, and Dr. Lirong Bao of National Starch & Chemical for their dedicated support.

I am grateful for the financial support provided by the National Science Foundation, SAIT, IBM, Center for Integrated Electronics of RPI, and the Department of Physics at the University of Michigan.

Last, but not least, I am fortunate to have the love and support I received from my wife Xiangyi, who has made my life enjoyable and wonderful. Without her, I could not imagine the loneliness throughout the course of these years. I am also deeply in debt for all the support and love of my parents and my being away from them all these years.

# TABLE OF CONTENTS

# LIST OF TABLES

# LIST OF FIGURES

**Figure**

# LIST OF APPENDICES

**Appendix**

# ABSTRACT

## PORE CHARACTERIZATION OF ULTRALOW-$k$ DIELECTRIC THIN FILMS USING POSITRONIUM ANNIHILATION SPECTROSCOPY

by

Ming Liu

Chair: David W. Gidley

In this thesis, a series of nanoporous ultralow dielectric constant (ULK) thin films fabricated using spin-coating and sacrificial pore generators (degradable porogens embedded in a host matrix) were studied as a function of porogen concentration and hence porosity to systematically vary the porogen-porogen and the porogen-matrix interactions. After porogen removal the resulting pore size and pore interconnectivity were characterized by beam-based (depth-profiled) Positronium Annihilation Lifetime Spectroscopy (PALS).

In a film series fabricated with the same methyl-silsesquioxane (MSQ)-based matrix, specific porogen-porogen interactions were induced by different functional end-groups of cyclodextrin (CD) porogens and by amphiphilicity of a calix-arene (CA[6]) porogen. Random, linear, and self-assembly growth modes respectively for the tCD, sCD and CA porogen domains were distinguished by PALS depth-profiling. In a sample series fabricated using the same nucleation and growth (N&G) porogen and

different MSQ-based matrices, distinct porogen-induced pore structures were observed which exhibit the significant role of porogen-matrix interactions in determining the pore morphology. Furthermore, *in-situ* thermal curing of nanocomposite hybrid samples to form nanoporous materials extends one's understanding of microphase separation, porogen degradation, and pore structure evolution with curing temperatures.

Monte Carlo simulations were conducted on a three dimensional cubic lattice to simulate the evolution of pore size and pore interconnectivity with increasing porosity. The calculated pore size evolution was found to be very consistent with the experimental results. The calculated pore interconnection length, while consistent with simple percolation concepts, did not follow the typical quadratic growth with porosity observed with PALS. The positronium annihilation intensity in the porogen-induced pores was simulated and compared with experiment. Such measurements appear to be promising as an absolute porosity calibration.

In an effort to successfully integrate ULK materials, chemical vapor deposited (CVD) Parylene-N has been found to be an effective sealant for interconnected pores to prevent copper diffusion and moisture uptake. However, in a depth-profiling experiment using PALS, it was found to penetrate the film to a depth of $\sim$200 nm. Characterization of penetrants in permeable systems is a broad area with a promising future for PALS applications.

# CHAPTER I

# Introduction

## 1.1 Low dielectric constant materials: a brief review

Gorden E. Moore in 1965 predicted, based on his observation, that the number of transistors in a single integrated circuit doubles every 24 months, which was later accepted as Moore's law [1, 2]. This prediction of an exponential development of the microelectronics industry has been surprisingly successful for several decades and came to serve as a goal and inspiration for the entire industry. Therefore, Moore's law eventually became a "self-fulfilling prophecy". Furthermore, not only is the evolution of the total number of transistors in a single chip exponential, almost every measure of microelectronic capabilities is linked to Moore's law, highlighted by the feature size, the computing speed, the storing capacity, and the unit price. This rapid evolution of the microelectronics industry for the last several decades has always been accompanied with the continuous miniaturization process, which allows the realization of all the evolutionary aspects mentioned above. The microelectronics industry has now worked its way down to the 45 nm scale and miniaturization has made it possible to integrate more than one billion transistors onto one single chip. Figure 1.1 shows the number of transistors on a single chip from the year 1970.

In recent years, however, the traditional Al/silicon-based processing infrastructure

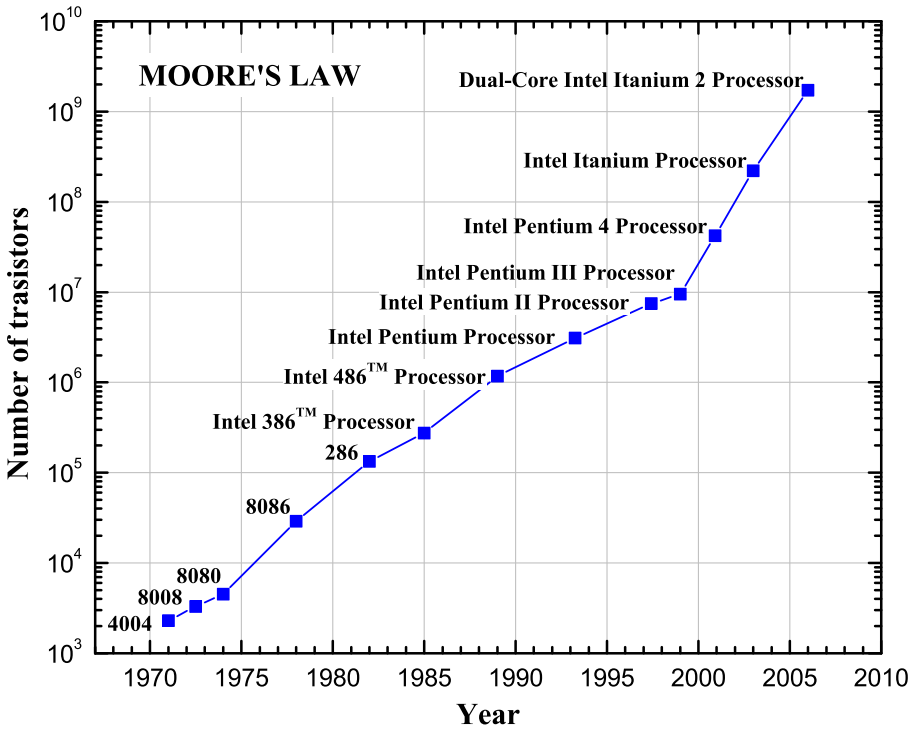


Figure 1.1: Total number of transistors in a single microchip.

has been pushed to its limit. Problems arise with the unceasing miniaturization process, including power consumption and heat dissipation issues when the density of transistors and wires keeps increasing. Generally, the power consumption of a circuit is given by

$$P = \alpha C f V^2, \tag{1.1}$$

where $\alpha$ is the activity ratio of the metal wires, i.e., the time fraction for the specific part of the circuit is *on*, $C$ is the overall capacitance, $f$ is frequency and $V$ is the voltage. Equation 1.1, although drastically simplified, suggests that when circuit density and frequency increase, one has to find a way to reduce the power consumption in order to keep the whole circuit from overheating.

To keep up with Moore's law, another obstacle that needs to be removed is the interconnect delay, which is also called resistive-capacitive (RC) delay. In the ultra-

large scale integration (ULSI) circuit, transistor gate delay and interconnect delay are the two major types of delay and their trends vs. feature size are plotted in figure 1.2 [3]. Based on Moore's law, the gate delay (red curve) decreases exponentially

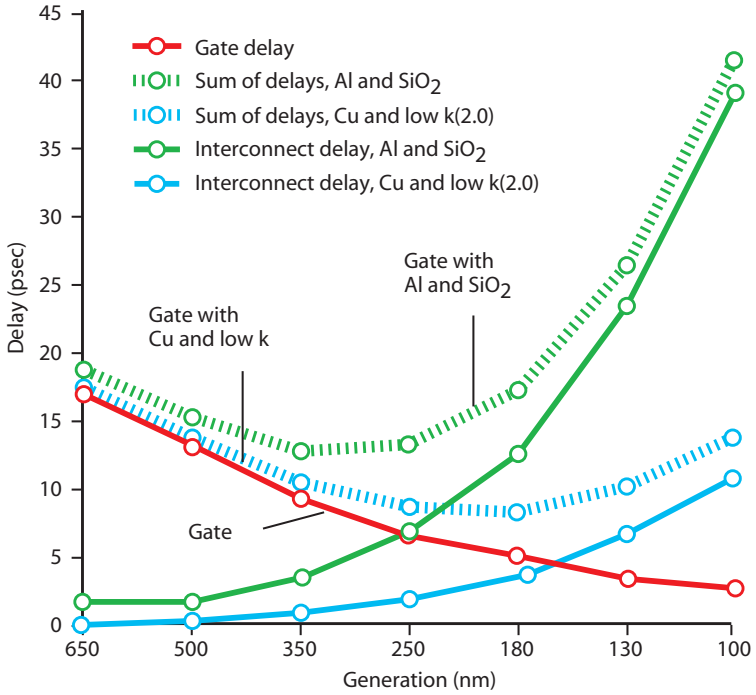


Figure 1.2: RC delay as a function of the gate length. The gate delay can be simply reduced by shorter feature size. The interconnect delay (RC delay) starts to dominate the overall delay at shorter feature size, especially at 100 nm generation and beyond. Courtesy of Laura Peters, Semiconductor International, 1998.

with the miniaturization process due to the shrinkage of transistor size. However, the RC delay, on the other hand, rises due to the higher wire density, and eventually exacerbates the overall delay. As seen in figure 1.2, in the 650 nm technology generation, the transistor/gate delay was ∼17 ps and the RC delay was only about 1 ps. At the 250 nm technological node, the gate delay becomes secondary while the interconnect delay plays an increasingly important role in the total delay. In the projected 35 nm technology generation, the transistor delay will be only 1 ps, and the RC delay will be ∼250 ps according to the International Technology Roadmap

for Semiconductors (ITRS) [4, 5]. As miniaturization continues, the delay that limits the integrated circuit (IC) speed becomes dominated by the interconnect $RC$ time constant,

$$\tau = RC, \tag{1.2}$$

where, $R$ is the resistance of the metal wire connections and $C$ is the capacitance of the wires. The actual delay is extremely difficult to calculate. In order to reduce the overall delay, both conduction via materials with lower resistance and interlayer dielectric (ILD) materials with smaller dielectric constant ($k$) are needed to continually increase the frequency, and reduce the cross talk between the conducting wires. Furthermore, a lower $RC$ value maintains or even reduces the power consumption of the ULSI circuit (see equation 1.1) at higher frequencies.

On the one hand, copper is used to replace the aluminum wires in the effort of lowering $R$. IBM, in 1998, announced the shipment of the world's first copper-based microprocessors. By 2002, almost all the microchips were using copper as interconnects. On the other hand, the interconnect capacitance, $C$, can be reduced straightforwardly by reducing the dielectric constant, $k$, of the ILD material. The traditional ILD material, silicon dioxide ($SiO_2$), with a dielectric constant of 4.2 has to be replaced by a novel "low-$k$" material. However, this evolution of ILD material has encountered many more difficulties than expected and the implementation of low-$k$ materials has been postponed several times by the semiconductor industry. Figure 1.3 shows the changes of projections of low-$k$ implementation schedule from several editions of ITRS.

The major problem associated with low-$k$ materials is that they are not compatible with the traditional integration processes due to their poor mechanical, chemical, thermal, and interface properties. In order to avoid dramatic processes changes

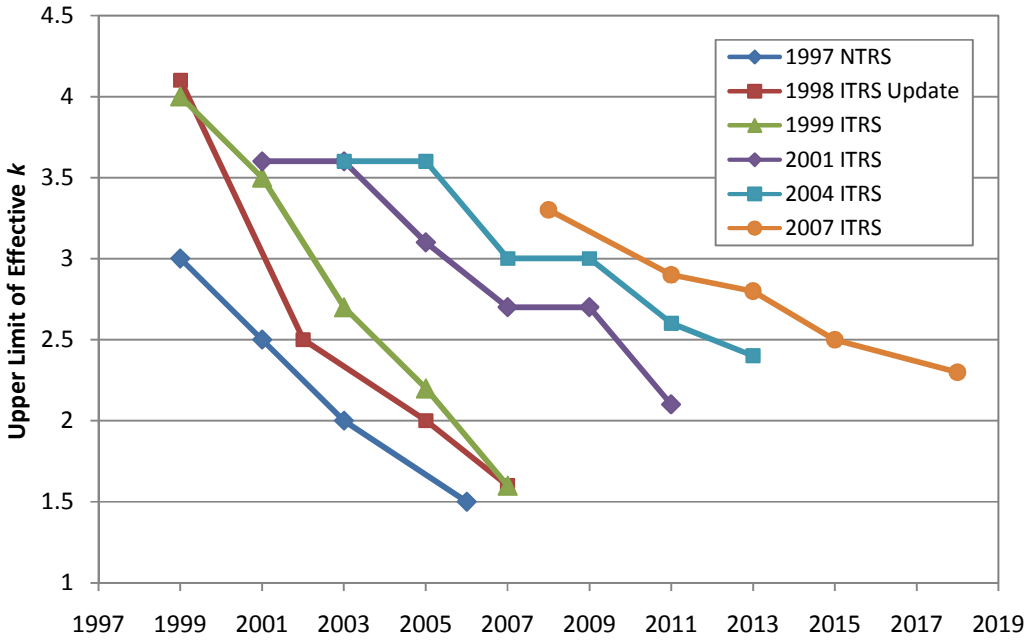


Figure 1.3: Delay in Low-$k$ materials implementation

and retooling during the implementation of low-$k$ materials, the microelectronics industry had to decelerate the deployment pace through the application of ingenious workarounds. Meanwhile, researchers have put tremendous efforts into the search for eligible low-$k$ materials that can be better implemented in industrial production and a variety of material candidates has been investigated [6, 7]. It has been found that the $k$ value of the traditional $SiO_2$ fabricated by plasma enhanced chemical vapor deposition (PECVD) of Tetraethyl orthosilicate (TEOS) can be lowered by fluorine or carbon doping/concentration. At the 180 nm technological node, fluorine was introduced into the $SiO_2$ network, forming fluorinated silicate glass (FSG), which has a $k$ value around 3.4 [8, 9]. This $k$ value is actually determined by the concentration of fluorine and also allowed the microelectronics industry to achieve the 130 nm feature size. However, introducing large quantities of fluorine into the film degrades the stability of the film in the face of moisture absorption, making reduction of the relative dielectric constant below 3.3 extremely difficult with SiOF. Besides fluorine,

organic/carbon groups introduced into the $SiO_2$ matrix can lower the $k$ value of silica to 2.7-3.0. These organosilicate glasses (OSGs) are also called SiCOH, SiOCH, or carbon-doped oxides. Some OSG low-$k$ materials have already been commercialized by different companies and used in mass production at the 90 nm technological node. (e.g. the Black Diamond plasma PECVD from Applied Materials; DEMS$^{TM}$ from Air Products; Coral® PECVD from Novellus, etc.) Besides the CVD dielectrics, some polymeric materials were found to be promising in low-$k$ applications [10]. These materials are generally deposited by a spin coating approach, hence are called spin-on dielectrics (SODs). SiLK® from Dow Chemical, methyl-silsesquioxane (MSQ or MSSQ), and hydrogen-silsesquioxane (HSQ or HSSQ), etc. fall into this category. However, solution spin-on thin film dielectrics will require a major shift from the current vapor deposition technology/equipment and hence there has always been resistance to SODs from the semiconductor industry.

## 1.2 Ultra low-$k$ (ULK) material and nanopore characterization

With the everpresent pressure to downscale the feature size, the $k$ value will also be pushed to its limit accordingly. The so-called ultra low-$k$ (ULK) material with $k$ <2.7 starts to be critical for the continued reduction of feature size, time delay and power consumption in the next several generations of microelectronic chips [4].

Table 1.1: ***ITRS Interconnect Technology Requirements — Near-term Years***

| *YEAR OF PRODUCTION* | *2008* | *2009* | *2010* | *2011* | *2012* | *2013* | *2014* | *2015* |
|---|---|---|---|---|---|---|---|---|
| *MPU/ASIC Metal 1 ½ Pitch (nm)(contacted)* | *59* | *52* | *45* | *40* | *36* | *32* | *28* | *25* |
| *MPU Physical Gate Length (nm)* | *22* | *20* | *18* | *16* | *14* | *13* | *11* | *10* |
| *Effective dielectric constant (κ)* | **2.9-3.3** | **2.6-2.9** | **2.6-2.9** | **2.6-2.9** | **2.4-2.8** | **2.4-2.8** | **2.4-2.8** | **2.1-2.5** |
| *Bulk dielectric constant (κ)* | **2.5-2.9** | **2.3-2.7** | **2.3-2.7** | **2.3-2.7** | **2.1-2.5** | **2.1-2.5** | **2.1-2.5** | **1.9-2.3** |

*Yellow shaded: manufacturable solutions are known; red: manufacturable solutions are NOT known.*

Table 1.1 shows the projection of $k$ values over the next several years from the

ITRS, 2007 edition [4]. As mentioned earlier, this schedule has been postponed several times because of the tremendous integration difficulties. However, the eventual shift from low-$k$ to ultra low-$k$ materials is believed inevitable. For the generations beyond the 45 nm technological nodes, nano-porous ultra-low-$k$ materials will start to play the critical role as interlayer insulators.

To obtain ULK dielectrics, nano-pores have to be engineered into the dense matrix to form an air-matrix structure since air has a $k$ value of 1. The shipment delays of ultra low-$k$ material implies that shifting from dense low-$k$ materials to nano-porous ultra low-$k$ materials is a huge challenge. The incorporation of nano-voids deteriorates the mechanical strength, lowers the films' resistance to copper intrusion, and brings many other integration issues [6]. These problems are drastically aggravated by introducing higher pore volume fractions (porosity) to further lower the $k$ value. Due to the high porosity, the pores become interconnected and susceptible to degradation during the integration process. In an effort to find *integrable* porous ULK dielectrics, a wide range of candidate materials was investigated and pore structures and their forming mechanisms are found to be very important in the search for eligible ULK materials. These morphological aspects in the ULK thin films are the emphasis of this thesis and will be further investigated in later chapters.

As a major impediment to ULK development, the characterization of the nanometer sized pores in amorphous thin films is a huge challenge for traditional pore characterization techniques. A number of new techniques, including positron annihilation spectroscopy (PAS), ellipsometric porosimetry (EP), X-ray porosimetry (XRP), and neutron porosimetry (NP) become more and more important for the characterization of the nanopore structure within ULK materials. PAS has its unique capability of probing nanopore characteristics by using positrons and many such studies in this

area have been conducted in the Michigan positron group. The group wrote a major review of PAS to study nanoporous materials, see reference [11]. The PAS results and the results from some other techniques are also compared to achieve a deeper understanding of the positron physics as well. PAS has been well recognized as a powerful probe to study porous materials, although the mechanism of positronium formation and diffusion is still not perfectly clear [12] and the studies on ULK porous materials may shine light on this topic. As for the application of PAS technique on the study of ULK materials, there are still a lot of questions to be answered both in the field of material science and positron physics.

### 1.3 Chemical vapor deposition (CVD) vs. spin coating

In order to understand the pore structure and its forming mechanisms, we have to look into the fabrication of these nanoporous materials. Currently, CVD is the standard technique used in the semiconductor industry to make thin deposition layers, including low-$k$ materials. In a typical CVD process, one or more volatile precursors flow by and interact with the substrate, producing the desired deposit layer on the substrate surface, and normally with gaseous byproducts. As mentioned earlier, CVD and spin coating methods are the two possible approaches in making low-$k$ dielectrics; as for making porous ultra-low-$k$ counterparts, CVD and spin coating will still be used. To make porous thin films, a straightforward approach is to selectively subtract pores from the original material, which can be accomplished by using pore generators (porogens). In the CVD approach, the porogens can be introduced by the gaseous precursors. The thin film deposited on the substrate is then exposed to plasma or ultra-violet light and as a result, the porogens degrade into gas and leave behind pores.

In this thesis, we mainly focus on ULK thin films made by the spin coating method. Spin-on deposition is a well known technology that has been used for fabrication of ultra low-$k$ thin films. It has the advantage of making films with large pore volume fraction by using sacrificial porogens. Figure 1.4 shows the schematic procedures of spin-on deposition. First, the solution of mixed matrix precursors and porogen molecules are deposited onto the spinning silicon wafer. At this stage, the porogens and the matrix precursors are miscible and can interact and move quite freely in the solution. The centripetal force can make the drop of solution spread evenly on the wafer into a thin layer. Then the whole wafer is baked at a low temperature (<150°C) to evaporate the solvent. Subsequently at higher curing temperatures, the hybrid nanocomposites of the porogen and the matrix undergoes phase separation; the matrix vitrifies and the porogen domains are fixed in place. Finally, the temperature rises to over 400°C where the matrix polymer precursors are fully cross-linked and the degradation of porogen leaves behind nanopores.

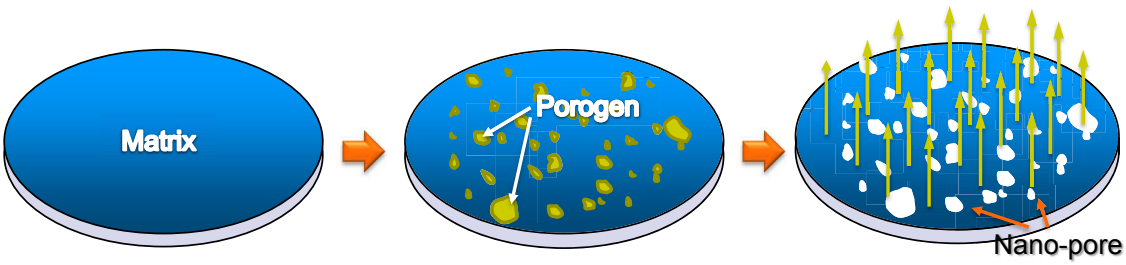


Figure 1.4: processing of spin-on ultra low-$k$ thin films

The choice between CVD and spin coating approaches can also be symbolized as the decision between evolutionary and the revolutionary methods, respectively, which has been a matter of debate [13]. The microelectronics industry prefers maintaining the current CVD processing infrastructure to reduce the capital investment. A major shift to new technologies that are not compatible with current instruments is seriously

discouraged. Here comes the contradiction between the reluctance to change and the need for development. The debate of using spin-on vs. CVD technology has been ongoing for years and the microelectronic industry still prefers the later approach. Spin-on ULK materials can achieve a $k$ value lower than 2.0 by introducing a large fraction of porosity, compared with the moderate porosity using CVD. But at high porosity, challenges of integration are presented to the microelectronics industry due to the unsatisfactory electrical, thermal, chemical, mechanical and structural liabilities.

One of the huge challenges of producing *integrable* porous low-$k$ ILD materials is maintaining the isolation between the nanopores. Since pore interconnectivity is unavoidable when their concentration approaches the percolation threshold of the system, study of percolation and emphasis on the pre-percolation regime in these systems are important. For both CVD and spin-on approaches mentioned above, the nanopore structure and its interconnectivity are very important issues that need to be addressed and understood. The studies on the formation of the pores using pore generators, pore size distribution, pore interconnectivity, the correlation between the pore structure and the mechanical, chemical, and thermal properties of the material provide valuable information on finding the right material for future ULK material applications.

## 1.4 Definition and nomenclature

There are a number of definitions that will be used frequently in later chapters and it is convenient to introduce them together here. All the acronyms and their meanings are summarized in appendix A. To distinguish different types of pores in ULK thin films, micropores and mesopores are defined by their different diameters. According

to the International Union for Pure and Applied Chemistry (IUPAC), micropores are pores with diameter <2 nm, while mesopores have diameters between 2 nm and 50 nm. This is not an absolute distinction of their characteristics and sometimes in our studies, some materials have a pore size distribution (PSD) that extends from the micropore regime to the mesopore regime. Therefore it is only for categorizing purposes.

The pore geometry in porous low-$k$ materials is often complex and difficult to deduce. Generally, we classify the pore geometries according to their basic idealized structures, such as spherical pores or cylindrical pores. We also define *closed* pores as pores isolated from the sample surface and *open* pores as pores connected to the surface. When the porogen loading gets larger (higher porosity), the interconnectivity of the pore structure becomes longer and more pores are open to the surface.

We normally define the porosity as the total volume fraction of voids within materials. Sometimes it is more straightforward to define the mesopore porosity which is the volume fraction of mesopores in materials. The latter definition is specifically convenient for study of porous low-$k$ materials when mesopores are normally *engineered* into a matrix material that intrinsically contains free volume micropores. It directly correlates with the porogen loading when the porous low-$k$ materials are made. The volume fraction of the porogen loading can normally be taken as the final porosity after the sacrificial porogens are evaporated. This is one of the crucial parameters that decides the $k$ value of the material since air has a $k$ value close to 1.

Pore interconnection length ($L_{int}$) is a measure of the nanopore interconnectivity in the pre-percolation regime before it jumps to infinity after percolation occurs. Crudely speaking, the $L_{int}$ of a porous thin film reflects the average length of the pores. Experimentally, it is defined using our positronium annihilation lifetime spec-

troscopy (PALS) analysis results. The details of this definition will be explained in chapter 2. Briefly, in PALS experiments, positrons can be implanted into a certain depth of a porous thin film where positronium (Ps) is formed using a specific implantation energy. The formed Ps can diffuse through interconnected pores and escape into vacuum if the pores are connected to the film surface. For a given pore connectivity, the deeper the positrons are implanted, the more difficult it is for the Ps to escape. Hence, the mean positron implantation depth at which 50% of the formed Ps can escape from the thin film and annihilate in vacuum is defined to be $L_{int}$. In chapter 3 and 4, we are going to discuss in detail how the pore interconnection length correlates with porosity and porogen interactions.

We use 4V/S as our mean free path (MFP) of Ps in a pore of volume V and surface area S. In the PALS technique, the Ps annihilation lifetime is directly related to the size of the pore where it annihilates. Actually, the Ps lifetime measures its average travel length between each collision (the MFP) with the wall material and correlates the pore size with positronium annihilation lifetime. By using the mean free path, the lifetime of positronium does not explicitly depend on the specific geometry of the pores.

## 1.5 Objectives and thesis overview

The nanopore structure of ULK materials has a crucial impact on their performance in the actual integration processes, and hence monitoring the pore structure becomes more and more important. In the fabrication of ULK materials, the rule of thumb is that the nanopore size should be less than 1/10 of the feature size, thus requires the porogen induced pores to be at least smaller than 4 nm in the future technological nodes. In order to characterize these nanometer-sized pores, a number

of techniques have been developed in recent years including the major tool used in this study, namely positronium annihilation lifetime spectroscopy (PALS). The objectives of this thesis is to characterize and understand pore characteristics of ULK thin films including:

- *pore size,*
- *pore size distribution,*
- *pore interconnectivity,*
- *pore structural evolution with porosity.*

All of these characteristics are determined by a number of factors including:

- *porogen and matrix type,*
- *porogen concentration,*
- *porogen-porogen interactions,*
- *porogen-matrix interactions,*
- *thermal curing temperatures.*

Moreover, a range of important fundamental problems will also be explored, including the effects on pore structure by varying matrix silanol concentrations and molecular weight of the matrix resins, the simulations of pore structural evolution, and further understanding of the PALS technique itself. An overview of this thesis is listed below.

This first chapter is a brief summary of low-$k$ materials and its characterization techniques. In chapter 2, the positron annihilation spectroscopy (PAS) technique, especially the positronium annihilation lifetime spectroscopy (PALS) technique and its applications in characterizing porous materials will be introduced. Several other techniques, such as ellipsometric porosimetry (EP), X-ray porosimetry (XRP) and small angle neutron scattering (SANS) will also be mentioned and compared with

the PAS/PALS technique.

Chapter 3 will mainly focus on the characterization of a series of porous low-$k$ ILD thin films (supplied by the Samsung Advanced Institute for Technology, SAIT) with increasing porosity (porogen loadings). Different growth patterns of the nanopore structure according to porogen loading are deduced by PALS analysis and the porogen-porogen interactions in the mixture with matrix precursors support our experimental results.

In chapter 4, a more detailed and complete study of nanopore structure forming mechanisms in ULK materials supplied by IBM will be carried out using PALS with in-situ heat treatments. Combinations of different types of porogen and matrices are going to be systematically investigated. A porogen used as a pore-blocking agent, its degradation, and its effects on the final pore size will also be studied.

In chapter 5, universal fittings of the PALS analysis results will be presented on various systems, followed by an attempt to model the nano-porous materials, especially focusing on pore evolution and its effect on PALS results. Pore agglomeration under different porogen interactive situations will also be explored.

Chapter 6 will deal with a possible method, parylene-N pore sealing, which can improve the integration feasibility of high porosity low-$k$ ILDs using the current processing infrastructure. The effect on the pore sealing effectiveness using different parylene deposition conditions will be investigated.

Chapter 7 will conclude this study on ULK materials and summarize the pursuit of ULK materials that can be used in the microelectronics industry. Furthermore, in the appendices, experiments of different detection efficiencies of $3\gamma/2\gamma$ annihilation events, use of depth profiled Doppler Broadening Spectroscopy (DBS) to study bulk metallic glasses, and the simulation code used in chapter 5 will be included.

# CHAPTER II

# PAS technique and its applications

## 2.1 New porosimetry techniques

As nanometer-sized pores are introduced into the very thin (∼200 nm) low-$k$ films to make ultra low-$k$ (ULK) interlayer/intermetal dielectric (ILD/IMD) materials, the characterization of these films becomes much more difficult than the characterization of traditional bulk, mesoporous materials. Researchers need to measure the absolute porosity, pore size, pore size distribution (PSD) and pore interconnectivity, etc. such that these results can be correlated with measured physical, chemical, and transport properties of the porous material and provide guidance for future studies. The processed porous thin films may also be heterogeneous in depth after annealing, plasma treatment, or etching; thus posing a further challenge to pore characterization. In recent years, several novel characterization and porosimetry techniques have been developed, including ellipsometric porosimetry (EP), Specular X-ray reflectivity (SXR), small angle X-ray scattering (SAXS), X-Ray porosimetry (XRP), small angle neutron scattering (SANS), Neutron porosimetry (NP) and positron annihilation spectroscopy (PAS). In our studies, PAS, and especially positronium annihilation lifetime spectroscopy (PALS), is our primary tool to investigate ULK nanoporous thin films. Results from other techniques, when available, are presented

in our studies for comparison. It is always better to combine results from different techniques since every technique has its limitations. The following sections provide a brief introduction of several techniques and present an overview of PAS technique.

### 2.1.1 Adsorption technique and ellipsometric porosimetry

Adsorption porosimetry is an important and very broadly used pore characterization technique. Generally speaking, the adsorption technique relies on the isotherms which relates the uptake amount of the adsorbate (gas or liquid) by the porous media to the relative pressure. If the adsorption/desorption amount can be measured, consequently, the pore size and pore size distribution (PSD) can be deduced from these experiments. There is a distinction between mesopore size distribution and micropore size distribution and different equations should be used to deduce the PSDs respectively. The adsorbate condenses in the pores at a vapor pressure $P$ below the equilibrium pressure of a flat surface $P_0$. For mesopores, the pore curvature and the relative adsorbate pressure, $P/P_0$, can be related by the Kelvin equation,

$$\frac{1}{r_K} = \frac{RT}{f\gamma V_L} \ln\left(\frac{P}{P_0}\right), \tag{2.1}$$

where the $r_K$ is the Kelvin radius, $R$ is the gas constant, $T$ is the temperature in Kelvin, $\gamma$ is the surface tension, $V_L$ is the volume of the adsorbed liquid in mole, $f$ is a coefficient which is directly related to the curvature/shape of the condensed adsorbate meniscus during adsorption and desorption. In simplified cases, we can take $f = 1$ for slit-shaped pores and $f = 2$ for cylindrical pores. The Kelvin radius $r_m$ is related to the pore radius $r_p$ by $r_p = r_K + t$, and $t$ is the thickness of the absorbed liquid layer on the pore walls. The value of $t$ can be obtained by the Brunauer, Emmet, Teller (BET) equation

$$t = \frac{t_0 C \cdot K \cdot (P/P_0)}{[1 - K(P/P_0)] \cdot [1 + K(C-1)(P/P_0)]}, \tag{2.2}$$

where $t_0$ is the thickness of one monolayer of the adsorbate, C is the $BET$ constant, and $K$ is a coefficient satisfying the requirement that at $P = P_0$, $t \leqslant 5-6$ monolayers [14].

Unfortunately, the above Kelvin equation is only accurate for mesopores that are larger than several nanometers in diameter. For sub-nanometer micropores of a few molecular diameters, the Kelvin equation is not valid anymore. The micropore size can be calculated from the Dubinin-Radushkevich equations,

$$V = V_0 \exp\left[-\frac{1}{(\beta E_0)^2}\left(RT\ln\left(\frac{P}{P_0}\right)\right)^2\right], \tag{2.3}$$

where $V$ represents the adsorbed volume of toluene. $V_0$ and $\beta$ can all be determined by experiment. $E_0$ is a characteristic energy that correlates directly with the radius of curvature of micropores,

$$r = \frac{K}{2E_0}, \tag{2.4}$$

where r is the radius of micropores, $K$ is a constant that can be determined empirically. $E_0$ can be found from equation 2.3.

Traditional $N_2$ adsorption porosimetry is based on the direct measurement of mass or volume of adsorbate condensed in the pores. However, it is limited by the precision of microbalances, especially when the total adsorbed amount is small in very thin films. Better sensitivity can be achieved by several means (e.g. see [15]) and we are going to focus on ellipsometric porosimetry [16]. Ellipsometric porosimetry (EP) (now commercially available) combines optical information obtained from light refraction of the film and the adsorption/desorption technique of an organic solvent, usually toluene. It measures the change of the refractive index and thickness of the materials during the adsorption and desorption of toluene. This information is then used to calculate the porosity and pore size distribution (PSD) inside the porous

media utilizing the traditional gas adsorption/desorption theory mentioned earlier.

In EP technique, porosity can be deduced from the Lorentz-Lorenz equation 2.5 [17, 18], which correlates the overall refractive index and the refractive indices of each material components,

$$\frac{(n_{eff}^2-1)}{(n_{eff}^2+2)} = \frac{(n_p^2-1)}{(n_p^2+2)} \cdot P + \frac{(n_m^2-1)}{(n_m^2+2)} \cdot (1-P). \tag{2.5}$$

In equation 2.5, $n_{eff}$ is the overall refractive index, $n_p$ is the refractive index of the material filling the pores and $n_m$ is the refractive index of the matrix material. We know the refractive index of a vacuum (or air) is 1, therefore without any liquid adsorption the first term is zero. It is then straightforward to calculate the total porosity if we know the refractive index of the matrix material and the effective overall refractive index. Actually, $n_p$ can be the refractive index of any material that fills up the pores. Generally in porosimetry methods, toluene is used to fill the pores and the refractive index of this two component mixture of toluene and matrix material can be used in calculating the porosity,

$$P = \frac{\frac{n_{sat}^2-1}{n_{sat}^2+2} - \frac{n_0^2-1}{n_0^2+2}}{\frac{n_{tol}^2-1}{n_{tol}^2+2}}. \tag{2.6}$$

In equation 2.6, $n_{tol}$ is the refractive index of toluene which is a well known number. The refractive index before and after the toluene adsorption are $n_0$ and $n_{sat}$ respectively. At certain pressure, equation 2.5 can also be used to calculate the amount of the adsorbed toluene, thus the adsorption/desorption isotherm is obtained for the calculation of PSD.

Adsorption techniques need interconnected porous networks to absorb and desorb the volatile solvent molecules, which is one limitation of this technique. It is not applicable to porous films with a dense barrier layer. It also require a solvent material

that does not interact with the pore structure. If the $N_2$ and toluene swell the matrix, the measured pore size will be larger.

### 2.1.2 SXR, SAXS and SANS

Specular X-ray reflectivity (SXR) and small angle X-ray/neutron scattering (SAXS /SANS) are three important techniques in characterization of porous thin films. The high-resolution SXR technique can measure thin film thickness, uniformity and depth dependence of density. It uses a highly focused X-ray source as the incident beam at some small angle $\theta$ and measures the reflected beam intensity at the same angle. The measured precision of the angles can be as low as $10^{-4}$ degree. A typical spectrum of SXR is shown in figure 2.1.

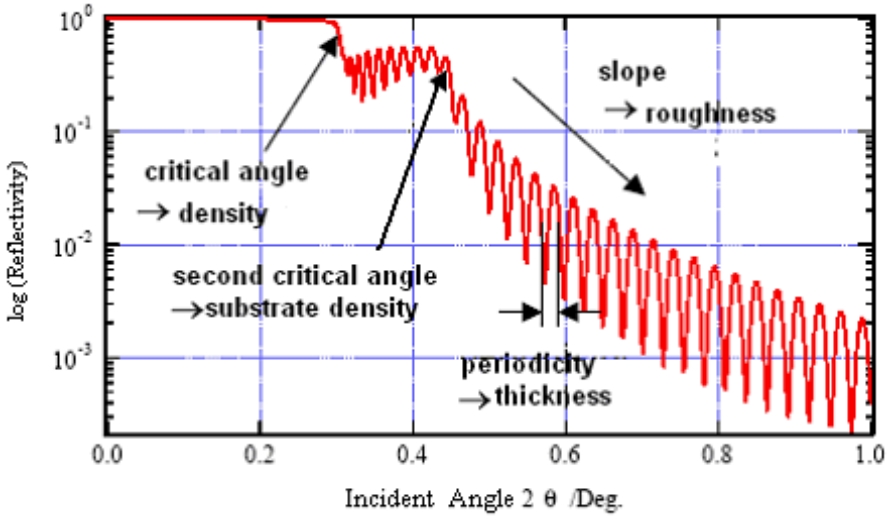


Figure 2.1: A typical SXR profile with indications of the critical angle, the second critical angle, slope and periodicity of fringes, which correspond to the density of thin film and substrate, surface roughness, and thickness, respectively (courtesy of IBM).

In the figure, the logarithm of the reflected intensity $(I/I_0)$ is plotted versus the angle $2\theta$. When $\theta$ increases from zero, the reflected intensity drops suddenly at two critical angles $\theta_c$ which correspond to the densities of the thin film and its substrate respectively. The oscillation period determines the film thickness. This is

very useful to measure the thermal expansion of thin films at different temperatures. The porosity of the film can be inferred from the film density, given the density of the skeleton material. However, the density of the nonporous, bulk prototype does not necessary have the same density as the skeleton. Moreover, sometimes the dense counterpart is not available.

SXR is normally used in combination with scattering techniques like SAXS and SANS. SAXS and SANS techniques are based on the same physical principle that at certain angle, the scattered beam intensity is directly correlated to the pore/particle size and its distribution [19]. (However pores and particles cannot be distinguished from each other.) They are also sensitive to the density change of samples by measuring the refracted beams. SANS always needs stacked thin films to produce enough scattering of neutrons and is also limited by the number of available neutron sources.

### 2.1.3 X-ray and neutron porosimetry

X-ray porosimetry (XRP) is a powerful technique that has many similarities with EP. It combines SXR, SAXS and adsorption/desorption isotherms of toluene to extract additional film characteristics [20]. From SXR and SAXS, wall density, porosity and pore diameter can be determined. The film density before and after the adsorption can be directly correlated with the amount of liquid absorbed since it can measure the porosity as well. Neutron porosimetry is quite similar to XRP and will not be discussed in detail.

The above porosimetry techniques all use liquid adsorption and desorption as a critical part of the metrologies. To absorb/desorb the condensate such as toluene, they need pores that are open to the surface of the film. At low porosities when most of the nano-pores are isolated, these techniques are limited in the accuracy of measuring the pore size distribution. When the thin film has a dense surface

barrier layer that prevents liquid penetration, we have to rely on other methods. Moreover, adsorption techniques require longer experimental cycles and may damage the materials.

### 2.1.4 PAS technique and its capabilities

Unlike the adsorption and scattering pore characterization methods discussed above, positron annihilation spectroscopy (PAS) uses the positron, the anti-particle of the electron, as a probe that utilizes the unique interaction between antimatter and normal matter. It has been demonstrated to be a successful technique over the past several decades. Accompanying the recent availability of low-energy beam-based positron sources, the capabilities of traditional PAS techniques have been extended tremendously into the studies of surfaces and thin films [21], especially into the field of porous materials [11]. The PAS technique has been used in the studies of a variety of porous materials, including ULK thin films, bulk metallic glasses (see appendix C), polymer nanocomposites [22], selectable porous membranes [23, 24] and more.

Within solid materials, positrons and electrons eventually annihilate with their total mass converted into photons. PAS monitors and analyzes various aspects of the annihilation radiation, which contains valuable information about the material in which the electrons and positrons annihilate. In our studies, the nanopore characteristics of porous materials can be deduced by analyzing these emitted photons. The complete conversion of mass to energy leaves no residues and very little damage to the subject material, and thus qualifies the PAS technique as a unique, unconventional and nondestructive way of studying nanoporous materials.

There are several different PAS techniques that focus on different aspects of the emitted gamma rays from positron-electron annihilation. Doppler Broadening Spectroscopy (DBS) mainly focuses on the *energy* domain [25]. It monitors the gamma ray

energy deviation from the 511 keV peak in the longitudinal direction of they travel, which is closely related to the momentum of the electron within the annihilating electron-positron pair and can tell us important information about vacancies/cracks in the material. A complementary PAS technique, angular correlation of annihilation radiation (ACAR), looks at the angular correlations of the two back-to-back gamma rays that are emitted from the annihilation. The small deviation from 180° also indicates the pair momentum in the transverse direction. Positron Annihilation Lifetime Spectroscopy (PALS) measures the *time* between the positron implantation and its annihilation. This lifetime is directly correlated with the size of voids/pores within materials and enables one to deduce many characteristics of porous material.

Besides being non-destructive, PAS is especially useful in studying porous films with sealed surfaces or barrier layers since positrons can be implanted into the subject material through these barriers. In our studies, beam based PALS and DBS are specifically useful due to their low and controllable positron implantation energy, hence their implantation depth. Because the typical ULK thin films are several hundred nanometers thick, it is necessary to use low energy positron beams that can implant positrons into different mean film depths varying from ∼10 nm - 1000 nm. In the following sections, the basic concept of positron interaction with matter and the details of PALS technique will be discussed.

## 2.2 PAS techniques overview

From the prediction [26] and discovery [27] of the positron more than seventy years ago, positron physics has undergone a gradual but significant shift from the study of the positron itself to the application of positrons as a technique in various materials studies. It is well known that a positron and an electron can annihilate and emit

a certain number of photons [28–32]. In metals, the annihilation emits two back-to-back 511 keV gamma rays. However, in insulating materials, a positron and an electron, before they annihilate, can sometimes form a meta-stable bound state called positronium (Ps). Ps can have singlet or triplet spin states with different intrinsic annihilation rates depending on the different alignment of its electron and positron spin. When the positron and electron has total spin zero, the bound state is called para-positronium (p-Ps) and the ground state has a lifetime of 125 ps and decays into two photons. When the total spin of the positronium is 1 (ortho-positronium, or o-Ps), it will finally decay into three gamma rays with the total energy equal to 1022 keV and with lifetime of 142 ns [33, 34]. Numerous studies have been carried out to investigate the behavior of positron and Ps in materials over the past several decades [35]. The discovery of Ps trapping and annihilation in defects and voids opens the door to tremendous applications in material science. With the availability of low energy positron beams, the positron as a useful probe of surfaces and thin films began to flourish in the 1980's. It not only makes some new techniques possible, but also extends the capability of the traditional researches.

### 2.2.1 Positron and positronium in solids

Positrons are stable in vacuum ($\tau > 2 \times 10^{21}$ year [36]), but once they are injected into normal materials, their lifetimes will be drastically shortened due to their annihilation with electrons in the matter. However, the behavior of an implanted positron in matter is not simple and straightforward. Several excellent reviews on this issue are available [21, 35, 37]. In summary, the process that positrons undergo in solids before they annihilate can be crudely put into several time scales: backscattering, thermalization, Ps formation, Ps diffusion and annihilation.

In the shortest time scale around $10^{-15}$s, when positrons hit the sample surface,

a small fraction is quickly reflected as backscattered positrons. Some positrons can form Ps on the surface of the material and annihilate in vacuum as backscattered fast Ps. The implanted positrons that are not reflected slow to a few eV in several picoseconds through ionizing collisions. Along the positron stopping process, positrons can sometimes form positronium. Our PALS study mainly involves the relatively "slow" processes related to Ps formation, diffusion and its annihilation lifetime, thus the acronym PALS also refers to *Positronium Annihilation Lifetime Spectroscopy*.

The exact formation mechanism(s) of Ps has been a matter of debate for a long time. It has been studied for several decades and the two major theories, "Ore model" and "spur model" [38, 39], have each had plenty of success. They are applicable under different conditions. The Ore model was originally used to explain the Ps formation in low-density gases, but has also been shown to be valid in solids under some circumstances. [40–43] In the Ore model, positrons pick electrons of ionization energy, $I$, from the gas molecules during their slowing down process and form Ps. When the positron energy falls to a range less than $I$-6.8 eV, where 6.8 eV is the ground state binding energy of Ps, then Ps formation is energetically no longer possible. At higher energies larger than $I$, the reverse process of Ps formation, Ps dissociating into unbound positrons and electrons, is possible and thus effectively reduces the formation probability. The energy gap between $I$ and $I$-6.8eV is the so-called Ps formation Ore gap within which the Ps formation is most probable. Another model, the so-called spur model, was developed by Mogensen in 1975[38, 39] to describe positronium formation in liquids. The spur model states that the incident energetic positron ionizes the atoms along its slowing-down path. After the positron finally slows down, in the region of the excited electrons (the spur), it can combine

with one of the spur electrons and form Ps. The combination probability is decided by the distance between the electron and the positron as well as the characteristics of the material [44]. The spur model has shown significant success in many experiments. However, there has not been a comprehensive model that can be used both in gases and solid materials. Jacobson in 1986 [45] proposed a semi-quantitative model to describe the Ps formation in molecular gases, which is effectively a combination of the Ore and spur model.

It has been observed in numerous experiments that the Ps formation depends on materials. In some organosilicate materials that are used in low-$k$ dielectric applications, we have observed Ps formation above 50%. The Ps intensity is not only material specific, but also depends on porosities of the material, which gives valuable information in the study of many nanoporous materials. Ps formation in these nanoporous materials is a competing process both from Ore model and spur model, but their relative contribution that depends on the specific physical and chemical properties of the materials is still unknown [46, 47].

The Ps diffusion behavior has been studied in a variety of materials for many years [48–50]. Specifically for the nanoporous materials we study, it has been found that Ps can diffuse and be trapped in the voids of the material where, the pores treated as potential wells, the lower energy states of the Ps particle in the well can be achieved. Once Ps loses a tiny fraction of its energy, it cannot diffuse back from the void into the solid anymore. Ps confined in mesopores may collide with pore walls more than a million times before it annihilates. During these collisions, it can diffuse across a significant length if the pores are interconnected and open to the surface [51]. The cartoon in figure 2.2 illustrates the several routes that Ps may take before it decays into photons.

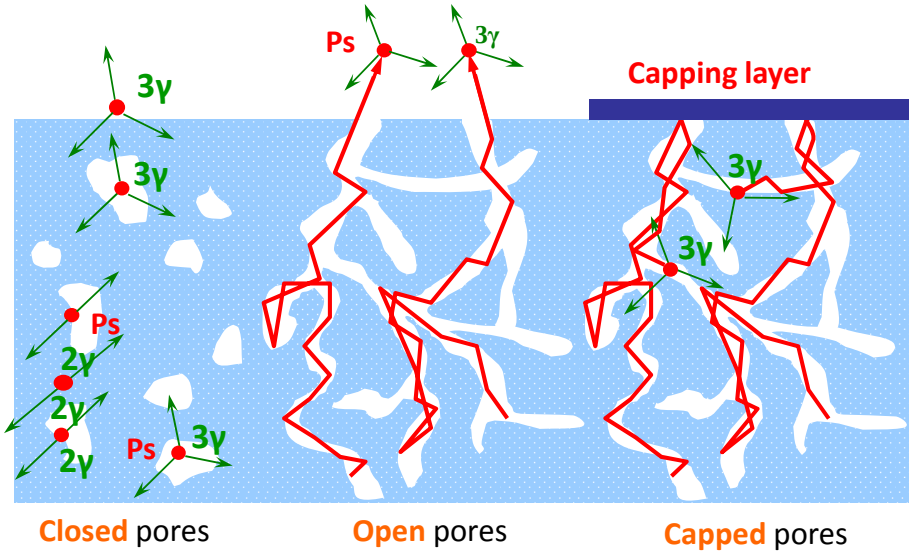


Figure 2.2: Ps diffusion and annihilation in porous materials. The left part shows the uncapped film with closed and open pores. Ps can either annihilate within closed pores with shortened lifetime or diffuse through interconnected pores into vacuum with lifetime of 142 ns. One the right half of the figure, the interconnected pore network is capped using the capping layer in order to confine the Ps inside the film. The Ps lifetime is then associated with the mean free path of the Ps diffusion.

Using this simple diffusion model illustrated in figure 2.2, most of the Ps can diffuse out of a porous thin (∼200 nm) film as long as the pores are open to the surface. Thus, the Ps diffusion behavior in porous thin films provides quite accurate information about the mesopore interconnectivity. Furthermore, near the sample surface, avoiding the Ps pore trapping process, a small fraction of Ps can diffuse back into the vacuum, which is called "slow" backscattered Ps. Unlike the fast backscattered Ps, the slow backscattered Ps has the vacuum lifetime of 142 ns. The fast and slow backscattered Ps intensity, in our experience, are each as small as 1% at beam energies higher than 4 keV and scale roughly as 1/E. At low beam energies, it also depends on the material and surface roughness.

Triplet o-Ps annihilating in vacuum decays into three gamma rays with a lifetime of 142 ns, while once a o-Ps is trapped inside a void, the surrounding molecular electrons of opposite spin can shorten its lifetime by mixing the fast $2\gamma$ decay mode

into the intrinsic 142 ns $3\gamma$ decay. The process wherein the positron in the Ps annihilates not with its bound electron but with a surrounding electron of opposite spin is called pickoff annihilation. Depending on the pore size affecting the o-Ps collision with the pore wall (also see figure 2.2), the 142 ns lifetime can be shortened to 1 ns. This shortened Ps lifetime can be directly related to the size of the pore it annihilates in, which is the foundation of the PALS technique of characterization nanoporous materials. The o-Ps lifetime and pore size calibration will be discussed in detail later. In our study, we will mainly focus on the o-Ps annihilation inside the nanovoids which are engineered into the dielectric thin films and o-Ps will simply be referred to as Ps.

### 2.2.2 PAS techniques

PALS and DBS are the major probes used in this study to characterize nanoporous thin films. As mentioned earlier, different PAS techniques rely on the detection of annihilation gamma rays and the different aspects of the observed radiations. PALS specifically examines the time scale of the annihilation of positrons and positronium, whose lifetime directly correlates with the characteristics of the media they annihilate in. DBS looks at the energy spectrum of the photons emitted from the positron-electron annihilation. This energy deviation from the 511 keV peak reflects the electron momentum where the annihilation occurs, and thus reveals the nature of the vacancies in the material at that specific location.

There are basically two ways to generate the positrons needed in these various applications [52]: radioactive beta decay such as Sodium-22; pair production in reactor-based facilities or linear particle accelerators (LINAC). On the one hand, the reactor-based or LINAC based facilities can possibly generate a high intensity of positrons. On the other hand, using radioactive isotopes like sodium-22, we can make

compact low energy positron beams. Sodium-22 is a convenient positron source and has been widely used in both bulk and beam based experiments. It has a half-life of 2.6 years and undergoes beta decay into neon, a positron, a neutrino and gamma rays. The reaction process is shown in equation 2.7 below,

$$^{22}_{11}Na \rightarrow ^{22}_{10} Ne + e^{+} + \nu_e + \gamma. \tag{2.7}$$

Traditional PALS has been used as a standard technique for more than 40 years in an explicit manner, in which a radioactive positron source (we used $^{22}$Na) is placed in juxtaposition with the subject materials or sandwiched by two pieces of a sample in which we are interested. The 1270 keV gamma ray that is concomitant with the $\beta^+$ decay can be monitored by a scintillator/photomultiplier as the start event of the production of a positron. The positron finally annihilates with an electron inside the material and generates two or three photons which can be detected by another phototube/scintilator. The discrimination levels are set differently according to the specific energies of the start gamma and stop gamma respectively. The lifetime of the positron or positronium event is therefore the time interval between the start and stop signal. This kind of system is called *bulk* PALS. In bulk systems, the timescale of the start and stop signal can be measured accurately, and high time resolutions ($\sim$200 ps) can be achieved with bulk PALS. However, due to the long positron stopping range of $\beta^+$ decay and its undirected positron emission, bulk PALS can only be used to study rather thick (mm) and homogeneous films.

Doppler Broadening Spectroscopy (DBS) monitors the energy spectrum of the emitted gamma rays from positron-electron annihilation, specifically of the $2\gamma$ annihilation events. The energy of radiated back-to-back photons from annihilation peaks at 511 keV, which equals the mass of the positron or the electron. Furthermore, the momentum of the positron-electron pair also contributes to the total energy of the

gamma ray. Although it is a small fraction, the energy spectrum will be Doppler shifted when we look at the longitudinal direction of the photon propagation. The decay energy shift can be detected by a high resolution detector, usually a high purity Germanium detector, down to several eV from the 511 keV peak. This Doppler shift is directly related to the momentum of the annihilating positron-electron pair, which is subsequently decided by the electron density and other properties at that specific location. Thus, the shift corresponds to the vacancy/void characteristics. The DBS spectrum is normally Gaussian-like, and a peak region around 511 keV and two wing regions are customarily distinguished by defining a W and S parameter. The W parameter is taken as the ratio of events in the "wing" region to the events in the peak region, and quantifies the fraction of high-momentum annihilations to other annihilation events. The most commonly used S parameter is defined as the ratio of events in a specified energy range of the peak to the total 511 keV events. Inside vacancies and voids, the positron tends to annihilate with lower-momentum electrons (fewer core electron annihilations) and yields a higher S parameter, and a lower W parameter. Thus the S and W parameters can reveal interesting and useful information about the void/vacancy information of the materials. A DBS study of the fracture face of bulk metallic glass specimens will be presented in the Appendix C.

The availability of low energy positron beams extended the capability of PAS techniques. Studies of very thin films requires the beam-based version of the various PAS techniques. The low mono-energetic positrons only penetrate several hundreds of nanometers into the material, the depth that is needed for thin film studies. Moderation from beta decay energies and slow positron beam transportation must be used in order to provide the focused low monoenergetic positrons. The study

of moderator materials has been going on for decades and there has been plenty of research on the material of positron moderator since 1950 [53]; a good review can be found at [52]. Originated from the Sodium-22 source, the high energy positrons rapidly lose energy and thermalize after they hit the moderator, wherein most of the positrons directly annihilate with surrounding electrons. However, a small fraction of the positrons can diffuse back to a surface and be re-emitted into the vacuum due to the *negative* positron work function of the moderator material. Currently, moderators made by tungsten or nickel can achieve moderation efficiency around 0.1%. The re-emitted positrons have energy of only several eV, and can be collected and transported to a target by electric or/and magnetic fields.

### 2.2.3 Michigan beam-based DBS and PALS

In the Michigan positron group, beam-based PALS and DBS are used in a variety of subjects from porous thin films, polymer nanocomposites and microencapsulation, to bulk metallic glasses. Currently, the porous low-$k$ films are several hundred nanometers in thickness, and some of them are inhomogeneous in depth, so PALS using a focused low energy beam of positrons becomes a necessity. The adjustable positron energy can implant positrons into different mean depths of the film for depth profiling. Because positrons can be produced either by radioactive decay ($\beta^+$ decay) or by pair production, there are also mainly two ways of making low energy positron beams. Figure 2.3 shows the apparatus of beam-PALS in the Michigan positron group. A $^{22}$Na radioactive source (half-life 2.6 years) is used as the positron source, which is commercially available with an activity of $\sim$60 mCi. The cylindrical source is placed on a manipulator that can be moved up and down with good precision. The $\beta^+$ decay emits positrons with a broad energy range peaked at 178 keV simultaneously with a 1.28 MeV gamma ray. We used thin nickel foil (5 micron thick) that

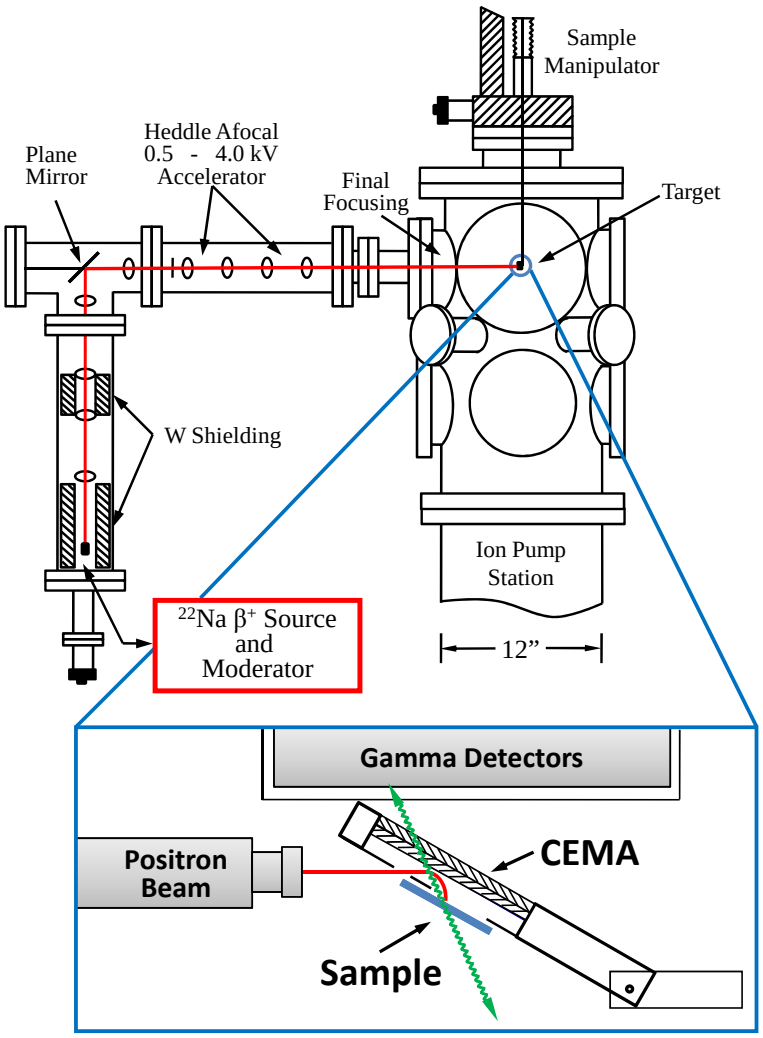


Figure 2.3: Low energy positron beam at the Michigan positron group

has been highly annealed over time and has a re-emission efficiency around $5 \times 10^{-5}$. The $^{22}$Na source is adjusted to a distance of 0.07 mm from the moderator. The re-emitted positrons have energy of several electron volts and are transported and focused to the target by electrostatic lenses. The positrons enter the target chamber with rate $3 \times 10^4$ to $6 \times 10^4$ counts per second. The electrostatic lenses can control the energy of the positron beam and at the same time focus the beam down to $\leq$2 mm in diameter in the target chamber. The energy of the positrons can be tuned from several hundred eV to 5 keV. The positron beam is bent 90° towards the front of the

chamber and the samples on the sample holder are facing to the back of the chamber at 45° (see figure 2.3). This geometry makes the implantation angle of positrons 45° as well. The bend of the positron beam makes the image size on the sample bigger, around 3∼5 mm in diameter.

The sample holder can be moved up and down using the manipulator shown in the figure. Various on-sample voltages can be applied through the sample holder to extract positrons onto the sample and help to reduce noise. *In-situ* heating can also be done using a heating stage sample holder, with heating element installed. The temperature can be monitored by the thermocouple attached to the back of the sample. It is found that at temperatures lower than 300°C, the temperature difference between sample front surface and the heating element can be safely ignored. When positrons hit the surface of the sample, secondary electrons that received the energy are ejected and accelerated by the same electric field that deflected the positrons through 90°. These secondary electrons are detected in the channel electron multiple array (CEMA) which is placed behind the sample. Because the exact birth time of positrons or positronium is unknown, we take the amplified signal of the secondary electrons as the start signal for a Lecroy time-to-digital converter (TDC). The CEMA is placed as close as possible to the sample surface so that the time of flight of the secondary electrons is effectively negligible. The stop signal for the TDC is obtained from the detection of any one of the gamma rays emitted by the annihilation of the positron or positronium in the photo scintillator/phototube. The digitized signal from the TDC can then be used as the input of an annihilation events-lifetime histogram.

## 2.3 PALS as a pore characterization technique

Ps lifetime and its conversion to pore size are the essential elements in the PALS technique. Once the lifetimes are fitted, they can be converted to pore sizes using quantum mechanical models. PALS is capable of studying pores in the 0.3 nm-30 nm diameter range. The one-to-one correlation between Ps lifetime and pore size is examined and confirmed by various other techniques in a series of round robin comparisons.

### 2.3.1 Ps annihilation lifetime spectrum and fitting program

A typical spectrum consists at least two lifetimes convolved with the spectrometer's time resolution. The shortest lifetime which is normally less than 0.5 ns is due to the fast annihilating components. Figure 2.4 shows two typical spectra: one from a sample with totally open pores with all the Ps inside the film effectively escaping the film surface and annihilating in vacuum, which yields a 142 ns Ps lifetime; the other is from the capped counterpart of that sample with all the Ps confined within the pore networks in the film, which produces a 37 ns Ps lifetime. In figure 2.4, the random background noise has been subtracted uniformly from both spectra, and then they have been normalized with respect to their peaks. The resolution of the spectra is decided by a number of factors. the full width at half-maximum (FWHM) of the prompt peak for our positron beam is around 0.5 ns. It can be approximately fitted by a Gaussian peak with different left and right hand exponential flanks, which are designated by $\tau-$ and $\tau+$. In beam based PALS, because the resolution is relatively lower than in the bulk system, the shortest lifetime we normally fit from spectra is around 0.3-0.5 ns. The fast annihilating positrons and p-Ps have short lifetimes around 100 picosecond and can be crudely taken as the

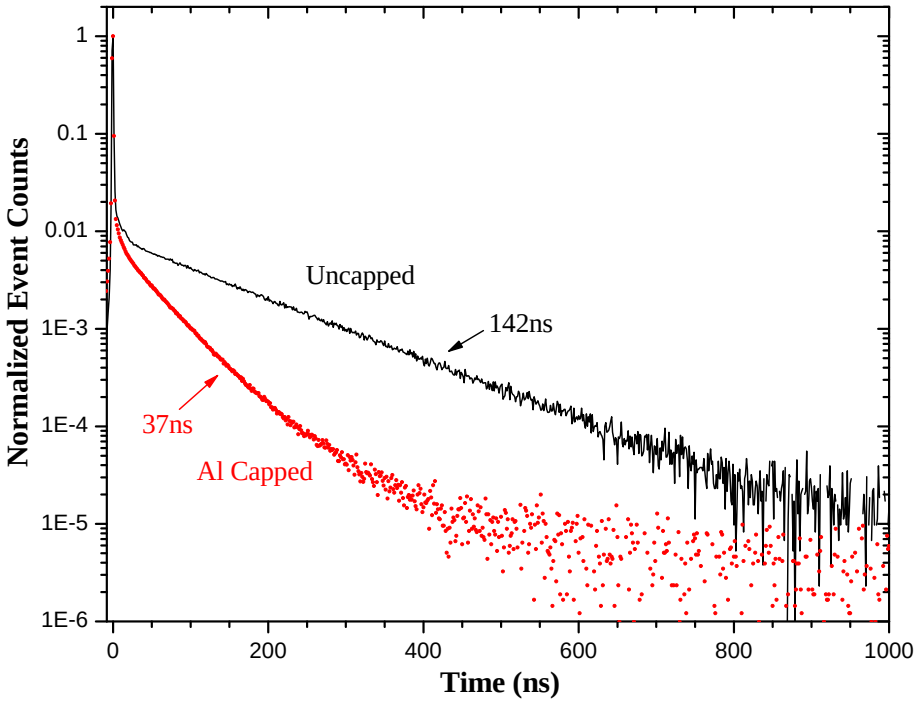


Figure 2.4: PALS spectra of an uncapped (black curve) and capped (red dots) porous organosilicate low-$k$ thin film of 30% porosity. Both spectra have been subtracted uniformly by the background noise, and then normalized according to their peaks respectively. The uncapped sample shows an obvious 142 ns vacuum Ps lifetime, indicating the Ps escaped from the sample. The capping layer on the other sample confines the Ps within the film, which yields a 37 ns Ps lifetime that associated with the specific Ps mean free path.

fastest exponential decay in our spectrum. We are mainly interested in the other longer lived components that correspond to o-Ps lifetimes that reflect different sized pore populations in nanoporous materials. There is always a ubiquitous 142 ns o-Ps lifetime which comes from o-Ps annihilating in vacuum, either from escaped Ps or from the backscattered slow Ps.

In our studies, the fitting routine, POSFIT [54], is normally used to fit the discrete lifetimes in the spectrum, and can fit as many as five coexisting exponential components. If the total number of annihilation events (or the total number of annihilating positrons) in a spectrum is designated by $N_{tot}$, then $N_{tot} = \sum_i N_i$, where $N_i$ is the number of annihilation events in the $i$th lifetime component. The intensity of the $i$th annihilation component, $I_i$, will be normally defined as the fraction $N_i/N_{total}$.

From time zero (the prompt peak), the time varying decay events at time $t$ (within an infinitesimal period of time) is,

$$\mathrm{d}N_{tot}(t) = N_{tot} \sum_{i=1}^{n} I_i \exp\left(-\lambda_i t\right) \lambda_i \mathrm{d}t, \tag{2.8}$$

where $I_i$ is the relative positron/Ps intensities that corresponds to the decay rate $\lambda_i$ and the fitted lifetime $\tau_i = 1/\lambda_i$. Consequently from equation 2.8, the number of events corresponding to a specific channel of finite width $\Delta t$ will be $\Delta N_{tot} = N_{tot} \sum_i I_i(\mathrm{e}^{-\lambda_i t} - \mathrm{e}^{-\lambda_i (t+\Delta t)})$. This is basically the same expression given in equation 2.8 to the first order. The digitizer can acquire 8000 channels with a minimum time per channel of 0.15625 ps, which means the channel width $\Delta t = 0.15625$ ps. In practice we store data in 1000 channel spectra: a short buffer of the first 156.25 ps of the spectrum; and a long buffer in which 8 channels are added together to accumulate counts in a wider time range with lower resolution and thus has a resolution of 1.25 ns and a range up to 1250 ns away from the prompt peak. In a typical spectrum, these two types of buffers are complementary and useful under different situations. The short buffer emphasizes the fast decaying, short-lived components originated from sub-nanometer voids, or the so-called micropores. But it has limitations when looking at long lived or vacuum Ps components, with lifetimes of tens to more than a hundred nanoseconds, where the important role of the long buffer comes into play.

Other issues need to be noted when fitting an annihilation spectrum. The fraction of backscattered Ps is found to be inversely related to the implantation energy of positrons. It is normally seen that the spectrum fitting deviates from pure exponential components at low positron beam energies. The annihilation component from the fast backscattered positrons and Ps, which is quite system dependent, normally can be handled fairly well by a 6-8 ns lifetime component with its intensity inversely related to the beam energy. Besides the fast backscattered Ps, slow-backscattered Ps

atoms are able to escape the sample surface with a lifetime close to 142 ns. The intensity of these backscattered slow Ps also varies inversely with implantation energy and should be correctly subtracted when acquiring the Ps escape fraction from the open pores. Surface roughness and chemistry also affect the intensity of backscattered Ps. In our experience, rough surfaces tend to backscatter more Ps.

Discrete fittings of the annihilation spectra is not always sufficient. To fit a broad distribution of lifetimes, *continuum* fitting is then more useful. Without assuming a number of discrete annihilation lifetimes ($i$=1 to n, see equation 2.8), the continuum lifetime fitting program, CONTIN [55, 56], assumes the annihilation events come from a continuum distribution of decay rates such that

$$N_{tot} = \int_0^\infty \frac{\mathrm{d}}{\mathrm{d}\lambda} N(\lambda)\mathrm{d}\lambda. \tag{2.9}$$

Then in time space the integral of the product of decay rates and their relative intensities are shown in equation 2.10,

$$\mathrm{d}N_{tot}(t) = \int_{\lambda=0}^\infty \frac{\mathrm{d}N(\lambda)}{\mathrm{d}\lambda} \lambda \exp(-\lambda t)\mathrm{d}\lambda\mathrm{d}t, \tag{2.10}$$

where $\lambda = 1/\tau$. Given the number of counts in each channel, $\Delta N_{tot}(t)$, CONTIN can actually produce a *plausible* continuum lifetime distribution (as many as 41 bins/lifetimes). However, the uniqueness of the fitting is determined by a free "regularization" parameter, which actually determines the "smoothness" of the fitting results. Complementary techniques and discrete fitting results will help to determine the continuum fitting results. From the distribution of decay rates or lifetime distribution, we can determine the pore size distribution using the calibration models which will be mentioned later.

### 2.3.2 Pore size calibration and round robin comparison

PALS is used as a successful pore characterization technique, with its fundamental concepts based on a one-to-one correlation between Ps decay rates (or lifetimes) and the pore sizes/diameters where Ps annihilates. This correlation originated from the basic physical principles of how Ps behaves within nano-voids. When o-Ps (the electron and the positron have the same spin) annihilates in media or voids/vacancies within media, the lifetime of o-Ps is reduced by its interaction with the environment. The bounded positron of the o-Ps can annihilate with a molecular electron with an opposite spin from the media through the $2\gamma$ decay channel, which allows a much higher decay rate, such that the effective decay rate of the original Ps is higher. This extra Ps annihilation decay rate ($\lambda_{\text{pickoff}}$) in addition to the intrinsic vacuum o-Ps decay rate ($\lambda_{\text{vac}}$) is called the pickoff annihilation rate (see equation 2.11). The reduced (by pickoff quenching) Ps lifetime is closely related to the probability of the bound positron finding an electron with opposite spin, which is directly correlated with the pore size when o-Ps annihilates in voids,

$$\lambda = 1/\tau = \lambda_{\text{vac}} + \lambda_{\text{pickoff}}. \tag{2.11}$$

The Tao-Eldrup (TE) model [57, 58] was first developed to calibrate Ps lifetimes (several nanoseconds) with the sizes of micropores. In this model, Ps inside a pore is simplified as a two-electron mass quantum mechanical particle with no charge. The pore is regarded as an infinitely deep potential well with the electron clouds extending into the wall to a certain distance $\Delta$R. Within this inner "skin" region of the pore, the intrinsic 142 ns o-Ps lifetime is reduced to the spin-averaged value of 0.5 ns, while outside this region, it is not affected. Therefore the overall Ps decay rate is the time average (or probability weighted average) of the vacuum annihilation

rate and the pickoff rate. The only free parameter, ΔR, is empirically determined to be around 1.6-1.7Å. The overall annihilation rate is given in equation 2.12

$$\lambda_{o-Ps} = \lambda_b \left[1 - \frac{R}{R+\Delta R} + \frac{1}{2\pi}\sin\left(\frac{2\pi R}{R+\Delta R}\right)\right] + \lambda_t, \tag{2.12}$$

where $\lambda_b$ and $\lambda_t$ are o-Ps annihilation rate in the bulk and vacuum respectively. $\lambda_b$ is usually assumed to be equal to the spin-weighted average of o-Ps and p-Ps intrinsic decay rates,

$$\lambda_b = \frac{1}{4}\lambda_s + \frac{3}{4}\lambda_t, \tag{2.13}$$

where $\lambda_s = 8\times10^9 s^{-1}$ and $\lambda_t = 7.04\times10^6 s^{-1}$ [34]. Sometimes, the $\lambda_t$ can be regarded as a small quantity and ignored due to the much larger rate $\lambda_s$.

The TE model works well for sub-nanometer pores. However, with only the ground state of the Ps particle in the potential well taken into account, the TE model is insufficient to calibrate larger pores when the pore size is then comparable to the DeBroglie wavelength of thermalized Ps (about 6 nm) and Ps thermally excited states in the well are also accessible by thermal activation. Therefore, to correlate the Ps lifetime of mesopores with their pore size, a modified model which accounts for Ps excited states within the well, such as the temperature dependence of the sample, should be considered. The modified Tao-Eldrup model [59–61] with the ability to characterize pores bigger than 2 nm, as well as micropores, was developed using the rectangular potential well and a Maxwell-Boltzman distribution of the Ps energy states in the well.

The actual pore geometry is presumably complicated and cannot be described as ideal shapes like spheres, rectangles or cylinders. This extended TE model uses a rectangular potential well to correlate the Ps lifetime to pore diameter, thus it is also called the rectangular Tao-Eldrup (RTE) model. It is useful to convert the Ps lifetime

vs. pore size calibration curves from a pore shape-specific dimension to a classical mean-free path (MFP), $l = 4V/S$, where $V/S$ is the pore's ratio of volume to surface area. As the mean distance between Ps pore wall collisions, the mean-free path is a linear measure of pore size that is not specific to any particular pore geometry. From the RTE model, the temperature dependence of Ps lifetime can be calculated and figure 2.5 shows the pore-size calibration curve at different temperatures. At K=0, there is only a ground state of the Ps in the potential well and the curve is exactly the TE model. By adjusting the only one universal parameter, the RTE model agrees with TE model as well as experimental data in the small pores regime (Tao-Eldrup regime in figure 2.5), and has also demonstrated good agreement with experimental results in the intermediate and classical regime [62]. Several calibration curves from the RTE model at different temperatures are presented in comparison to the TE model in the figure as well.

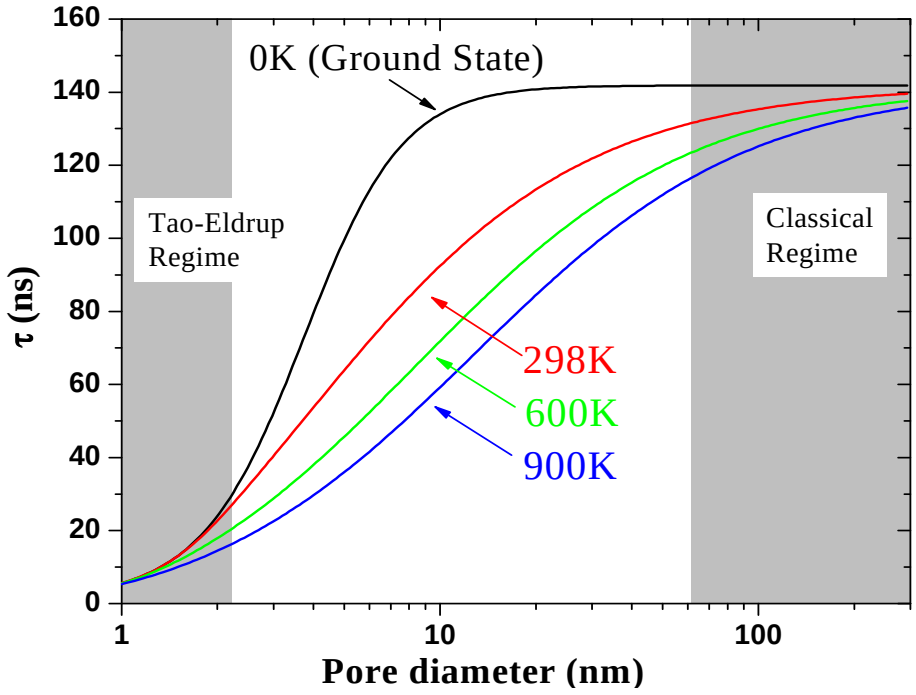


Figure 2.5: Pore size calibration curves calculated at different temperatures, using the rectangular Tao-Eldrup model. The ground state curve agrees with Tao-Eldrup.

In addition to the conversion from discrete lifetimes to pore size or mean free path, it is important to develop a model to determine the pore-size distribution from the results of continuum fitting. CONTIN fitting gives the distribution of $\tau$, or the number of annihilation events over different $\tau$'s. However, we need to convert this into a geometry-independent volume distribution over pore size (or mean free path). This can be done by assuming the linear relationship between pore (potential well) trapping rate and pore surface area [63]. PALS results of different MSSQ films at different temperatures confirm the consistency of pore size distribution and give reasonable relative volume fractions in a bimodal pore distribution [64]. The peaks of PSDs are normally in good agreement with the average pore sizes determined from discrete fitting.

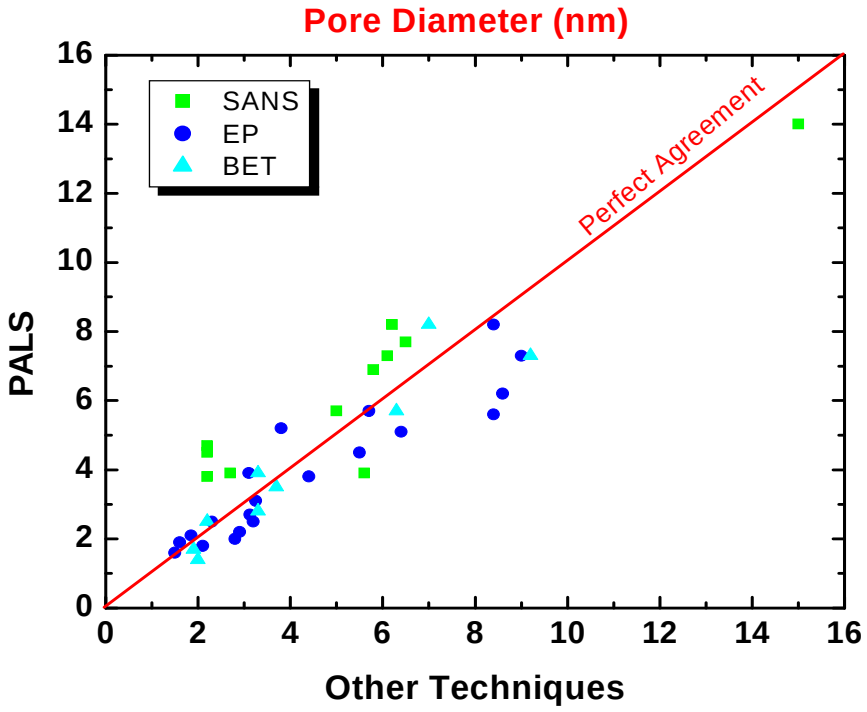


Figure 2.6: Round robin comparisons between PALS technique and other techniques.

Over the years, systematic round robin comparison experiments have been conducted between PALS and other techniques [62]. The same samples provided to dif-

ferent techniques were characterized by independent measurements before the comparisons are made. The traditional $N_2$ adsorption technique (BET) is conducted on the bulk counterpart of the specific samples. In figure 2.6, the comparison results are summarized. It is noticed that EP at larger pore size region tends to give larger values than PALS, while SANS, on the other hand, gives smaller values at lower pore diameter region. Overall, the agreement between PALS and other techniques is quite good.

In the nanoporous materials we study, Ps diffusion is an important aspect closely related to the fitted Ps annihilation lifetimes and their corresponding pore sizes. Under certain conditions, the Ps overall decay rate also needs to include a Ps "disappearance" rate. Since Ps has lower energy levels in a broader potential well (bigger pore) than in a narrower one, pore interconnectivity can allow Ps to escape into bigger pores from smaller pores where this Ps disappearance acts as an extra decay rate. The shortening of the fitted Ps lifetime is also seen in the pores when the film is open. A capping or barrier layer is always needed to confine the Ps within the material and reveal the "true" Ps lifetime in the interconnected mesopores. Sometimes this effect is also descriptively called the Ps "drainage" effect, which includes both the Ps draining from micropores into mesopores and the escape from interconnected mesopores to vacuum. A fully quantitative description of this disappearance rate is not forthcoming because it depends on all the unknown details of Ps diffusion within the porous materials.

Recent studies [65] have also shown that the confined Ps lifetime in voids can also be affected by surface chemistry of pore walls. This pore surface effect needs to be taken into account properly by varying the $\Delta$R parameter in the conversion models when comparing the pore sizes in dramatically different chemical environments.

### 2.3.3 Ps intensity and $3\gamma/2\gamma$ detection efficiency

Besides the information of pore size and PSD deduced from the Ps lifetime to mean free path conversion, the fitted Ps intensities also play very important roles in the characterization of pore structures. Unlike the quite universal calibration of Ps lifetime (or decay rate) with pore size, the relationship between the fitted Ps intensity with the film porosity is more complicated. This is due to the rather complicated Ps formation mechanism in different materials. In addition to porosity, Ps intensity is determined by a number of other aspects of the material, including its pore size, chemistry, and free radicals. Therefore, the absolute porosity is difficult to determine solely from the fitted Ps intensity.

Under certain circumstances, using a series of samples with constant film chemistry, we can indeed correlate the fitted Ps intensity to porosity. The evolution of fitted Ps intensity according to porogen loading fraction and *in-situ* curing temperature will also give novel insight of the ULK materials, which will be discussed in chapters three and four. Although it is difficult to take the fitted Ps intensity as a gauge of absolute porosity, relative Ps intensities in different pore populations and their changes with porosity are still very useful in understanding the pore interconnection length, pore structure evolution (without any drastic chemical change) and Ps diffusion from smaller pores to larger pores.

Before we can compare the fitted Ps intensities in different pore populations meaningfully, another factor that could affect the observed Ps intensity needs to be properly considered. In order to compare the relative Ps intensities from different locations, the annihilation photons from both the $2\gamma$ decay events (due to the pickoff annihilation in pores) and $3\gamma$ decay events (mostly from vacuum Ps annihilation) need to be detected with the same efficiency by the gamma detectors. However, due

to the bigger phase space of $3\gamma$ events, the annihilations of $2\gamma$ and $3\gamma$ events are detected with different efficiencies. It is important to correct for the higher detection efficiency of the $3\gamma$ events before comparing Ps intensities in all the short and long Ps lifetime components. The detection efficiency from the $3\gamma$ annihilation events is found to be approximately 1.2 times the efficiency of $2\gamma$ events. A detailed discussion of determining the $3\gamma/2\gamma$ efficiency ratio is in appendix B. The Ps vacuum intensity can be simply divided by 1.2 to compensate the higher detection efficiency of $3\gamma$ annihilation events. Although the Ps intensity from mesopores also needs to be adjusted, this adjustment is normally small, since the mesopore lifetime is an average of intrinsic vacuum lifetime and $2\gamma$ annihilation. A 20 ns lifetime has only about 15% $3\gamma$ events, which then produces an overall correction factor of only 1.03 and can therefore be neglected. In later chapters, the quoted numbers of "corrected Ps vacuum intensities" will normally refer to the Ps intensities that have first had the Ps backscattering subtracted, and then divided by 1.2 to account for the detection efficiency difference. The Ps intensity of other lifetimes is typically not corrected by this detection ratio.

### 2.3.4 Depth profiling capability

One unique and crucially important feature of beam-based PALS and DBS is the depth profiling capability. The low energy and mono-energetic positron beam makes the study of very thin films possible. Furthermore, by implanting positrons into different depths into materials, one has the capability of studying the characteristics of inhomogeneous materials. The positron penetration depth, which is also called stopping depth, depends on both the positron initial energy, E, and the material density, $\rho$. This stopping distribution has been studied by both Monte Carlo simulations and by many experiments [21, 66–68]. If only a uniform and continuous material is con-

sidered, the implantation profile $P(x)$ as a function of depth $x$ can be estimated as a Makhovian distribution with different coefficients at different energies. The depth dependence and the mean implantation depth is shown in equations 2.14 to 2.16,

$$P(z) = \frac{mz^{m-1}}{z_0^m} \exp\left[-(z/z_0)^m\right], \tag{2.14}$$

where $z_0$ is the penetration parameter:

$$z_0 = \frac{\bar{z}}{\Gamma[(1/m)+1]}, \tag{2.15}$$

and $\bar{z}$ is the mean stopping depth,

$$\bar{z} = \frac{40E^{1.6}}{\rho}, \tag{2.16}$$

which depends on the implantation beam energy and m is the shape parameter which is normally taken as 2 ($\Gamma[3/2] = \sqrt{\pi}/2$) [21].

The depth profile of positrons determined by the Makhovian distribution is a bell-shaped distribution with its maximum at $\sim \bar{z}$ with FWHM $\sim \bar{z}$. The Makhovian distributions of positrons at different energies, from 1.1 keV to 5.0 keV, are shown in figure 2.7. As is clearly seen at low energies, the distribution is narrow and close to the film surface, which means excellent resolution to near-surface features. As implantation energies increase, the positron distribution becomes broader and extends deeper into the material. It roughly extends from the surface of the film to twice as deep as the mean implantation depth.

When positrons have a short diffusion length (typically in porous materials), the Ps formed by the locally restricted positrons also have similar depth distributions. The Ps annihilation including the positrons' direct annihilation reveal the depth-dependence of the material properties. Depth profiling is very useful when studying nanoporous materials, especially inhomogeneous porous materials. If the nanopore

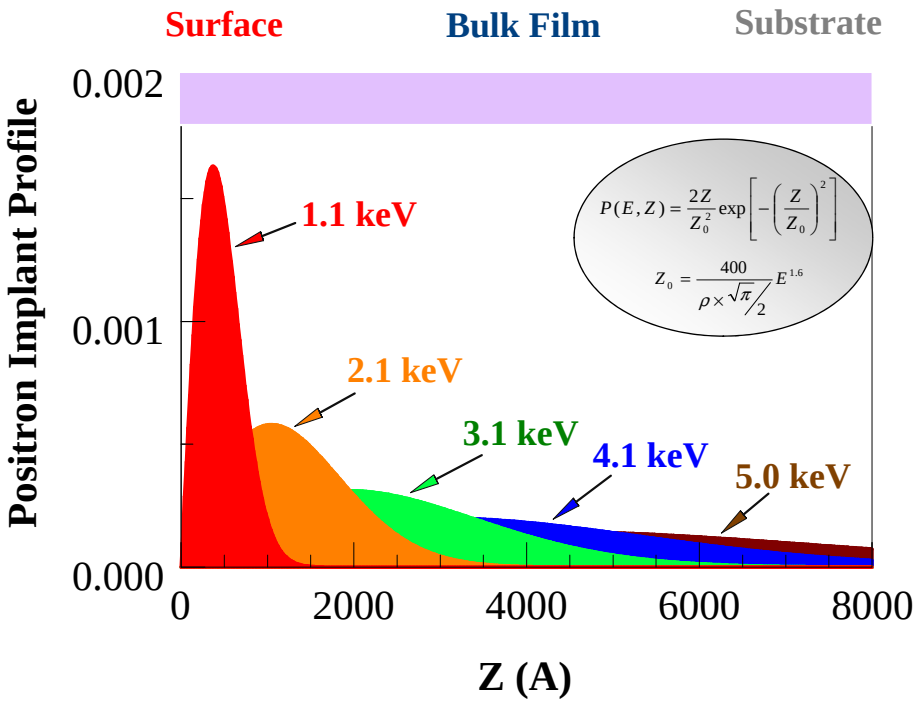


Figure 2.7: Makovian distribution of positrons implantation at different energies from 1.1keV to 5.0keV. The density of the material is assumed to be 1 g/cm$^3$.

structure is connected to the surface, Ps has a good chance to escape out of the material and annihilate in vacuum with a 142 ns vacuum lifetime. A corresponding Ps escape fraction, $F_{esc}$, of the total Ps intensity can be calculated. With regard to beam energies, fewer Ps atoms can escape the film at higher beam energies (with deeper implantation depths). By adjusting the beam energy, a 50% Ps escape fraction can be found at certain mean implantation depth, which is defined as the pore interconnection length, $L_{int}$, of the film (see figure 2.8).

$L_{int}$ is effectively the deduced Ps diffusion length in the porous network. To obtain $L_{int}$, several positron beam energies are typically needed to reveal the trend of Ps escape fraction versus depth. The Ps escape fraction is calculated using the mesopore Ps intensity divided by the total Ps intensity both in mesopores and in vacuum. Specifically for a porous ULK media, when more porogen is mixed with its

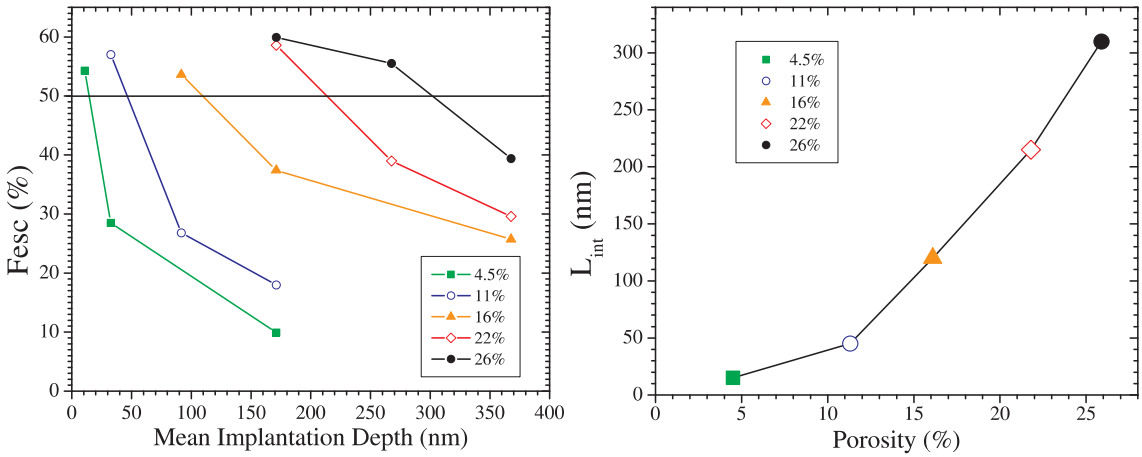


Figure 2.8: Plot of the Ps escape fraction ($F_{esc}$) as a function of mean positron implantation depth (left), and the mean depth at which the curves cross $F_{esc}$=50% are taken to be the pore interconnection lengths ($L_{int}$) of a series of films with different porosities (right).

matrix resin and fully cured, the pores begin to interconnect and form a network, from which it is easier for Ps escape. The rule of thumb is that higher porosity makes more interconnected pores and longer $L_{int}$. However, the porogen and matrix materials and their interactions can also largely affect the pore morphology even at the same porosity, and subsequently affect other features of ULK materials. Using PALS to investigate $L_{int}$ gives an important view of a porous films' interior structure and its change, which is one of the important aspects in ULK characterization.

## 2.4 Summary

In this chapter, several techniques other than PALS are briefly mentioned and their advantages and limitations are discussed. PAS as a unique technique using positrons to probe matter is discussed in detail. Two specific configurations of PAS, namely PALS and DBS, will be used extensively in the studies of this thesis. Beam-based PALS is the primary tool in our ULK characterizations in later chapters, thanks to its unique capabilities in probing nanopores of thin films and their depth dependence. PALS is particulary useful when the surface of the sample is closed

(non-porous) since positrons can be implanted into certain mean depths through the barrier layer.

The calibration of Ps lifetime with pore size is crucial in the pore characterization. The Rectangular Tao-Eldrup model has been demonstrated to be quite accurate in the round robin comparisons with other techniques and will be used extensively in the later chapters. Relating Ps intensity to porosity, unlike the direct link between Ps lifetime and pore size, is rather difficult. There is still quite fundamental information we can extract from Ps intensity, such as Ps escape fraction $F_{esc}$ and pore interconnection length $L_{int}$. Pore size and pore interconnection length are important parameters that we normally deduce in characterizing a film sample. Besides these factors, there is plenty of other information that we can obtain from PALS analysis, like PSD, heterogeneity information of the film, pore evolution according to *in-situ* heating and porogen loading, pore blocking effects, Ps drainage and chemical effects on Ps formation, etc. Therefore, PALS is a very unique and useful technique to study the pore morphology as well as its evolution in porous thin films. In the next chapter, the pore structure generated by several different types of porogens and its evolution with film porosity will be investigated using low energy beam-based PALS.

# CHAPTER III

# Study of nanopore characteristics using PALS

## 3.1 Introduction and motivation

The implementation of dense low-$k$ dielectrics, although has been postponed for years by the semiconductor industry, finally prevailed in the current 65 nm and 45 nm technological nodes. However, further shrinkage in the feature size of ULSI circuits requires even lower $k$ values for the interlayer dielectrics (ILD), which is difficult to achieve using dense materials. It is straightforward to incorporate porosity into dense dielectrics to make ultra-low-$k$ (ULK) ILD materials [69, 70]. A commonly used method is blending a labile pore generator (porogen) into the dense matrix resins. These porogen molecules, either in the form of nanoparticles or polymer aggregates to form a nanocomposite (nm-sized porogen domains in the resin), can be later removed by thermal and/or ultraviolet treatment and leave behind voids after matrix vitrification. However, the computer industry later noticed that the porous ULK material also raises tremendous integration problems related to the pore interconnectivity, its low mechanical strength and chemical stability, incompatible differential thermal expansion and many other aspects [6, 71]. For example, compared to their dense predecessors, the porous counterparts have much worse strength (<5 Gpa) at high porosity. At high porosity, the induced pores tend to be interconnected, which

permits copper diffusion and moisture absorption.

It is commonly accepted that the pore size in the ULK materials that could be successfully implemented should be no more than one tenth of the feature size. Since the industry will eventually be moving into 32 nm and 22 nm technological node, the engineered nanopores in the ULK materials should be no bigger than several nanometers. Furthermore, studies have shown that the size and the morphology of the engineered nanopores both significantly affect the performance characteristics of ULK materials mentioned above. Since these nanopores are originated from the sacrificial porogen that was mixed with the matrix resin, the final pore structure and its evolution with porogen loading depend greatly on the choice of porogen and matrix materials and their cohesive and adhesive interactions.

Ideally, the porogen domains should be separated from each other in the low-$k$ matrix, thus forming isolated nanopores with the size of the porogen domains. However, with increasing porogen concentration, the porogen-porogen interaction is enhanced, leading to greater aggregation of the porogen domains. Thus, lowering $k$ by increasing porosity reaches a limit when the pore structure becomes unacceptably open and susceptible to integration damage. Therefore, understanding the formation process of the engineered nano-voids and its morphology are critical in making viable ULK materials in integrated circuits (IC).

Characterizing the porogen-induced nanopores as well as their morphology is a huge challenge for characterization techniques. In this chapter, PALS is used to reveal the pore structure of a series of thin, amorphous ULK films in which the porogen concentration is increased. These spin-on dielectrics are fabricated using three different types of pore generators in a silsesquioxane (SSQ) matrix material. Their pore forming mechanisms associated with the porogen interaction and degradation

will be investigated using Beam-based PALS, which provides direct information on the pore size and pore interconnection length, $L_{int}$. The results of this chapter have been published in Applied Physics Letter [72].

## 3.2 PALS experiments on ULK materials made by three types of porogens

The porous SSQ low-$k$ films are prepared with three porogens of different functional groups. PALS is then utilized to deduce the mean free path (MFP), and $L_{int}$ of the pores. As the porogen content of a film is increased, the morphological evolution of the pore structure left by the porogen provides critical input as to how the porogen molecules aggregate, eventually leading to film percolation (a porous network throughout the film).

The detailed experimental procedure for making the porous SSQ films has been published elsewhere [73]. A modified cyclic SSQ (mCSSQ) with controlled Si-OH content is used as the low-$k$ matrix precursor [74]. Solutions of the mCSSQ precursor and porogen of varying weight loadings [using propylene glycol methyl ether acetate (PGMEA), as the solvent] were spin coated onto a silicon substrate. Porous films were then made after successive hot-plate bakes at 100°C and 250°C followed by final curing/degradation in a vacuum furnace held at 420°C. The film thickness (nominally 1 micron) and refractive index were measured by a surface profiler and a prism coupler. The *porogen-induced porosities (p)* of the films are calculated from the Lorentz-Lorenz equation and the measured refractive index of a pure matrix film which defines $p$=0.

The model porogens, whose chemical structures are shown in figure 3.1, consist of two modified cyclodextrins (tCD and sCD) and one calix-arene (CA[6]) that have been demonstrated to be promising supramolecular pore generators [73]. The CDs

are cyclic oligosaccharides consisting of six glucopyranose units that are joined together by $\alpha(1\rightarrow4)$ linkages. CA[6] is a six-member arene ring with acetoxyl and *tert*-butyl groups. All of the porogen molecules assume a truncated cone structure. For the CDs, the rigid core has a maximum diameter of ∼1.5 nm and a height of ∼0.8 nm [73]. The corresponding dimensions of CA[6] are slightly larger at 1.6 nm and 0.9 nm [75, 76].

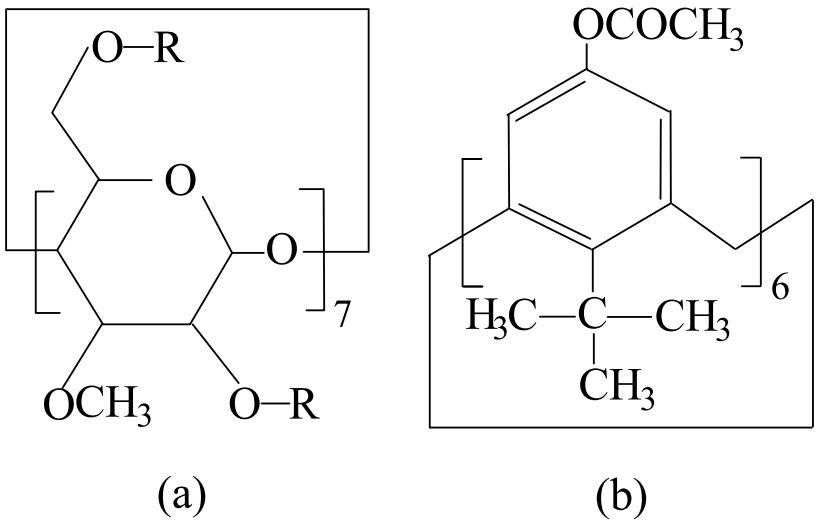


Figure 3.1: Chemical structures of the porogen molecules: tCD, Heptakis(2,3,6-tri-O-methyl)-$\beta$-cyclodextrin, (a)tCD with R=$CH_3$; sCD, Heptakis(3-O-methyl-tetradecakis-2,5-di-O-[3-(trimethoxysilyl)propyl]-$\beta$-cyclodextrin, (a) with R=(trimethoxysilyl)propyl; and (b) CA[6] 5,11,17,23,29,35-hexa-tert-butyl-37,38,39,40,41,42-hexa-acetoxyl calix arene, (b).

### 3.2.1 mCSSQ and tCD porogen

PALS experiments are first conducted on the 0% porogen-loaded mCSSQ pure matrix. Since there are no porogen-induced pores in this film PALS analysis of the matrix allows us to directly probe the micro-porosity inherent to the host material. The PALS spectra of this matrix film are fit with two short Ps lifetimes of ∼2.5 ns and 7 ns, which correspond to micropore diameters (spherical pore model) of 0.6 nm and 1.1 nm respectively. These lifetimes are quite typical of MSSQ's. The Ps formation

intensity in these two short lifetime components are about 11% and 27% respectively for a total Ps formation fraction of 38% (i.e. 38% of the incident positrons form Ps in the film - a very typical fraction). Since over 70% of the Ps formed in the film annihilates from the larger 1.1 nm pores we conclude that this matrix has rather high microporosity owing to its large micropores. For comparison, a typical organic polymer with about 5-7% "free volume" would also have ∼38% Ps formation with all of it in the short lifetime component (no 1.1 nm pores). Thus an EP-based estimate of about 10% matrix microporosity seems very reasonable to us. This matrix film was also used to determine the intensity of the backscattered Ps produced from the other porous films. The beam energy-dependent values of backscattered Ps are subtracted from the fitted intensity of Ps in vacuum. The quoted total Ps intensity produced in the mesopores (lifetimes > 15 ns), $I_{Ps,film}$, is the sum of the Ps intensity in the mesopores plus the backscatter-corrected Ps intensity in vacuum and is a relative measure of film meso-porosity.

The film thickness is nominally 1 micron. The tCD porogen *volume* loading (estimated from the matrix density, porogen density, and porogen weight loadings) starts at ∼5% and increases up to 50%. Details of the PALS methodology have been presented in chapter two. Briefly, on each sample, lifetime spectra are acquired at positron beam energies ranging from 0.55 keV to 5.0 keV which provide mean positron implantation depths ($\overline{h}$) of roughly 10 to 400 nm. These spectra require one very short positron lifetime and four Ps lifetimes for adequate fitting. The shortest two Ps lifetimes are 2.5 and 7 ns and correspond to 0.5-1.0 nm micropores inherent to the mCSSQ matrix. The longest component corresponds to the 142 ns vacuum annihilation lifetime of Ps. The nonzero intensity of this component after backscattering subtraction is attributed to Ps that has diffused out of the

film through interconnected mesopores. The typical backscattered Ps intensity we used are 1.1%, 1.4%, 2.0%, 3.2%, 6.7%, and 12% for positron implantation energies of 5.1 keV, 4.1 keV, 3.1 keV, 2.1 keV, 1.1 keV and 0.55 keV respectively. The fourth, intermediate lifetime component ranging from 12-60 ns corresponds to Ps annihilating in the porogen-induced mesopores. The intensity of this Ps component is zero from the matrix, and increases with porogen content (at the expense of the micropore Ps intensity), but then decreases at higher porosities as Ps escape into vacuum shifts its intensity into the 142 ns component. If Ps escape is still significant at high positron implantation energy, then a capped film was required to confine Ps to the interconnected pores.

Table 3.1: **Summary PALS results for the tCD films. The mesopore lifetimes in red are taken from capped films. The prefix A, B, and C refer to different batches of the samples received at different times.**

| Sample | Thickness (nm) | Porosity (%) | $\tau_{mesopore}$ (ns) | $I_{Ps,film}$ (%) | $D_{cylindrical}$ (nm) | $D_{spherical}$ (nm) | $L_{int}$ (nm) |
|---|---|---|---|---|---|---|---|
| mCSSQ | 1260 | 0.0 | matrix | — | — | — | closed |
| A/tCD 10% | 1285 | 7.7 | 17±1 | 24.0 | 1.45±0.04 | 1.71±0.05 | ≤ 5 |
| A/tCD 20% | 1193 | 13.9 | 19.5±0.5 | 30.0 | 1.54±0.02 | 1.83±0.02 | 20-25 |
| A/tCD 30% | 1144 | 18.3 | 24.2±0.5 | 30.7 | 1.71±0.02 | 2.05±0.02 | 50 |
| A/tCD 40% | 1417 | 19.4 | 25.3±0.5 | 31.1 | 1.76±0.02 | 2.39±0.02 | 65 |
| A/tCD 50% | 942 | 23.9 | 26.1±0.5 | 28.6 | 1.78±0.02 | 2.26±0.02 | 125 |
| B/tCD 05% | 1517.3 | 5.4 | 15.6±0.5 | 15.1 | 1.38±0.02 | 1.64±0.02 | closed |
| B/tCD 10% | 1446.4 | 8.5 | 17.2±0.5 | 28.2 | 1.44±0.02 | 1.72±0.02 | 5 |
| B/tCD 15% | 1330.9 | 13.5 | 17.5±0.5 | 32.2 | 1.46±0.02 | 1.73±0.02 | 25 |
| B/tCD 20% | 1334.1 | 15.9 | 20.2±0.5 | 33.1 | 1.56±0.02 | 1.86±0.02 | 52 |
| B/tCD 25% | 1183.8 | 18.1 | 21.2±0.5 | 35.9 | 1.60±0.02 | 1.90±0.02 | 70 |
| B/tCD 30% | 1318.1 | 20.7 | 23.7±0.5 | 34.1 | 1.70±0.02 | 2.03±0.02 | 82 |
| B/tCD 35% | 1038.7 | 21.8 | 24.9±0.5 | 32.1 | 1.79±0.02 | 2.09±0.02 | 85 |
| B/tCD 40% | 1095.4 | 24.6 | 26.9±0.5 | 31.4 | 1.81±0.02 | 2.18±0.02 | 140 |
| B/tCD 45% | 1003.6 | 28.6 | 32.9±0.5 | 34.7 | 2.04±0.02 | 2.49±0.02 | 210 |
| B/tCD 50% | 985.7 | 31.8 | 32.2±0.5 | 31.8 | 2.01±0.02 | 2.45±0.02 | 225 |
| C/tCD 05% | 1368.1 | 4.0 | 15.6±0.5 | 16.6 | 1.38±0.02 | 1.66±0.02 | closed |
| C/tCD 15% | 1215.7 | 12.5 | 20.2±0.5 | 27.2 | 1.56±0.02 | 1.86±0.02 | 20 |
| C/tCD 25% | 1191.3 | 20.7 | 25.5±0.5 | 30.8 | 1.76±0.02 | 2.12±0.02 | 115 |
| C/tCD 35% | 1177.4 | 28.8 | 29.4±0.5 | 29.8 | 1.91±0.02 | 2.31±0.02 | 220 |
| C/tCD 45% | 1037.4 | 37.9 | 32.9±0.5 | 29.5 | 2.04±0.02 | 2.49±0.02 | 390 |

Table 3.1 shows the summary PALS results of tCD/mCSSQ samples with vary-

ing porogen concentrations. Actually, three batches of samples with different tCD concentrations were measured using PALS (shaded in different colors in the table). We detect a total Ps formation fraction of about 38% (similar to that of the matrix) but now most of this Ps annihilates in the porogen-induced mesopores. These films produce a robust Ps intensity in the Ps lifetime component of 15.6 ns to 32.9 ns, which corresponds to a mesopore diameter of ∼1.5-2.0 nm (this is the cylindrical pore diameter or the mean free path of the pores in the film). The deduced cylindrical pore diameter increases gradually as a function of porogen loading fraction.

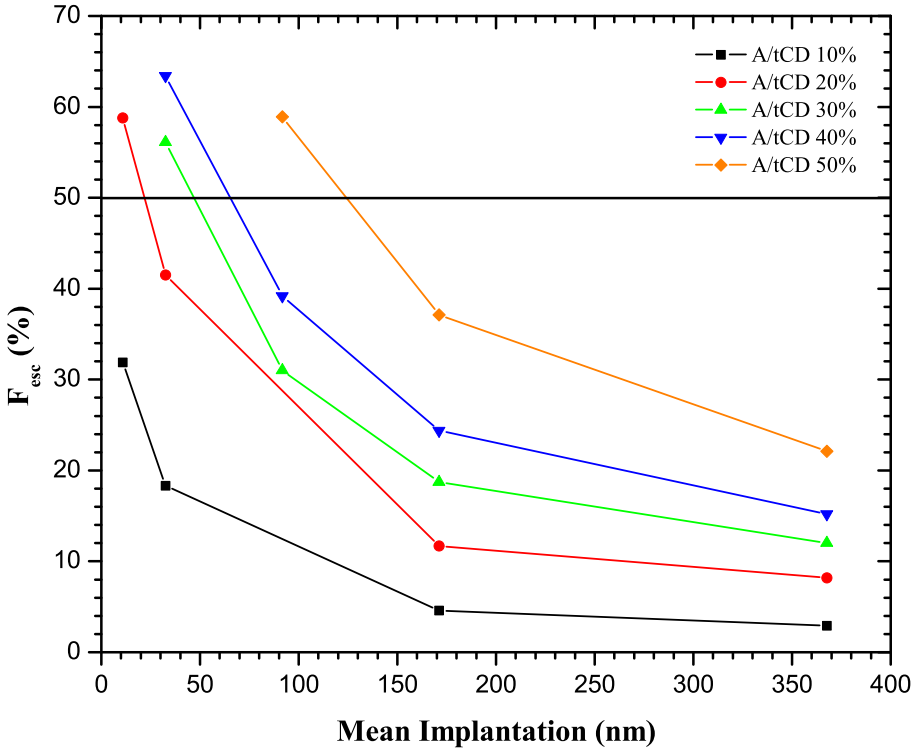


Figure 3.2: The Ps escape fraction as a function of mean positron implantation depth in the film for the tCD porogen. The mean implantation depth is calculated from the positron beam energy and is based on a film density of 1 g/cm$^3$. The interconnection length quoted in Table 3.1 is defined to be when the escape fraction has reached 50%.

The interconnection length of the pores is defined to be the mean implantation depth at which 50% of the Ps escapes from the mesopores into vacuum. The Ps

escape fraction, $F_{esc} = 1-(I_{meso}/I_{Ps,film})$, is determined at each positron implantation energy and plotted versus mean positron implantation depth in Figure 3.2. (Note that only the first batch of the tCD samples are shown in the figure. The other samples show similar $F_{esc}$ trends, thus are not plotted in the figure.) Figure 3.2 is used to determine the interconnection lengths by interpolating or extrapolating to 50% escape. The deduced pore interconnection lengths range from ∼5nm (essentially closed pores) for the 10% film to 125 nm for the 50% film (a porous network). These values are included in the summary table 3.1 and are later plotted in Figure 3.5 with other tCD films.

### 3.2.2 sCD porogen

Five samples using a sCD porogen with weight percent loadings of 10%, 20%, 30%, 40%, and 50% were then measured by PALS. Similar positron beam energies are used to probe the different depths of each film.

Table 3.2: **Summary PALS results for the sCD films.**

| Sample | Thickness (nm) | Porosity (%) | $\tau_{mesopore}$ (ns) | $I_{Ps,film}$ (%) | $D_{cylindrical}$ (nm) | $D_{spherical}$ (nm) | $L_{int}$ (nm) |
|---|---|---|---|---|---|---|---|
| sCD 10% | 1263 | 4.5 | 18.7±0.5 | 15.1 | 1.50±0.02 | 1.61±0.02 | 15 |
| sCD 20% | 1356 | 11.3 | 20.5±0.5 | 18.7 | 1.57±0.02 | 1.79±0.02 | 45 |
| sCD 30% | 1271 | 16.1 | 21.0±0.5 | 17.4 | 1.59±0.02 | 1.72±0.02 | 120 |
| sCD 40% | 1460 | 21.8 | 20.5±0.5 | 18.2 | 1.57±0.02 | 1.76±0.02 | 215 |
| sCD 50% | 982 | 25.9 | 20.5±0.5 | 19.7 | 1.57±0.02 | 1.84±0.02 | 310 |

The results for the films with the sCD porogen are shown in table 3.2 and detailed in Table D.1, appendix D. Compared to the tCD films, these films form less Ps overall (∼30% vs. 38%) with typically 10% (not shown in the table) in the micropores and 20% (shown in table 3.2 as $I_{Ps,film}$) in the mesopores. The micropore and mesopore intensities reach a constant by a porosity of 11.3% (the 20% film). The very interesting feature seen in figure 3.4 is that the pores are the same size (cylindrical pore diameter of ∼1.57 nm) regardless of porosity. The interconnection lengths are

significantly longer that those in the tCD films as seen in Figure 3.5.

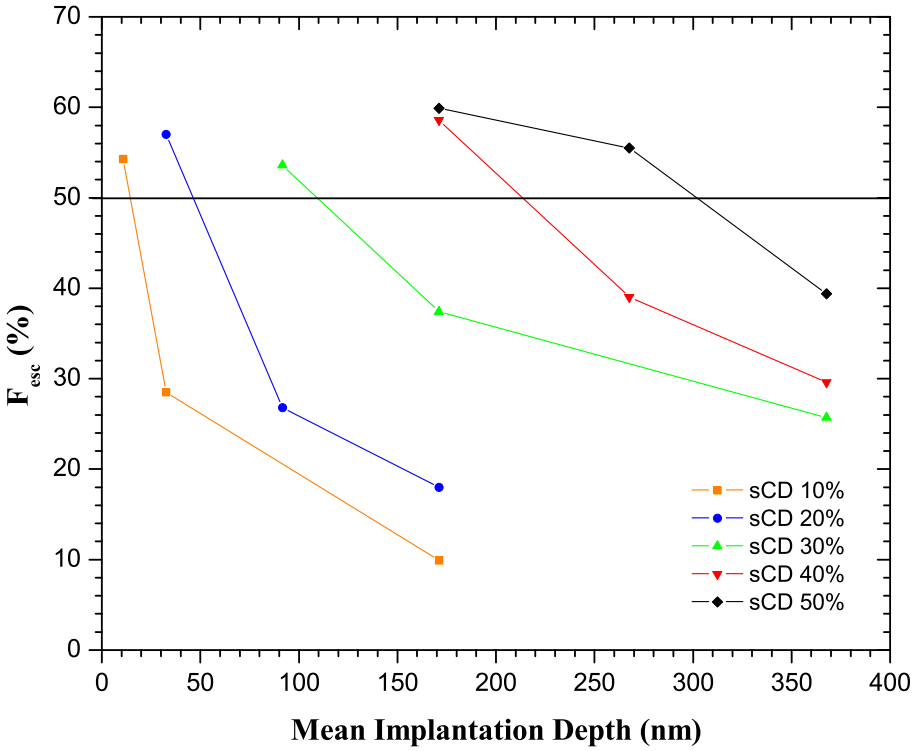


Figure 3.3: The Ps escape fraction as a function of mean positron implantation depth in the film for the sCD porogen. The mean implantation depth is calculated from the positron beam energy and is based on a film density of 1 g/cm$^3$. The interconnection length quoted in Table 3.1 is defined to be when the escape fraction has reached 50%.

The interconnection lengths quoted were determined using the same methodology as those quoted for the tCD films (see figure 3.2). Given the large interconnection lengths, however, there were some difficulties in determining the Ps escape fractions from the spectrum fitting. An alternate fitting procedure, using the shorter time range spectrum referred to as the "short buffer", produces shorter interconnection lengths of approximately 160 nm and 200 nm for 40% and 50% porogen loading respectively. These "short buffer" fits will tend to fit shorter lifetimes for Ps in the film, because of the micropores, and hence larger intensities. This results in a systematically lower $F_{esc}$ and thus these interconnection lengths quoted are lower limits. Using the same procedure for the 30% film results in consistent results for the

interconnection length of 120 nm. Regardless, the important conclusion is that the sCD porogen tends to produce interconnected pores of constant MFP and this may be due to an affinity for the porogen to linearly agglomerate (polymerize?) domains in the matrix. The reduction of Ps formation fraction from 38% to ∼30% suggests a chemical influence on Ps formation as if the sCD porogen has left a residue in the pores or at least induced a chemical change at the pore surface.

### 3.2.3 CA porogen

Four films with different CA[6] porogen loadings are examined using PALS. Analysis of the CA[6] films is more complicated than the CD porogen films. These films appear to have very large and highly interconnected pores. In fact, in the delayed spectrum fitting of the capped films given in appendix D, table D.2, Ps appears to be escaping from the film as evidenced by a measurable intensity of Ps annihilating in the longest lifetime component which normally corresponds to Ps annihilating in vacuum. There are two possible explanations for this observation. The first is that the capping barrier applied by SAIT has failed allowing some fraction of Ps to escape from the film. This would be the first capping barrier that SAIT provided that had failed. A second possibility assumes that the capping layer is good and that the pores in the film are so large that Ps effectively annihilates with the vacuum lifetime in the pore, and we are unable to distinguish it from vacuum Ps. The only conclusions we can draw from our standard analysis are that the interconnection lengths are long, 400 nm for 20% loading and fully interconnected for 30% and 40% loading. Only the 10% loading samples have a short interconnection length of 5 nm. Additionally, the lifetimes in the 10% loading film are shorter, requiring fitting of the full spectrum to three pore lifetimes the spectrum is fit to five lifetimes of which three represent Ps annihilating in the pores); the results are given in table 3.3. Only 10% of Ps

annihilates in the largest, 1.24 nm, pores.

Table 3.3: **Summary PALS results for the CA films.**

| Sample | Thickness (nm) | Porosity (%) | $\tau_{mesopore}$ (ns) | $I_{Ps,film}$ (%) | $D_{cylindrical}$ (nm) | $D_{spherical}$ (nm) | $L_{int}$ (nm) |
|---|---|---|---|---|---|---|---|
| CA6-10 | 1162.2 | 6.52 | 12.5 | 9.9 | 1.24 | 1.47 | <5 |
| CA6-20 | 1325.4 | 14.79 | 27, 65 | 21.1 | 1.82, 3.65 | 2.19, 4.88 | 400 |
| CA6-30 | 1309.1 | 28.72 | --- | 30.6 | --- | --- | percolated |
| CA6-40 | 1207.7 | 39.28 | --- | 22.3 | --- | --- | percolated |

This series was unique as the film made with 10% CA[6] had isolated pores the size of the porogen, while the film made with 20% CA[6] had much larger pores of 3.6 nm near percolation. Quite understandably, the films made with 30% and 40% CA[6] had percolated pores, and it seemed that the pores were so large that we had difficulty capping the films. We suspect that the CA[6] porogen, being amphiphilic, is able to form micelles beyond some critical concentration in the solution prior to spin-coating, so that the pores in the three higher porosity films can grow much larger than the size of a single CA[6] molecule.

## 3.3 Comparison and summary of the three porogens

In figures 3.4 and 3.5, we present the deduced MFP and $L_{int}$ versus porosity of the three systems. At all but the lowest porosities, we favor a cylindrical pore model as physically more reasonable given the nonzero values of $L_{int}$. However, the resulting MFP=$4V/S$, which is the cross-sectional diameter in a long cylinder, is only about 20% larger than the MFP deduced using a spherical pore model. (We are not a priori implying the pores are cylindrical.) The trends in the figure 3.4 and figure 3.5 suggest three distinct growth modes of porogen aggregation with concentration.

The sCD system clearly forms pores with constant MFP throughout the porosity range, despite the fact that $L_{int}$ increases rapidly with porosity. Even at low 4%

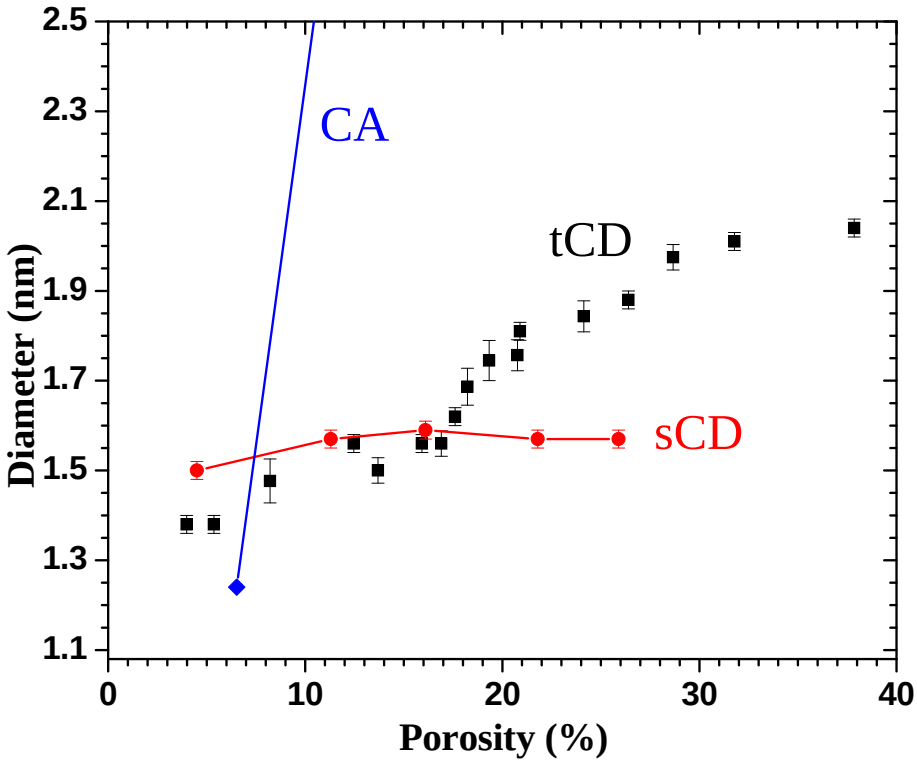


Figure 3.4: MFP vs porosity for films made with different porogens.

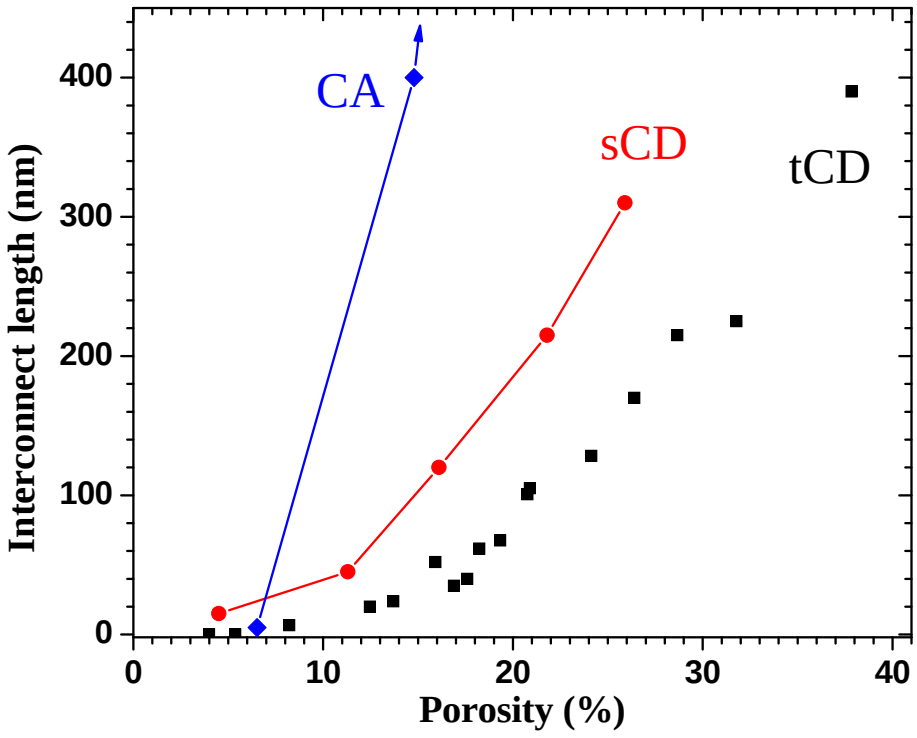


Figure 3.5: $L_{int}$ vs porosity for films made with different porogens.

porosity the 1.5 nm MFP pores have interconnection length ten times this value. The pores are clearly not isolated, but instead display the effect of strong linear polymerization of the sCD molecules through polycondensation. Apparently, water residue in the solvent/precursor or produced by condensation of the mCSSQ precursor promotes fast hydrolysis of the trimethoxylsilyl end groups, through which Si-O-Si bonds are formed between neighboring sCD molecules. The porogen domains are driven by strong covalent bonding to be cylindrical and increased porogen concentration simply lengthens them. The MFP of 1.5-1.6 nm corresponds nicely to the sCD ring diameter which becomes the cylindrical diameter of the porogen template as end-group bonding polymerizes the sCD rings axially. A schematic description of the pore structural evolution in the sCD system is shown in figure 3.6.

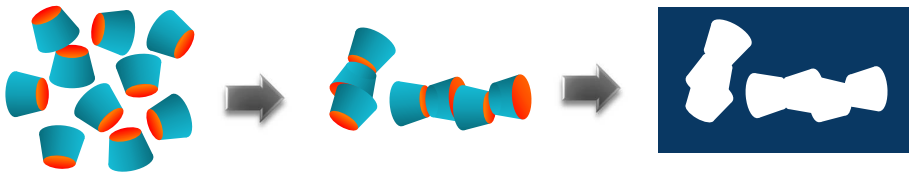

Figure 3.6: The pore structural evolution induced by sCD porogen. The sCD porogen domains are driven by strong covalent bonding to be cylindrical rods and increased porogen concentration elongates the cylindrical pores.

For the tCD porogen, figure 3.5 indicates that for $p \leqslant 5\%$ the tCD-induced pores are isolated since $L_{int} \approx 0$. For $p \geqslant 8\%$, pores start to interconnect and the size of pores continuously increases. The MFP of pores at low porosity, 1.3-1.4 nm, is larger than the calculated 4 V/S for a single tCD molecule, which is ~0.8 nm. However, a long cylinder is not a good model for isolated pores, so we should instead use a spherical pore model to convert the fitted Ps lifetime of 16 ns into a spherical pore diameter of 1.65 nm (MFP=1.1 nm). This size is consistent with *two* (1.0 nm) or three (1.15 nm) back-to-back tCD molecules, suggesting that tCD molecules are predominantly not singly dispersed even though no chemical bonding exists between them.

For molecules such as tCD, there are simulations and experiments demonstrating such self-assembly capability [77]. The preferred organization is neighboring tCD molecules align their bottom planes (or upper planes) parallel to each other through van der Waals interactions. Our PALS measurements corroborate these findings. The minimum porogen domains appear to be at least two tCD molecules. The MFP steadily increases with porosity well beyond that of the cylindrical pores in the sCD system. This must result from some degree of three dimensional (3D) aggregation of these small porogen domains (see figure 3.7). We will consider this random 3D growth mode again in the simulation work presented in chapter 5.

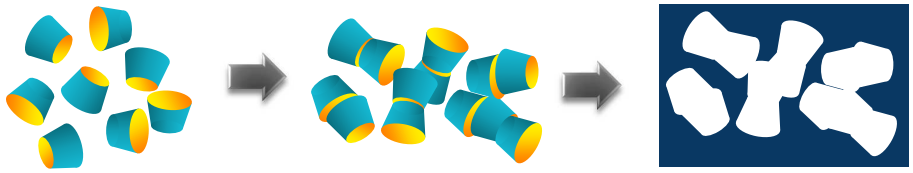

Figure 3.7: The pore structural evolution induced by tCD porogen. The tCD porogen domains are driven by van del Waals interactions.

The CA[6] system is quite different. In figure 3.1(b), the upper plane of CA[6] molecules are hydrophilic, while the bottom plane is hydrophobic. Only the upper plane can form hydrogen bonds with hydroxyl groups from the SSQ matrix and, thus CA[6] may act as a supramolecular "surfactant" in the SSQ precursor solution with a hydrophilic solvent PGMEA. At low porosity of 7%, figures 3.4 and 3.5 indicate isolated pores $L_{int}$=0 that are consistent with the size of the CA[6] molecule. The fitted 12.5 ns Ps lifetime should again be interpreted using a *spherical* pore model to yield a diameter of 1.45 nm with a MFP just below 1.0 nm, in agreement with the calculated 4 V/S=0.9 nm for a single molecule. In stark contrast, at $p$=14%, the pore interconnection length of 400 nm indicates film percolation accompanied with explosive growth in pore size to 3.9 nm. This pore size far exceeds the dimension of

random 3D cluster growth of the porogen domain, as suggested for tCD. Percolation occurring at such low porosity as 14% strongly suggests that the pores are highly elongated. A simple explanation of cylindrical micelle formation appears a very likely interpretation for the sudden onset of such large and interconnected pores (see figure 3.8). Quite clearly a *critical concentration* for micelle formation exists between 7% and 14% porosity. A study with much finer concentration increments is warranted to observe the evolution of this special mode of porogen aggregation through its threshold for micelle formation.

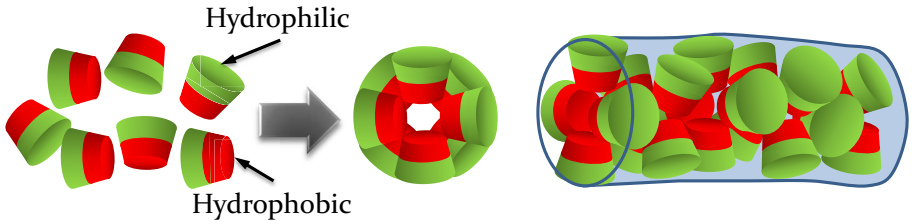


Figure 3.8: The pore structural evolution induced by CA[6] porogen. A simple explanation of cylindrical micelle formation appears a very likely interpretation for the sudden onset of such large and interconnected pores.

## 3.4 Conclusion

In conclusion, simultaneously resolving the evolution with porosity of the mean size (4 V/S) and extent $L_{int}$ of porogen-induced pores over the range from isolated porogen molecules to large self-assembled clusters provides powerful clues to deduce fundamental pore structure and growth. The sCD porogen system demonstrates 1D linear growth driven by covalent bonding to form ever longer pores of constant cross section (constant MFP with increasing $L_{int}$). The sudden jump in both MFP and $L_{int}$ in CA[6] is consistent with surfactant driven cylindrical self-assembly above a critical porogen concentration below which the CA[6] domains are simply isolated single molecules. The tCD system displays elements of short-range 1D growth to form two to three molecule clusters that give way to a more dominant, random

3D growth with porosity, all driven by weaker van der Waals interactions. The discovery of these three distinctly different domain/pore growth modes demonstrates the versatility and capability of depth-profiled PALS to characterize pore structure. As such, these PALS results appear to be quite unique in probing pore structure evolution in the prepercolation regime.

# CHAPTER IV

## Study of pore evolution including thermal treatments

The characteristics of pore size and pore structure are among the most important features of ultra low-$k$ (ULK) dielectrics [6, 11]. When we mainly focus on the subtractive porous dielectrics fabricated using spin coating and pore generators, the nanopore formation process is a very important aspect in understanding the final pore size and pore structure. In the previous chapter, the impact of porogen-porogen interaction on nanopore morphology has been deduced and confirmed by PALS. In addition, specific porogen-matrix combinations may also play a significant role in determining the pore size and pore structure [78, 79]. Investigations of matrix cross-linking and condensation, the phase separation of the porogen and matrix, and porogen degradation are all interesting and important issues that need to be understood. In this chapter, the pore structure and its formation process according to both curing temperature and porogen loading/concentration will be investigated. In order to do this, combinations of three types of matrices and two types of porogens with different loadings will be explored. *In-situ* heat treatments will be conducted to focus on the pore formation mechanism in the curing process. Furthermore, $N_2$ adsorption data will be used together with and compared to the PALS analysis results to give a more definitive description of the nanopore morphology and its evolution

with temperature as well as porogen loading in these ULK thin films.

## 4.1 Introduction and overview of the OS series matrices

In this study, three types of matrix materials labeled OS1, OS2, and OS3, are involved. They are variations of MSQ based materials, either made from low or high molecular weight resins, or particle like resins. Two types of pore generators, a nucleation and growth (N&G) porogen (P12) and a particle templating porogen (PJB) are introduced into these matrices at different concentrations. These two types of porogen generate pores based on two different mechanisms, the details of which will be discussed in later sections.

Table 4.1: **Information of the three OS matrix materials**

| Matrix Name | R.I. | Material | Pore Characteristic | Density (g/cm$^3$) |
|---|---|---|---|---|
| JSR 2015 (OS1) | 1.3703 | Low MW resin | microporous | 1.273 |
| JSR 2022 (OS2) | 1.3596 | High MW resin | low mesoporous | 1.388 |
| JSR 5109 (OS3) | 1.286 | Particle resin | high mesoporous | 0.945 |

The three types of matrices we used are commercialized by JSR Corporation that has developed a series of low-$k$ dielectric candidates for the implementation in new generations of microchips. These matrices are basically low-$k$ and ULK materials by themselves obtained by sol-gel chemistry (see [80], *Chapter 2*) using a mixture of methyltrimethoxysilane (MTMS) and tetraethoxysilane (TEOS). JSR 2015 (OS1) and JSR 2022 (OS2) are both organosilicate matrices that contain siloxane bonds, Si-OH and Si-Me groups. The neat OS1 thin film is fabricated with low molecular weight resin with high Si-OH content and is expected to be only microporous due to the free volume occupied by Si-Me groups. The neat OS2 matrix resin has high molecular weight with low Si-OH content and should contain a small fraction of interstitial porosity. JSR 5109 (OS3) is produced using particle-like resins and has

a quite low density of 0.945 g/cm$^3$ and a high porosity. Information for these three types of matrix materials is listed in table 4.1.

The characterization of the three pristine matrices will be carried out first. These three organosilicate matrix thin films are spin-coated onto silicon wafers with thicknesses of 651 nm (OS1), 471 nm (OS2), and 414 nm (OS3). PALS experiments are done on all these samples with a positron beam energy of 3.1 keV, implanting positrons with a mean depth of 172 nm into the films. The PALS spectra were taken at coincidence rates of 500-700 s$^{-1}$ and the total annihilation events in a spectrum are about one to two million.

The PALS analysis data for the neat matrices are shown in table 4.2. The spectra were fitted using the discrete fitting routine POSFIT wherein four to five positron/Ps annihilation lifetimes were typically found. The shortest fitted lifetime is nominally about 0.4 ns, which corresponds to the *positron* annihilation near the prompt peak and is not interesting (not shown in the PALS results). We will mainly focus on *positronium* annihilation lifetimes. The first and second fitted *Ps* lifetime $\tau_1$ ($\sim$2 ns) and $\tau_2$ (7$\sim$8 ns) correspond to Ps annihilation events in *micropores* (generally defined $<$2 nm in diameter). In addition to these two micropore lifetimes, we deduced a third Ps lifetime, $\tau_3$, ($\sim$18 ns in OS2, and 50 ns in OS3) that corresponds to the *mesopore* (generally $>$2 nm in diameter) Ps lifetime. Moreover, the longest Ps lifetime of $\sim$140 ns is ubiquitously found, which corresponds to Ps annihilation in vacuum. The intensity of this component, $I_{vac}$, shown in the last column has been subtracted by the backscattered Ps intensity and divided by 1.2 to compensate the different detection efficiencies of $3\gamma/2\gamma$ events.[1]

As seen in table 4.2, each of the three matrices has different micropore and meso-

[1]The details of $3\gamma/2\gamma$ differential detection efficiencies are shown in appendix B.

Table 4.2: **Summary of PALS analysis results of the three matrix resins acquired at 3.1 keV beam energy (5.1 keV for the capped sample).**

| Sample | $\tau_1$ (ns) | $I_1$ (%) | $\tau_2$ (ns) | $I_2$ (%) | $\tau_3$ (ns) | $I_3$ (%) | $I_{vac}$ (%) |
|---|---|---|---|---|---|---|---|
| OS1 | 2.5 | 8.1 | 7.1 | 28 | — | — | 0 |
| OS2 | 2.0 | 5.6 | 8.8 | 19 | 17.8 | 11 | 0 |
| OS3 | — | — | — | — | — | — | 31.2 |
| OS3 capped | 3 | 2 | — | — | 50.1 | 21.2 | 0 |

*The $\tau_1$ and $I_1$ of OS3 capped in red is significantly affected by the Ps draining into mesopores.*

pore compositions deduced from PALS. In OS1, two fitted Ps lifetimes are deduced (2.5 ns and 7.1 ns) with Ps intensities of 8.1% and 28% respectively. These two Ps lifetimes correspond to micropores diameters of 0.65 nm and 1.1 nm respectively. For convenience, we define these two micropore populations as ultra-micropore (UMP) and super-micropore (SMP), which are originated from the free volumes in the matrix related to the Si-Me groups and the specific MSQ structures. No mesopore Ps intensity is observed in OS1.

In OS2, besides the two micropore lifetimes of 2.0 ns (0.56 nm) and 8.8 ns (1.2 nm), there is a third pore population with Ps lifetime around 17.8 ns (1.7 nm in diameter). This actually falls between the size of micropores and mesopores. From the continuum pore size fitting (will be mentioned again later), it can be regarded as a broader range of pore size distribution that peaks around 1.3-1.4 nm. The PSD fitting result of OS2 is consistent with the fact that OS2 is made by high molecular weight resins which result more interstitial free volume.

OS3 has totally open/interconnected mesopores from its high Ps intensity escaping into vacuum. To deduce the "real" 50 ns Ps lifetime ($\sim$2.74 nm cylindrical diameter) in the mesopores, Ps has to be confined by an Al capping layer. There is hardly any Ps annihilation signal observed from micropores in OS3 since almost all the Ps can diffuse into the highly interconnected mesopores. In table 4.2, we can barely see a 3 ns Ps lifetime from the micropores, which is not quite reliable due to its low

(only 2%) Ps intensity. As a summary, PALS experimental results have confirmed the features of these three distinct matrix materials. OS1 is only microporous; OS2 has some bigger pores that come from a broader pore size distribution; OS3 is highly mesoporous with 2.74 nm interconnected pores with a high porosity.

In a comparison with the PALS analysis results, nitrogen absorption experiments are also conducted at 77K on these three pristine matrix materials. The pore size distribution of the three matrices are shown in figure 4.1.

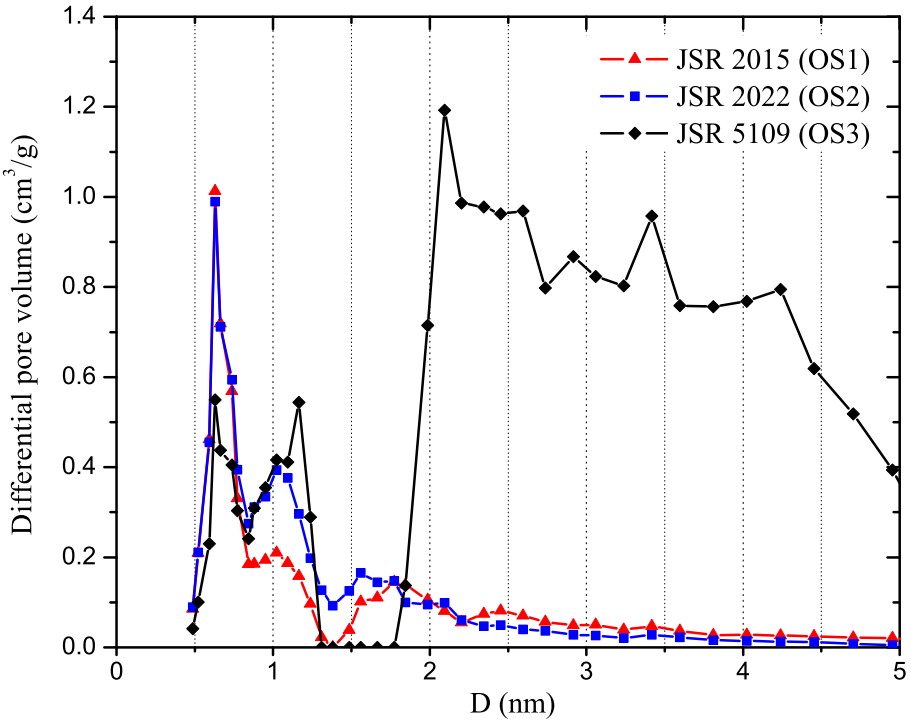


Figure 4.1: Pore size distribution of neat OS1, OS2 and OS3 matrices from the $N_2$ absorption experiments. Courtesy of R. D. Miller, IBM.

From figure 4.1, the results of $N_2$ absorption technique agree well with the PALS results. The peaks at pore sizes of 0.7 nm, 1.1 nm, and 1.6-4 nm correspond to the three pore populations, UMP, SMP, and mesopore that deduced from PALS analysis. Furthermore, one can also see that in OS3 micropores do exist, like in OS1 and OS2, although little is observed in the in PALS results due to the Ps drainage

effect. This actually confirms the existence of microporosity in the neat OS3 system and the Ps escaping from micropores to mesopores. These three types of matrices show distinct pore characteristics and the evolution of different porogen molecules in these matrices will be investigated.

## 4.2 Thermal curing of the three OS matrices and hybrid samples

In the following sections, the *in-situ* thermal treatments will be conducted on the *uncured* [2] version of these matrices in our vacuum system. The PALS analysis results of the pristine matrices along the curing processes will be compared with their porogen loaded hybrid counterparts that underwent similar vacuum curing process. The pore size evolution will be monitored at different curing temperatures using PALS. The initial (*uncured*) and final (*fully-cured*) states of the films will also be analyzed by $N_2$ absorption technique for comparison.

### 4.2.1 Thermal curing of the neat OS1 matrix and P12-OS1 hybrid

The neat uncured OS1 matrix was first heated in our vacuum chamber at elevating temperatures every 50°C. The heating filament is installed on the backside of the sample and is controlled by a temperature controller with a voltage transformer and a relay. In each heat treatment, it took about 10-15 min to reach the designated temperature and another 5 minutes (unless otherwise stated in table 4.3) to guarantee the temperature equilibrium between the sample surface and back. The sample was then cooled down to room temperature before the PALS spectra were taken. A beam energy of 4.1 keV is used to implant the positrons into an average depth of 270 nm for all the runs. The summary of the PALS analysis results is also shown in table 4.3.

[2] Normally, the spin-on thin films we refer to are *fully-cured* by heating to temperatures higher than 400°C. These *uncured* samples we use here only went through 85°C or 100°C to only evaporate the spin-on solution (also see chapter 1).

Table 4.3: **Heat treatment results of neat OS1 resin, spectra were taken at the beam energy of 4.1keV.**

| Sample | $\tau_1$ (ns) | $I_1$ (%) | $\tau_2$ (ns) | $I_2$ (%) | $\tau_3$ (ns) | $I_3$ (%) | $I_{vac}$ (%) | $I_{total}$ (%) |
|---|---|---|---|---|---|---|---|---|
| OS1 85˚C* | 2.4 | 20.8 | 5.0 | 5.3 | --- | --- | 0 | 26.1 |
| OS1 100˚C | 2.5 | 21.9 | 5.5 | 4.8 | --- | --- | 0 | 26.7 |
| OS1 150˚C | 2.4 | 21.0 | 4.8 | 7.9 | --- | --- | 0 | 28.9 |
| OS1 200˚C | 2.5 | 17.9 | 4.8 | 12.4 | --- | --- | 0 | 30.3 |
| OS1 250˚C | 2.6 | 17.7 | 5.0 | 13.4 | --- | --- | 0 | 31.1 |
| OS1 300˚C | 2.7 | 15.4 | 5.2 | 17.0 | --- | --- | 0 | 32.4 |
| OS1 350˚C | 2.9 | 16.0 | 5.8 | 18.5 | --- | --- | 0 | 34.5 |
| OS1 400˚C 1hr | 2.7 | 13.1 | 6.0 | 23.8 | --- | --- | 0 | 36.9 |

**The 85°C sample is as-received that underwent 85°C at IBM.*

The discrete fitting results of the neat OS1 matrix gave us two micropore lifetimes as also seen in the previous section for the fully cured OS1 sample. The first fitted Ps lifetime, $\tau_1$, around 2.4-2.9 ns corresponds to the ultra-micropores (UMP) of diameter 0.63-0.71 nm. $\tau_2$ is around 4.8-6.0 ns, corresponding to the super-micropore (SMP) population with diameter of 0.93-1.03 nm. With the increasing curing temperature, slight increases in both the fitted Ps micropore lifetimes were observed. The UMP Ps lifetime increases from ∼2.4 ns to ∼2.7 ns, which could be solely statistical. The Ps lifetime of the SMPs increases from 5 ns to 6 ns, which corresponds to an increase of pore diameter from 0.93 nm to 1.03 nm, which is not substantial but infers that there is a slight increase in SMP size during the curing process. This slight expansion of micropores is more obviously seen in the pore size distribution (PSD) fitting results at increasing curing temperatures.

Figure 4.2 shows the PSD fitting results of neat OS1 at different curing temperatures. Instead of bimodal, only one broad distribution is shown. Note that this is only a *plausible* result (see chapter 2) since the shape of the PSD (more narrow peaks vs. less broader peaks) is controlled by a free "regularization" parameter. Here the PSD fitting results emphasize the second micropore population which corresponds to the 6 ns∼8 ns Ps lifetime. In figure 4.2, the area under the PSD peaks at different

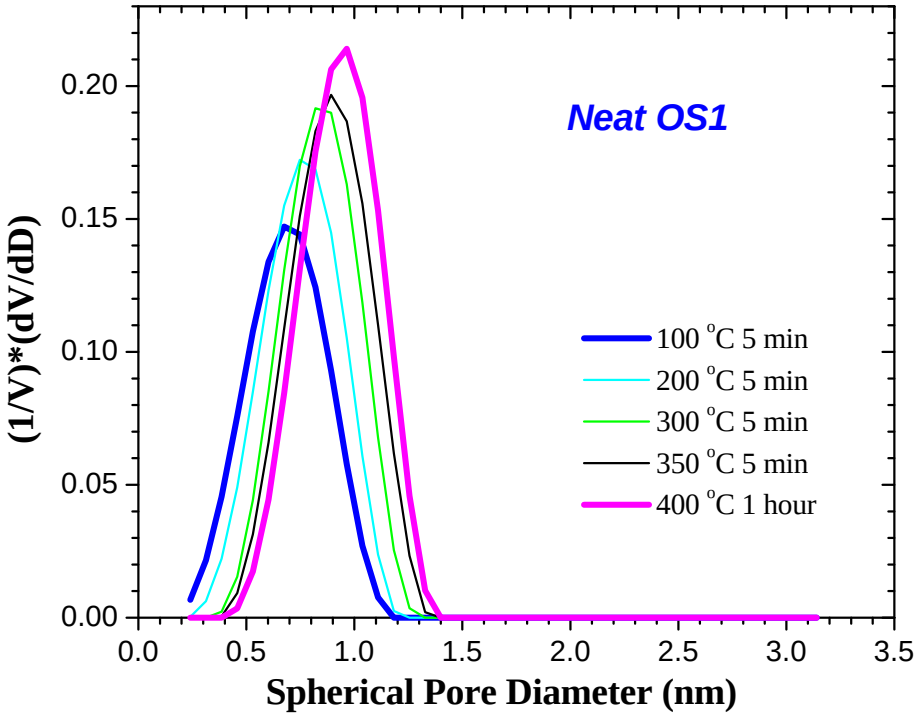


Figure 4.2: Pore size distribution evolution of neat OS1 resin according to curing temperatures. There is only micropore population seen in the PSD at all temperatures. The PSD at different temperatures are represented by different colors.

temperatures have been normalized using the corresponding Ps intensities from the discrete fitting and thus they clearly display both pore size and Ps intensity increases at higher curing temperatures.

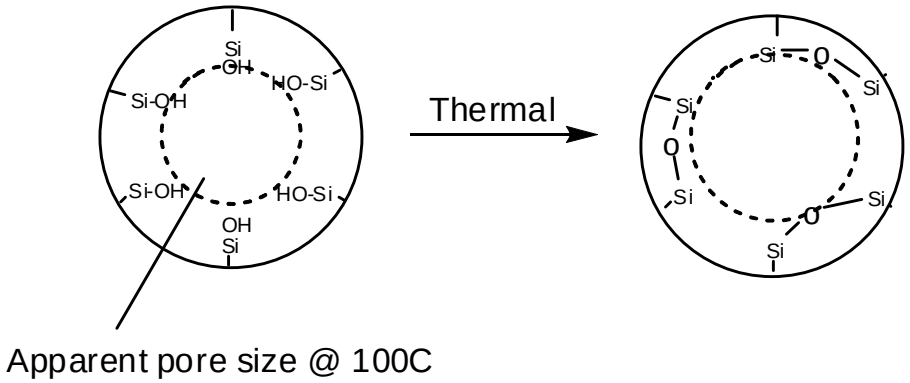


Figure 4.3: Intrinsic micropores in matrix and the micropore size increase due to matrix condensation. Courtesy of IBM.

As we briefly mentioned earlier, the intrinsic microporosity in these MSQ based matrix materials is due to the free volume occupied by Si-Me, silanol groups, and

the specific packing structure and polymerization. During the curing process, silanol groups (Si-OH) can form Si-O-Si bonds, and this condensation process in the matrix can cause an increase in micropore size, which is illustrated in figure 4.3. From PALS analysis, the increase in Ps lifetime and consequently the corresponding micropore size corroborate this matrix condensation behavior.

In comparison with neat OS1, in order to understand the mesoporosity formation and porogen degradation process, we comparatively investigated the curing and degradation processes of an *uncured* hybrid sample of OS1 with 19% "P12" porogen loading, which will be called P12-OS1 in following context. The P12 pore generator is a nucleation and growth (N&G) porogen, which utilizes the very commonly used N&G process to fabricate nanoporous low-$k$ thin films [80]. Similar curing process, PALS experiments, and fitting procedures have been conducted on this P12-OS1 hybrid sample compared to the neat OS1 matrix. The discrete fitting results of P12-OS1 hybrid are shown in table 4.4. Note that this thermal curing process of the hybrid P12-OS1 sample effectively mimics the fabrication of porous thin films following the spin-coating procedure.

Table 4.4: **Heat treatment results of OS1/P12 hybrid (19 wt.% loading), spectra were taken at at the beam energy of 4.1keV.**

| Sample | $\tau_1$ (ns) | $I_1$ (%) | $\tau_2$ (ns) | $I_2$ (%) | $\tau_3$ (ns) | $I_3$ (%) | $I_{vac}$ (%) | $I_{total}$ (%) |
|---|---|---|---|---|---|---|---|---|
| P12-OS1 85˚C | 2.2 | 26.2 | 7.2 | 1.8 | — | — | 0 | 28.0 |
| P12-OS1 100˚C | 2.3 | 27.2 | 6.5 | 2.0 | — | — | 0 | 29.2 |
| P12-OS1 150˚C | 2.3 | 27.5 | 6.2 | 2.4 | — | — | 0 | 29.9 |
| P12-OS1 200˚C | 2.5 | 27.7 | 5.8 | 3.4 | — | — | 0 | 31.1 |
| P12-OS1 250˚C | 2.6 | 26.1 | 5.4 | 5.7 | — | — | 0 | 31.9 |
| P12-OS1 300˚C | 2.7 | 24.7 | 5.3 | 7.7 | — | — | 0 | 32.4 |
| P12-OS1 350˚C | 2.6 | 18.8 | 4.9 | 12.0 | 32.0 | 2.7 | 0 | 33.5 |
| P12-OS1 400˚C | 2.4 | 9.0 | 6.1 | 8.1 | 25.4 | 16.9 | 0.5 | 34.5 |
| P12-OS1 400˚C 1hr | 2.2 | 4.7 | 7.6 | 5.7 | 25.1 | 26.1 | 0.9 | 37.4 |
| P12-OS1 450˚C 1hr | 2.2 | 4.2 | 7.4 | 3.6 | 26.0 | 29.5 | 2.4 | 39.7 |

The first column of table 4.4 shows the sample name with curing temperatures.

Below 350°C, the PALS results suggest that this P12-OS1 hybrid sample is not significantly different from the neat OS1 matrix. Similar micropore Ps lifetimes are found for this hybrid sample. One important thing that needs to be noticed is that the hybrid sample has a higher initial UMP intensity ($I_1$) than that of the pristine OS1 (26.2% vs. 20.8%). In the uncured hybrid sample, we expect the matrix and the P12 porogen both contribute to the total Ps formation fraction. Under this hypothesis, a PALS experiment on the pure P12 porogen was conducted. Bulk PALS was used since P12 porogen itself is a liquid polymer at room temperature. It is found that bulk P12 porogen has a micropore population (∼3 ns) with a 31% Ps intensity. Consequently, when mixed with OS1 resin to form a nanocomposite, the 19% P12 porogen contributes to the UMP Ps intensity concomitantly with the OS1 matrix and increases the overall UMP Ps intensity.

In spite of the high UMP Ps intensity, the P12-OS1 hybrid has very low SMP intensities ($I_2$). At low temperatures such as 85°C and 100°C, $\tau_2$ and $I_2$ are consistent with purely fast Ps backscattering. As the temperature increases to 350°C, this SMP Ps intensity, $I_2$, gradually rises to a maximum of about 12% simultaneously with the drop of $I_1$. Above that, a distinct mesopore population ($\tau_3$) emerges with a significant Ps intensity due to the degradation of P12 porogen. Here, the relative Ps intensities related to different pore populations are important indicators of the pore formation process. The Ps lifetime ($\tau_3$) of 25∼26 ns, which corresponds to 2.09∼2.14 nm, is the diameter of P12 porogen domains before they evaporate. The Ps diffusion from micropores to mesopores is clearly seen after 350°C, when both $I_1$ and $I_2$ drop drastically. The micropores still exist after high temperature curing, but they are "invisible" since almost all the Ps atoms have diffused into mesopores.

The whole pore evolution with the thermal curing process is also apparent in the

PSD fitting results shown in figure 4.4. The micropore diameter peaked at about 0.6 nm slightly increases along with the curing temperature up to 350°C. This is the same effect due to matrix condensation, which was seen in the curing process of the pristine OS1 matrix (see figure 4.3). Above 350°C, the P12 porogen degrades and forms much bigger mesopores in the film with an average pore size of ∼2.1 nm. This is consistent with the discrete PALS analysis results. The emergence of the mesopores "drain" the Ps from micropores and it seems as if the micropores disappeared. We can refer to the $N_2$ adsorption experimental results, which confirms the existence of micropores after the whole curing process.

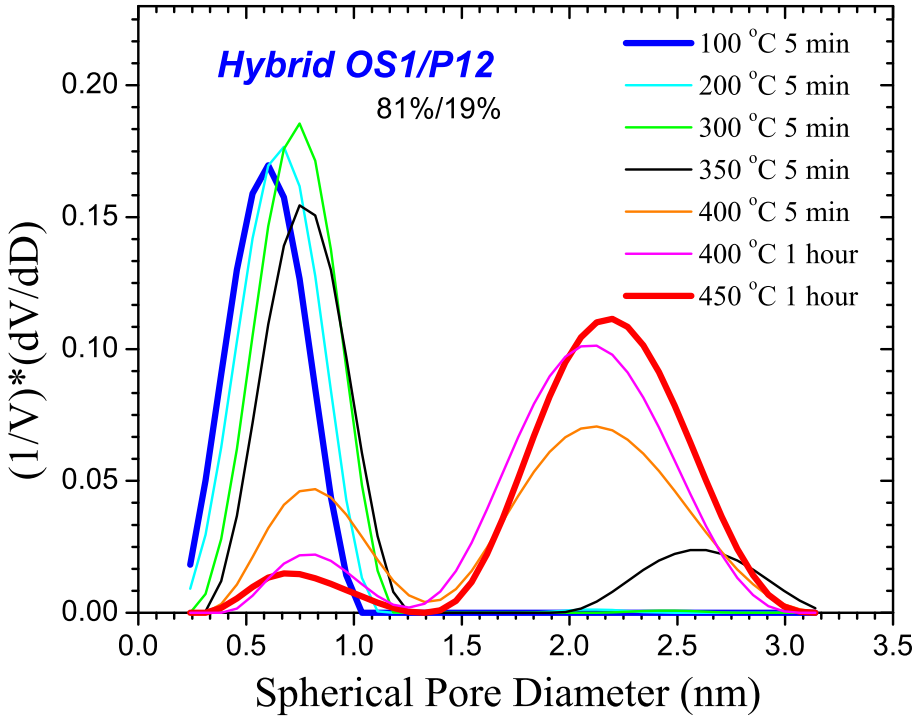


Figure 4.4: Pore size distribution evolution of OS1/P12 hybrid according to curing temperatures. There is only micropore population seen in the PSD at low temperatures. At higher temperatures the mesopores start to grow in and drain the Ps in micropores. The PSD at different temperatures are represented by different colors.

Figure 4.5 shows the pore size distribution from the $N_2$ adsorption technique of the *fully cured* P12-OS1 hybrid as well as the neat OS1 matrix. The two micropore peaks are clearly seen for both fully cured samples. It is also interesting to compare

the pore characteristics in these two samples. For P12-OS1, both the second and the third peak are much higher than that in neat OS1. It seems that P12 porogen not only generates mesopores, but also increases the SMP porosity. The mesopore size distribution is quite broad, ranging from 2 nm to 5 nm with decreasing concentrations. The peak of the mesopore distribution (∼2 nm) agrees quite well with the discrete fitting and PSD results from PALS (see figure 4.4).

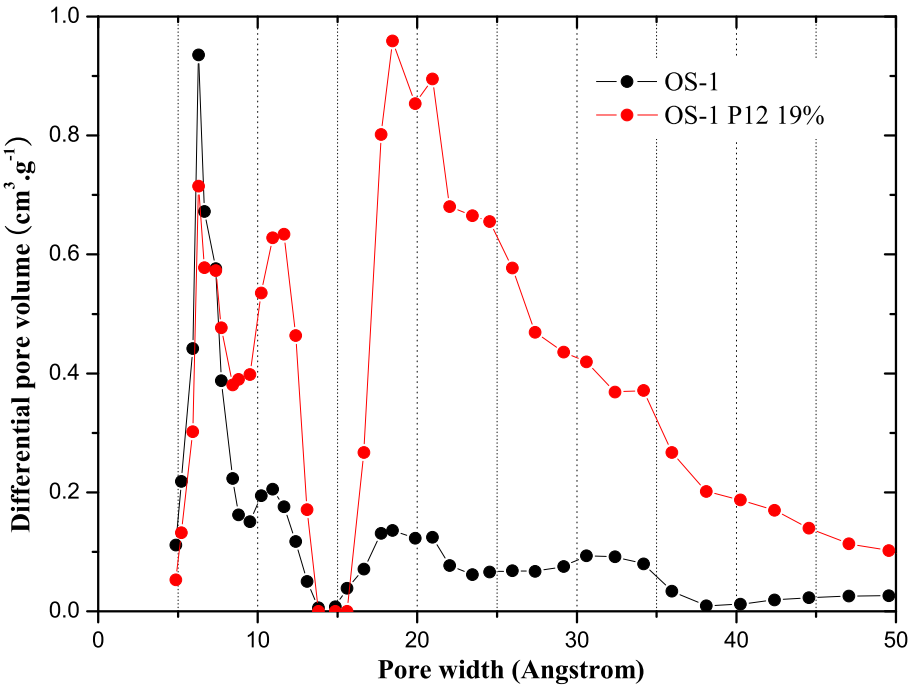


Figure 4.5: NLDFT pore size distribution from $N_2$ absorption experiments. Courtesy of IBM.

Comparison of the Ps intensities during the curing processes between neat OS1 matrix and P12-OS1 hybrid is shown in figure 4.6. Figure 4.6 shows the Ps intensities in UMP, SMP, mesopores (if any) and their sums according to curing temperatures (a) for the neat OS1, (b) for the P12-OS1 hybrid.

For the neat OS1, at 100°C, the Ps intensities from UMPs and SMPs are 20.8% and 5.3% respectively, which sum up to a total Ps intensity of 26.1%. As the temperature increases, the $I_1$ drops concomitantly with the increase of $I_2$. Finally at 400°C, the

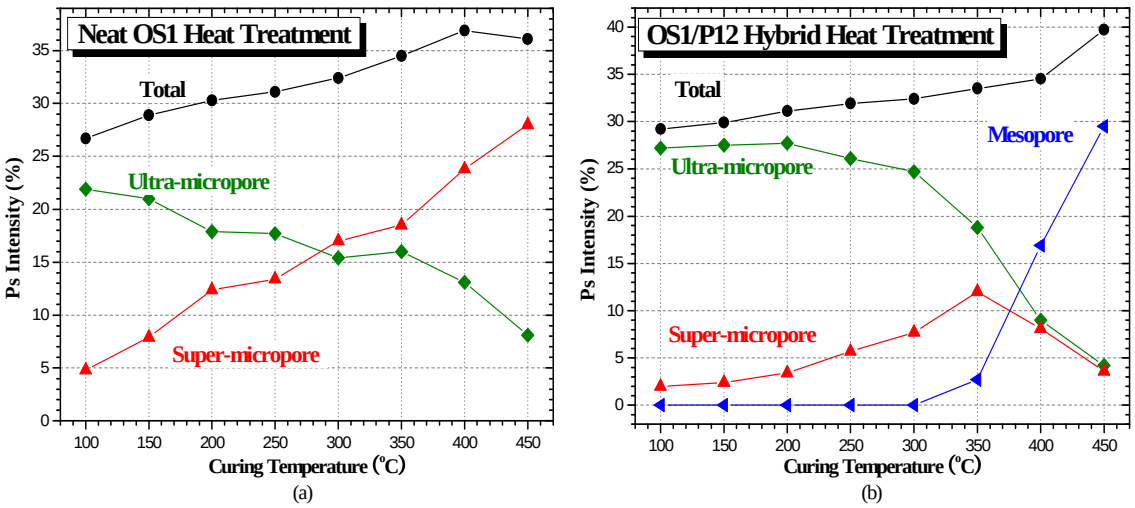


Figure 4.6: Ps intensities of the pore populations in (a) neat OS1 and (b) P12-OS1 hybrid vs. curing temperature

relative intensity of UMP and SMP has nearly flipped. The first row in table 4.1 shows the fully cured neat OS1 by IBM. Note that for the fully cured sample, the ultra micropore intensity is even lower which is 8.1% and super micropore Ps intensity is 28%. The increase of SMP Ps intensity is due to the vitrification and cross-linking process of the matrix resin, which generates more SMPs during the heat treatment. The simultaneous drop of UMP Ps intensity is due to the Ps drainage to SMP and is confirmed by $N_2$ adsorption experimental results. Total Ps intensity from all the pore populations increases from 26.1% to 36.9%. However, this Ps intensity increase cannot be directly correlated with the porosity increase since the total Ps intensity could be affected by many other factors including chemistry change, electron scavenging, and dangling bonds. Here, the total Ps increase could be due to the loss of dangling hydroxyl groups.

When we look at the curing results of the P12-OS1 hybrid in figure 4.6 (b), at temperatures below 350°C, the trends of $I_1$ and $I_2$ look similar with 4.6(a), except the hybrid has more UMP intensity and less SMP intensity, which is due to the higher Ps formation from positrons stopping in the P12 porogen (31%). The lower Ps intensity

from the SMPs in the hybrid indicates that the P12 porogen may preferentially fill the SMPs of the matrix. As the curing temperature increases, the originally miscible P12 porogen starts to phase separate with the matrix due to the condensation and cross-linking occurred in the matrix. The P12 porogen forms nanocomposite domains and at above 350°C, these P12 porogen domains start to degrade and leave behind the mesopores. The corresponding Ps intensity is distinctly shown by the blue curve in figure 4.6 (b). This sudden emergence of mesopores almost drained all the Ps from micropores and it is clearly shown where the fitted SMP Ps intensity bends down along with the UMP Ps intensity.

### 4.2.2 Thermal curing of the neat OS2 matrix and P12-OS2 hybrid

In this section, the thermal curing of the second *uncured* matrix, OS2, from the three matrix series will be examined. A P12-OS2 *uncured* hybrid with the same porogen loading (19%) will also be investigated in comparison with its pristine counterpart. The *fully cured* OS2 neat resin is intrinsically porous from the interstitial spaces, which is found by PALS analysis (see table 4.1). The discrete PALS fitting found three Ps lifetimes that correspond to two micropore (UMP and SMP) and one mesopore populations. The two micropore lifetimes are close to what we have seen in OS1 except that the intensity of $\tau_1$ is much lower than that in OS1. The third mesopore lifetime 15∼18 ns (1.60 nm∼1.75 nm) with a solid intensity is new. From the continuum fitting result, the second and the third Ps lifetimes of neat OS2 come from one broad SMP distribution.

The uncured neat OS2 resin and the P12-OS2 hybrid have been thermally cured only up to 100°C and 85°C respectively. Similar PALS experiments have been conducted on these two samples as described in the previous section. We first focus on the PALS analysis results of the neat OS2 curing, which are shown in table 4.5. At

Table 4.5: **Heat treatment results of neat OS2 resin, spectra were taken at the beam energy of 4.1 keV.**

| Sample | $\tau_1$ (ns) | $I_1$ (%) | $\tau_2$ (ns) | $I_2$ (%) | $\tau_3$ (ns) | $I_3$ (%) | $I_{vac}$ (%) | $I_{total}$ (%) |
|---|---|---|---|---|---|---|---|---|
| OS2 100˚C | 3.0 | 7.1 | 9.0 | 15.3 | — | — | 0 | 22.4 |
| OS2 150˚C | 2.8 | 6.9 | 9.2 | 16.9 | — | — | 0 | 23.8 |
| OS2 200˚C | 3.1 | 7.9 | 9.8 | 18.1 | — | — | 0 | 26.0 |
| OS2 250˚C | 3.2 | 8.0 | 10.0 | 20.3 | — | — | 0 | 28.3 |
| OS2 300˚C | 2.8 | 7.7 | 9.8 | 22.9 | — | — | 0 | 30.6 |
| OS2 350˚C | 3.2 | 8.5 | 10.2 | 23.3 | — | — | 0 | 31.8 |
| OS2 400˚C 1hr | 3.1 | 8.6 | 10.2 | 25.7 | — | — | 0 | 34.3 |
| OS2 450˚C 1hr | 3.5 | 9.5 | 10.6 | 26.8 | — | — | 0 | 36.3 |
| OS2 350˚C | 1.9 | 5.8 | 7.8 | 19.0 | 14.1 | 8.3 | 0 | 33.1 |
| OS2 400˚C 1hr | 2.2 | 7.5 | 8.5 | 23.7 | 15.4 | 6.6 | 0 | 37.8 |
| OS2 430˚C 1hr | 2.3 | 6.3 | 8.3 | 22.9 | 14.7 | 8.4 | 0 | 37.6 |
| OS2 450˚C 1hr | 2.4 | 6.8 | 8.6 | 24.4 | 15.6 | 6.9 | 0 | 38.1 |
| OS2 fully cured | 2.0 | 5.6 | 8.8 | 19 | 17.8 | 11 | 0 | 35.6 |

low temperatures (<350°C), the discrete fitting does not distinguish three nanopore Ps lifetimes. Only $\tau_1$ and $\tau_2$ with their Ps intensities are shown in table 4.5. Above 350°C, the PALS spectra can be fitted either by two or three nanopore components and the results from these two discrete fitting methods are both shown in table 4.5. The lower part of the table shaded in darker orange shows the three component fitting results. This ambiguity from the discrete fitting can be actually diminished in the continuum fitting (shown in figure 4.7).

Figure 4.7 shows the continuum fitting results of the neat OS2 curing process at a series of temperatures. The first peak associated with the UMPs does not change over all the temperatures. The sizes of the second micropore domain (∼1.2 nm) and the mesopores (∼1.7 nm) are close to each other and they are merged into one broad distribution. This second peak in the PSD (0.8 nm-1.7 nm) gets broader and bigger at higher temperatures (>350°C) before the discrete fitting can separate the whole pore size distribution into three components. The area under the PSD curves at each temperature is normalized by the total Ps intensity from the discrete fitting results. It is worth mentioning that the pore size increase of the pristine OS2 through the

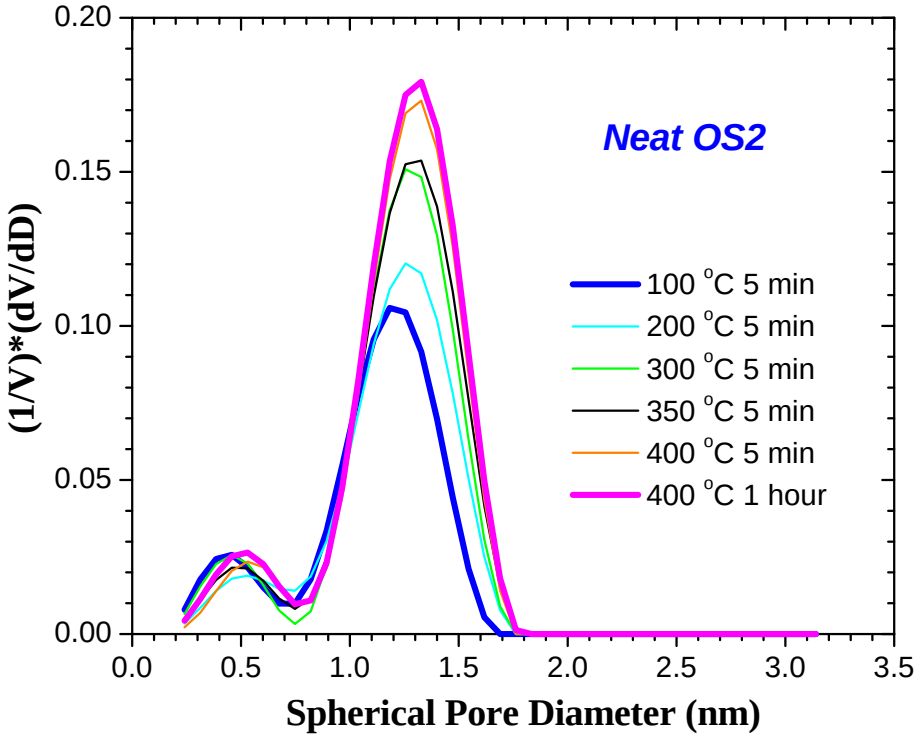


Figure 4.7: PSDs of neat OS2 at different curing temperatures are presented by different colors. The distribution of pore population around 1.3 nm in diameter grows gradually at higher temperatures.

curing temperatures seems not as significant as in OS1. This is actually consistent with the fact that there is less Si-OH content in OS2 resin and subsequently less pore size expansion from the matrix condensation effect (see figure 4.3).

The discrete lifetime fitting results are very useful in analyzing the Ps intensity change quantitatively. Instead of a drastic increase of SMP Ps intensity as observed in neat OS1, we only see a modest rise of $I_2$ in the neat OS2 during the curing process. The UMP intensity is quite low and constant throughout the curing temperature range. This indicates that due to the bigger intrinsic pores of OS2 compared to that of OS1, the Ps diffusion from UMPs into SMPs and even mesopores is easier at all temperatures. More discussion of the Ps intensities of the neat OS2 will be carried out later together with the hybrid sample.

We next examine the effects of putting 19% P12 porogen into the pristine OS2

matrix. In comparison with the neat OS2, the PALS analysis results of P12-OS2 hybrid sample are listed in table 4.6, with the PALS results of the fully cured neat OS2 matrix shown in the first row. The discrete Ps lifetime fittings are carried out in a consistent way as in the neat OS2 matrix. A $\tau_3$ is fitted when necessary. The $\tau_3$ and $I_3$ at 150°C, 200°C and 250°C are marked in red, which means the uncertainty of these results is larger due to their low Ps intensities.

Table 4.6: **Heating of OS2/P12 hybrid (19% loading), spectra were taken at the beam energy of 4.1keV.**

| Sample | $\tau_1$ (ns) | $I_1$ (%) | $\tau_2$ (ns) | $I_2$ (%) | $\tau_3$ (ns) | $I_3$ (%) | $I_{vac}$ (%) | $I_{total}$ (%) |
|---|---|---|---|---|---|---|---|---|
| neat OS2 fully cured | 2.0 | 5.6 | 8.8 | 19 | 17.8 | 11 | 0 | 35.6 |
| P12-OS2 85˚C | 2.4 | 18.6 | 5.4 | 5.0 | — | — | 0 | 23.6 |
| P12-OS2 100˚C | 2.5 | 18.3 | 5.4 | 6.3 | — | — | 0 | 24.6 |
| P12-OS2 150˚C | 2.4 | 16.2 | 4.9 | 9.9 | 14.8 | 1.0 | 0 | 27.1 |
| P12-OS2 200˚C | 2.6 | 17.7 | 5.7 | 8.0 | 17.3 | 1.3 | 0 | 27.0 |
| P12-OS2 250˚C | 2.7 | 17.0 | 5.8 | 9.1 | 16.9 | 2.4 | 0 | 28.5 |
| P12-OS2 300˚C | 2.6 | 15.9 | 5.8 | 10.5 | 18.5 | 3.8 | 0 | 30.2 |
| P12-OS2 350˚C | 2.6 | 14.1 | 6.2 | 8.8 | 19.0 | 9.2 | 0 | 32.1 |
| P12-OS2 400˚C | 2.6 | 10.1 | 8.0 | 7.0 | 19.9 | 16.3 | 0 | 33.4 |
| P12-OS2 400˚C 1hr | 2.5 | 5.0 | 9.2 | 5.0 | 19.6 | 26.3 | 0 | 36.3 |
| P12-OS2 450˚C 1hr | 2.2 | 4.0 | 7.2 | 2.8 | 19.3 | 30.5 | 1.5 | 38.8 |

This hybrid sample at low temperatures does not show any hint of the intrinsic mesopores of OS2 (Also shown in figure 4.8). Both $\tau_2$ (5.4 ns at 100°C) and $I_2$ (5%) of this hybrid P12-OS2 are smaller than the uncured version of pristine OS2, which suggests that the P12 porogen has occupied the intrinsic interstitial pores of OS2, or at least the large end of this pore distribution, and meanwhile increased the UMP Ps intensity ($I_1$ from 7.1% in neat OS2 to 18.6% in P12-OS2 hybrid) as also seen in the P12-OS1 hybrid. The UMP component is quite similar to that in the neat OS2. At higher temperatures, the emergence of $\tau_3$ and $I_3$ is directly related to the P12 porogen degradation.

Figure 4.8 shows the PSD fitting results of the P12-OS2 hybrid sample at different temperatures. The evolution of pore size and the relative intensity change is clearly

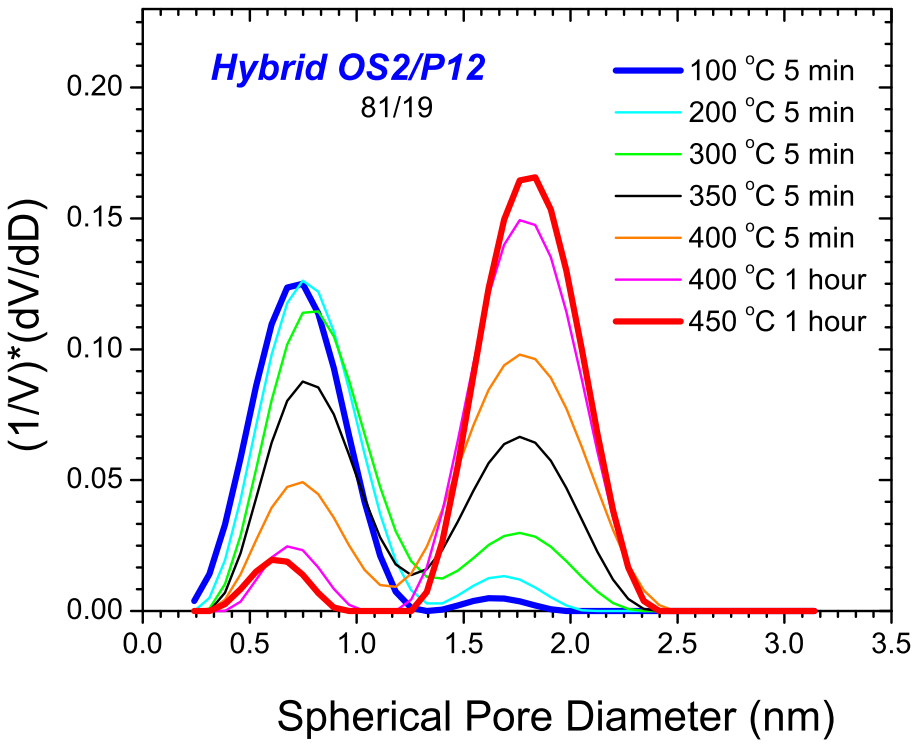


Figure 4.8: Pore size distribution evolution of OS2/P12 hybrid according to curing temperatures. There is almost no mesopore population presents in the PSD at low temperatures. At higher temperatures the mesopores start to grow in and drain the Ps in micropores. The PSD at different temperatures are represented by different colors.

seen. The area under each PSD curve is normalized by the total Ps intensity from discrete fittings respectively. However, only the relative intensity between different pore size populations is meaningful, and the change of area under the PSD curves does not directly convert to the total porosity change.

The P12 porogen, as a better Ps former (31%), filled the OS2 SMPs and mesopores (lower $I_2$ and no $I_3$) while increases the UMP Ps intensity ($I_1$). Beyond 300°C heat treatment, the $\tau_3$ *reappears* with solid and increasing intensity due to the P12 porogen degradation (see table 4.6). Note that this "reappeared" mesopores are bigger than the mesopores in pristine OS2 (compare figure 4.7 and 4.8), indicating that only part of all the P12 porogen molecules reside inside the intrinsic pores of OS2 since the mesoporosity of the neat OS2 is presumably insufficient to accommodate all the P12

porogen (at 19% weight loading). The remaining P12 porogen that could not fit into these OS2 mesopores form its own nanocomposite domains which contribute to the overall mesopore size and Ps intensity. The $I_3$ of the hybrid is over 30% after curing to 450°C, which is much higher than that of the intrinsic mesopores of OS2 (∼11%).

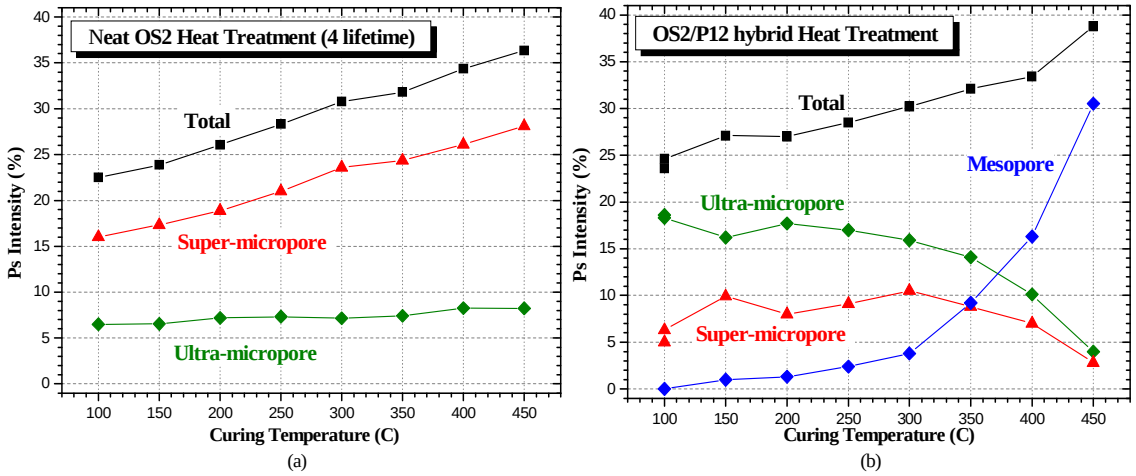


Figure 4.9: Ps intensities of the pore populations in (a) neat OS1 and (b) P12-OS2 hybrid vs. curing temperature

As a brief summary for both pristine OS2 and hybrid P12-OS2, the Ps intensity vs. curing temperature for both the two samples are shown in figure 4.9. The SMP Ps intensity of the neat OS2 (red curve in figure 4.9 (a)) actually includes the small amount of intrinsic mesopore Ps intensity and should not be directly compared to the SMP Ps intensity in hybrid P12-OS2. Comparing the sum of Ps intensities of SMP and mesopores of the hybrid would be more reasonable. One can also compare these figures with figure 4.6. During the heating process for neat OS2, only the Ps intensity of SMP (actually the sum of SMP and mesopore) increases from 16% to 27%. The UMP and SMP intensities "cross" each other, which is different from neat OS1. The UMP intensity stays pretty constant and is much lower from the very beginning (∼7%) comparing to 27% in neat OS1. It is possible that Ps drainage already happens at the very beginning, and the intensity left in UMP is only due to

the very isolated UMP. (In neat OS1, this UMP intensity also drops to ∼7% after final curing.) The P12-OS2 hybrid looks quite similar as P12-OS1 hybrid in figure 4.9 (b) except we do not see an obvious trend of UMP and SMP at low temperatures. At higher temperatures when mesopore intensity starts to dominate, we see the drop of both UMP and SMP intensities. The SMP intensity of the hybrid at low temperatures is always <10%, which is lower than neat OS2 SMP intensity (>15% and increases to more than 20%). This is due to the P12 porogen filling as mentioned earlier, which concomitantly raises the UMP intensity as well.

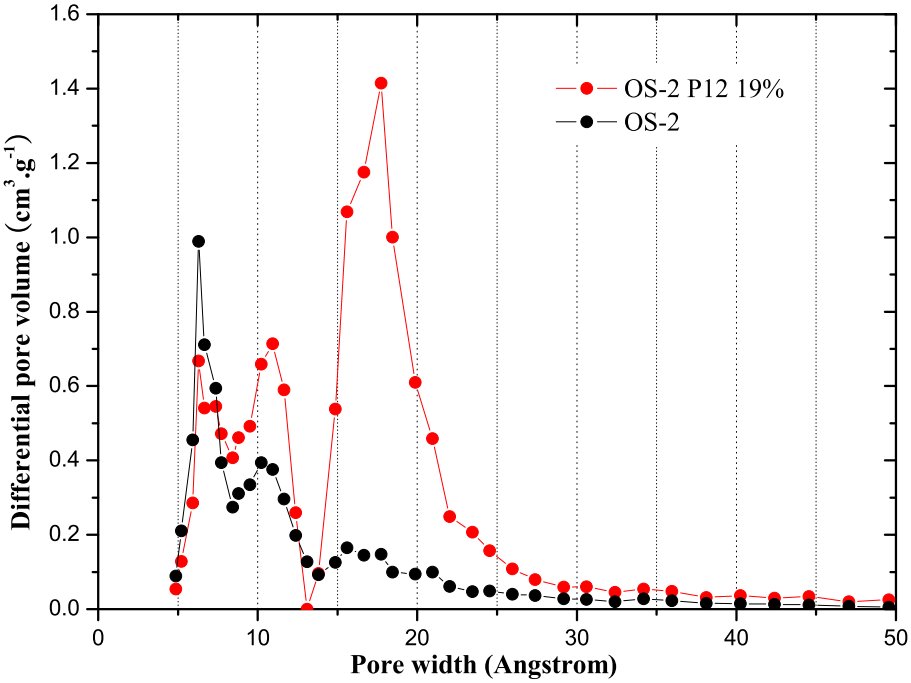


Figure 4.10: NLDFT pore size distribution from $N_2$ absorption experiments. Courtesy of IBM.

Similar to the previous section, the $N_2$ absorption data from IBM was acquired on the fully cured neat OS2 and hybrid P12-OS2 samples to compare their pore size distribution to each other, which is shown in figure 4.10. Note that the three peaks from the fully cured P12-OS2 sample correspond to the UMP, SMP and mesopore respectively and they agree very well with the PALS results (see table 4.6, where Ps

lifetimes of 2.0 ns, 8.8 ns, and 17.8 ns convert to pore diameters of 0.6 nm, 1.2 nm, and 1.7 nm respectively). One interesting feature to be noticed is that the mesopore size distribution (peaks at ∼1.7 nm) is much narrower than that of the P12-OS1 (see figure 4.5). It indicates that with the same P12 loading in the two matrices, OS1 and OS2, the induced mesopores in OS2 are smaller and more regular in size than in OS1.

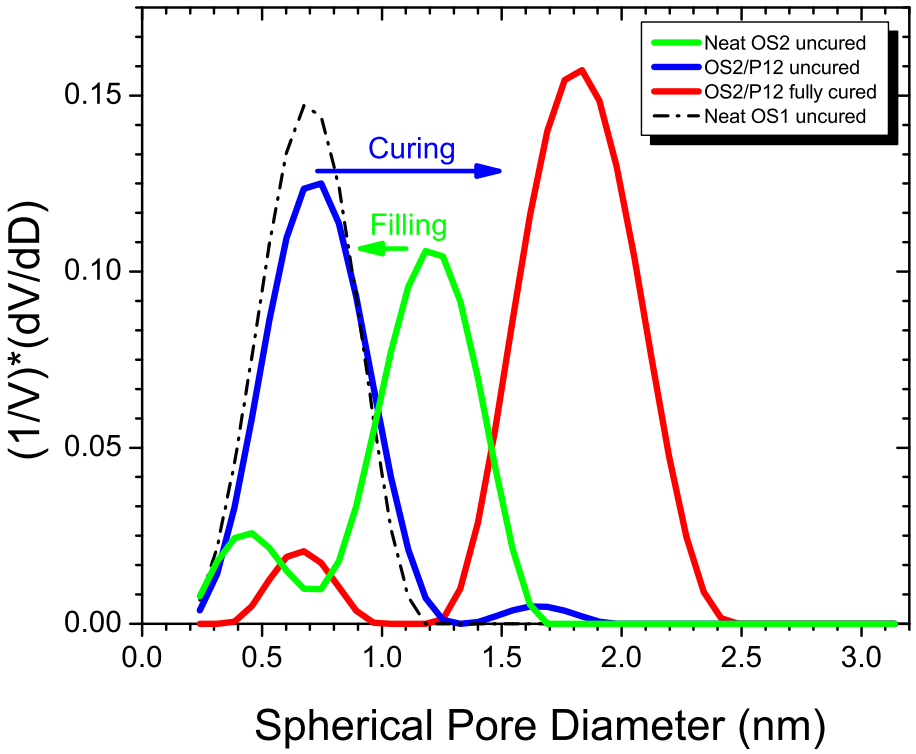


Figure 4.11: Pore size evolution and comparison before and after curing.

Figure 4.11 shows the PSD fitting results of both the neat OS2 and the P12-OS2 hybrid samples (either uncured or cured). It graphically illustrates the entire filling and degradation picture in OS2. The green curve shows the PSD of neat OS2 *before curing*. The average super micropore size around 1.2 nm (∼8 ns). The blue curve shows the PSD of *uncured* 19% porogen loaded P12-OS2 hybrid sample. Notice that the pore size shifts to the left significantly (comparing to neat OS2), to around 0.7

nm (∼2.9 ns) (the green arrow pointing to the left). This drastic shift to the left is due to the P12 filling of SMPs and mesopores intrinsic to the OS2 matrix. There is still a hint of super micropores at 1.7 nm (∼17 ns) in OS2 that could be due to incomplete filling of pores. After curing, P12 porogen degrades and leaves behind pores with average diameter of 1.7-1.9 nm. (Shown in red PSD curve) This is also consistent with the discrete fitting results. Larger mesopores are generated during the degradation of P12 porogen (The blue arrow). The PSD of the uncured neat OS1 is also drawn in dotted line, it is nominally similar with the uncured P12-OS2 hybrid sample. It seems reasonable that P12 porogens filled most of the large pores of OS2 that are bigger than those in OS1. They both have ultra micropores that correspond to the intrinsic voids due to their similar chemistry that are too small and cannot be filled by the P12 polymer.

#### 4.2.3 Thermal curing of the neat OS3 matrix and P12-OS3 hybrid

OS3 (JSR 5109) is the third neat matrix which is going to be studied in this section. An *uncured* and a *cured* neat OS3 resin with their Al capped counterparts were first examined by PALS. The long buffer delayed fitting results are shown here which mainly focus on the long Ps lifetimes far away from the spectrum prompt peak (in this case, fitting begins 106.25 ns beyond the prompt peak). The long buffer and short buffer of a spectrum focus on long and short Ps lifetimes respectively (also see chapter 2). The long buffer fitting result gives us a robust fitting on big mesopores and the vacuum Ps intensity. The summary of PALS analysis results of these samples is shown in table 4.7.

From the PALS results in table 4.7, it is clear that the neat OS3 shows large interconnected mesopores, both before and after curing. Without capping layers, most of the Ps can escape through this pore network into vacuum. There is not

Table 4.7: **PALS results of neat OS3. (Fitted from long buffer with two lifetimes, starting channel 85, 106.25 ns)**

| Sample | Energy (keV) | $\tau_{meso}$(ns) | $I_{meso}$ (%) | $I_{vac}$ (%) | $I_{total}$ (%) | $F_{esc}$ (%) |
|---|---|---|---|---|---|---|
| OS3 100°C | 3.2 | 20.8 | 3.2 | 18.3 | 21.5 | 85.0 |
| OS3 150°C capped | 4.2 | 48.2 | 16.9 | 0 | 16.9 | 0 |
| OS3 cured | 3.2 | 31.2 | 3.5 | 29.4 | 32.9 | 89.4 |
| OS3 cured capped | 4.2 | 49.8 | 21.1 | 0 | 21.1 | 0 |

much change over the curing processes from the PALS perspective, except the total Ps intensity increases at curing. As mentioned in the first section, the capped samples show a 50 ns mesopore lifetime, with good intensity, which corresponds to mesopores with 2.74 nm tubular diameter.

Based on OS3, a series of hybrid P12-OS3 samples were made, with increasing P12 porogen wt% loadings from 17% to 30% with roughly 2% steps. They have only undergone a curing process up to 150°C for an hour to evaporate the spin-on solution. Their film thicknesses (around 300 nm to 400 nm) and refractive indices are given in the appendix D, table D.5. Three samples with the P12 porogen loading of 17%, 23%, and 30% are selected from this series and similar heating processes stated in previous sections have been done on these samples. The 3.2 keV beam energy is used on uncapped samples to give us a positron mean implantation depth of ∼181 nm. 4.2 keV is used on the capped ones to penetrate the Al capping layer. The fitting results are shown in table 4.8.

Table 4.8 shows the results of three hybrid samples we selected to perform PALS on from the whole series of P12 loadings. $\tau_1$, $\tau_2$, and $\tau_3$ with their corresponding I's are Ps lifetimes and Ps intensities in the UMP, SMP, and mesopores respectively. The Ps lifetimes in red have correspondingly low Ps intensities and have bigger uncertainties than the other results. It is obviously seen that at low curing temperatures with the P12 porogen loadings, these uncured hybrid samples are not as open as OS3 as if

Table 4.8: **PALS analysis Results of LKD5109/P12 System (150°C/1hr) at 3.2keV (~180 nm mean)**

| Porogen Loading | Curing Temp. | $\tau_1$ (ns) | $I_1$ (%) | $\tau_2$ (ns) | $I_2$ (%) | $\tau_3$ (ns) | $I_3$ (%) | $I_{vac}$ (%) | $I_{total}$ (%) |
|---|---|---|---|---|---|---|---|---|---|
| 17% | 150˚C | 2.6 | 5.3 | --- | --- | 13.1 | 4.3 | 15.8 | 25.4 |
| | 200˚C | 2.5 | 3.9 | --- | --- | 14.9 | 5.5 | 18.5 | 27.9 |
| | 300˚C | 2.6 | 3.5 | --- | --- | 15.3 | 5.5 | 20.9 | 29.9 |
| | 400˚C | 2.2 | 2.7 | --- | --- | 15.9 | 6.5 | 23.5 | 32.7 |
| | 460˚C | 1.7 | 2.6 | --- | --- | 16.1 | 6.3 | 24.2 | 30.5 |
| 23% | 150˚C | 2.4 | 7.9 | 5.9 | 4.3 | 35.6 | 6.7 | 4.9 | 23.8 |
| | 200˚C | 2.2 | 4.6 | 6.6 | 4.4 | 35.3 | 9.7 | 7.5 | 26.2 |
| | 300˚C | 1.9 | 5.1 | 7.5 | 5.1 | 36.3 | 11.5 | 7.5 | 29.2 |
| | 350˚C | 2.0 | 4.7 | 8.8 | 4.3 | 38.1 | 12.0 | 9.8 | 30.8 |
| | 400˚C | 1.5 | 3.3 | 7.6 | 3.5 | 32.4 | 11.7 | 14.0 | 32.5 |
| | 450˚C | 1.5 | 2.9 | 9.1 | 0.9 | 16.9 | 6.6 | 21.5 | 31.9 |
| | 460˚C | 1.3 | 3.7 | --- | --- | 11.6 | 5.2 | 23.6 | 32.5 |
| 30% | 150˚C | 2.0 | 10.8 | 5.0 | 10.0 | 37.8 | 3.2 | 0.0 | 24.0 |
| | 200˚C | 1.6 | 8.1 | 4.7 | 9.9 | 35.1 | 8.1 | 1.1 | 27.2 |
| | 300˚C | 1.7 | 8.1 | 5.0 | 8.5 | 36.5 | 10.6 | 1.2 | 28.4 |
| | 350˚C | 1.8 | 7.8 | 6.0 | 7.3 | 37.6 | 13.1 | 0.8 | 29.0 |
| | 400˚C | 1.5 | 5.1 | 5.5 | 5.0 | 34.5 | 15.9 | 5.0 | 31.0 |
| | 450˚C | 1.3 | 2.9 | 7.1 | 2.3 | 30.7 | 14.1 | 13.6 | 32.9 |
| | 460˚C | 1.1 | 4.0 | --- | --- | 10.1 | 4.1 | 24.4 | 32.5 |

the P12 polymers fill the intrinsic mesopores of the neat OS3 matrix. One or two micropore Ps lifetimes can be fitted from the spectra. The samples with 23% and 30% P12 porogen loadings produce robust Ps intensities of both UMP (~2 ns) and SMP (~5-7 ns) at low temperatures. When curing temperatures gradually increase, the P12 degradation occurs. Note that the lifetime drop of UMP is due to the Ps disappearance from these pores into bigger pores, and should not be regarded as an actual pore size change. After the final curing at 460°C, the degradation of P12 porogen leaves behind widely open and interconnected mesopores, which are denoted by the vacuum Ps intensities (for all the three samples) increasing to over 30%. These fully cured hybrid films look almost like the fully cured neat OS3. The mesopore sizes of these widely open samples need to be extracted from their capped versions, which will be discussed later.

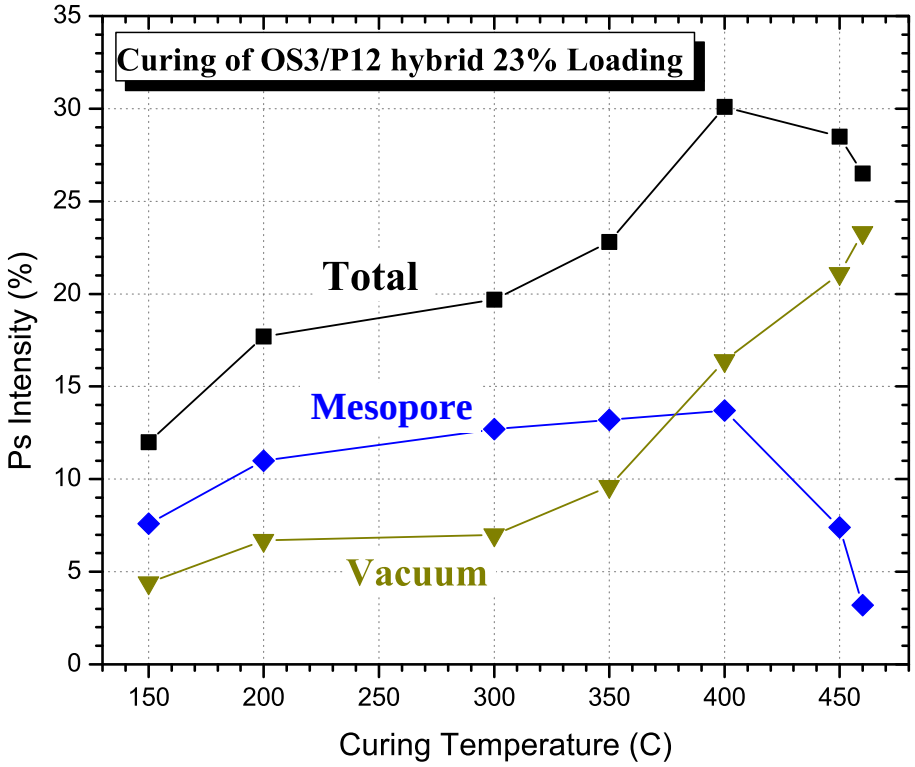


Figure 4.12: the Ps intensity in mesopore (blue) and vacuum (dark yellow) according to curing temperature. The black curve represents the total Ps intensity.

During the curing process, the mesopore Ps intensity tends to grow to a maximum, after which point the pores start to be so interconnected that more Ps escape into vacuum and mesopore intensity drops. The sample with 23% P12 loading and its Ps intensity evolution is shown clearly in figure 4.12. Now the Ps intensities in mesopores and vacuum act like the Ps intensities in micropores and mesopores in the P12-OS2 system.

The uncured samples with different P12 porogen loadings also shows an interesting trend. At 17% before curing (150°C), the hybrid is quite open with 65% Ps escape fraction. For the 23% loading sample, this fraction drops to 37%. The 30% loading sample shows no escape. It suggests that P12 porogens are filling the OS3 pores, thus aggressively blocking the routes of Ps escape at higher loadings when they reduce the pore interconnectivity. This pore blocking effect will be discussed more later.

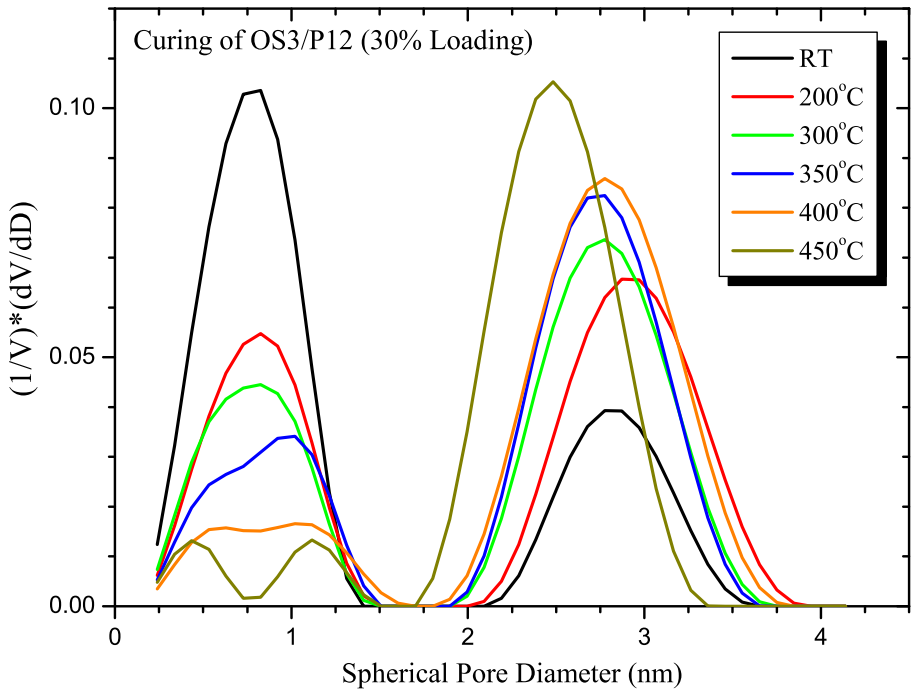


Figure 4.13: Continuous fitting results of OS3/P12 with 30% porogen loading at different heating temperatures

The continuum pore size fitting results of the 30% P12 loaded sample at different curing temperatures are shown in figure 4.13. Again, the continuum fitting is only reliable when the escape fraction is low, and only fitting results of P12 with 30% loading are shown in the figure. From figure 4.13 it is clearly seen that at room temperature there is a micropore population of 0.6-0.8 nm in diameter, which corresponds to the two micropore lifetimes in table 4.8. The larger pore size peak at ∼2.8 nm is the mesopore with Ps lifetime about 37 ns. Due to the heating process, degradation of P12 porogen induce more and more mesopore volume which drains almost all the Ps intensity from the micropores because of its lower potential energy state of Ps in the potential well. Furthermore, the fitted mesopore lifetime also shifts to the left drastically after the final cure at 450°C when the film becomes open and Ps escapes into vacuum.

### 4.2.4 Summary of the thermal curing results and discussion

The thermal curing experiments of the three neat matrices (OS1, OS2, and OS3) and their P12 porogen loaded hybrid nanocomposites (P12-OS1, P12-OS2, and P12-OS3) showed distinct pore formation and evolution behaviors which are closely related to the different characteristics of the matrices. From a pure microporous matrix (OS1) to a low-mesoporous matrix (OS2), and then to a highly mesoporous matrix (OS3), the P12 porogen, after its degradation, induced distinctly different pore structures. These pore structural evolution with the curing temperatures has evidently been characterized and confirmed by PALS and the complementary $N_2$ gas adsorption technique. Furthermore, unlike in chapter 3, where the different porogen-porogen interactions determined the final pore morphology, the hybrid nanocomposites of a single P12 porogen and MSQ based matrices (with different molecular weights and Si-OH contents) generated significantly different pore morphologies due to the evidently different porogen-matrix interactions.

The understanding of the structural evolution of the porogen induced nanopores during thermal curing on a molecular level is still not definitive. Specifically for the fabrication of ULK thin films using sol-gel organosilicates and sacrificial porogens, studies have shown that the final pore structure can be affected significantly by a number of factors [80]. The porogen should be compatible/miscible with the matrix to be dispersed at a molecular level in the matrix resins. As the thermal curing temperature increases, the polymer porogen molecules lose compatibility with the matrix and form polymer/supramolocular domains due to the matrix cross-linking. During this porogen-matrix microphase separation, the vitrification of the matrix should prevent the pore collapse when finally the porogen decomposes. It has been observed that using a *same* porogen, a high Si-OH content in the MSQ matrix

promoted an improved miscibility of the porogen polymer and enhanced the matrix cross-linking at relatively low curing temperatures, which generated smaller pores compared to a MSQ matrix with roughly the same molecular weight but a lower Si-OH concentration [81].

According to our observation, however, the hybrid P12-OS2 generated smaller pores than P12-OS1 while OS2 has a lower silanol concentration. The major difference here is that OS2 resins also have higher molecular weights, which may have hindered the diffusion mobility of P12 polymers (the P12 polymers were observed filling the OS2 matrix intrinsic pores), although it has a lower Si-OH content. The P12 induced mesopores in P12-OS2 was also observed to have a narrower size distribution than that of P12-OS1, which is a very interesting aspect that needs to be further investigated. The P12-OS3 hybrid is more complicated due to the intrinsic mesoporosity of OS3. From the thermal curing results, it seems that the P12 porogen largely fills these interstitial pores of OS3 and leave these pores intact after the P12 thermal decomposition. In the next section, this porogen filling will be further explored utilizing a series of P12-OS3 hybrid samples with different P12 loadings.

## 4.3 Nanopore structural evolution with the P12 porogen content

In the previous section, the evolution of P12 porogen and pore structure evolution with heating treatment temperature have been systematically investigated and distinct characteristics of the three matrix materials have been observed. It is also intriguing to study the evolution of the nanoporous structure induced by these porogens according to their increasing concentrations in the matrix. Thus, only the pore size and pore structure of uncured and fully cured samples will be the main focus in this section.

### 4.3.1 Pore filling effects of P12 porogen in OS3

In table 4.9, the fitting results from uncured (150°C-porogen loaded) and fully cured (porogen degraded) samples are listed. Ps lifetimes in mesopores, $\tau_{meso}$, and their corresponding Ps intensities, $I_{meso}$, are listed. The $\tau_{meso}$'s in red designate Ps lifetimes with a low corresponding Ps intensity. The Ps escape fraction, $F_{esc}$, is the fraction of the vacuum Ps intensity out of the total Ps intensity, which is calculated using $I_{vac}/I_{total}$.

Table 4.9: **The long buffer fitting results of uncured and cured OS3/P12 samples at different porogen loadings.**

| Porogen Loading | Energy (keV) | Curing Temp. | $\tau_{meso}$ (ns) | $I_{meso}$ (%) | $I_{vac}$ (%) | $I_{total}$ (%) | $F_{esc}$ (%) |
|---|---|---|---|---|---|---|---|
| 0% | 3.2 | 150°C | 34.0 | 2.0 | 19.3 | 21.3 | 90.6 |
| | 3.2 | cured | 31.2 | 3.5 | 29.4 | 32.9 | 89.4 |
| 13% | 3.2 | cured | 32.4 | 2.7 | 24.7 | 27.4 | 90.3 |
| 15% | 3.2 | cured | 29.5 | 4.0 | 24.5 | 28.5 | 85.9 |
| 17% | 3.2 | 150°C | 37.2 | 6.9 | 12.9 | 19.8 | 65.2 |
| | 3.2 | cured | 34.5 | 3.0 | 23.8 | 26.8 | 88.8 |
| 17% capped | 4.2 | 150°C | 49.4 | 14.0 | 0 | 14.0 | 0 |
| | 4.2 | cured | 48.7 | 18.9 | 0 | 18.9 | 0 |
| 19% | 3.2 | 150°C | 36.0 | 6.6 | 9.5 | 16.1 | 59.1 |
| | 3.2 | cured | 31.9 | 3.0 | 24.3 | 27.3 | 89.0 |
| 21% | 3.2 | 150°C | 38.9 | 8.5 | 5.2 | 13.7 | 38.0 |
| | 3.2 | cured | 29.0 | 3.0 | 24.2 | 27.2 | 90.0 |
| 23% | 3.2 | 150°C | 40.3 | 8.0 | 4.2 | 12.2 | 34.7 |
| | 3.2 | cured | 36.2 | 2.3 | 24.1 | 26.4 | 91.3 |
| 23% capped | 4.2 | 150°C | 49.0 | 7.6 | 0 | 7.6 | 0 |
| | 4.2 | cured | 45.4 | 18.0 | 0 | 18.0 | 0 |
| 25% | 3.2 | 150°C | 41.2 | 8.0 | 1.6 | 9.6 | 16.9 |
| | 3.2 | cured | 44.4 | 1.9 | 24.1 | 26.0 | 92.7 |
| 27.5% | 3.2 | 150°C | 42.1 | 6.4 | 0.5 | 6.9 | 6.7 |
| | 3.2 | cured | 53.2 | 1.4 | 24.5 | 26.0 | 94.2 |
| 30% | 3.2 | 150°C | 40.7 | 3.5 | 0.0 | 3.5 | 0 |
| | 3.2 | cured | 66.6 | 1.2 | 25.1 | 26.3 | 95.4 |
| 30% capped | 4.2 | 150°C | 42.3 | 2.9 | 0 | 2.9 | 0 |
| | 4.2 | cured | 47.3 | 16.7 | 0 | 16.7 | 0 |
| 32.5% | 3.2 | cured | 54.6 | 1.1 | 25.8 | 26.9 | 95.9 |
| 35% | 3.2 | cured | 68.1 | 1.3 | 25.1 | 26.4 | 95.1 |
| 37.6% | 3.2 | cured | 75.6 | 1.5 | 24.9 | 26.4 | 94.3 |

The pore filling effect is more obviously seen in figure 4.14, where the fitted Ps

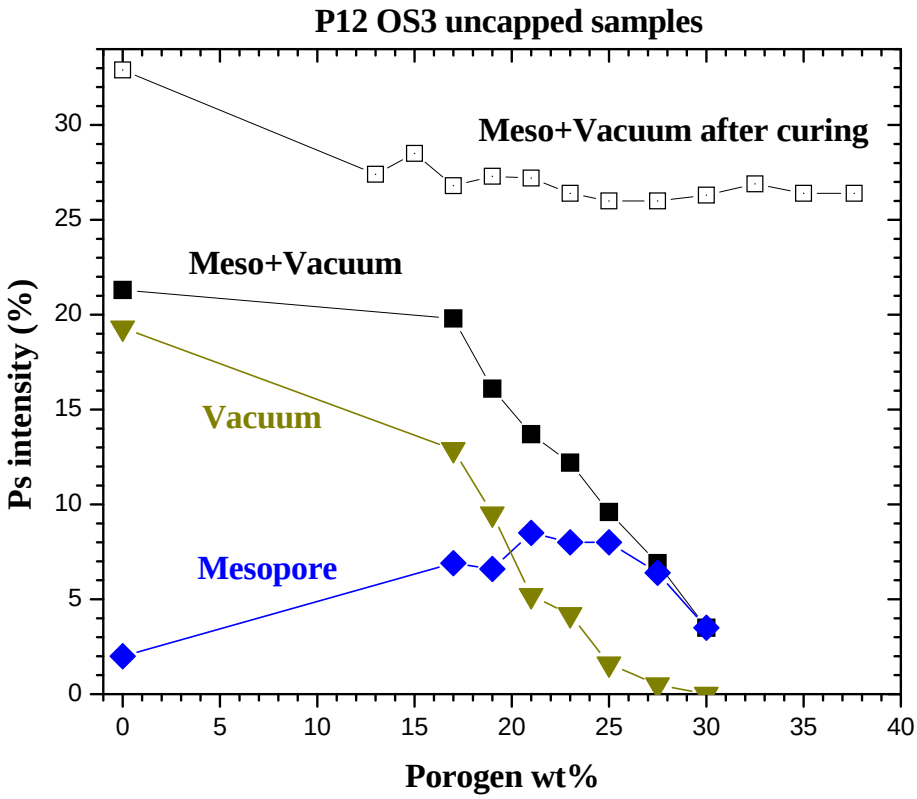


Figure 4.14: Ps intensity of P12-OS3 uncured and cured samples vs. porogen loading from long buffer fitting. Hollow symbols present the total Ps intensity of cured samples (mesopore + vacuum). Solid symbols show the Ps intensities, of uncured samples, from mesopore, vacuum and their sum.

intensity values are plotted at different porogen loadings. The hollow black symbols present the summed mesopore + vacuum Ps intensities of the fully cured (uncapped) P12-OS3 samples, while the solid symbols are the Ps intensities from uncured, porogen-loaded samples. It is clear that after curing, $I_{meso}$ + $I_{vac}$ is quite constant. Before thermal curing, the sum of Ps intensities in mesopores and vacuum drops drastically at higher P12 loadings, as expected from the porogen filling the intrinsic OS3 interstitial pores and preventing Ps from simply migrating from the micropores into the mesopores. The trends presented in figure 4.14 show the vacuum Ps intensity drops to zero at 27-30% loading while mesopore intensity increases to a maximum of 8% at 23% loading, and then decreases to 2.9% at 30% loading. The extinction of the vacuum component indicates pore sealing is occurring-but it is seal-

ing by basically filling the pores. As pores seal, the intensity of Ps annihilating in the mesopores increases to a maximum in the 20-25% loading range but inevitably has to then decrease as more porogen continues to fill in the mesopores. This residual mesopore intensity may never go completely to zero since the P12 porogen may never perfectly fill every pore space in OS3.

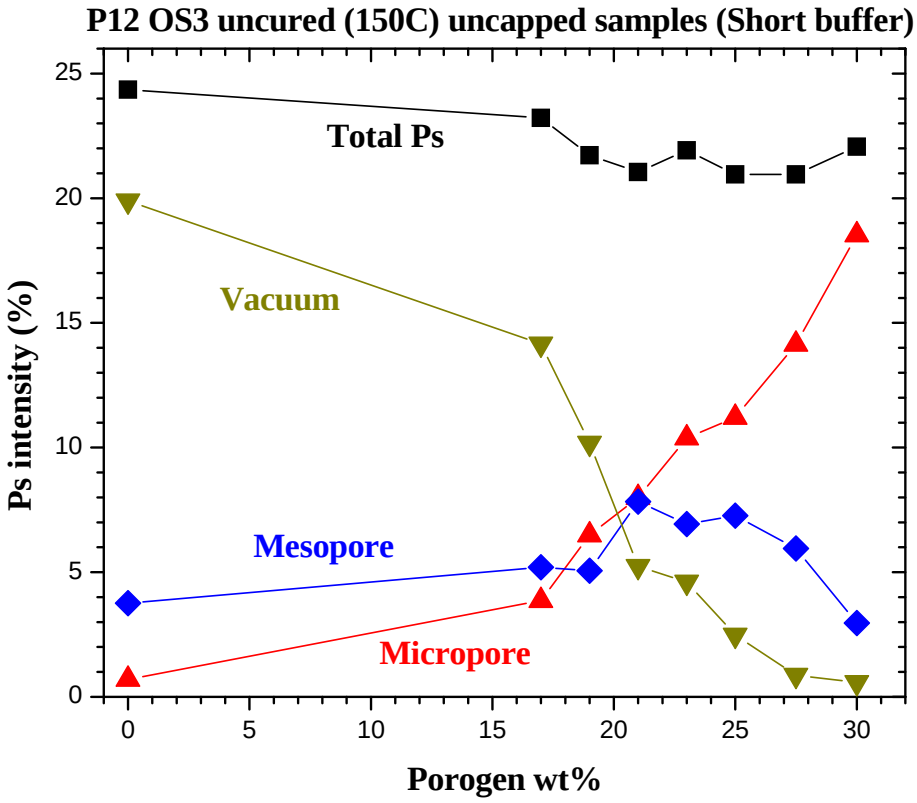


Figure 4.15: Ps intensity of uncured P12-OS3 from short buffer fitting according to porogen loadings.

Despite this pore filling by the P12 porogen, the Ps mesopore lifetime is still 49 ns up through 23% loading, which suggests that the pore filling is not a layer by layer coating of the pore walls with a gradual decrease in Ps lifetime. The P12 porogen seems to entirely fill the cross section of a pore over some of its "length" leaving other lengths undisturbed with the original Ps lifetime in OS3 (50 ns). Hence, the nominally constant mesopore lifetime with strongly decreasing intensity. This is consistent with the fact that OS3 is formed by particle like resins, which leave

space in between the particles where P12 polymer can easily locate when the resins and the P12 polymer are still miscible. At porogen loadings larger than 23%, the sealing/filling of mesopores becomes so severe that even the mesopore intensity itself goes down - more Ps are constrained inside micropores as shown in figure 4.15.

### 4.3.2 PALS experiments and analysis of the *fully cured* P12-OS samples

P12 porogen is added into the three types of matrix materials, OS1, OS2 and OS3 with different concentrations. The basic information of these *fully cured* thin film samples made by P12 porogen (P12-OS1, P12-OS2, and P12-OS3) are listed in appendix D, table D.3, D.4, and D.6, where the film thicknesses, P12 porogen weight% loadings, and R.I. can be found.

Different positron beam energies were used to implant the positrons into different depths into these thin films in order to deduce the pore interconnection lengths. Five beam energies, 0.55 keV, 1.1 keV, 2.1 keV, 3.1 keV, and 5.1 keV, which nominally correspond to positron mean implantation depths of 11 nm, 33 nm, 90 nm, 170 nm and 380 nm respectively, were applied to different films when necessary to find the interconnection length. It has been mentioned before that the distributions of the positrons are bell shaped profiles (Makhovian distribution) around the mean implantation depths. The implantation profile is broader at high energies. The PALS analysis results of these samples are shown in table 4.10. In the third column, the porosities are calculated using the refractive index values of each sample from L.L. equation. The interconnection lengths of the samples are defined as the positron mean implantation depth at which 50% of the formed Ps can escape from the sample surface of the film and annihilate in vacuum. In appendix D, the figures for the deduction of the interconnection length of P12-OS1 and P12-OS2 sample series are shown (figure D.1 and D.2). The P12-OS3 series has total interconnected pores and

Table 4.10: **PALS analysis results of the OS/P12 fully cured samples. The Ps lifetimes in red are deduced from capped versions of the specific film.**

| Matrix | P12 Loading (%) | Porosity From L.L*(%) | Average Ps Lifetime (ns) | Cyl. Pore Diameter (nm) | Spher. Pore Diameter (nm) | $I_{ps,\ film}$ (%) | Intercnt. Length (nm) |
|---|---|---|---|---|---|---|---|
| OS1 | 3 | 1.7 | 16.7 | 1.42 | 1.69 | 19.2 | 0 |
| | 7 | 6.1 | 19.7 | 1.54 | 1.84 | 28.1 | 5 |
| | 10 | 11.0 | 24.8 | 1.74 | 2.08 | 30.4 | 20 |
| | 15 | 14.0 | 28.7 | 1.88 | 2.27 | 33.5 | 42 |
| | 20 | 23.7 | 38.6 | 2.26 | 2.81 | 37.4 | 125 |
| | 25 | 23.2 | 41.6 | 2.38 | 2.99 | 38.7 | 200 |
| | 30 | 36.0 | 57.0 | 3.14 | 4.12 | 40.3 | fully int. |
| OS2 | 2.5 | 0.9 | 13.9 | 1.30 | 1.55 | 18.8 | ~5 |
| | 5.0 | 2.5 | 14.8 | 1.34 | 1.59 | 24.9 | ~5 |
| | 7.5 | 3.7 | 13.5 | 1.28 | 1.53 | 21.5 | 20 |
| | 10 | 5.0 | 13.5 | 1.28 | 1.53 | 27.4 | 30 |
| | 10 | 5.7 | 15.0 | 1.36 | 1.60 | 29.1 | 32 |
| | 15 | 10.0 | 15.5 | 1.37 | 1.63 | 30.1 | 40 |
| | 20 | 14.7 | 18.0 | 1.48 | 1.75 | 31.1 | 90 |
| | 25 | 20.1 | 23 | 1.67 | 1.99 | 29.9 | 140 |
| | 30 | 26.0 | 28 | 1.86 | 2.23 | 33.3 | 240 |
| | 35 | 31.8 | 34 | 2.08 | 2.54 | 33.4 | fully int. |
| | 40 | 38.0 | 43 | 2.44 | 3.06 | 31.6 | fully int. |
| OS3 | 0 | 37.4 | 49.8 | 2.74 | 3.52 | 32.9 | fully int. |
| | 13 | 35.2 | 49.4 | 2.72 | 3.49 | 27.4 | fully int. |
| | 15 | 34.9 | 49.0 | 2.70 | 3.46 | 28.5 | fully int. |
| | 17 | 34.4 | 48.7 | 2.69 | 3.44 | 26.8 | fully int. |
| | 19 | 34.1 | 48.1 | 2.66 | 3.39 | 27.3 | fully int. |
| | 21 | 33.9 | 47.0 | 2.61 | 3.32 | 27.2 | fully int. |
| | 23 | 33.4 | 45.4 | 2.53 | 3.21 | 26.4 | fully int. |
| | 25 | 35.0 | 44.6 | 2.50 | 3.16 | 26.0 | fully int. |
| | 28 | 36.5 | 45.6 | 2.54 | 3.23 | 26.0 | fully int. |
| | 30 | 38.5 | 47.3 | 2.62 | 3.34 | 26.3 | fully int. |
| | 33 | 41.1 | 50.0 | 2.74 | 3.53 | 26.9 | fully int. |
| | 35 | 43.3 | 52.0 | 2.85 | 3.68 | 26.4 | fully int. |
| | 38 | 46.0 | 56.0 | 3.06 | 4.00 | 26.4 | fully int. |

$L_{int}$ cannot be deduced (fully interconnected). Ps lifetimes shown in the table were taken at 3.1 keV, (since all the films are around 600 to 700 nm thick with density about 1 g/cm$^3$, there should be few positrons penetrating the films) and the ones in red are obtained from the capped version of the specific samples at 4.1 keV (4.2 keV for OS3 samples) positron beam energy. The Ps lifetimes were converted to cylindrical or spherical pore diameters using cylindrical and spherical models. The cylindrical model assumes the pores are long tubular shaped, which is more physical

when the pores are interconnected. At low porosities when most of the mesopores are isolated, the spherical model is a better choice for Ps lifetime to pore diameter conversion. The total Ps intensities from mesopores are also shown in table 4.10.

We mainly focus on the Ps lifetimes that correspond to the mesopores generated by the P12 porogens. It is obvious that when the P12 porogen loadings increased from 3% to 30%, the Ps lifetime increased from 16.7 ns to 57 ns. The average Ps lifetimes from 20% to 30% loadings in red were deduced from the capped versions of these films since the Ps escape at those porogen loadings distorts the Ps lifetimes to their lower end. The lifetime corresponds to a mesopore diameter growth from 1.42 nm to 3.14 nm in the cylindrical model, and 1.69 nm to 4.12 nm in the spherical model. This obvious growth of pore size due to the porogen loading indicates the nucleation and growth is not purely linear/1-dimensional, unlike the pore size evolution of sCD porogen (linear growth) in chapter 3, where the size of the mesopore produced by sCD porogen is quite constant at all the porogen loadings. Here instead of forming cylindrical-like long chains, the P12 porogen grows more in 3-dimensions, including the growth of pore size as well as the interconnection length.

The experiments done on P12-OS2 samples are similar to P12-OS1. The average Ps lifetimes from 25% to 40% loadings in red are deduced from the capped versions of these films. The pore sizes from the summary do not greatly differ from P12 in OS1. The pore size of P12 in OS2 has similar trend but is smaller than in OS1. The low porosity samples indicate at loadings less than 10%, the pore size of P12 is pretty constant around 1.3nm. The interconnection length starts to grow earlier than pore size. It is larger than several diameters even at 5% ($\sim$5 nm). Interestingly, the interconnection length of P12-OS2 is longer than that of P12-OS1. Crudely speaking, in OS2, P12 looks more cylindrical like with smaller diameter and slightly

longer length.

The OS3 matrix itself and the P12 porogen in OS3 shows drastically different behavior compared with OS1-P12 and OS2-P12 systems, shown in table 4.10. Furthermore, the basic information of the fully cured (at 425°C) uncapped OS3-P12 is listed in the Appendix D, table D.6. At all the P12 porogen loadings from 13% to 38%, the fully cured samples have fully interconnected mesopores similar to the intrinsic mesopores in the pristine OS3 matrix. The Ps intensities gradually decrease with P12 concentration. This is believed to be an aggravating positron penetration as the film becomes more and more porous. The average Ps lifetime in mesopores are deduced from capped versions of the P12-OS3 samples and it shows a very interesting trend, which will be discussed later. Since the neat OS3 matrix is highly mesoporous, it is more reasonable to compare the three P12 systems based on the actual porosity, not the P12 weight percentage loading. In order to calculate the porosity of the various films of the P12-OS3 system from the L.L. equation, special procedure needs to be used to accommodate the intrinsic mesoporosity of the OS3 matrix. Note that the pristine OS3 matrix has a nominal density of 0.945 g/cm$^3$, but the P12 porogen weight percentage loading is relative to the weight of the backbone material of the OS3 resin ($\sim$1.5 g/cm$^3$) and the density of P12 porogen is around 1 g/cm$^3$. The mesopore porosity of OS3 was found to be about 37% from the $N_2$ adsorption experiment done by IBM. Based on this porosity, the R.I. of the dense backbone material of OS3 can be extrapolated and used as a baseline of 0% porosity. Then the porosities of the other fully cured samples fabricated by varying P12 loadings can be deduced. More discussions of the parallel comparison between these three systems will be elaborated in the next section.

### 4.3.3 Comparative study of P12 porogen in the three OS matrices

The fitted lifetimes and deduced pore interconnection lengths from Table 4.10 are plotted in figures 4.16 and 4.17. The pore size in OS1 increases rapidly with porosity and is always much larger than the intrinsic OS1 pore size(s). The low loading/low porosity samples indicate that at loadings up to ∼15%, the pore size of P12 in OS2 is quite constant around 1.3 nm, the pore size of the neat OS2 resin (figure 4.7). This suggests that the P12 porogen initially fills the intrinsic OS2 matrix pores. The interconnection length in OS2 starts to grow before the pore size does and this suggests that either cylindrical-shaped pores are getting longer (Ps lifetime determined by the cross sectional pore diameter, not length) or, constant-sized pores are becoming more plentiful and randomly overlapping to form pore interconnections. It is possible that volatilizing P12 in OS2 pores effectively produce pore interconnections that are not intrinsic to the neat resin. The interconnection length in cured OS2 is larger than several pore diameters even at 5% loading (∼5 nm). Through all the porosities, the P12 generated pore size is bigger in OS1 than in OS2, which requires a closer look.

The pore size and pore structure in N&G systems depend on many factors and are very difficult to control. As mentioned earlier, the originally compatible/miscible solution of matrix resins and porogen molecules has to undergo a phase separation process to form a nanoporous structure. During the heat treatment, the sequence of matrix condensation due to cross-linking and the phase separation of porogen is a crucial factor that determines the final pore size and pore structure. Generally speaking, matrix resins with more Si-OH content vitrify at relatively lower temperatures, which could lead to a smaller pore size because the lower mobility of the porogen molecules at phase separation [81]. However, this is not the case we have

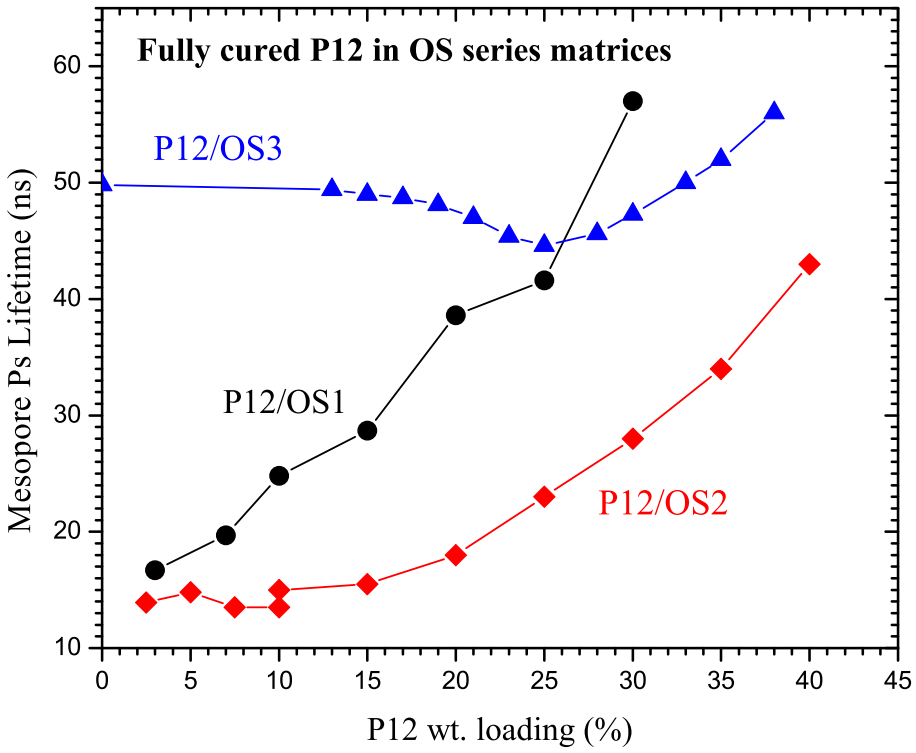


Figure 4.16: Ps lifetime at different P12 porogen loadings in OS1, OS2 and OS3

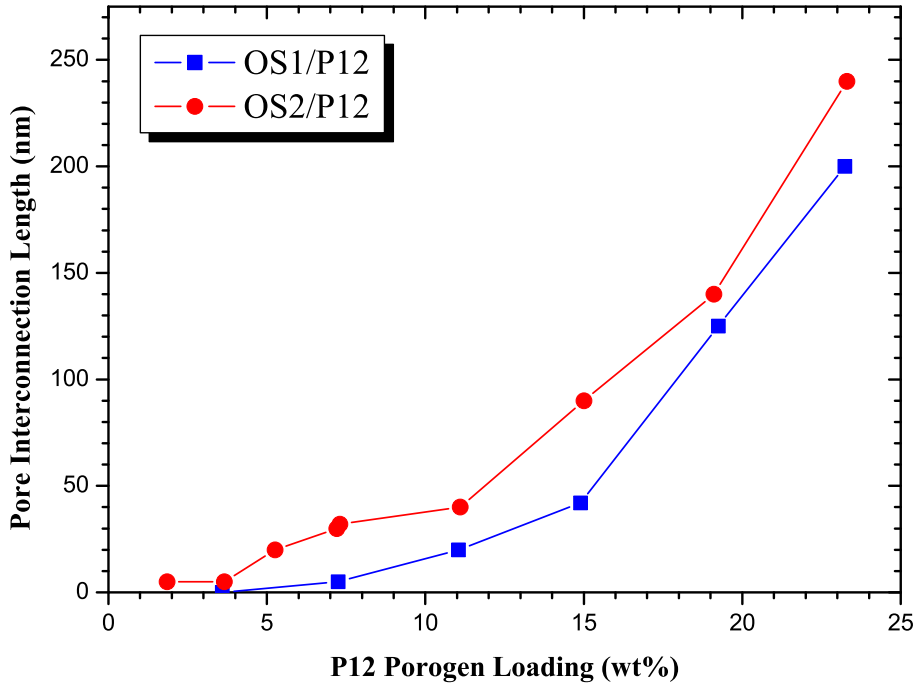


Figure 4.17: Pore interconnection lengths at different P12 porogen loadings in OS1 and OS2

seen in the OS1 and OS2 systems. The OS1 resin has higher Si-OH content than OS2, but generates bigger pores, which may be attributed to the intrinsic pores in OS2, or in other words, the higher molecular weight of the OS2 resins. This might be a confinement related issue that at low porosity (<10%), the generated pore size from P12-OS2 is quite constant, and fairly consistent with the intrinsic pore size of the pristine OS2 matrix. But at higher porogen loadings, the diffusion or phase separation might be hindered when the P12 polymer managed to partially reside in these intrinsic pores, and thus these P12 polymers produce smaller domains and finally smaller mesopores than in OS1. This suggests that not only the choice of porogen is critically important, but the matrix resins with "correct" Si-OH content and molecular weight and a correct combination of porogen and matrix materials are crucial as well.

The lifetime evolution trend of cured P12 in OS3 in figure 4.16 looks very interesting, and also puzzling. Unlike in OS1 and OS2 systems, where Ps lifetimes monotonically increase, the porogen induced pore size in OS3 decreases first with porogen loading up to ∼25%. Can adding porogen and curing actually decrease porosity? The R. I. curve in figure 4.18 supports this hypothesis: at ∼23% loading the refractive index R.I. reaches a maximum, which is roughly coincident with the lifetime minimum and then sharply drops. The R.I. data is telling us that the overall porosity after curing is actually decreasing up to 23% loading even though we added in more and more P12 porogen. As mentioned earlier, P12 porogen is filling the intrinsic pores of OS3. Furthermore, up to the point where porogen overflows the intrinsic OS3 pores one might expect no effect on pore size or porosity and then increasing porosity and pore size thereafter. *Evidently, P12 porogen filling of and curing in the OS3 intrinsic pores produces some minor pore collapse that one might*

*not have anticipated in the naive pore filling model.* The Ps lifetime in the uncured porogen-filled OS3 does not reflect this initial decrease in fitted Ps lifetime. Despite the pores filling with porogen the Ps lifetime in the remaining unfilled OS3 pores stays close to 50 ns through 23% loading (see figure 4.20) but drops to 45 ns after curing. Attraction (like capillary forces) between P12 polymer and OS3 resin particles could have caused this optimized packing. If one can assume that there is no obvious interaction between the P12 porogen and OS3 particle resins in the solution state, it seems as if curing of P12 in OS3 is the key to understanding this densification of the film.

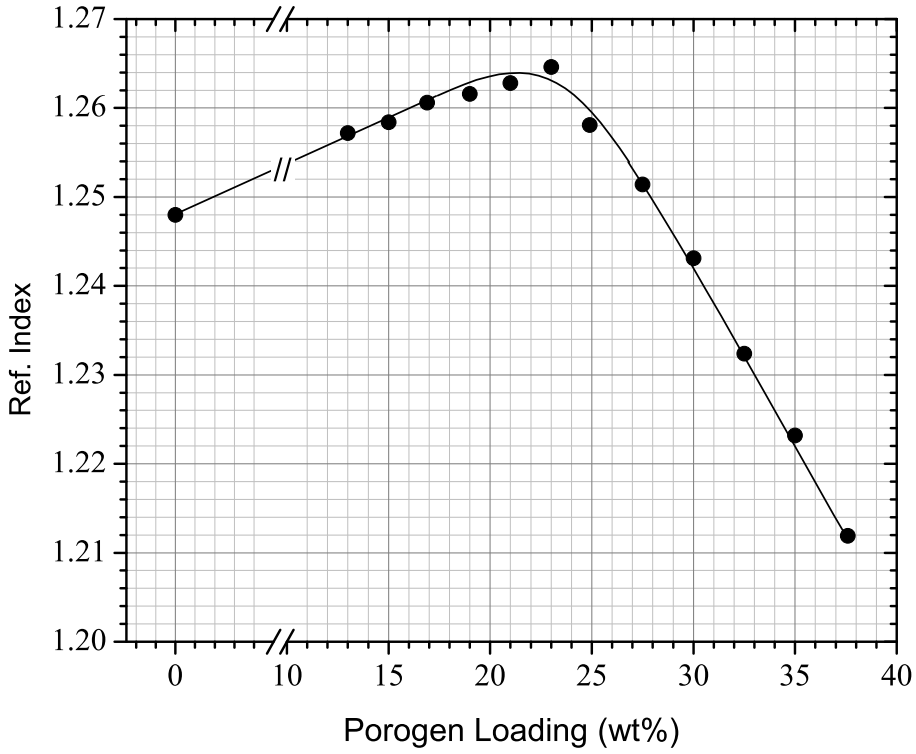


Figure 4.18: Refractive indices of the *fully cured* P12-OS3 hybrid samples vs. P12 porogen weight% loading that indicates the porous film densification up to ∼23% loading.

Another possibility that still cannot be ruled out is that the P12 porogen domains are distinctly different from the OS3 intrinsic pores, which could generate two distinct mesopore populations: one from the inherent OS3 interstitial mesopore; the other

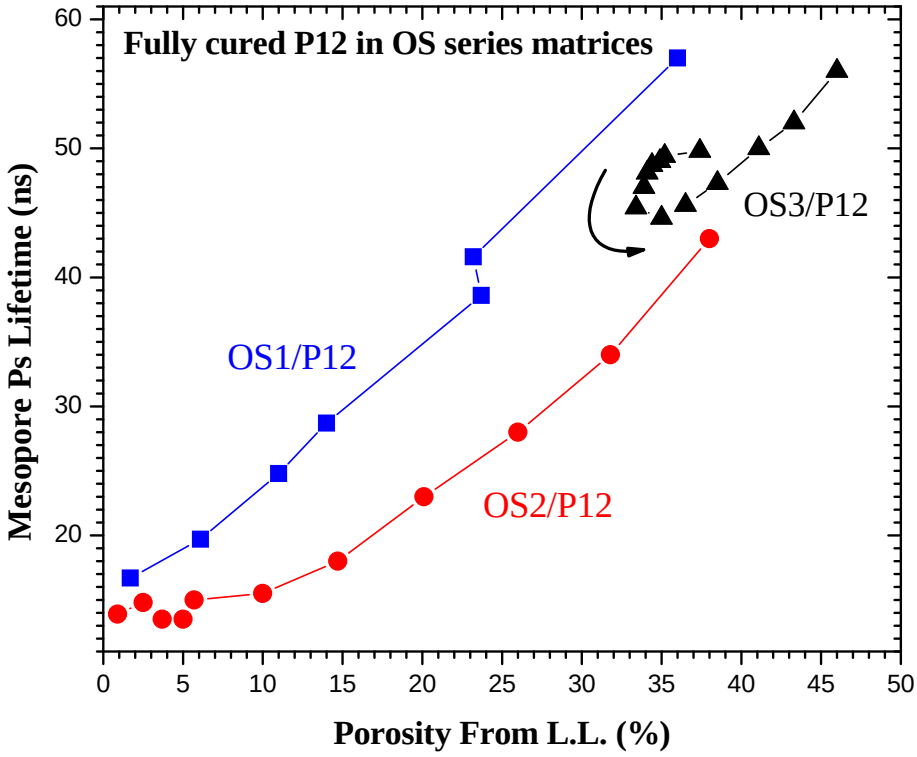


Figure 4.19: Mesopore lifetime according to the mesoporosity that calculated from L.L. equation

from the P12 N&G porogen. The size of the P12 domains increase according to the P12 porogen loading (which we have seen in OS1 matrix), and the intrinsic OS3 interstitial pores stay unaffected. At low loadings, all the Ps atoms escape from the smaller P12 pores to OS3 interstitial pores, which gives us lifetime around 50 ns. As the P12 loading increases, due to the N&G process, the pore size of P12 starts to be comparable to the OS3 pores and the Ps lifetime starts to look like an average of these two populations. This average could be lower than 50 ns. At really high loading, P12 increases fast and even exceeds the size of OS3, which drives the overall average pore size up to 56 ns. However, it is impossible to distinguish these two mesopore populations from our PALS analysis.

In figure 4.19, the mesopore lifetimes versus the porosity calculated from the L.L. equation are re-plotted. It needs to be mentioned that because OS3 is mesoporous

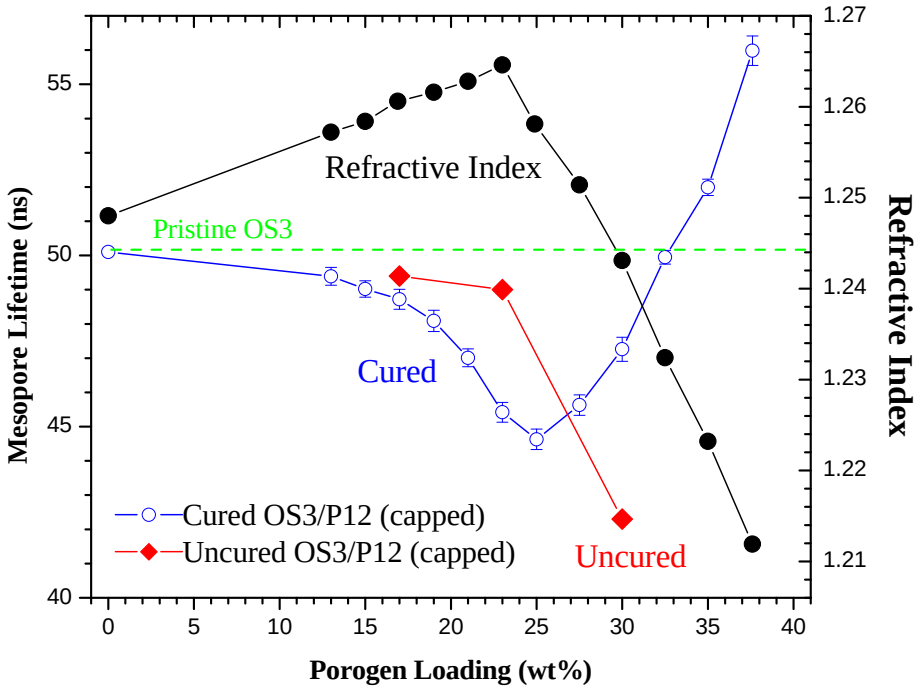


Figure 4.20: Mesopore lifetimes of P12-OS3 change before and after curing. At low P12 loading, the lifetime does not change much. At 23%, lifetime drops from 49ns to 45.4ns after curing. At 30%, lifetime increases from 42.3ns to 47.3ns.

with ∼37% porosity. (From $N_2$ absorption data, the total porosity is 45% with 83% mesopores.) The $n_m$ (see equation 2.5 in chapter 2) of the wall material is first calculated using the $n_{eff}$ of neat OS3, which is 1.248 and the R.I. of the wall material is calculated as 1.414, which can be treated as the R.I. of the totally "microporous" backbone material of the OS3 matrix. The lifetime of P12-OS3 first decreases as porosity decreases, reaches a minimum, and then starts to increase with porosity. The arrow shows the direction of increasing P12 loading. It seems that, within certain range, porosity can always be achieved by two porogen loadings. The lower loading gives bigger pores with a little less concentration, while the higher loading gives slightly smaller pores with higher concentration.

It is interesting to compare the pore size before and after curing. At low loadings, they do not differ much since no drastic effect has occurred. At 23%, the uncured

Ps lifetime is still around 50 ns, but the curing can drop this number to 45 ns. It is hard to imagine that the degradation of P12 can reduce the pore size if they all reside in OS3 interstitials. One explanation, which is mentioned before, is that the P12 porogen optimizes the packing of OS3 resin particles by filling in their interstitial spaces at low loadings (<25%). This condensation is seen on the R.I. curve. There could be also P12 nanocomposites that leave behind smaller pores after evaporation and drag down the average lifetime. When the P12 concentration reaches some critical value, the N&G process starts to dominate. The agglomeration of P12 porogens starts to form big nanocomposites that swell the OS3 pores and that will stop the optimization of packing.

#### 4.3.4 Summary of the structural evolution with the P12 porogen concentration

As a overall summary of P12 porogen in these three matrices, the intrinsic pores of neat OS1 are the smallest with $D_{sph}$ <1.3 nm, and they are not interconnected. Although these small pores may be sites for P12 nucleation the pore sizes formed from P12 incorporation and degradation in OS1 are always larger than the intrinsic pores and the pore diameter grows relatively quickly with porogen loading. These larger pores tend to be isolated at low P12 loading and the pore interconnection length grows relatively slowly as one might expect from random pore overlap.

The intrinsic pores of neat OS2 are of intermediate size in the range 0.9-1.7 nm diameter and, like OS1, they are also not interconnected. In this case the P12 seems to initially fill these nominally 1.3 nm diameter pores and degradation of the porogen does not alter the 1.3 nm pore size - it does however foster pore interconnection - converting the 1.3 nm diameter isolated pores of the neat OS2 resin into equal sized pores connected over 10-100 nm (many pore diameters).

The intrinsic pores of OS3 are large ($D_{sph}$=3.5 nm or $D_{cyl}$=2.7 nm) and fully

interconnected (percolated) and of high porosity. P12 incorporation appears to completely fill segments of the pore network leaving other segments pristine. As a result the mesopore lifetime in porogen-loaded (but uncured) films presents the neat OS3 matrix lifetime of about 50 ns but with decreasing Ps intensity while the Ps intensity in the micropores rises with pore segment filling. After porogen degradation there is an interesting decrease in the mesopore lifetime consistent with RI data showing a decrease in porosity up to about 23% loading. Additional porogen loading presumably overfills the intrinsic OS3 pores and generates increased porosity with larger average pore sizes. The transition to filled pores is first marked by pore sealing (curtailing of Ps escape into vacuum) and then by pore filling saturation (extinction of the Ps mesopore component) followed by swollen pores after porogen degradation.

## 4.4 PALS experiments on PJB porogens in OS series matrices

Forming ordered nanopore structure is believed to be a way of maintain short pore interconnectivity at fairly large porosities. This kind of ordered structures can be realized through self-assembly using pore generators that, when mixed with matrix resins, can interact through amphiphilicity or miscibility. The PJB porogen is a star-shaped copolymer with a polystyrene core and a polyethylene glycol (i.e., polyethylene oxide) corona (with up to 30 arms) [82]. The polyethylene oxide (PEO) is hydrophilic and interacts with the MSQ precursor; the polystyrene core is hydrophobic. The size of the PEO corona can be controlled by the length of the PEO chain arms. This micellar PJB particles can form, to some extent, ordered structures. For a true templated process, the pore size should be determined by the particle size and not affected by the porogen concentration. This is the unique feature that separates the templated process from the N&G process [83].

In appendix D, the information of the three series of PJB samples, PJB-OS1, PJB-OS2 and PJB-OS3, is summarized in table D.9, table D.10 and table D.11. The film thicknesses of PJB-OS1 and PJB-OS2 samples are all around 600 nm. The thicknesses of the PJB-OS3 samples vary from 350 nm to 440 nm. The weight fractions of the PJB porogen loading and the estimated PJB volume fractions are calculated from the density of the PJB porogen and the OS matrices. The porosities calculated from the L.L. equation are shown in the last column using the R.I. data. The porosity of the samples ranges from about 5% to 40%. The PALS analysis results of these three systems are shown in table 4.11.

#### 4.4.1 PJB in OS1

The OS1 neat resin is fit to four lifetimes with two components - 8.1% Ps annihilating in a 2.5 ns lifetime component and 28% annihilating in a 7.1 ns lifetime component - representing UMPs and SMPs of the film respectively. Any engineered pores from the porogens in OS1 should produce easily separable components in the lifetime fitting. As such, the mesopores in these OS1 films can all be effectively analyzed by fitting the long buffer spectra (delayed fitting) to two Ps lifetimes. The longest lifetime is due to Ps annihilating in vacuum, either from backscattering or Ps escaping the film, while the shorter lifetime is due to Ps annihilating in the mesopores. Ps annihilates with a 53.9 ns lifetime at the lowest porosity increasing up to 85.2 ns for the 40% (48.2% volume fraction) film. This corresponds to cylindrical pore diameters ranging from 2.94-5.52 nm. The Ps intensities slowly increase from 9.5% for the 5% film to 32.9% in the 40% film. (see figure 4.24)

The detailed PALS fitting results of PJB-OS1 at each beam energies are shown in appendix D, table D.12. We need to note that at 5% PJB loading, the Ps intensities in vacuum at each beam energy are roughly consistent with pure backscattering.

Table 4.11: **PALS analysis results for the PJB-OS1-OS3 films. The average Ps lifetimes determined from the capped films are shown in red. The Ps intensity, $I_{Ps,film}$ is determined at a beam energy of 3.1 keV in an uncapped film.**

| Matrix | PJB vol. (%) | Porosity L.L (%) | $\tau_{average}$ (ns) | $D_{cylinder}$ (nm) | $D_{sphere}$ (nm) | $I_{Ps,film}$ † (%) | $L_{inter}$ (nm) |
|---|---|---|---|---|---|---|---|
| OS1 | 6.4 | 5.4 | 53.9 | 2.94 | 3.83 | 9.5 | ~closed |
| | 12.4 | 9.2 | 56.8 | 3.10 | 4.06 | 17.3 | <5 |
| | 18.5 | 14.8 | 59.8 | 3.28 | 4.33 | 25.4 | 10 |
| | 24.9 | 20.1 | 64.0 | 3.55 | 4.73 | 29.4 | 25 |
| | 30.3 | 25.9 | 66.9 | 3.75 | 5.04 | 31.1 | 45 |
| | 35.7 | 31.4 | 70.2 | 4.00 | 5.41 | 32.3 | 70 |
| | 46.6 | 42.1 | 85.2 | 5.52 | 7.68 | 32.9 | 270 |
| OS2 | 2.50 | 3.5 | 55-57 | 3.03-3.14 | 3.92-4.08 | 12.1 | ~5 |
| | 4.65 | 6.4 | 55-57 | 3.03-3.14 | 3.92-4.08 | 14.0 | 20 |
| | 7.45 | 10.2 | 55-57 | 3.03-3.14 | 3.92-4.08 | 17.7 | 38 |
| | 9.95 | 13.5 | 55-57 | 3.03-3.14 | 3.92-4.08 | 21.5 | 50 |
| | 13.7 | 10.2 | 55-57 | 3.03-3.14 | 3.92-4.08 | 24.0 | 43 |
| | 20.0 | 14.3 | 55-57 | 3.03-3.14 | 3.92-4.08 | 27.1 | 63 |
| | 26.2 | 21.5 | 62.4 | 3.46 | 4.57 | 30.7 | 130 |
| | 32.1 | 26.3 | 66.7 | 3.77 | 5.02 | 32.2 | 190 |
| | 37.8 | 32.9 | 70 | 4.01 | 5.39 | 32.0 | /* |
| | 43.3 | 38.2 | 76.5 | 4.59 | 6.24 | 31.6 | / |
| | 48.6 | 44.1 | 77 | 4.65 | 6.31 | 32.8 | / |
| OS3 | 0.0 | 37.4 | 50.2 | 2.76 | 3.54 | 31.2 | / |
| | 4.8 | 37.6 | 50.3 | 2.76 | 3.55 | --- | / |
| | 9.5 | 37.9 | 52.4 | 2.87 | 3.71 | --- | / |
| | 14.3 | 38.2 | 56.0 | 3.06 | 4.00 | 31.6 | / |
| | 16.8 | 38.5 | 54.7 | 2.99 | 3.89 | --- | / |
| | 19.1 | 38.8 | 54.9 | 3.00 | 3.91 | --- | / |
| | 21.5 | 39.0 | 55.6 | 3.04 | 3.96 | 29.7 | / |
| | 23.9 | 39.2 | 54.7 | 2.99 | 3.89 | --- | / |
| | 26.5 | 40.1 | 56.6 | 3.09 | 4.05 | --- | / |
| | 28.7 | 40.9 | 57.6 | 3.15 | 4.13 | 29.2 | / |
| | 31.2 | 42.2 | 58.7 | 3.21 | 4.23 | --- | / |
| | 33.7 | 44.6 | 60.4 | 3.32 | 4.38 | --- | / |
| | 36.0 | 46.3 | 63.7 | 3.53 | 4.70 | --- | / |

†*$I_{Ps,film}$ are taken at beam energy 3.1keV.*
** indicates the interconnection length is long due to percolation.*

There might be a hint of Ps escape from inside the film through interconnected pores, but this intensity is mostly less than 1%. The interconnection lengths at different PJB loadings are deduced from the Ps escape fraction shown in figure 4.21. Additionally, while $I_{Ps,film}$ increases for fixed beam implantation energy as the porogen loading increases, $I_{Ps,film}$ decreases at higher positron beam energies (deeper

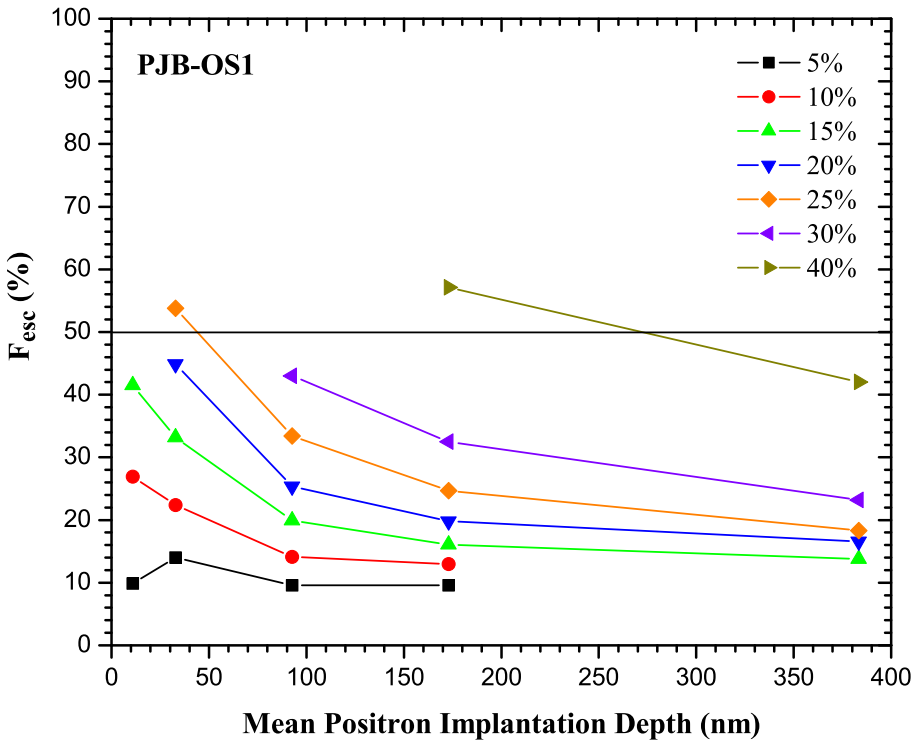


Figure 4.21: The escape fraction, $F_{esc}$, as a function of mean positron implantation depth. The interconnection length is defined as the depth where 50% of Ps escapes from the film. These results do NOT follow the usual diffusion law behavior with implantation depth.

implantation) for any given porosity. Five lifetime fitting indicates that the intensity of Ps annihilating in a 2.0-2.5 ns component shows a concomitant increase while $I_{Ps,film}$ shows a decrease for a particular porosity. Normally, we would expect to see an increase in the 7-8 ns component intensity in the film (which remains constant as a function of positron beam energy). This may be an indication that pores (or some fraction) deeper in the film remain filled with porogen.

### 4.4.2 PJB in OS2

Information on the PJB-OS2 series supplied by IBM is shown in table D.10 in appendix D. Fitted PALS results are in table 4.11, shaded in orange. For the low PJB loaded films, while the pores in this film are quite large the relatively low intensity of Ps annihilating in them at low porosity requires that the spectra be fit

to 3 discrete lifetimes with one of them fixed at 18 ns to account for Ps annihilating in the inherent porosity of OS2 resin. We find all the PJB films to have some degree of pore interconnectivity - there is always some Ps escaping into vacuum. The nominal pore interconnection length is deduced for each film from the plot of $F_{esc}$ vs. mean implantation depth. (See figure 4.22) There is perfect correlation observed for the interconnectivity vs. porosity. Capping is required to determine the correct Ps lifetime in the mesopores for samples at high porosities (note that the fitted Ps lifetimes in the uncapped films are always systematically shorter). Other than the obvious differences in interconnection length between PJB-OS1 and PJB-OS2, the mesopores in PJB-OS2 samples have slightly smaller size for a given porosity than PJB-OS1. The only significant difference is for the largest porogen loading where the OS1 pores are 5.49 nm and the OS2 pores are 4.65 nm. It needs to be mentioned that when fitting the PJB-OS2 samples, we need to distinguish the ∼18 ns intrinsic lifetime due to the OS2 resin from the engineered mesopores lifetime of 56 ns which comes from the PJB particle porogen. Fortunately, these two pore populations are rather easy to disentangle.

The mesopores from PJB has a quite constant lifetime, ∼56 ns, at porosities <20%, which is a pretty distinct feature for the PJB-OS2 series. We have not observed this feature in PJB-OS1 system, where the Ps lifetime gradually increases throughout the whole porosity range. The 56 nm Ps lifetime corresponds to a pore diameter of 4.0 nm or 3.1 nm for a cylindrical model.

#### 4.4.3 PJB in OS3

The last section in table 4.11 shaded in blue shows the PALS results of PJB-OS3 samples. As we know, the OS3 matrix is inherently mesoporous with a Ps lifetime of 50 ns, which is seen in the 0% loaded sample. Because the OS3 pores

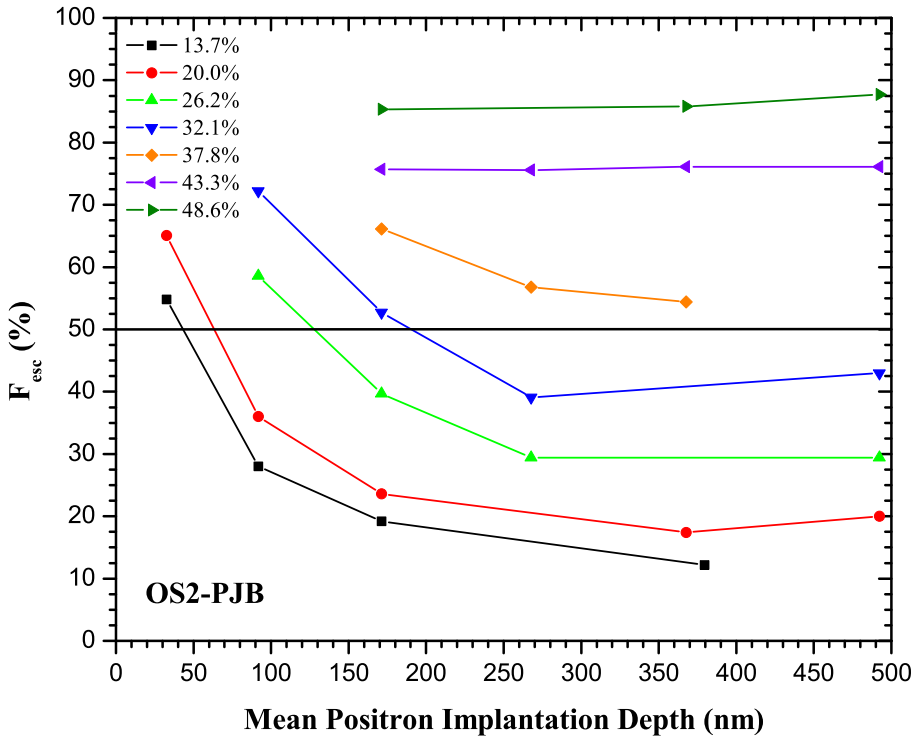


Figure 4.22: Ps vacuum escape fractions vs. mean positron implantation depth for the various porosity films in the PJB series.

are interconnected from the outset, all the PJB-OS3 samples need to be capped to achieve reliable mesopore lifetimes, which are shown in red in table 4.11. All the PJB-OS3 lifetime results were deduced from 4.2 keV energy runs. The lifetime varies from 50 ns to 64 ns, corresponding to a spherical pore diameter of 2.76-3.53 nm, or a cylindrical pore diameter of 3.54-4.7 nm. At the same porogen loadings PJB in OS3 generates significantly smaller pores than in the other two matrices. However, this is somewhat misleading since they do not have the same porosity at the same porogen loading due to the intrinsic mesoporosity (∼37%) of OS3. The lifetimes need to be compared at same porosities calculated from R.I. using the L.L. equation.

The Ps intensities of the film are taken from uncapped samples at 3.2 keV beam energy. Unlike the OS1 and OS2 system, we see 31% intensity and gradually decrease slightly at higher porogen loadings. This could be simply due to positron penetration

through the film at 4.2 keV (mean implantation depth ∼280 nm at density 1 g/cm$^3$) because the films are less than 400 nm thick and even thinner at higher porosities (∼340 nm).

#### 4.4.4 Comparisons and summary

As a summary, the PJB porogen, which is a star shaped particle with hydrophilic corona and hydrophobic core, has pore diameter in OS1 of 3.19 nm (cylindrical model) at low porosity and goes up to 7.64 nm at 40% porosity. The pores seem to be interconnected from the outset. In OS2, the pore size is constant at porogen volume loading <20%, and grows more gradually than in OS1. In OS3, the pore size increase from 2.75 nm to 3.53 nm at porosities of 37% to 46%.

The pore evolution trends of PJB in OS1 and OS2 are similar to that of P12 in OS1 and OS2. The Ps lifetime evolution of all the three systems according to PJB loading is shown in figure 4.23. The PJB-OS1 samples have the largest Ps lifetime at the same loading (consequently the largest pore size) among the three systems. The PJB-OS2 system has similar pore sizes at high loadings, but shows quite constant Ps lifetime at loadings less than 15%. Considering porogen P12 and PJB, the two porogens both generate smaller pores in OS2 than in OS1. However, P12 in OS2 produces much smaller pores than in OS1, which is dominated by the N&G mechanism. On the other hand, the mesopores produced by PJB in OS2 are only slightly smaller than in OS1. Because the PJB porogen has the self-organization capability, it produces pores in a more controlled way that is largely decided by the size of the PJB porogen itself, not like in the N&G process.

The intensity of Ps produced in the mesopores, $I_{Ps,Film}$, (here defined as the intensity of the mesopore lifetime >50 ns in PJB-OS systems) is plotted versus porosity in Figure 4.24. (The parameter $I_{Ps,Film}$ also includes any Ps escaping into vacuum

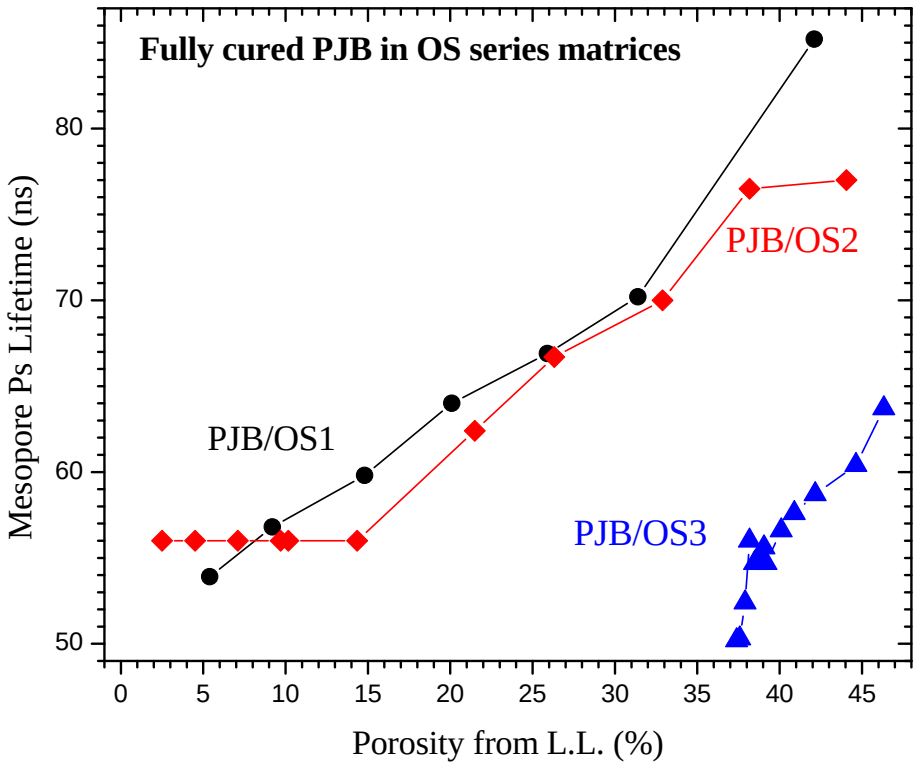


Figure 4.23: Mesopore Ps lifetime evolution according to the PJB porogen volume percentage loadings.

through the mesopores.) The data for PJB-OS1 and PJB-OS2 clearly roll over at lower porosity, a clear sign that the measured pores are due to the porogen, and in fact should without doubt extrapolate to zero (indicated by the dashed line). The slower rise in the PJB-OS1 data should be due to the much larger pore size - any given porosity is achieved in PJB with a lower density of bigger pores with an attendant thicker wall of non-mesoporous matrix around each pore. The lower mesopore intensity is a result of Ps not being able to diffuse far enough in the matrix micropores to find a mesopore. In effect, we can nominally deduce the Ps diffusion length in the resin micropores in this PJB-OS2 system using the PJB data: assuming an isolated pore size of 4 nm, we deduce that the Ps micropore diffusion length is $\sim$2 nm in OS2 from the Monte Carlo simulations. There will be more on this topic in the next chapter.

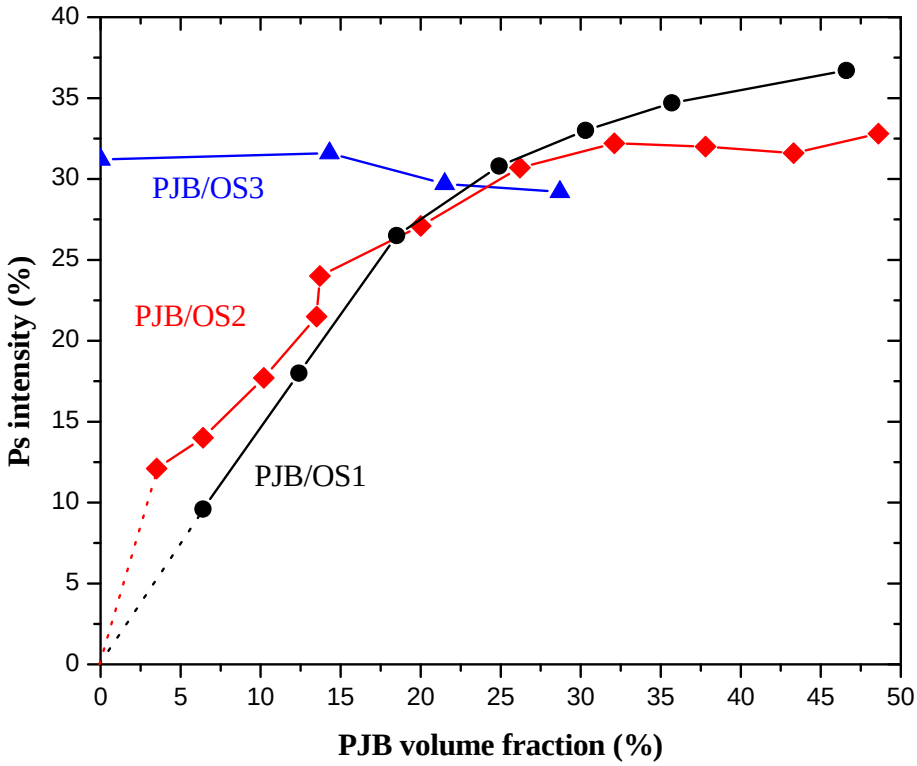


Figure 4.24: The mesopore Ps intensity evolution according to the PJB porogen volume percentage loadings.

The capped pristine OS3 matrix shows a pore diameter of 3.56 nm in spherical model and 2.78 nm in cylindrical model, comparable to (but still a little smaller than) the size of PJB porogen at low concentration. From the PALS analysis results, one would guess the PJB porogen may also fill the intrinsic mesopores of OS3 in the uncured state, which may be responsible for the much smaller induced pore sizes at same porosity compared to the other two systems (PJB-OS1 and PJB-OS2). Therefore, in the next section, the curing process of hybrid PJB-OS3 will be carried out.

### 4.4.5 PJB-OS3 hybrid heat treatment

Eight PJB-OS3 hybrid samples received from IBM were heat treated at 150°C for 1 hour. The thicknesses of the films are around 350 nm to 440 nm. More information of these samples is summarized in table D.14.

Three samples with 15%, 22.5% and 30% PJB porogen loadings, were selected from the PJB-OS3 (150°C/1hr) sample series. These samples have been treated under 150°C for one hour. At this temperature, the PJB porogen is still intact. PALS spectra were taken on each sample at room temperature using 3.2 keV beam energy, which corresponds to a mean implantation depth of 181 nm. (Since the thickness of the films is around 400 nm, this beam energy will implant the positrons with a bell shaped distribution around 181nm and without a lot of penetrations into the substrate.) The samples were heated to escalating temperatures at steps of 50°C from 200°C to 450°C in our vacuum system. The samples were kept at each temperature for about 5-10 minutes giving the time of the chemical reactions, then cooled down to take the spectra. At 450°C, the annealing time was around an hour to make sure the cure is complete. In comparison, beam energy of 4.2keV was used on the capped counterparts to compensate the thickness of the capping layer (∼280 nm mean implantation depth at density 1 g/cm$^3$).

The long buffer PALS results are summarized in table 4.12. The long buffer PALS spectra mainly focus on the long lived positronium (Ps) which annihilate inside mesopores and vacuum. If the formation of Ps in the film is taken as time zero (peak of the spectrum), only part of the spectrum (∼37.5 ns away from the peak) is fitted where almost all the short lived Ps and positrons (correspond to micropores) have annihilated. Therefore, no micropore lifetime and intensity are shown in the long buffer PALS results. Besides the mesopore lifetime and intensity, vacuum Ps intensities are also shown. The vacuum Ps lifetime is around 142 ns, and the intensity mainly comes from two sources. One is the backscattered Ps from the sample surface right at the beginning (not related to pores), the other is from the Ps diffusion through the interconnected pores (escaped Ps). The vacuum intensity normally

Table 4.12: **PALS Long Buffer Results of OS3/PJB System (150°C/1hr) at 3.2keV (∼180nm)**

| Loading (%) | Energy (keV) | Temp.* (˚C) | $\tau_{meso}$ (ns) | $I_{meso}$ (%) | $I_{vacuum}$ (%) | $I_{vac}+I_{meso}$ (%) | $F_{esc}$ (%) |
|---|---|---|---|---|---|---|---|
| OS3 matrix | 3.2 | --- | --- | --- | 31.2 | 31.2 | 100.0 |
| OS3 capped | 4.2 | 150 | 48.7 | 16.9 | 0 | 16.9 | 0 |
| 15 | 3.2 | 150 | --- | --- | 20.8 | 20.8 | 100.0 |
| | 3.2 | 250 | --- | --- | 23.3 | 23.3 | 100.0 |
| | 3.2 | 300 | --- | --- | 24.3 | 24.3 | 100.0 |
| | 3.2 | 350 | --- | --- | 25.9 | 25.9 | 100.0 |
| | 3.2 | 400 | --- | --- | 30.1 | 30.1 | 100.0 |
| | 3.2 | 450 | --- | --- | 30.8 | 30.8 | 100.0 |
| | 3.2 | 450 1hr | --- | --- | 31.6 | 31.6 | 100.0 |
| 15 capped | 4.2 | 150 | 49.9 | 15.1 | 0 | 15.1 | 0 |
| 22.5 | 3.2 | 150 | 31.2 | 4.7 | 11.6 | 16.3 | 71.1 |
| | 3.2 | 200 | 29.9 | 4.7 | 13.3 | 18.0 | 73.9 |
| | 3.2 | 300 | 28.0 | 5.1 | 15.0 | 20.1 | 74.7 |
| | 3.2 | 350 | 28.1 | 5.0 | 17.4 | 22.4 | 77.7 |
| | 3.2 | 400 | 30.3 | 5.8 | 19.8 | 25.6 | 77.3 |
| | 3.2 | 450 | --- | --- | 29.7 | 29.7 | 100.0 |
| 22.5 capped | 4.2 | 150 | 52.1 | 11.7 | 0 | 11.7 | 0 |
| 30 | 3.2 | 150 | 46.8 | 5.2 | 0.8 | 6.0 | 13.6 |
| | 3.2 | 200 | 45.3 | 5.6 | 1.3 | 6.9 | 19.1 |
| | 3.2 | 300 | 48.6 | 6.7 | 1.7 | 8.4 | 19.8 |
| | 3.2 | 350 | 46.8 | 7.9 | 2.4 | 10.3 | 23.5 |
| | 3.2 | 400 | 39.4 | 12.8 | 14.3 | 27.1 | 52.8 |
| | 3.2 | 450 | --- | --- | 29.2 | 29.2 | 100.0 |
| 30 capped | 4.2 | 150 | 48.9 | 4.0 | 0 | 4.0 | 0 |

***The curing temperature at 150˚C is done by IBM; all the spectra are taken at RT after heating.**

refers to the latter, escaped Ps intensity. The escaped Ps intensity directly correlates with the interconnectivity of the film (crudely speaking, more escape means more interconnected) since it is easier for the Ps to escape through more interconnected pores. The escape fraction is defined as the vacuum intensity divided by the total Ps intensity (including mesopore and vacuum Ps intensity). When the positrons are implanted deeper into the film, it is harder for the Ps to escape, and we have lower escape fraction accordingly. Then it is reasonable to define the interconnection length of the film as the depth where 50% of the Ps can escape and annihilate in vacuum.

Figure 4.25 above is a summary of the changes of Ps intensities according to

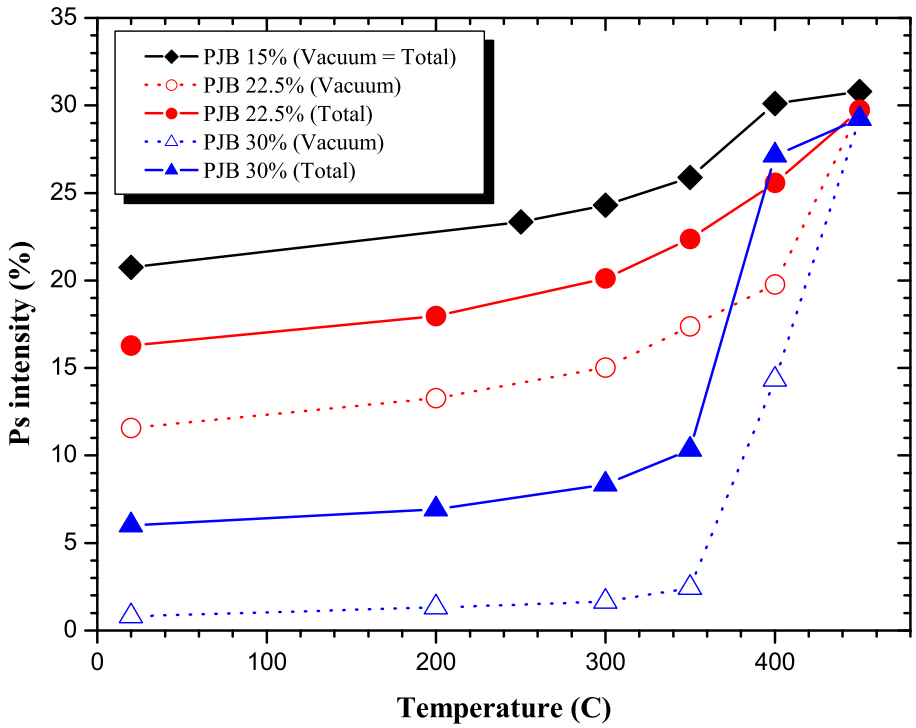


Figure 4.25: Ps intensity vs. temperature for PJB-OS3 samples. Solid lines with symbols are total Ps intensities (mesopore + vacuum), and dashed lines with symbols are Ps vacuum intensities.

temperature changes. It is clearly seen that the PJB degradation mainly happened above 350°C, where the vacuum and total Ps intensities (excluding the micropore intensity) jump up suddenly. In table 4.12, the sample with 15% porogen loading has 100% escape fraction, which is typical for totally interconnected pores and hence no mesopore component is detected. To deduce the size of these mesopores, capping layers are needed for the films in order to confine the Ps inside the film and give us an average mesopore lifetime. Before the Ps annihilates, it bounces against the pore walls millions of times and the Ps lifetime is actually an average associated with its mean free path inside the pore network. As the baking temperature increases, the vacuum intensity increases from 20.8% to 31.6%. This 10% increase is due to the degradation of PJB porogen. At 450°C, the $I_{vac}$ looks almost the same as OS3 matrix (shaded in orange).

For the other two higher PJB-loaded samples, the vacuum intensities after the final heating all went up to ∼30%. Note that the 150°C uncured capped samples all gave a ∼50 ns Ps lifetime which is similar to the Ps lifetime of pristine OS3 and were not affected by the PJB porogens. It indicates that PJB particles are dispersed in the porogen-matrix mixture and occupied some of the interstitial pores of OS3. The PJB porogen may also swell the OS3 intrinsic pores but as long as they are not burned out, only the remaining unfilled OS3 mesopores are "visible" in the mesopore component. At higher loadings, the PJB porogen occupies more and more interstitial spaces, thus lower the Ps intensity in the 50 ns component. For the uncured samples, at higher loadings, the vacuum intensities are lower and the interconnection lengths are also shorter. This is consistent with the suggestion that PJB porogens simply fill or occupy the interstitial spaces of OS3 matrix. The more porogen is added, the more clogged/isolated the OS3 pore network becomes. But after being heated to 450°C, they all look nominally similar.

To further understand the total intensity change here, we need to look at the short buffer results in table 4.13. The short buffer fitting focuses on the fast annihilating Ps populations. It gives detailed information of micropores but less reliable long lifetime components. We expect that before the PJB porogens are volatilized, they should contribute to the micropore intensity to some extent. This contribution should actually depend on the Ps formation ability of PJB and may be decided by the specific chemistry of PJB. After the burnout of PJB, the micropore Ps intensity part of PJB will be lost and contribute to the meso-intensity instead.

The PALS results in table 4.13 confirm the longer mesopore lifetimes and intensities and also provide supplementary information about the micropore lifetimes and intensities. There are two micropore populations with lifetime of ∼2 ns (0.56 nm

Table 4.13: **PALS Short buffer Results of LKD5109/PJB System (150°C/1hr) at 3.2keV (∼180nm)**

| Porogen Loading (%) | Curing Temp.* (˚C) | $\tau_1$ (ns) | $I_1$ (%) | $\tau_2$ (ns) | $I_2$ (%) | $\tau_{meso}$ (ns) | $I_{meso}$ (%) | $I_{vac}$ (%) | $I_{total}$ (%) |
|---|---|---|---|---|---|---|---|---|---|
| 15 | 150 | 2.0 | 3.9 | 11.4 | 3.9 | --- | --- | 20.1 | 27.9 |
| | 250 | 1.8 | 3.7 | 10.6 | 4.2 | --- | --- | 22.7 | 30.6 |
| | 300 | 1.9 | 4.0 | 11.7 | 4.3 | --- | --- | 23.8 | 32.1 |
| | 350 | 1.8 | 3.9 | 11.6 | 4.5 | --- | --- | 25.4 | 33.8 |
| | 400 | 1.6 | 3.1 | 12.2 | 4.5 | --- | --- | 29.6 | 37.2 |
| | 450 | 1.0 | 3.9 | 10.9 | 4.0 | --- | --- | 30.4 | 38.3 |
| | 450 1hr | 1.1 | 3.6 | 11.2 | 3.9 | --- | --- | 31.7 | 39.2 |
| 22.5 | 150 | 2.2 | 7.6 | 6.5 | 2.2 | 24.7 | 3.8 | 12.1 | 25.7 |
| | 200 | 2.1 | 6.5 | 6.6 | 3.2 | 25.2 | 3.8 | 13.6 | 27.1 |
| | 300 | 2.0 | 6.3 | 5.2 | 3.6 | 22.9 | 4.2 | 15.4 | 29.5 |
| | 350 | 1.8 | 6.6 | 6.3 | 3.8 | 23.4 | 4.0 | 17.7 | 32.1 |
| | 400 | 1.9 | 5.4 | 7.0 | 3.3 | 25.4 | 4.4 | 20.4 | 33.5 |
| | 450 | 1.0 | 5.4 | 10.2 | 4.6 | --- | --- | 34.4 | 44.4 |
| 29.9 | 150 | 2.1 | 13.6 | 5.3 | 4.3 | 36.3 | 3.9 | 2.1 | 23.9 |
| | 200 | 2.2 | 12.6 | 5.6 | 5.5 | 38.7 | 4.6 | 2.2 | 24.9 |
| | 300 | 2.1 | 12.9 | 5.0 | 6.7 | 36.2 | 4.9 | 3.5 | 28.0 |
| | 350 | 2.0 | 12.6 | 5.5 | 7.9 | 41.1 | 6.7 | 3.5 | 30.7 |
| | 400 | 1.6 | 4.8 | 5.5 | 4.1 | 30.4 | 9.7 | 17.0 | 35.6 |
| | 450 | 1.2 | 3.7 | 10.3 | 3.7 | --- | --- | 33.7 | 41.1 |

in diameter) and ∼4 ns (0.84 nm in diameter). In the uncured samples, we did see higher micropore intensity associated with higher PJB loading. The curing process generates mesopores which drain almost all the Ps from the micropores. Specifically at 29.9% loading, $I_1$ decreases from 13.6% (at 150°C) to 3.7% (after 450°C). However, this 10% drop of the micropore intensity cannot fully account for the total increase of the mesointensity, which is about 20%. This may be due to the weak Ps formation capability of PJB porogens. It is also possible that the chemical environment changed during the curing process which enhanced the Ps formation, making the total Ps intensity increase. The severe drainage effect at high temperatures drove down the micropore lifetime (like ∼1 ns) which should not be taken as an actual change of the micropore size. We also see this similar effect on mesopores driven by Ps escape into vacuum. Figure 4.26 is a summary of the Ps intensity change

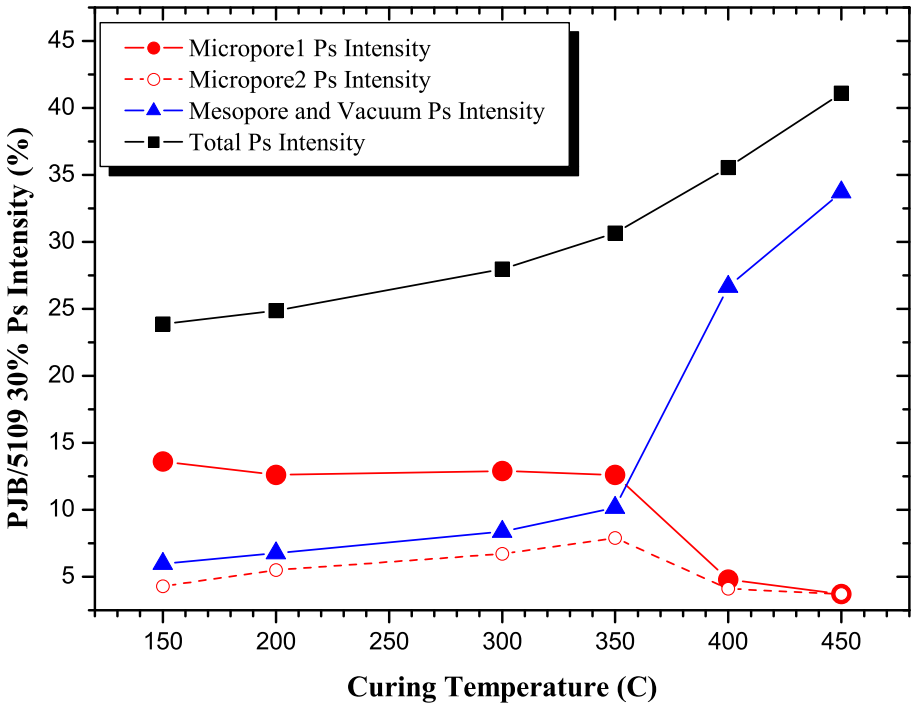


Figure 4.26: Change of Ps intensities in micropore and mesopore at curing for the 29.9% loaded sample

according to curing temperature.

The refractive index vs. weight percentage porogen loading is included in figure 4.27. The downward trend of R.I. curve suggests that the total porosity of the PJB-OS3 series slowly increase at low porogen loadings till ∼27%. above that, it suddenly rises at a much faster rate. Combined with the R.I. curve, the PALS results shows that before the porogen loading of PJB exceeds some critical value (∼27% from R.I. curve), the PJB porogens are mainly filling the inherent interstitial pores of OS3. After the porogen loading exceeds ∼27%, the filling process starts to be frustrated because almost all the OS3 interstitial pores have already been filled and cannot accommodate any more PJB porogen molecules. Consequently the PJB porogens begin to form extra PJB domains which make the overall porosity increase at a much faster rate.

Figure 4.28 shows the mesopore Ps lifetimes of uncured and cured PJB-OS3 sam-

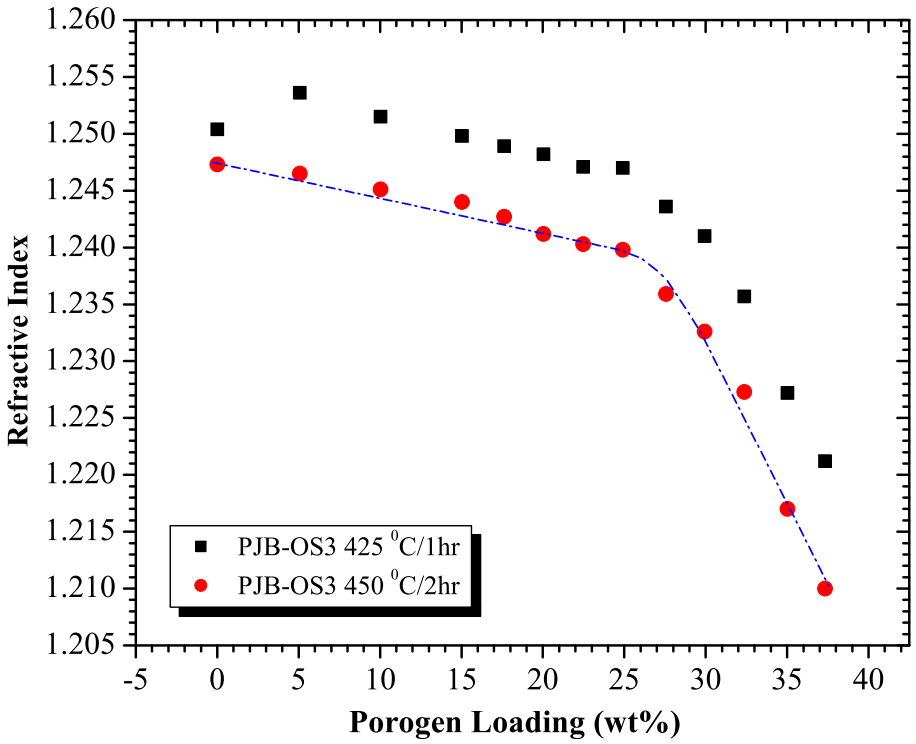


Figure 4.27: Refractive indexes of the cured (black and red dots for 425°C/1hr and 450°C/2hr respectively) PJB-OS3 hybrid samples vs. PJB porogen weight percentage loading.

ples at different porogen loadings. The mesopore Ps lifetimes of PJB-OS1 are also shown in comparison. It is clear that the growth of mesopore lifetime (or average mesopore size) is slower compared with the PJB mesopore lifetime in OS1. The fitted average Ps lifetimes are all bigger than the inherent OS3 interstitial pores. The pore size of PJB-OS3 can be taken as an average of mesopores directly induced from the PJB porogen and the intrinsic OS3 pores. With low PJB porogen loading, OS3 has a higher weight in the average; or in other words, more Ps annihilate in the OS3 intrinsic pores and produce a Ps lifetime around 50 ns. As more and more PJB porogens are added in, they swelled some of the OS3 pores and finally leave behind more and more larger pores. The average pore size then starts to rise. Before somewhere around 25% PJB loading, the pore size increase is slow. But after 25%, it seems that the pore size increases at a faster rate according to porogen loading.

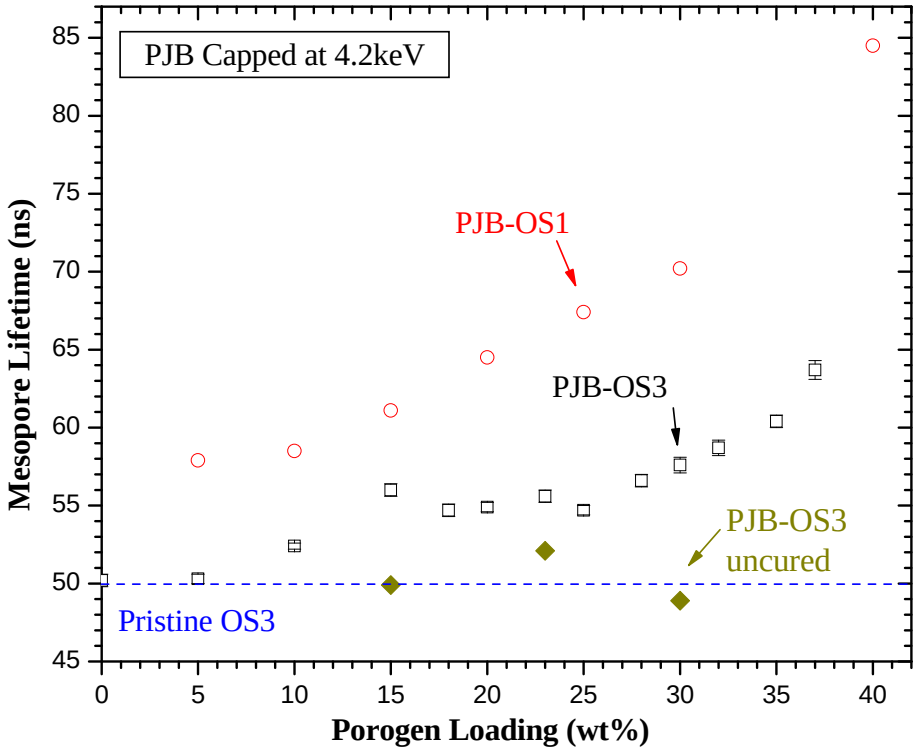


Figure 4.28: Pore size produced by PJB porogen in cured and uncured OS3 matrix

This is in agreement with the R.I. curve shown in figure 4.27 and it indicates that when PJB loading exceeds some critical number, much more nanocomposites of PJB are forming instead of filling into the OS3 interstitial pores.

From the PALS results, we do see the blocking effect due to the PJB porogens. A series of samples with successive larger PJB porogen loadings are examined before and after curing. The PJB porogens prefer to fill the interstitials of OS3 at low loadings because PJB molecules tend to be dispersed and miscible with the matrix. It is clearly seen that from 0% to 25% loading before PJB degradation, the rest interstitial pores are not affected. (50 ns Ps lifetime for all porogen loadings) After curing, PJB actually leave slightly larger pore size and the Ps lifetime average of OS3 and PJB grows gradually. At high loadings above 25%, there are not enough interstitial pores of OS3 to accommodate PJB porogens and PJB porogens will make extra porosity. When we look at the Ps intensity in micropores at different loadings

of PJB, we saw the UMP and SMP both have increasing intensities at higher PJB loadings. This is consistent with our hypothesis that as PJB block more and more of the drainage routes, we see more and more Ps annihilate inside micropores.

#### 4.4.6 Summary of PJB pore generator

PJB porogen is a star shaped particle with hydrophilic corona and a hydrophobic core. Presumably the core should decide the pore size after PJB degradation. Basically, when PJB porogen is mixed with MSQ precursors, the PEO chains in the corona penetrate into the matrix due to hydrophilic interactions. After porogen removal, PEO component can either contribute to the microporosity of the wall material, or nothing because of the collapse of the MSQ scaffold. The polystyrene core, however, determines the actual pore size. Presumably, the pore size can be controlled by the molecular weight of the PS core. Although PJB is called a particle templating porogen, it is still soluble in the solvent, or more technically correct, compatible with the matrix resin in the solvent. After evaporation of the solvent, the matrix and the porogen move to phase separation to form a nanocomposite. The size of the PJB particle in solution is more than 10 nm in diameter, which is much larger than the final pore size it leaves behind. That is to say, the polystyrene arms in the star-shaped core is swollen by the solvent. During and after phase separation with the matrix, the polystyrene arms coil back to assume a much tighter structure.

The PJB porogen generated increasing pore sizes in all the three matrices, which is not expected for a particle templating porogen. In OS1, the mesopore generated by PJB grows pretty fast right from the beginning. In OS2, the mesopore size remains constant below 20% then rises. It seems that the mesopores in OS2 are more constrained and grow slower than in OS1. In OS3, since PJB porogen has comparable size of the interstitial pores of OS3 (actually even larger), PJB porogen

can be used as a pore blocking agent to block the interconnected mesopores in OS3 and the drainage of Ps can be suppressed/blocked by the PJB porogen. We could see the micropore populations in both the OS3 wall material and PJB porogen itself, although the micropore of OS3 and PJB may not be distinguishable. After curing, PJB porogen degrades and leaves behind the similar structure of pristine OS3.

## 4.5 Summary and conclusions

In this chapter, two distinct types of pore generators, namely P12 and PJB, are studied in a series of matrix materials. P12 is a N&G polymer porogen and PJB is a particle templating porogen. They showed unique porogen evolution and growth behavior in the matrices, where the matrix itself also plays a very important role.

The heating treatments of the uncured hybrid (composite) samples have given us a better understanding of the matrix vitrification and porogen degradation processes. From the relative Ps intensities in different pore populations, the formation of super-micropores and the slight increase in their sizes due to the matrix condensation and cross-linking have been observed. This process takes place gradually throughout the whole curing process. On the other hand, porogen degradation is observed at temperatures higher than 350°C and it occurs quite abruptly.

The Ps behavior we observed corroborates theoretical predictions that Ps will diffuse from smaller pores to bigger pores. These series of diffusing actions, from ultra-micropores to super-micropores, from super-micropores to mesopores, and from mesopores to vacuum, have been a good systematic demonstration of Ps diffusion. In addition to the PALS analysis, $N_2$ absorption experiments were also conducted on some of the fully cured samples, the results of which agree very well with the PALS analysis results. The absorption data also confirms the existence of micropores after

porogen degradation.

Very interesting results have been obtained on the intrinsically porous matrix materials. The porogen molecules are observed to be not only filling these interstitial pores but also interacting with the matrix resins, thus producing different pore sizes and pore structures in different matrices. This is an especially important issue in the control of pore morphology using nucleation and growth pore generators. It has been found that in addition to the Si-OH concentration, the molecular weight of the MSQ resins even has an even more significant effect on the pore morphology, which may be due to the change of porogen mobility during the microphase separation of the porogen and matrix. The difference in matrix condensation temperatures also plays an important role in determining the final size of the porogen nanocomposites.

In this and the previous chapter, the evolution of nanopore structures induced by porogens in a variety of systems has been investigated. Some similar trends of pore size and pore interconnection length have been observed. Furthermore, the Ps intensity has been demonstrated to be useful in characterizing pore structure evolution. Monte Carlo simulations addressing both the pore structure and the Ps behavior in these porous materials might be very useful and will be explored in the next chapter.

# CHAPTER V

## Survey on nanoporous thin films and computer simulations

In the previous chapters, combinations of different pore generators and matrix materials were studied. We have seen various types of pore evolution behavior and investigated their forming mechanisms. However, these results are selected from our broader studies on ultralow-$k$ dielectric thin films. Besides the collaboration with SAIT [72, 73] and IBM [82], we have also used PALS on a wide range of nanoporous low-$k$ thin films from other research institutes and industrial partners, such as SEMATECH, Seoul National University (SNU), NIST [84–86], Air Products, Dow Chemical [87], Applied Materials, and Novellus, etc. A large collection of PALS results has been accumulated over the past several years. It is a stimulating and challenging problem to treat these results as a whole, instead of separately, to understand some common features or phenomena underlying these systems, e.g. the percolation process [88]. In this chapter, computer simulations will be used to explore the percolation process in the ULK systems, particularly with the emphasis on the pore interconnectivity, pore size, and Ps intensity characteristics and their evolutions. This attempt could also shine light on the behavior of positronium in nanoporous materials. Further understanding on this issue could consequently enhance the capability of PALS used as a nanopore characterization technique.

## 5.1 Sample survey using PALS

### 5.1.1 Pore size and interconnection length

In chapter 3, we have studied the pore structure and its evolution of several ULK systems in a MSQ-based matrix from SAIT. In chapter 4, a more complete study was carried out for two porogens in three different types of matrices from IBM. The pore forming mechanisms were confirmed by PALS and in-situ heat treatments. The pore interconnectivity ($L_{int}$) and pore size (or mean free path, MFP) are the two very important and complementary quantities in our studies. In addition to $L_{int}$ and MFP, the fitted Ps intensity was also a key to understand the evolution of the pore structure in ULK thin films. The PALS results indicate that there are underlying correlations between different types of systems and we are going to look at it in a collective way in this section. In figure 5.1 and 5.2, the deduced $L_{int}$ and pore size evolution with porosity in various systems are shown. The tCD and sCD porogen in MSQ matrices from SAIT [72, 73], P12 and PGD porogen in LKD matrices from IBM [82], block copolymer systems from SNU and porous SiLK (pSiLK) samples from Dow Chemical [87] are included.

A parallel comparison between these different systems is interesting. The CD porogens interact with each other on a molecular level. By changing the functional groups attached to the CD molecules, different porogen agglomeration behavior is obtained, which were also confirmed by PALS experiments. The sCD system has the fastest growth of the interconnection length versus porosity, and perhaps the lowest percolation threshold among these systems. As seen in figure 5.1 and figure 5.2, the long interconnection length and the constant pore size at all porosities confirmed the 1-dimensional growth of the sCD porogens. In the application of ULK interlayer materials, this early onset and fast rise of pore connectivity will deteriorate the

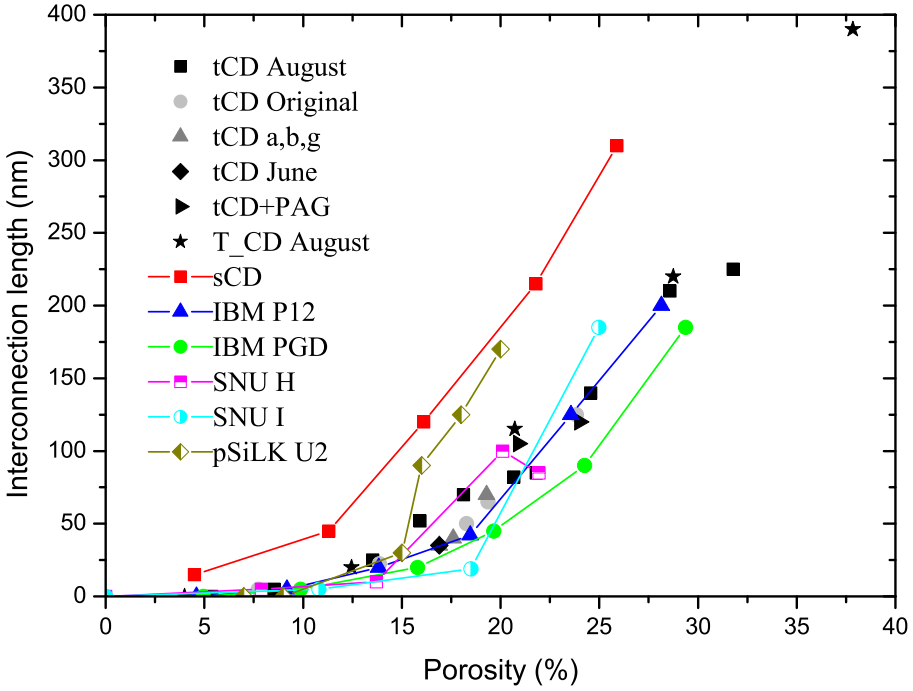


Figure 5.1: Summary of pore interconnection length in several ULK systems.

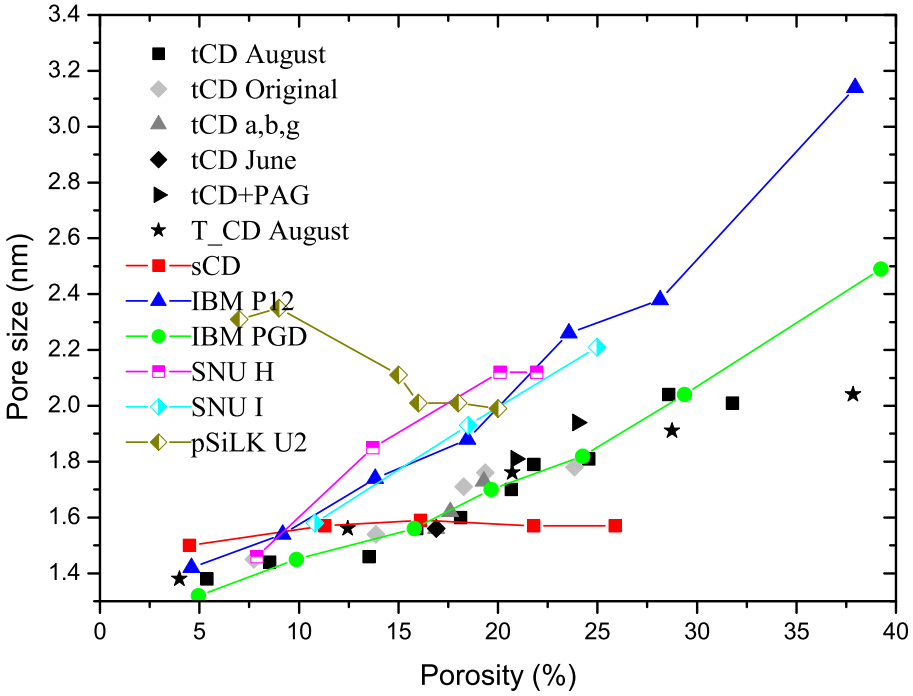


Figure 5.2: Summary of porogen induced mesopore size in several ULK systems.

mechanical strength of the material and is conducive of copper diffusion. The several other systems, except the pSiLK U2 system, have quite similar evolution trends of pore size and $L_{int}$. They all have gradual increases in pore size due to a more random, 3-dimensional like porogen agglomeration (instead of being linear as in sCD). The increase of $L_{int}$ of these systems are slower than in the sCD system. Note that the interconnection lengths of all the systems grow smoothly without any obvious abrupt jump or threshold. From the simple Ps diffusion model we use, in which all the Ps can escape into the vacuum when there are routes connected to the sample surface, any porosity corresponds to a measurable/finite $L_{int}$ would be in the pre-percolation regime for that specific system. This evolution in pore size and $L_{int}$, which is directly related to the percolation process, will be investigated using computer simulations in later sections.

The correlation between pore size and pore interconnectivity is also an interesting problem and might provide insights to ULK material research. One of the recent studies [89] shows that in certain system, the pore size and pore interconnectivity are inversely related. However, this connection is drastically weakened when various systems are involved, especially when a strong porogen-porogen interaction exists.

### 5.1.2 Universal quadratic fits of the interconnection lengths

In some of the ULK systems, we found interesting quadratic trends of the $L_{int}$ versus porosity with different fitting parameters. As shown in figure 5.3, the interconnection lengths of several systems are shown versus porosity. The porogens of sCD system interact through covalent bonds and form long cylindrical chains; P12 porogen from IBM is a nucleation and growth based polymer and form small composites after the matrix/porogen phase separation; PGD porogen is a small molecule.

Simple quadratic fits, $L_{int} = A(P - P_0)^2$, where P is the porosity, with different $A$

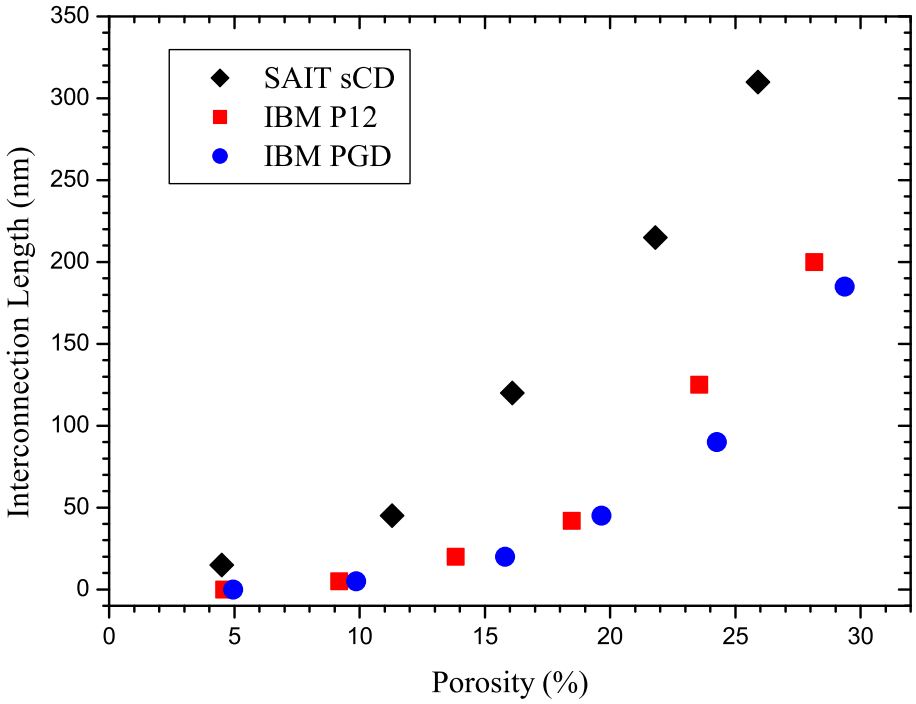


Figure 5.3: Interconnection length of three selected systems. The porogen of sCD system from SAIT interacts through covalent bonds on the molecular level and porogen molecules form long cylindrical chains; P12 polymer from IBM is a nucleation and growth based porogen and form small composites after phase separation; PGD is a small molecule porogen.

and $P_0$, can produce very good fitting agreement on these systems. By shifting all the curves to the left by $P_0$, which makes $(P - P_0)$ zero, we found that the three data sets virtually fall on an universal quadratic curve, as shown in figure 5.4. The $L_{int}$ curves of P12, PGD and sCD systems are shifted by 8.0%, 10.4% and 0.87% respectively. The $P_0$ to some extent represents the onset porosity of porogen agglomeration. It seems that the $L_{int}$ in these three systems, except the different starting points of porogen aggregation, has a quite universal growth constant, $A$. The P12 porogen is a nucleation and growth system, which is much different from the sCD system. But they all have similar trends in $L_{int}$. This is encouraging for an exploration of the universal characteristics of these nanoporous systems, where the variations of their interactions are largely ignored. The addition of pores into a dense matrix material epitomizes a percolation process, and it can suitably describe the pore structure

evolution in these systems.

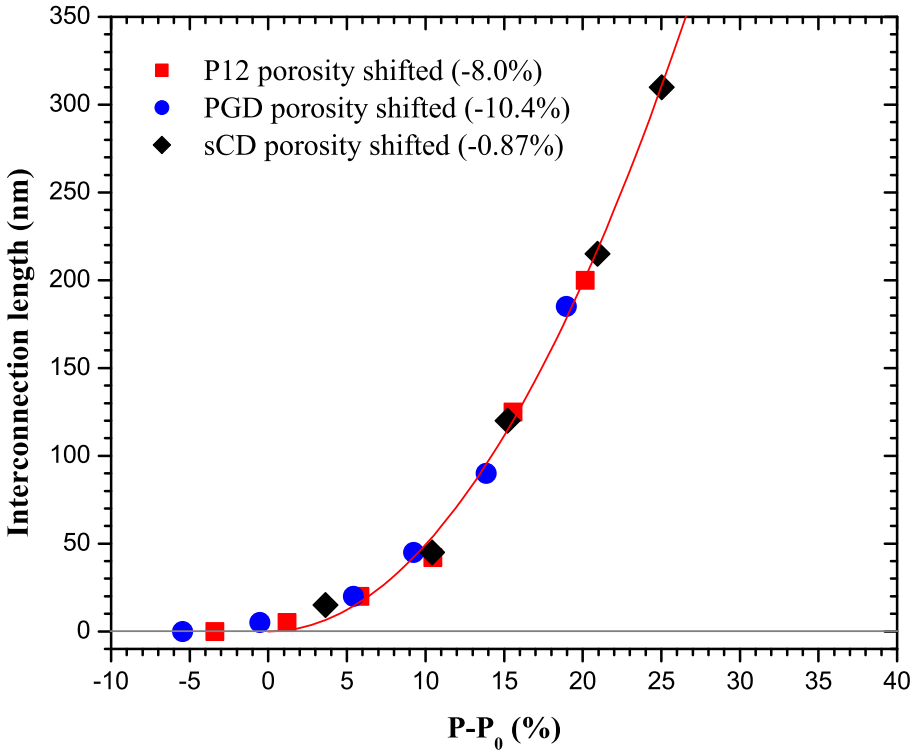


Figure 5.4: universal quadratic curve of SAIT sCD, IBM PGD and IBM P12 interconnection length after shifting the interconnection length curves to the left by different quantities.

### 5.1.3 Percolation process in ULK systems

The percolation process has been extensively studied for several decades to understand the sudden phase transition at the critical threshold ($P_c$) in various systems [88]. It summarizes a variety of phenomena in nature. The process of porogen agglomeration due to the increasing porogen loads is basically a percolation process. In ULK dielectric materials, we want to achieve a low pore connectivity at high porosity, which eventually requires a higher percolation threshold. Porogen-porogen and porogen-matrix interactions can considerably affect the pore morphology in the pre-percolation regime and the percolation threshold itself.

It is well known that for a large three dimensional cubic lattice, if voids/cubes are randomly drawn from the lattice, at about 31% porosity percolation will occur and

this is a simplified resemblance of the nanoporous systems we studied. Computer simulations have been carried out and the results will be shown in the following sections in order to understand the pore evolution process. These simulations will be hugely simplified compared to the real pore formation processes of the ULK materials. There are several issues that need to be considered in our simulations.

First, a cubic lattice is used in most of the simulations. Percolation thresholds are significantly different for different geometries [90–94]. Two dimensional and three dimensional models also produce very different results. In our simulations, we rely on three dimensional models which are much more realistic for the nanoporous systems. Regular model (cubic lattice) and continuum spherical model are all investigated. The cubic model is good to maintain the simplicity, although the nanopores are certainly not cubical. Non-lattice model is also examined to remove the lattice artifact.

Secondly, the interactions between the cells should be considered. When voids are randomly drawn from a lattice, there is no porogen-porogen interaction involved. However, interaction between the porogens plays a big role in pore evolution. Simplified correlations between the "cell drawings" are involved in our simulations. Dynamic models could be used in order to mimic the porogen interactions and kinetics, but it will be out of the scope of this thesis.

Thirdly, the size of the system is limited by computing power. The lattice size used here is normally $200^3$ (L=200), which is eight million total sites. Considering the ULK thin films thickness (several hundred nm) and pore size (typically 2-4 nm), it is large enough to be close to the real systems, and small enough to run in a short period of time.

## 5.2 Monte Carlo simulation of mesopore evolution

### 5.2.1 Random pore generation in a 3-dimensional cubic lattice

The simulations of random pore creation are conducted on a three dimensional cubic lattice, each side containing 200 cells, hence the total number of sites/cells in the lattice is eight million. We take the $x - y$ plane as the thin film surface and $z$ direction as the film depth direction. Periodic boundary conditions in $x$ and $y$ directions are implemented, but not in the z direction (depth direction). A sequence of random x, y and z coordinates between 0 and (size-1) (here size=200) are then generated using the "Mersenne twister" random number generator [95] with each cell$(x, y, z)$ has a unique index number starting from 1 to size$^3$. The porosity is then equal to the number of voids drawn divided by the total number of sites. The randomly generated locations should reproduce the behavior of non-interactive porogens.

In the simulation, we typically run from 0% to 50% porosity at every 1% step. When the target porosity is reached, clusters are marked using a similar method as described in the Hoshen-Kopelman algorithm [96] (two cells share a common side is treated as one cluster). Here, the algorithm marks all the distinct clusters with the smallest index number (smallest x, y, z coordinates) within this cluster, which is related to the position of that "root" cell. When the cluster marking is done, the number of distinct clusters, the volumes of each clusters, mean free path, and cluster lengths can be calculated.

The simulation is mainly focused on interconnection length and mean free path because these two quantities are customarily measured by PALS in our experiments. Positron implantation distributions are taken as the Makhovian distributions with different beam energies. The Ps distribution at certain implantation energy is also

taken as a Makhovian distribution. The interconnection lengths are calculated using the cluster lengths weighted by their volumes. The mean free path of Ps in a specific cluster is calculated by $4V/S$, where $V$ is the volume of the cluster, and $S$ is the surface area of that cluster. In order to obtain the overall Ps mean free path, we need to average the mean free path weighted by the Ps populations in each clusters. Therefore the mean free path,

$$MFP = \sum_n (\frac{4V_n}{S_n} \cdot N_n) / \sum_n N_n, \tag{5.1}$$

where $N_n$ is the number of Ps in the $n^{th}$ cluster. Assuming that mesopores trap Ps atoms at a trapping rate proportional to its surface area, the $N_n$ in the equation 5.1 can be replaced by $S_n$, and therefore the MFP is,

$$MFP = \sum_n (\frac{4V_n}{S_n} \cdot S_n) / \sum_n S_n = \frac{4V_{total}}{S_{total}}. \tag{5.2}$$

In the models we use, the pore distribution is homogeneous in depth, i.e. no variation in MFP with depth is assumed, hence equation 5.2 gives a very convenient way to calculate the overall MFP for the whole lattice. The simulation results are normally in the unit of cells. In order to compare the results with the experimental data, we can scale the cell size to obtain best fits.

The random model in a cubic lattice produces pore MFP which are in a decent agreement with our experimental results when random pore growth is expected. In Figure 5.5, the tCD data and its simulation are shown. Note that the cell size is scaled to 2nm in order to produce a good agreement. Interestingly, a 2 nm cell size is consistent with the size of two or three back-to-back tCD porogens. (The size of a single tCD porogen molecule has a maximum diameter of ∼1.5 nm and a height of ∼0.8 nm.) The agreement of the random model with the experimental data indicates

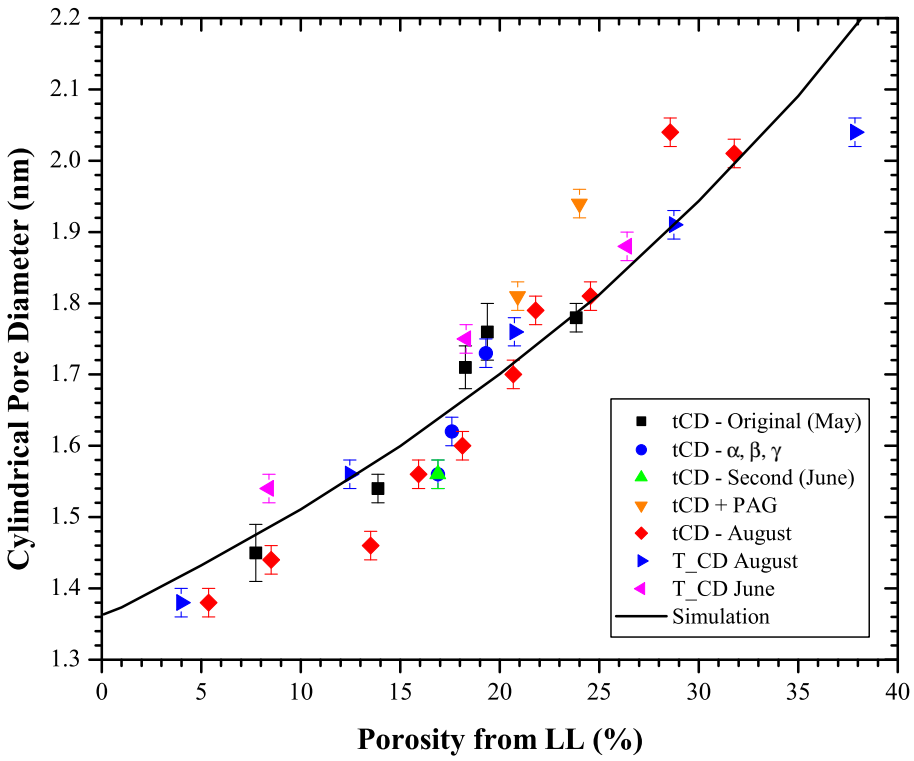


Figure 5.5: Simulation results of pore size with cell size scaled to 2 nm

that the tCD porogens are not singly dispersed, but randomly dispersed in two or three back-to-back molecular units. However, the interconnection length from the Monte Carlo simulation does not agree with the experimental results, which is shown in figure 5.6. The shape of the $L_{int}$ curve is expected from the percolation process in a cubic lattice, where the averaged length of the clusters should take off at the percolation threshold, which is about 31% porosity.

As we have discussed in chapter three, the tCD porogen molecules interact with each other very weakly. The agreement on pore size evolution between the experimental results and simulation indicates that the weak interaction between porogens does not affect the pore size significantly, thus it is very close to a random growth. On the other hand, the length of the pores could grow in a much different manner than random growth. Even though very weak interaction is involved, the porogens tend

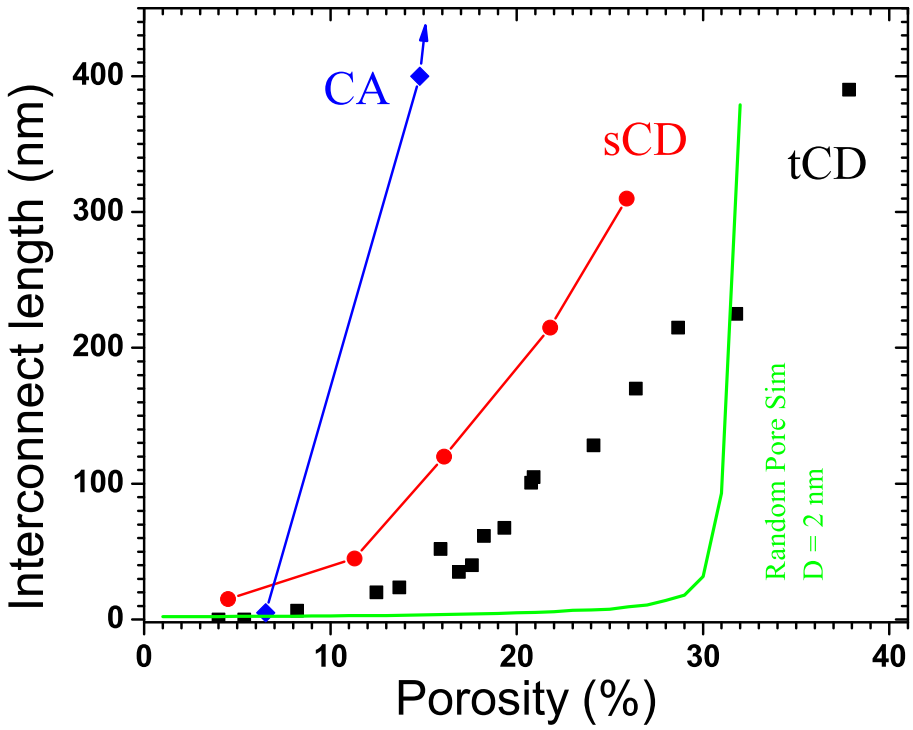


Figure 5.6: Simulation results of pore interconnection length

to preferentially link with their ends and grow longer. This attractive interaction can also lower the percolation threshold.

It is interesting that there is no obvious threshold observed in the experiments, even though the interconnectivity of the pore networks should "jump" up at the percolation threshold. According to the simple Ps diffusion model we mentioned before, PALS principally measures the interconnectivity before the percolation actually occurs. As the pores get totally interconnected at high porosity, the Ps escape fraction and the deduced $L_{int}$ are closely related to the Ps diffusion length in the pore network. This diffusion effect is always convolved with the porogen growth and is difficult to untangle. Fortunately, for the thin films we study, the $L_{int}$ should be predominantly determined by the pore connectivity itself due to the relatively long Ps diffusion length compared to the mesopore structure.

### 5.2.2 Random spherical pore generation in a continuum space

Because the cubic lattice is a considerably simplified model, a more realistic spherical model has been investigated. In this model, spherical porogens are randomly dispersed within a continuum three dimensional space; every spherical porogen/cell has a hard-core and a soft skin outer layer [97]. Two porogens can overlap their soft parts, but their cores are exclusive. $R_{min}$ and $R_{max}$ are defined as the radii of the spherical core and the outer sphere respectively. When two spheres touch each other by their outer shells, they are treated as interconnected. In other words, the minimum center-to-center distance to keep two cores isolated from each other is $2(R_{max} - R_{min})$. The interconnection length is defined as the volume weighted average of the pore/cluster length in certain direction. (In the simulation, only the z-direction length is actually calculated.) Because the pores are dispersed in a continuum space and no lattice is involved, the Holshen-Kopelman algorithm is not convenient anymore. The algorithm used in this model is modified based on Mark Newman's algorithm in a cubic lattice [98]. Before a new spherical pore is placed at a certain position, a checking routine will search for any neighbors within the range of $R_{max}$ and there should be no other cores within the range of $R_{min}$ due to the exclusiveness of the inner cores. In order to expedite this search whenever a new pore is generated, the space is gridded in such a way that every pore is assigned a unique index correlated to its position. Then only the neighboring region within $2R_{max}$ of the newly generated cell needs to be searched. The C++ code of the model is shown in appendix E.

The $L_{int}$ is calculated similarly as in the previous model and the simulation result is shown in figure 5.7. The region size is $100^3$ with periodic boundary conditions in the $x-y$ directions. There are two straightforward ways of defining the porosity of the

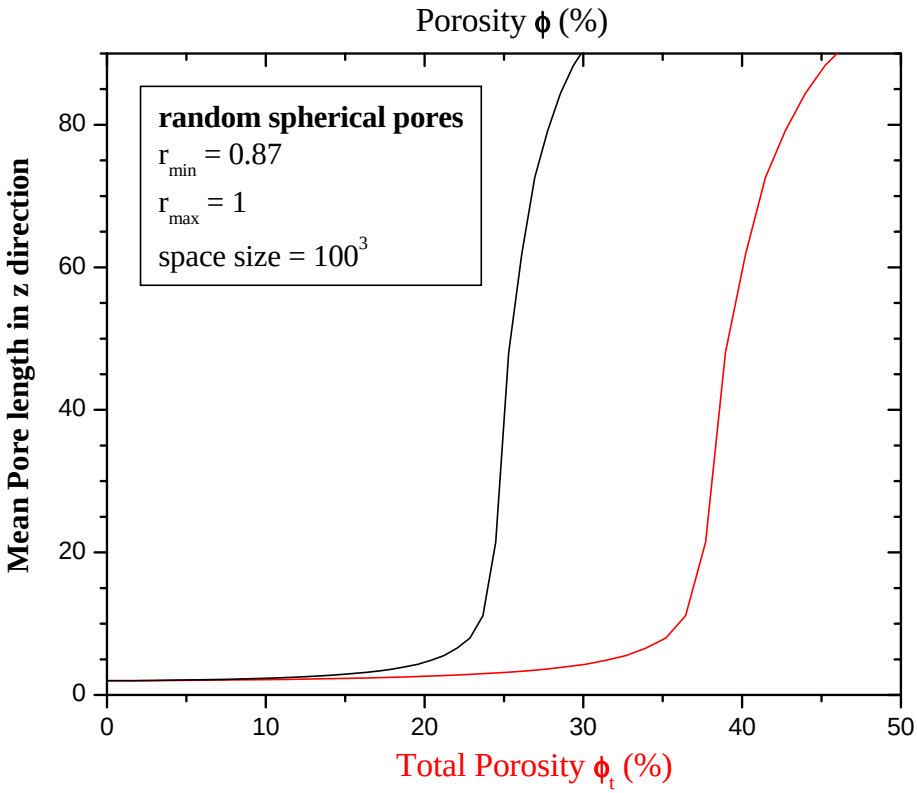


Figure 5.7: Simulation results of pore interconnection length versus porosity. $\phi_t$ is the total porosity calculated by the outer surface of the voids including the interpenetrable part, which is actually double counted when they overlap. $\phi$ is the porosity only counting the hard core of the spheres. The actually porosity can be calculated using the method given by P. A. Rikvold and G. Stell.

system: one is to only count the inner core; the other is to include the whole sphere but double counting the overlapped region. The more accurate porosity without double counting can be calculated from these two porosities using the method given by P. A. Rikvold and G. Stell [99]. When the relative thickness of the soft shell of a pore, $((R_{max} - R_{min})/R_{min})$, is small, the overlapped region is insignificant and can be largely ignored, especially at low porosities.

It is clearly seen from figure 5.7 that the trend of the interconnection length is very similar to that in the cubic lattice model except for the different percolation threshold. $L_{int}$ is small at low porosity, and at the percolation threshold, it increases abruptly. The similar trends of $L_{int}$ in these two models are expected and suggest that random pore-selecting models with different geometries only produce different

percolation thresholds, not the gradual increase of $L_{int}$ below the percolation threshold observed in the experimental results. Interactions between porogens might play the crucial role of pore aggregation when the porogen concentration is very low.

Note that the definition of $L_{int}$ in our simulations is solely geometric, which does not depend on Ps escape. However, in the PALS experiments, the interconnection length is defined as the mean positron implantation depth where 50% of Ps can escape. The experimental definition of $L_{int}$ should coincide with the morphologically defined interconnection length. The $L_{int}$ obtained from our experiments can be complicated by the Ps distribution and its diffusion in the porous films. In later sections, the Ps diffusion in the materials will be considered, which will give us more information of the Ps intensity and its correlation with the pore evolution.

## 5.3 Simulations that consider Ps distribution and diffusion

In the previous sections we have investigated two aspects of the morphology of nanoporous materials, namely the pore interconnection length, $L_{int}$ and Ps mean free path (MFP) in the porous materials, using the Monte Carlo simulations. The simulations on MFP agreed well with the PALS experiment results, while the simulation of $L_{int}$ was drastically inconsistent with the experimental data.

The Ps lifetime and its intensity are the two fundamentally important quantities in PALS spectrum fitting and they both rely on the positron and Ps behavior in materials. It is also interesting to investigate the possible causes of the $L_{int}$ evolution with porosity when Ps diffusion is also considered. In this section, we are going to combine the positron implantation profile and Ps diffusion into the Monte Carlo simulation in order to further explore the Ps intensity property and its evolution.

### 5.3.1 Marhkovian distribution of positrons and Ps

Over the years, there have been extensive theoretical and experimental studies on the stopping of positrons and the Ps formation processes [21]. The Markhovian distribution, with empirically determined parameters, has been demonstrated to be a good positron stopping profile in the materials we study [66–68]. However, the Ps formation mechanism is still not fully understood. It is believed that the spur model would be mainly responsible for the Ps formation in the ULK porous materials we study. In the ULK films, micropores exist almost ubiquitously, causing a short (compared with film thickness) Ps diffusion length before they are trapped into these sub-nanovoids. Therefore, in the following models, the Ps initial distribution in the micropores is also taken as the Markhovian distribution before any diffusion occurs in the media. In later sections, the "Ps diffusion length", unless otherwise stated, will be specifically referring to the Ps diffusion length before the Ps is trapped into the mesopores. In our simulation, the positron stopping and Ps formation processes will not be included.

In porous materials, following the birth of a positronium atom, the Ps can diffuse into the nearby micropores or mesopores wherever a lower energy state of the Ps in the potential well can be achieved. The Ps trapping rate into the voids is considered to be proportional to the surface area of the pore (the potential well). The Ps diffusion length could vary significantly in the wall material or micropores and Ps has a large chance to diffuse into the mesopores if the micropores are connected/close to a mesopore. According to our experiments, this effect is typically called the Ps draining effect, which tends to be very substantial at high mesopore porosities.

In our first model, all the Ps start from a Markhovian distribution determined by the film density and the positron implantation energy. The Ps located in the

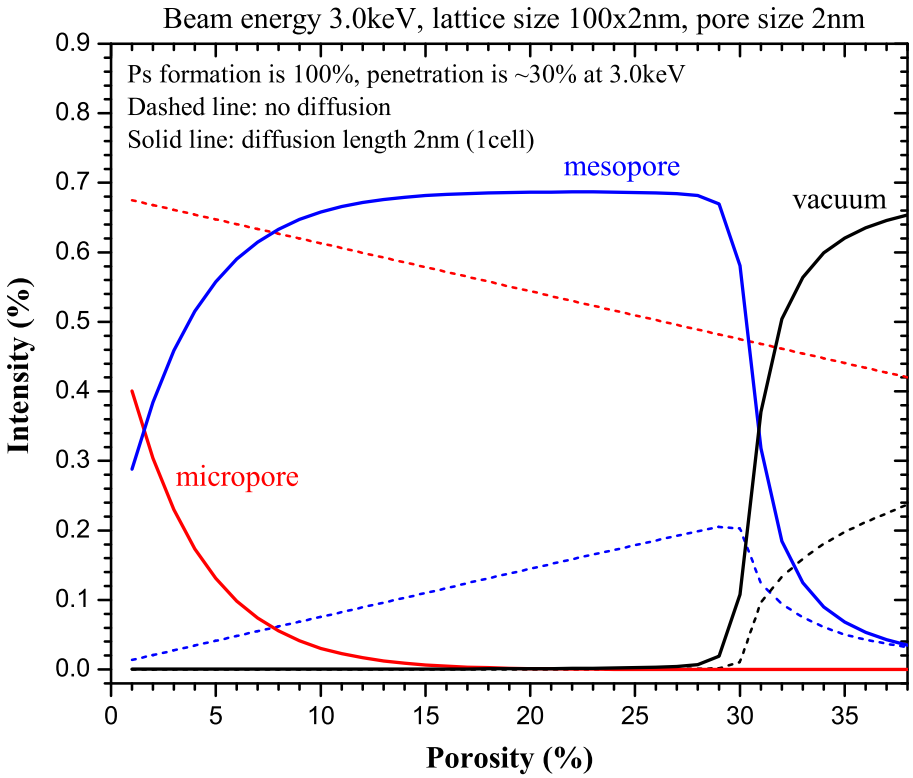


Figure 5.8: Simulation results of Ps intensities. The dashed lines are Ps intensities without Ps diffusion. The solid lines are Ps intensities with Ps diffusion length set to 2nm. The void size is set to 2 nm in diameter. The film thickness is 200 nm, which actually corresponds to a lattice size of $100^3$. Beam energy is set to 3.0 keV, at which about 30% positrons penetrate the film, assuming the density of the film is 1 g/cm$^3$. Ps formation is unrealistically set to be 100% to just illustrate the Ps intensity trends. Other values of Ps formation will just change the numbers fractionally.

solid will annihilate as micropore Ps intensity ($I_{micro}$) while the Ps in mesopores will contribute to the mesopore Ps intensity ($I_{meso}$). If the mesopore is connected to the sample surface (open pore), the corresponding Ps intensity is counted as Ps vacuum intensity, $I_{vac}$. This definition of $I_{vac}$ assumes the Ps intensity in open mesopores can certainly diffuse into vacuum. This is a reasonable assumption because the Ps can collide with the pore walls millions of times before it annihilates, it has a quite long diffusion length (compared to the film thickness) in the interconnected mesopores. The escape fraction, $F_{esc}$, is calculated as the ratio of $I_{vac}$ to the total meso-intensity ($I_{meso}+I_{vac}$). In this model, the Ps intensities in each pore population including vacuum are simulated at every 1% porosity steps. The pores are generated

at random locations within the $100^3$ lattice.

In this model, because all the Ps within the diffusion length of a mesopore will be trapped into it, the volume of mesopores can be simply expanded by a diffusion length to account for the Ps mesopore intensity from diffusion.

In figure 5.8, the intensities of Ps annihilating in micropores, mesopores and vacuum versus porosity are shown. The diameter of each cell is set to 2nm. We have assumed a constant total Ps formation (the fraction that positrons can form Ps, which is set to be 100% in figure 5.8) and thus a constant total intensity from each pore populations. The positron implantation energy is 3.0 keV. Note that at 3.0keV (mean implantation depth $\sim$180 nm), there is about 30% positrons penetrate the film and land in the substrate, and thus do not form Ps. The dashed lines in figure 5.8 shows the simulation results without Ps diffusion from micropores to mesopores, and the solid lines corresponds to 2nm diffusion length. Note that this diffusion length here does not affect the Ps diffusion in the mesopores, where Ps can collide with the pore walls and diffuse very long distances.

From our simplified model, the Ps intensity changes its distribution among micropores, mesopores and vacuum according to the film porosity. When the Ps diffusion length is set to zero, the Ps micropore intensity decreases linearly concomitantly with the increase of Ps mesopore intensity due to the increase of mesopore porosity/volume. For Ps diffusion length of 2 nm, the decrease of $I_{micro}$ and the increase of $I_{meso}$ are much more rapid. The $I_{meso}$ almost saturates at 10% porosity. For both cases, below the percolation threshold, the vacuum intensity is almost zero; at the threshold, the vacuum intensity abruptly increases concomitantly with the drop of the mesopore intensity.

All the results above are straightforward and are anticipated. However, the trend

of Ps intensity is not what we typically observe in the PALS experiments, where the vacuum intensity increases much earlier and gradually than what the simulation predicted. The phase transition to percolation should be responsible for this sudden rise, which we have seen for $L_{int}$ in the previous sections. The actual diffusion length of Ps is unknown and in the simulation, is treated as a free parameter. As we observed, the diffusion length affects the Ps intensities significantly, which can also be reasonably estimated given the fact that the model effectively adds a trapping skin in addition to the mesopore volume.

### 5.3.2 Ps diffusion and Ps intensity

It is non-physical in our previous model that some fraction of the Ps can directly form inside the mesopores. It is known from the "spur" model, that Ps should form in the solid material with one of the "spur" electrons that the positron ionized along its slowing-down path. It is more reasonable to let the Ps atoms start from a Markhovian distribution in the wall material/micropores and diffuse into mesopores and vacuum. In addition, the positron stopping position can be generated using a random number generator. To obtain a Markhovian distribution from a uniform random number generator, we can use the cumulative density function of the Markhovian distribution, which is 1-exp$[-(z/z_0)^2]$. The inverse function of the cumulative density function is given by equation 5.3,

$$z = z_0\sqrt{-\ln(1-\omega)}, \tag{5.3}$$

where $z$ is the generated positron implantation depth. $z_0$ is given by $\bar{z}/(\sqrt{\pi}/2)$, with $\bar{z}$ being the positron mean implantation depth. The details of positron implantation profile and PALS depth profile capability is discussed in chapter 2. $\omega$ is a random variable between 0 and 1 generated from the Mersenne twister random number gen-

erator. From 0% to 50% at 1% porosity steps, the positron stopping position in the $z$ direction is generated using equation 5.3, and its $x$ and $y$ coordinates are random between 0 to the size of the lattice. The penetration depth of a positron is further corrected according to the number of mesopores a positron goes through. The increase in porosity will accordingly reduce the density of the film, thus enhance the positron penetration into the substrate. At high porosity, the total Ps intensity will decrease drastically due to the more severe positron penetration into the substrate.

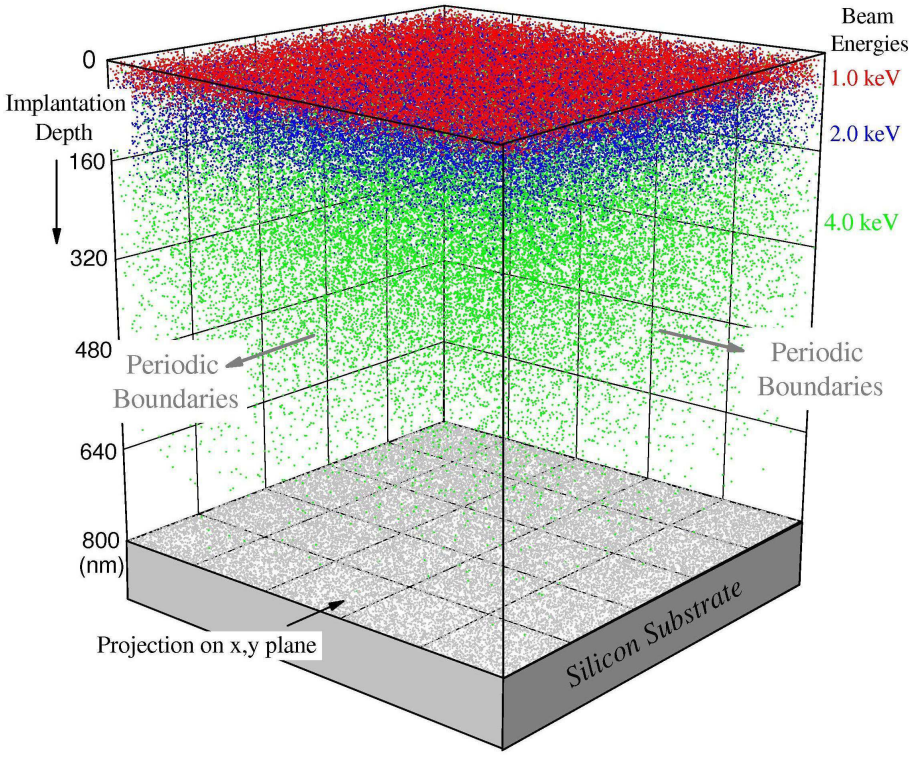


Figure 5.9: Mote Carlo simulation of positron implantation

In figure 5.9, the simulation of positron stopping profiles at several implantation beam energies are shown. The positron depth dependence is Marhkovian at each energy, with mean implantation depth of 28 nm (red dots), 86 nm (blue dots) and 260 nm (green dots) at 1.0 keV, 2.0 keV and 4.0 keV respectively for a film density of 1 g/cm$^3$. The projection of points on the $x - y$ plane is random and uniformly

distributed, which is shown in figure 5.9 by gray dots. If the film density is 2.0 g/cm$^3$ and pore size is 2.0 nm, the thickness of the film is then around 800 nm for a $200^3$ lattice. In the horizontal directions, periodic boundary conditions are used to expand the thin film infinitely. Beneath the 800 nm film is the substrate, where the implanted positrons will not produce Ps intensities. In each simulation run at a specific porosity, there are normally 100000 positrons implanted using the Markhovian distribution and their $(x, y, z)$ coordinates are taken as the Ps starting positions.

The Ps diffusion process is very complicated and the model we used here is drastically simplified and phenomenological. There are no Ps random walks and collisions involved. Only the distance from the Ps starting position to a mesopore or vacuum is considered. The Ps searches for mesopores or vacuum within the range of a preset diffusion length and can diffuse into any available mesopores. If there is more than one mesopore within the diffusion distance, the Ps will randomly choose one to diffuse into.

In figure 5.10, the total Ps intensities from the micropores, mesopores, and vacuum are shown versus porosities in black, and they are identical for different diffusion lengths. The Ps intensities largely agree with the intensity trends from the previous section (shown in figure 5.8) except here the positron penetration depends not only on the films thickness, but also on the film porosity. The lattice size is $100^3$, with pore size 2 nm and a film density of 1 g/cm$^3$, thus the effective film thickness is 200 nm. The total Ps intensity trends of several energies are generated to see the penetration effect at different energies. At 2.0 keV, the total Ps intensity decreases due to the positrons penetrating the film more severely at higher porosities with a decreasing film density. At 3.0 keV, the total Ps intensity changes more drastically from 68% to

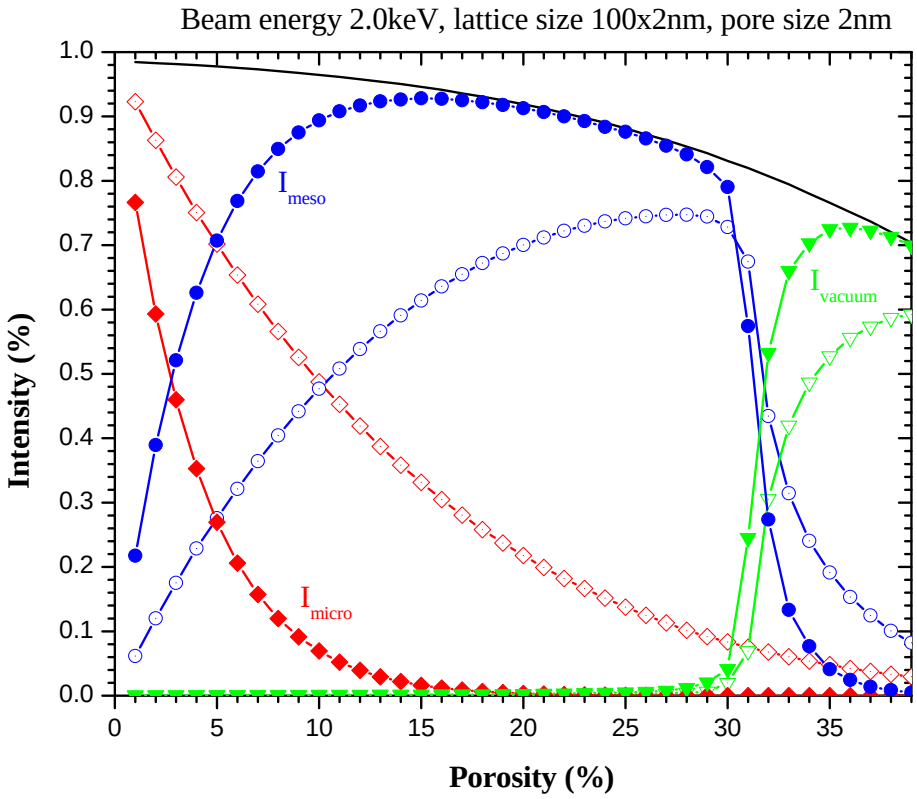


Figure 5.10: Monte Carlo simulation results of Ps intensities. The red, blue, and green curves present the Ps intensities in micropores, closed mesopores, vacuum, respectively. The hollow symbols and solid symbols distinguish the Ps intensities with Ps diffusion lengths of 1 nm and 2 nm respectively in the solid wall material. The black curve shows the total Ps intensity for both 1 nm and 2 nm Ps diffusion length in solid. The void size is set to 2nm in diameter. The film thickness is 200 nm, which actually corresponds to a lattice size of $100^3$. Beam energy is set to be 2.0 keV. Ps formation is unrealistically set to be 100% to just illustrate the Ps intensity trends. Other values of Ps formation will just change the numbers fractionally.

25% (not shown in the figure). At 1.0 keV, there is hardly any penetration observed at all porosities. The red, blue, and green curves present the $I_{micro}$, $I_{meso}$, and $I_{vac}$ respectively. The solid symbols present the Ps intensity results from a 2 nm diffusion length, while the hollow symbols present the 1 nm diffusion length. The Ps intensity trends of the three pore populations are quite similar to what we have seen in the previous section. It is obvious that the micropore and mesopore intensities are very sensitive to the Ps diffusion length in the matrix.

According to the spur model, Ps is formed in the matrix, and the formation depend on many factors, like the positron energy, matrix material, scavenging, and

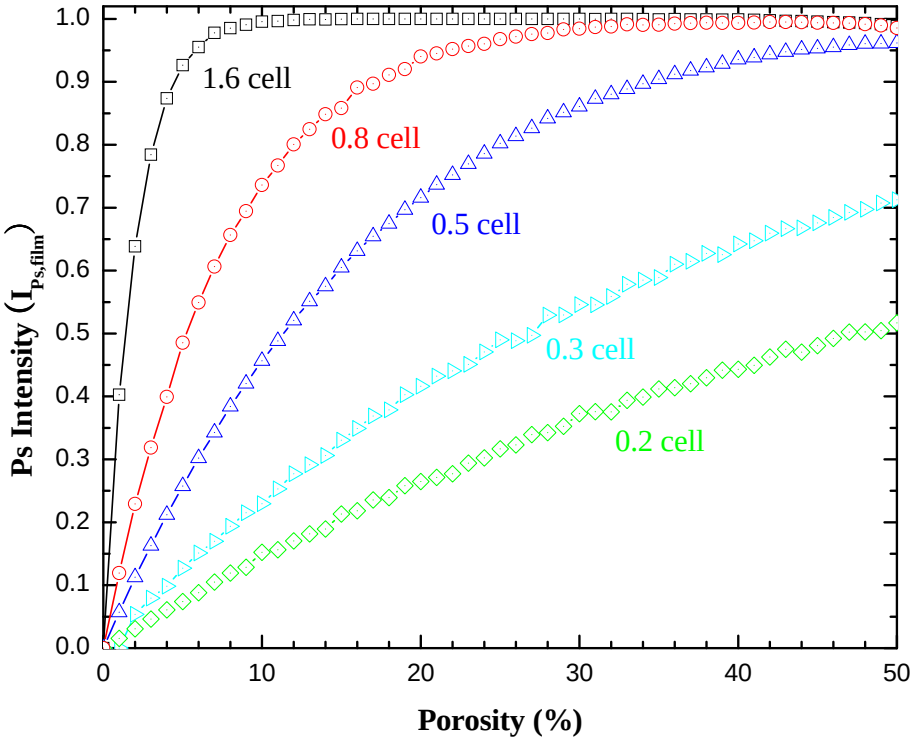


Figure 5.11: Mote Carlo simulation results of Ps total intensities from mesopores and vacuum with different Ps diffusion length. The lattice contains 8 million sites ($200^3$) with the void size set to 2nm in diameter, the film density set to $2 g/cm^3$, which actually corresponds to 800nm film thickness. Beam energy is set to be 3.0keV. Ps formation is unrealistically set to be 100% to just illustrate the Ps intensity trends. Other values of Ps formation will just change the numbers fractionally.

dangling bonds, etc. After the Ps is formed, it may diffuse through the matrix's micropores, and consequently populate the mesopores. The sum of Ps intensity in vacuum and in mesopores, $I_{Ps,film}$ is customarily measured in our experiments and could be largely decided by the film pore size and Ps diffusion length.

The $I_{Ps,film}$, which is a very important quantity, is directly related to the Ps diffusion length in the matrix materials. The simulation results of $I_{Ps,film}$ at different diffusion lengths are shown in figure 5.11, where the cell size of the lattice is set to 2 nm. The longer the Ps diffusion length, the faster Ps drains from the micropores and $I_{Ps,film}$ saturates. We have assumed within the diffusion length, the probability for a Ps to diffuse into a mesopore or vacuum is 100%. If this probability is smaller, to produce the same trend of $I_{Ps,film}$, the diffusion length should be accordingly

longer. Actually, the mechanism of Ps diffusion from micropores to mesopores and vacuum is still not fully understood and the interconnectivity of the micropores and Ps tunneling may both contribute to this process.

The $I_{Ps,film}$ is also directly related to the film mesopore size, which was observed in the PALS experiments. At a given porosity, as the mesopore size decreases, Ceteris paribus, the wall thickness between the mesopores decreases, thus enhancing the diffusion of Ps into the mesopores. As a result, the Ps intensity in mesopores increases at the given porosity and it saturates more rapidly when porosity increases. In figure 5.12, the $I_{Ps,film}$s of several series of samples with incremental porogen loadings are shown together with simulation results. The simulation produces very interesting

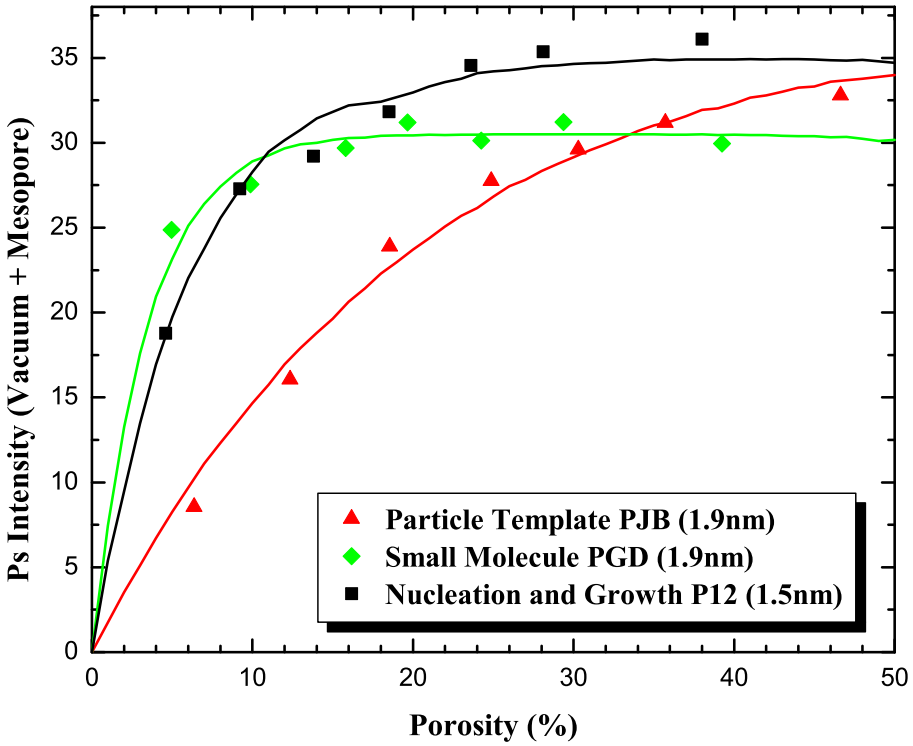


Figure 5.12: Monte Carlo simulation results of Ps total intensities from mesopores and vacuum with some experimental results. The lattice contains 8 million sites ($200^3$), the film density set to 2 g/cm$^3$. Beam energy is set to be 3.0 keV. Ps formation is set to be consistent with the asymptotic value of the experimental results. Diffusion lengths are adjusted to fit the experimental results.

results. By varying the diffusion lengths in the micropores, we obtained excellent

fits to the PALS experimental data. For the *particle template* porogen samples (PJB in OS1) and *small molecule* porogen samples (PGD in OS1), the diffusion lengths are both 1.9 nm. The *nucleation and growth* porogen (P12 in OS1) samples have Ps diffusion length of 1.5 nm. The pore sizes of the PJB, PGD, and P12 systems, at low porosity, are about 4.19 nm, 1.56 nm, and 1.69 nm respectively. These pore diameters are taken as the cell sizes in the simulations to calculate the Ps diffusion length. Given the error of the Ps intensities and the fitting, their Ps diffusion lengths are quite consistent, which indicates the possibility of an absolute porosity calibration using Ps intensity (if diffusion length is known). As mentioned earlier, the Ps formation capability in a material and its intensity depend on many other factors. The Ps diffusion length in micropores/matrix may not be consistent in wildly different materials. Nonetheless, it is still a possible direction to porosity calibration in the similar type of materials.

In figure 5.13, three types of samples are shown with their simulation results. The difference between these samples with the samples shown in figure 5.12 is that these samples are based on an intrinsically porous matrix. Without any porogen loading, the matrix shows some Ps intensity in mesopores, which is around 8%. Therefore, in our simulation results, all the curves are offset by certain porosity to give a consistent 8% intensity at 0% porogen-induced porosity. The fitted Ps diffusion length is around 2nm for all the three systems, which is quite consistent with the previous systems. Note that when the pore size is small, the Ps mesopore intensity saturates at very low porosity. Under these conditions, more samples with very low porosities are needed to extract the Ps diffusion length more reliably from the simulation.

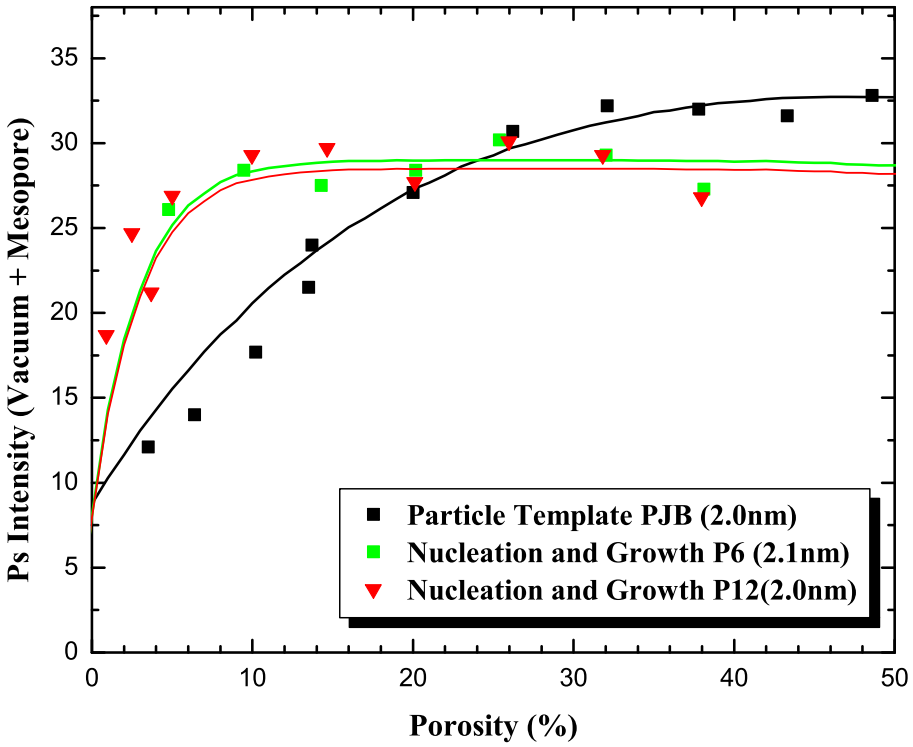


Figure 5.13: Monte Carlo simulation results of Ps total intensities from mesopores and vacuum with some experimental results. The lattice contains 8 million sites ($200^3$), the film density set to 2 g/cm$^3$. Beam energy is set to be 3.0 keV. Ps formation is set to be consistent with the asymptotic value of the experimental results. Diffusion lengths are adjusted to fit the experimental results. Note that the matrix (OS2) is intrinsically porous, thus the Ps intensity starts at ∼8%, not zero.

### 5.3.3 Ps diffusion and its effects on measured interconnection length

It is conceivable that the interconnection length we measure is decided by both the pore evolution itself and Ps diffusion. The way that we obtain the interconnection length could be significantly affected by Ps diffusion behavior in porous films. In this section, the Ps diffusion and its effect on the deduced interconnection length will be investigated. We have assumed that the Ps in open mesopores can finally diffuse into vacuum through the interconnected pore networks before its annihilation. By varying the positron implantation energy, we can use the simulated $F_{esc}$ to deduce the interconnection length.

In figure 5.14 and 5.15, the Ps escape fractions at beam energies from 0.1 keV to

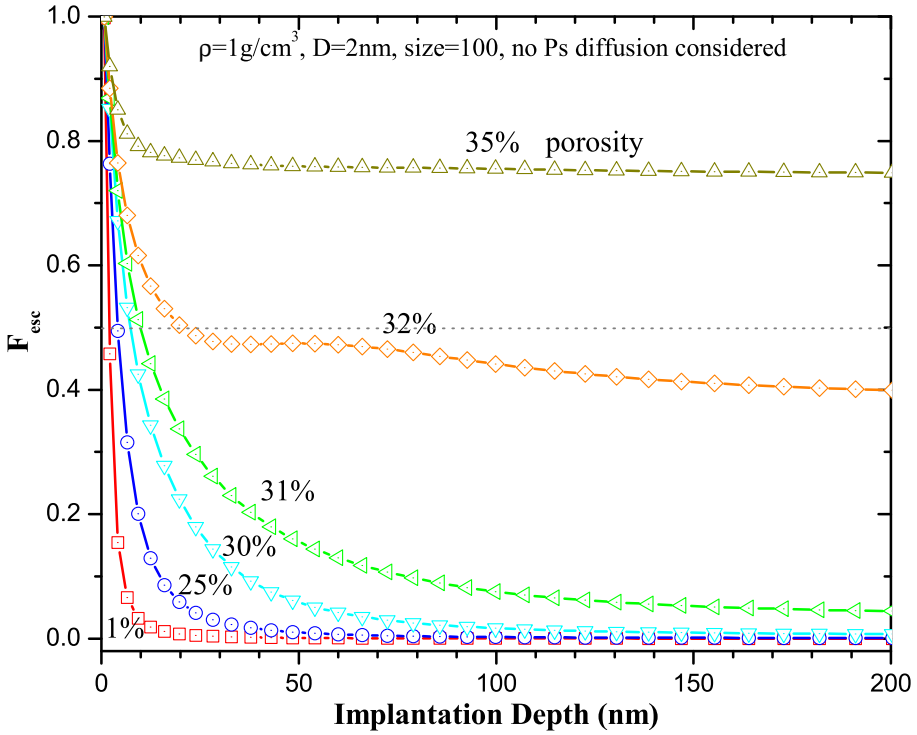


Figure 5.14: Ps escape fractions at beam energies from 0.1 keV to 6.0 keV at every 0.1 keV. Results of different porosities are shown. The density $\rho$ of the film is set at 1 g/cm$^3$. Pore size is 2 nm, lattice size is $100^3$. The diffusion length is zero.

6.0 keV at every 0.1 keV and at different porosities are shown. The density $\rho$ of the film is set to 1 g/cm$^3$. Pore size is 2 nm, lattice size is $100^3$. The Ps diffusion length in the micropores is zero in figure 5.14, and 2 nm in figure 5.15.

With a 2 nm Ps diffusion length in matrix, the $F_{esc}$ values are consistently higher than the results without Ps diffusion. Consequently, the $L_{int}$ increases according to the diffusion length. However, in both figures, the escape fractions at porosities lower than 25% are quite similar. They jump significantly at about 31% porosity, which are consistent with the percolation threshold in this regular cubic lattice. At low porosities, the escape fractions asymptotically approach zero at higher positron implantation depths. At porosities of 31% and above, the asymptotical values abruptly jump up at the 200 nm end. The effect of Ps diffusion in matrix on $F_{esc}$ and $L_{int}$ should be related to the average larger surface area of open clusters since they tends

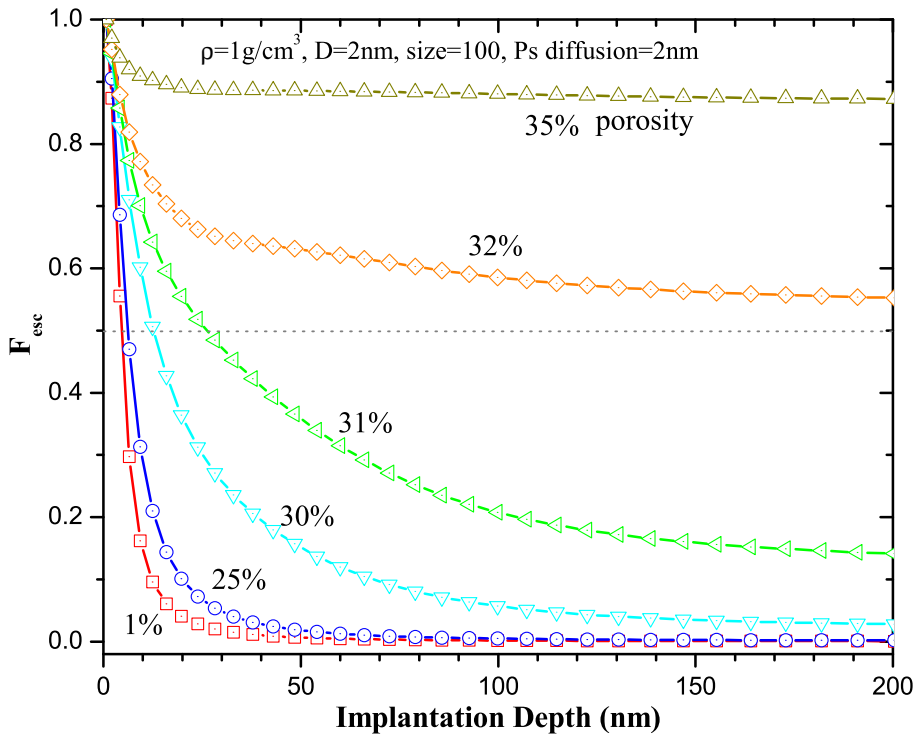


Figure 5.15: Ps escape fractions at beam energies from 0.1 keV to 6.0 keV at every 0.1 keV. Results of different porosities are shown. The density $\rho$ of the film is set at 1 g/cm$^3$. Pore size is 2 nm, lattice size is $100^3$. The Ps diffusion length is 2nm.

to be bigger than closed clusters. This effect is more clearly seen around the percolation threshold when the percolated and open cluster start to dominate the lattice. Since the Ps randomly diffuses into the mesopores within the range of the Ps diffusion length, it has proportional higher probability of diffusing into larger pores with bigger surface area. Furthermore, the Ps diffusing back to the surface of the film also enhances the vacuum Ps intensity and increases the apparent $F_{esc}$, thus the $F_{esc}$ is more affected at shallow positron implantation depth.

In the above model, the simple Ps mesopore diffusion model is used which presumes that all the Ps can escape as long as interconnected routes are available, the $F_{esc}$ should approach zero very gradually after percolation only because of the positrons' penetration through the lower density film. This could be inaccurate if the thickness of the film is comparable to the Ps mesopore diffusion length or the

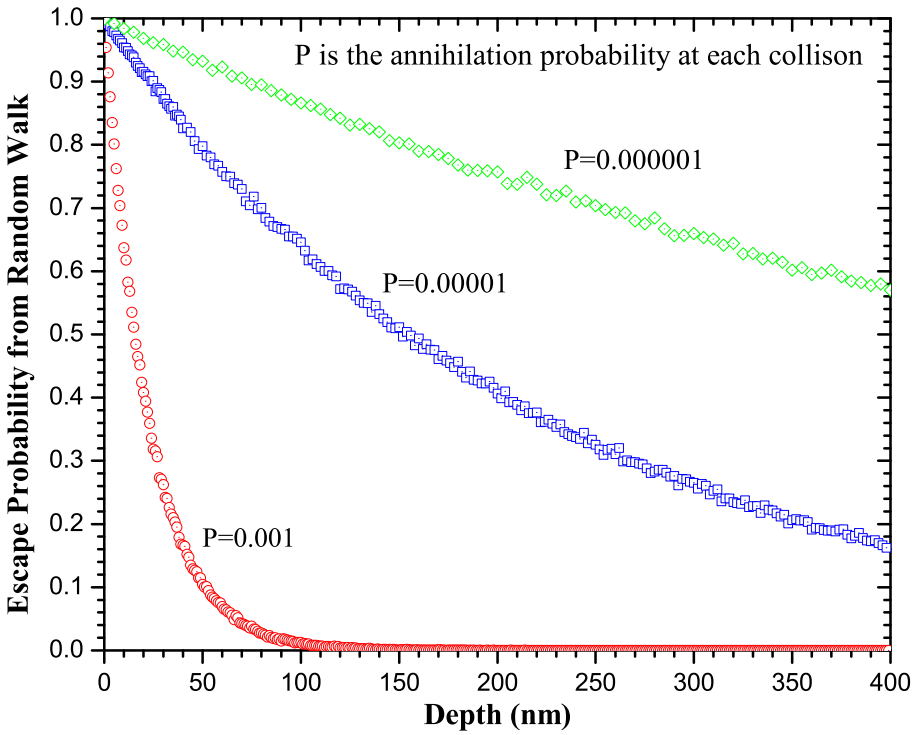


Figure 5.16: One dimensional Monte Carlo simulation results of Ps escape fraction at different depth assuming at each collision between the Ps and the walls, the annihilation probability is 0.001, 0.00001, and 0.000001.

mesopores in the film are very tortuous. There has been simulation of a one dimensional random walk to study Ps diffusion and escape behavior from the film [100]. If we assume at every collision between the Ps and the wall material, the Ps has some probability of annihilating, the Ps can bounce in the pore network ∼million times before annihilating [101]. Assuming a film boundary, we can obtain the probability for Ps to escape (pass the boundary) from a certain depth. It is an exponential curve, with its e-folding length, $\beta$, determined by the Ps mean free path and the probability of Ps annihilating at each collision (see figure 5.16). From the simulation, when the Ps annihilation probability is close to one part in a million, the interconnection length for a total interconnected pore network is approximately 500 nm (given the MFP=1 nm). Therefore, $L_{int}$ measured from a thick film with percolated pores will be determined by the Ps diffusion length itself, and will be close to 500 nm with a

MFP of 1 nm. For thin films as we mentioned earlier, this effect would reduce the deduced $L_{in}$ at the higher end (high porosities) and it would be small.

Briefly speaking, Ps diffusion has a moderate effect on the deduced interconnection length $L_{int}$. Ps diffusion in solids can increase the deduced $L_{int}$, especially by affecting the Ps escape fraction close to the surface region. A finite Ps diffusion length in mesopores shortens a longer $L_{int}$, which mostly happens in thick films. Given a totally percolated and thick enough film, the routinely measured $L_{int}$ should be equal to the actual Ps diffusion length in the mesopores of this film, which could be tested by future experiments if the positron beam energy limit can be extended.

## 5.4 Interactive porogens to produce desired morphology

### 5.4.1 Attractive interactions between porogens

Because the interconnection length from our experiments is growing much faster at low porosity than what the simulation yields, we suspect attractive interactions among porogens and that could lead to porogen agglomeration at very low porosities as well as lower the percolation threshold [102]. Attractions between porogens are implemented in the simulation to investigate the effects of porogen-porogen interactions on pore interconnection length and the MFP. In a cubic lattice, a Leonard-Jones potential field is generated by the first single cell placed at a random position; after that, every cell located consequently is affected by the attractive force from the existing cells, and also changes the overall potential field. The cells are not real-time dynamic, which means once a pore is located, it will not be affected by later added pores. A critical force (CF) is implemented, as a simple viscosity force, to prevent the aggregation below a certain attraction. When the attractive force exceeds CF, the newly located cell can move and merge to an existing cluster. A cutoff range, r, of the field is defined to see how the range of the attraction can also affect the

aggregation of cells.

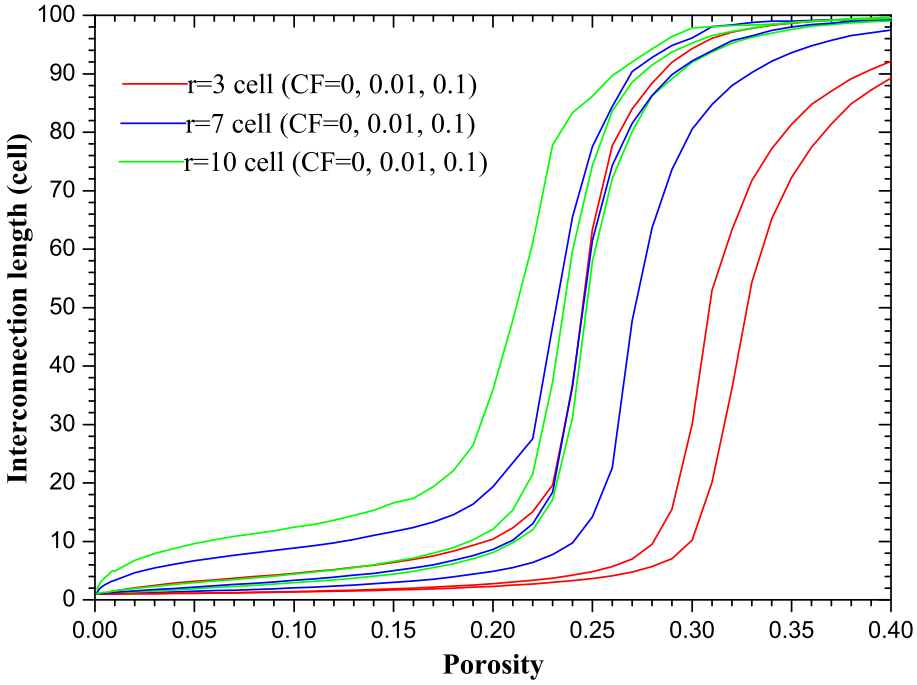


Figure 5.17: Simulation results of pore interconnection length for different cutoff range, r, and critical force, CF.

In figure 5.17 and figure 5.18, the interconnection length and mean free path with different cutoff ranges and critical forces are plotted versus the system porosity. In figure 5.17, three cutoff ranges are shown, each with different CF levels. At certain r, decreasing the CF will also lower the system's percolation threshold. At certain CF level, increasing the force range will lower the threshold as well. All these are understandable results. In figure 5.18, the Ps mean free paths are shown under various range and CF. Note that at large r with small CF, the pore size increases rapidly at very low porosities. However, at porosities higher than 10%, they all have similar growth rates. It indicates that at very low porosities when the pores have not formed big clusters, they quickly form some units of only two or three single cells. After that, these small clusters are dispersed fairly randomly. This behavior reminds us of the tCD system, where the tCD porogens may form two back-to-back units

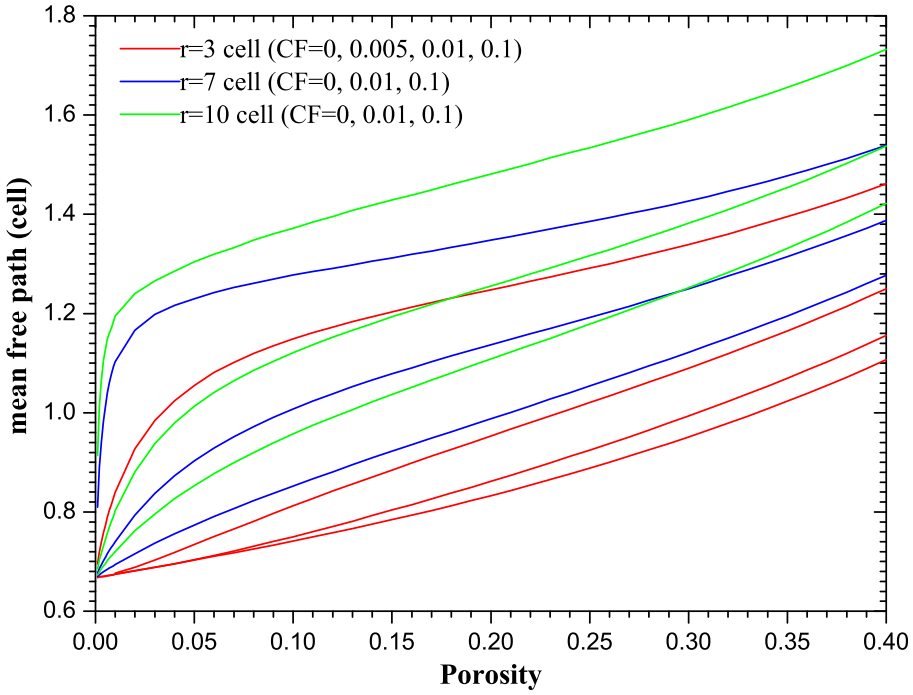


Figure 5.18: Simulation results of pore size for different cutoff range, r, and critical force, CF.

at very low porosity, but after that at higher porosities, these units are dispersed randomly with small interactions.

### 5.4.2 Random walk models

In figure 5.1 and figure 5.2, the sample prepared with sCD porogen shows a faster increase in the interconnection length than the other systems and a quite constant pore size at all porosities. The sCD system has been investigated in chapter three. Briefly speaking, these trends of $L_{int}$ and MFP confirmed a cylindrical growth of porogen domains, which is expected by the covalent bonds between two porogens. This interactions can linearly link the porogens together into a long chain (polymerize) and also explains the stability of the mean free path at different porogen concentrations. This mean free path is equivalent to the diameter of the cylinder-like chains and is consistent with the actual porogen molecule size.

To mimic the sCD-like porogen agglomeration, instead of the 3-D aggregation

in the previous section, a one dimensional growth mode should be used. A self-avoiding random walk model is implemented. The simulation is carried out in a cubic lattice, which contains one million lattice sites ($100^3$). Periodic boundary conditions are applied in the $x-y$ directions (along the film surface direction), but not on the $z$ direction (film depth direction). A self-avoiding random walk in the lattice is started with the first pore located at a random location. At each step, the direction is randomly chosen within the available directions. Due to the self-avoidance, the random walk cannot choose the backward, or any direction that will run into another pore. Once the random walk dead-ends in a "worm-hole", it starts from another available random location. This perfect random walk corresponds to a perfect linking between the pores, resulting a very large interconnection length. The mean free path is calculated by $4V/S$ and the interconnection length is calculated as the volume weighted cluster expansion in the $z$ direction. The interconnection length of this random walk model is shown in figure 5.19 (black curve). It is clearly seen that at very low porosity, the $L_{int}$ reaches the full lattice size. However, in actual porogen-matrix systems, the porogen agglomeration could not perfectly link into one single chain.

In order to make a more realistic pore growth, there should be many local random walks scattered in the lattice. A "power law" growing method designates a random number P between 0 and 1 at every lattice site. At each step, the site with the lowest designated P is found to be a new pore location. Following the cell picking, the P of one of its adjacent cells is decreased by applying a $n^{th}$ power to its P to increase the probability for that cell to be selected thereafter. This probability increase does not guarantee a random-walk from existing pores.

Simulation results are shown in the figures 5.19 and 5.20. The experiment results

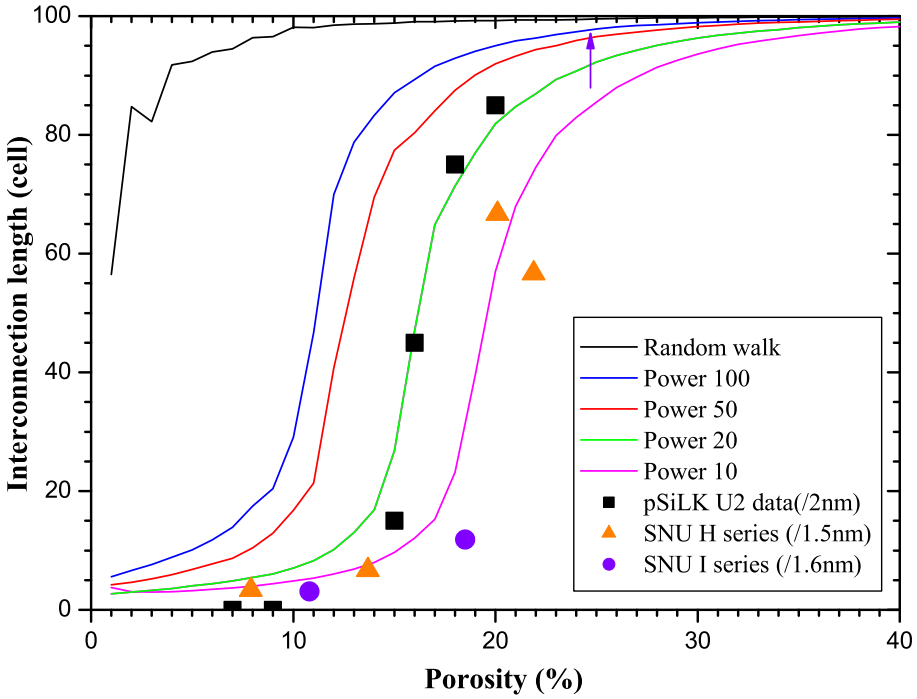


Figure 5.19: Simulation results of pore interconnection length from random walk model

of pSiLK U2, SNU H, I series samples are also shown in the figure for comparison. Note that the pore interconnection length and mean free path are in the unit of cells. The pSiLK and SNU results are divided by their single pore size which is around 2 nm, 1.5 nm and 1.6 nm respectively. Due to the limited lattice size used in the simulation, one of the data points of SNU I series sample is out of the range.

From figure 5.20 we can see the mean free path of pSiLK U2 samples stays quite constant, which may indicate a linear porogen agglomeration. Note that the first two data points are from the spherical pore model and the other four are from the cylindrical pore model, which is more realistic due to the long interconnection length at the corresponding porosities. On the other hand, the SNU samples demonstrate a slightly faster growth of mean free path.

In a variation of the above random walk model, a site-bond percolation is implemented. In addition to the site lattice geometry, between every two sites, there is a

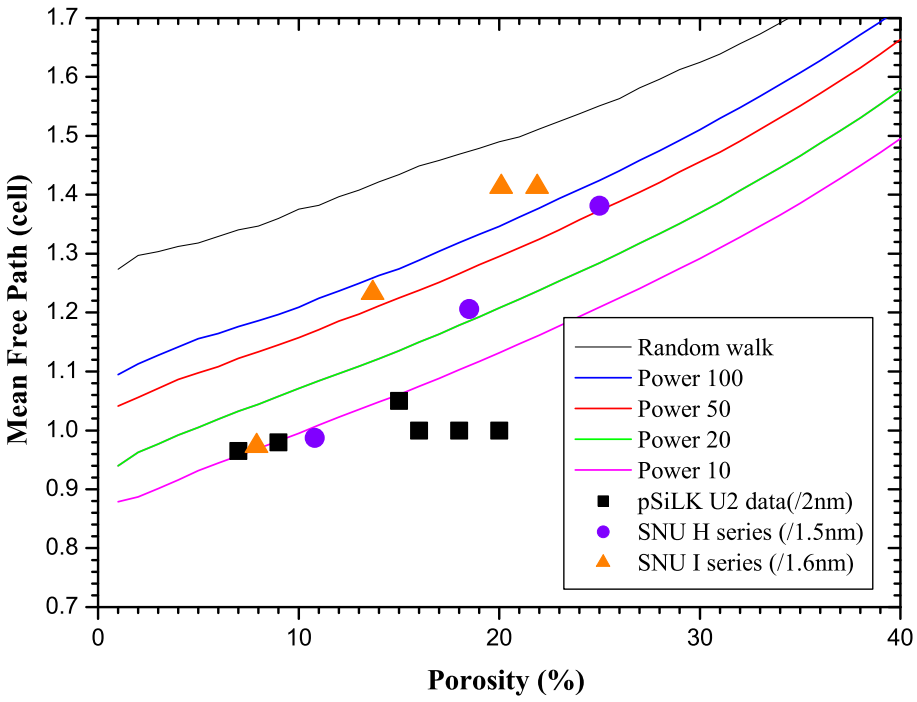


Figure 5.20: Simulation results of pore mean free path from random walk model

bond/wall that can connect or isolate two existing cells. A growth parameter $P_g$ is implemented as a probability of continuing the current walk. In other words, a random walk can start at a new position at a probability of $(1 - P_g)$. When $P_g$ is 1, the random walk will not end until it goes into a dead end; on the other hand, when $P_g$ is zero, this model is equivalent to a random cell selection. It is clear that a higher $P_g$ produces a higher interconnection length at the same porosity. Furthermore, when a new random walk should start at a new position, the algorithm searches within a region of radius r for any existing pores. If the region is occupied, the simulation will only continue that pore aggregation instead of starting a new one.

Figure 5.21 shows the simulation result of pore interconnection length at different growth probabilities ($P_g$) and searching ranges (r). Increasing $P_g$ and r can lower the percolation threshold, and also change the behavior of $L_{int}$. It seems that both $P_g$ and r can shift the percolation threshold significantly and can also increase the

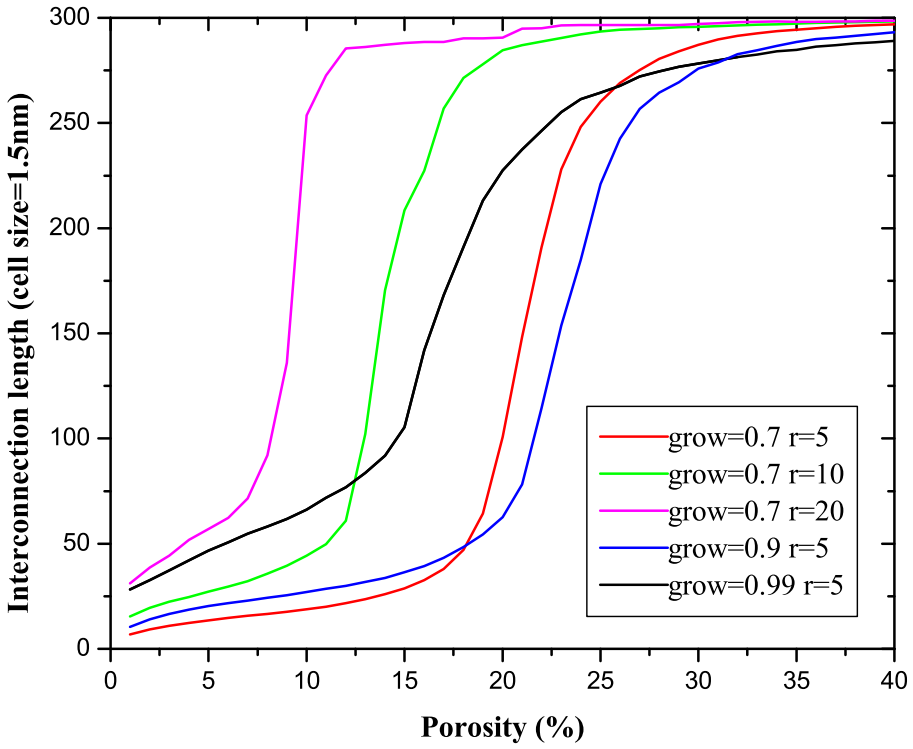


Figure 5.21: Simulation result of pore interconnection length at different growth probabilities ($P_g$) and searching ranges (r). The cell size is set to be 1.5 nm.

$L_{int}$ drastically at very low porosity. The random walk models are more realistic for the porogen agglomeration behavior and some of the simulations produce $L_{int}$ results that are more closer to our experimental data. The linking process between different clusters/polymers could also be included in the simulation, thus induces even longer interconnection length, which could be the future direction of these types of simulations.

In figure 5.22, the simulation results of MFP are shown with the sCD experimental results. The cell size is set to 1.63 nm to give the best agreement. The simulation result from the Monte Carlo simulation and tCD data are also shown for comparison.

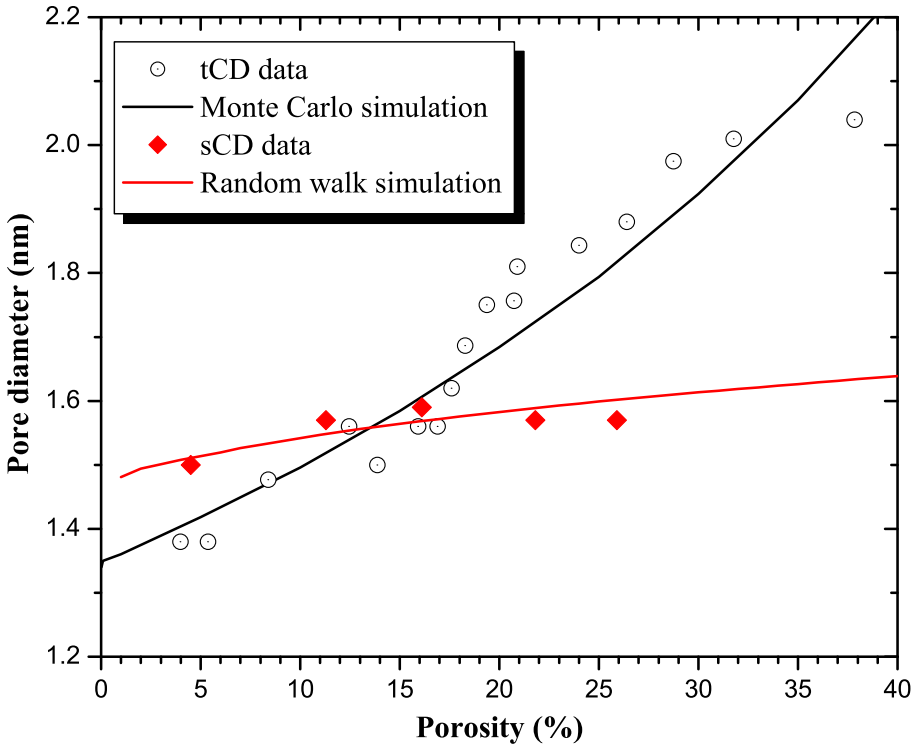


Figure 5.22: Simulation result of pore mean free path from random walk model and its comparison with the experimental data. The cell size is set to be 1.63 nm and the grow probability of the random walk is set to be 80% for the random walk model. The tCD data and Monte Carlo simulation are also shown in the figure in comparison.

## 5.5 Summary and discussion

The evolution of pore size and its connectivity in nanoporous low-$k$ thin films is closely associated with the percolation process. When the porosity of the ULK films reaches the percolation threshold, the film properties change drastically. At porosities larger than the percolation threshold, the pore networks of the thin film are interconnected and its integration process is difficult to succeed. In the recent studies, reducing the pore size as well as the pore interconnectivity have been the major goals to make the ULK thin films compatible with the integration processes.

Because the porosity should not exceed the percolation threshold significantly, the characterization of these porous thin films in the pre-percolation regime is important. Using PALS, we have studied a number of low-$k$ systems and found very

interesting common features among these systems, which may originate from the percolation process. Computer simulations are used in this chapter to investigate the different patterns of the porogen growth in the ULK thin films and their impact on the percolation process, especially the effects on the explicit quantities we customarily measure in our experiments, including the averaged Ps MFP, $L_{int}$, $F_{esc}$ and Ps intensity. Most of our simulations are carried out in a regular cubic lattice.

The simulation of Ps diffusion using a simplified model and its fitting to the experimental data reveal very interesting results. In several ULK systems, the evolution of Ps intensity according to porosity is closely related to the mesopore size. The Ps diffusion lengths in solids from the simulation are quite consistent in these systems. Although the morphology of the thin films and its evolution are never reproduced by the simulation, the Ps intensity results are still intriguing for the further understanding of Ps formation and diffusion in these materials. More importantly, an absolute porosity measurement/calibration from the Ps intensities under certain conditions might be possible.

The simulation of a totally random system shows an abrupt increase of the interconnection length at the percolation threshold, unlike the gradual increases seen in PALS experimental results. The involvement of porogen attractions in a pseudo-dynamic system lowers the percolation threshold, but no gradual/quadratic trends of $L_{int}$ is observed in the simulations. It is found that Ps diffusion in solids can increase the deduced interconnection length, while a finite Ps diffusion length in mesopores can decrease the interconnection length. Furthermore, using true dynamic models seems to be a reasonable step for the future simulation works, but it would be much more complicated to realize in this large scale and it is out of the scope of this thesis.

# CHAPTER VI

# Parylene pore sealing of ultralow-$k$ dielectrics

Making a material with a low $k$ value might be just the beginning of the whole story of the ultra low-$k$ application. The susceptibility of porous ultra-low-$k$ (ULK) materials to diffusion of copper, moisture, and solvents is still an important issue, causing the dielectric constant to increase, increased leakage current and even a dielectric breakdown. Pore sealing becomes a straightforward approach to avoid the problem and thin layers of CVD Parylene-N have been shown to be effective pore sealants [103]. In this chapter, PALS analysis will be conducted on a series of ULK thin films with Parylene-N sealant layers that have been deposited under different CVD conditions. The dependence of the Parylene-N penetration depth on the initial deposition conditions will be explored.

## 6.1 Introduction on Parylene-N pore sealing

*Porous* ULK dielectric material is the most pursued way of making integrable low-$k$ interlayer dielectric (ILD) materials for the next several generations of ultra-large scale integration (ULSI) circuits. However, the incorporation of high porosity into ULK thin films causes many processing problems. The implementable ULK materials need to survive a series of integration processes involving high temperature, high stress, chemical reactions, metal (Cu) diffusion, plasma exposure, and chemical

mechanical polishing (CMP). These requirements eliminate a large fraction of all the ULK candidates. The promising candidates still have the problem of maintaining their integrity and bulk $k$ value during the processing. Apart from the mechanical strength, chemical compatibility and heat stability issues, problems associate with metal precursor, moisture, and solvent penetration through the barrier layer/seed layer during CVD and subsequent processes remain unresolved.

This specific problem is clearly due to the interconnnectivity of the nanopore structure when high porosity is introduced to the film. Among the several methods and materials that have been investigated in recent studies, CVD Parylene-N has been found to work as an effective pore sealant for porous low-$k$ materials. The Parylene-N deposition is selective such that it only seals the side-walls of the ULK materials but does not deposit on the metal surface at the bottom of the trenches [104]. The major concern of using Parylene-N as the pore sealant is that Parylene-N can penetrate the interconnected pore network of the ULK thin film. Parylene-N itself has a fairly low $k$ value of about 2.6, however it still causes an increase of overall $k$.

Study has shown that the Parylene-N penetration can be controlled by deposition pressure [105]. A lower penetration can be achieved by a higher deposition pressure or adding a carrier gas, hence a higher deposition rate is achieved to seal the surface quickly. Meanwhile, the pore size and pore interconnectivity directly determine the penetration depth of the Parylene-N as well. Other factors may also affect the pore sealing process, such as the material temperature and the deposition thickness. All these factors that can affect the resultant sealing quality are actually decided by the underlying growth mechanism of the sealant layer and its interactions with the interconnected pores and it is important to understand the growth mode of the

sealant layer.

## 6.2 PALS experiments and analysis

### 6.2.1 The ULK thin films and different conditions of pore sealing

PALS analysis is used to investigate the effects of different Parylene-N sealing processes. Results from several other techniques, including Argon DFT and ellipsometric porosimetry (EP), are also presented as comparisons. Parylene-N thin films were deposited using the method described in detail elsewhere [105, 106]. The deposited Parylene-N film thickness was measured on flat silicon samples and was assumed similar on dense MSQ films. The depth profile of Parylene-N in *porous* MSQ films will be analyzed by PALS. Five silicon-supported films based on JSR 6013 low-$k$ dielectric are analyzed: a pristine JSR film (300 nm thick), an aluminum capped film (50 nm Al on 300 nm of JSR), a thick ($\sim$200 nm) deposit of Parylene-N on a silicon wafer, and two 300 nm thick JSR layers exposed to 5 nm CVD deposition of Parylene-N - one at room temperature (RT) and the other at -30°C. From gas adsorption and EP with toluene the JSR 6103 is known to have high porosity at 49%, percolated/interconnected mesopores, with pore MFP (cross sectional diameter) nominally in the 3-4 nm diameter range.

EP and Ar DFT measurements were conducted on the JSR 6013, JSR 5109 and JSR 5115 for comparison. In chapter 4, we have studied the intrinsic matrix material JSR 5109 (OS3). It was found by PALS that the JSR 5109 is highly interconnected with a mesopore size of $\sim$3 nm in diameter. In figure 6.1 and figure 6.2, the experimental results from EP and Ar DFT are in excellent agreement with the PALS results.

Based on EP and Argon DFT, the mesopores in all these three materials are interconnected. The porosities of 5115, 5109 and 6103 are 33%, 39% and 49% respectively.

5109 and 5115 have comparable pore size, while JSR 6103 has larger pores, which are clearly seen in figure 6.1 and 6.2. No micropores are found from Ar. DFT, but EP indicates microporosity in these films.

### 6.2.2 PALS experiments and results on pristine Parylene-N thin film

Depth-profiled PALS is conducted to address the depth dependence on pore characteristics of these samples. Various positron beam energies are used to implant positrons into different depths of the films. Typical energies used are 0.6 keV, 1.2 keV, 2.2 keV, 3.2 keV, 4.2 keV, and 5.0 keV corresponding to mean implantation depths of 12 nm, 37 nm, 100 nm, 180 nm, 280 nm, and 400 nm respectively, assuming a film density of 1 g/cm$^3$. At higher densities, the stopping depth will be proportionally reduced by a factor of the specific density. The density of Parylene-N is around 1.1 g/cm$^3$, which is not significantly different from density 1 g/cm$^3$ and hence the correction on implantation depths will be small.

We first consider the pure Parylene-N film on Si to demonstrate the well-known ability of PALS to probe the naturally occurring "free volume" voids inherent in

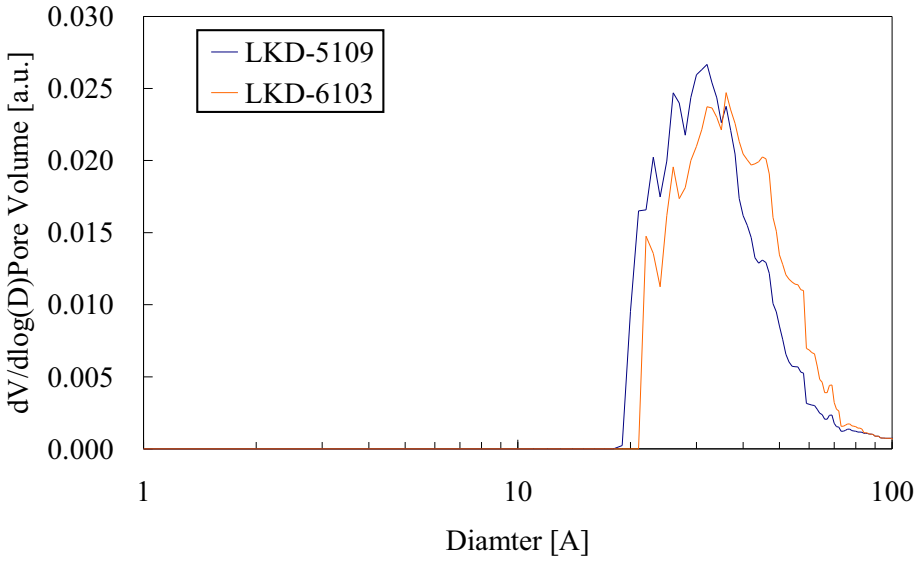


Figure 6.1: Pore size distribution measured by Ar. DFT technique.

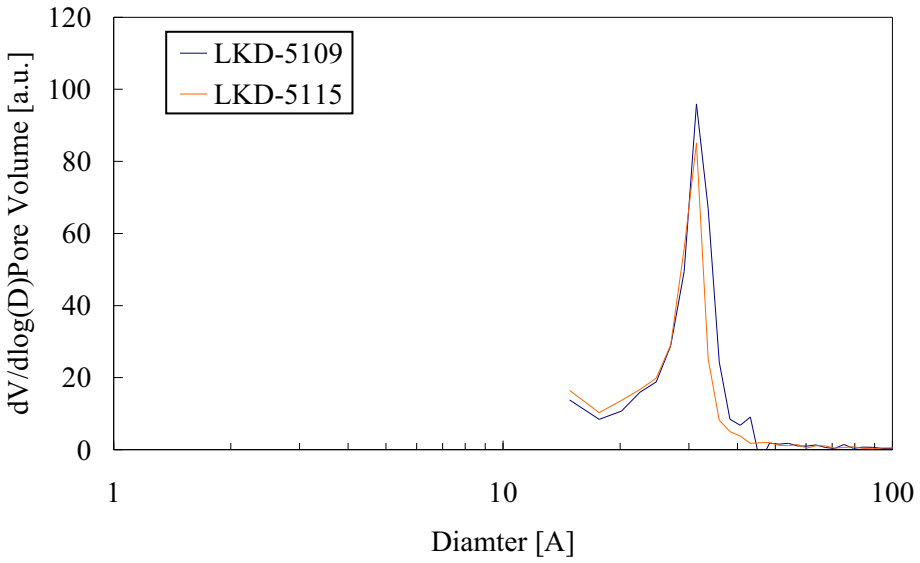


Figure 6.2: Pore size distribution measured by EP.

polymers. Adequate discrete lifetime fitting of the beam-PALS lifetime histograms requires 4 lifetime components: the shortest around 0.3 ns is just due to annihilating positrons that do not form Ps and is therefore uninteresting. The remaining lifetimes are characteristic of Ps annihilation-the first Ps component has lifetime $\tau_1 = 1.6$ ns, the second has lifetime $\tau_2 \sim 7$ ns, and the third has a lifetime very near the lifetime of Ps in vacuum, 142 ns. This long-lived vacuum Ps will be important in the JSR films because it signals the diffusion and escape of Ps in the mesopore network-the observable sign of an interconnected pore network. In the case of Parylene-N this vacuum Ps component of low relative intensity is due to a well-known effect inherent to positron beam research-some fraction of the incoming positrons will backscatter and capture an electron at the surface to form Ps in vacuum that has nothing to do with pores in the film. This backscattered Ps is a nuisance systematic that is ever-present in all beam data and needs to be corrected from the JSR data. The fitted lifetimes, $\tau_1$ and $\tau_2$, and their relative intensities, $I_1$ and $I_2$, (relative to all positrons hitting the film) together with the fitted intensity of the vacuum Ps intensity $I_{vac}$ are

presented in Table 6.1.

Table 6.1: **PALS discrete fitting results of the 200nm pure Parylene-N film deposited on silicon substrate.**

| **Energy (keV)** | $\tau_1$ **(ns)** | $\mathbf{I}_1$ **(%)** | $\tau_2$ **(ns)** | $\mathbf{I}_2$ **(%)** | $\mathbf{I}_{vac}$ **(%)** |
|---|---|---|---|---|---|
| 0.6 | 1.5 | 14.30 | 8.5 | 3.60 | 4.80 |
| 1.2 | 1.5 | 16.90 | 7.8 | 3.00 | 2.90 |
| 2.2 | 1.6 | 14.70 | 6.5 | 2.90 | 2.00 |
| 3.2 | 1.7 | 11.50 | 6.6 | 2.80 | 1.80 |
| 4.2 | 1.9 | 9.40 | 7.0 | 1.80 | 1.30 |

The PALS results for Parylene-N are quite typical of free volume voids in glassy polymers that typically present a Ps lifetime around 2 ns with intensity around 30%. The highest intensity Ps component has a lifetime of 1.6 ns corresponding to pores with a diameter (spherical pore model) of 0.5 nm. We are not totally sure whether the low-intensity component with $\tau_2 \sim 7$ ns is actually Ps in some larger voids with diameter around 1.1 nm or whether it is an artifact of backscattered Ps. We will definitely detect pores of this lifetime/size in the matrix of the JSR but we don't expect it for Parylene-N, nor is it important here as we will key on the 1.6 ns lifetime as the important observable characteristic of Parylene-N. Relative to glassy polymers such as polystyrene, PC, and PMMA (and even JSR for that matter) the Ps formation intensity in the 0.5 nm diameter voids ($I_1$=16-17%) is smaller by a factor of two. We note the decrease in $I_1$ at 3.2 and 4.2 keV - this is simply penetration of the positrons through the Parylene-N and into the Si substrate which has no Ps lifetime in this range. The vacuum Ps intensity is completely consistent with being solely due to backscattered Ps - i.e. there is no indication of Ps diffusing out into vacuum through interconnected pores. Backscattered Ps has a well-documented 1/E beam energy dependence to $I_{vac}$ and the values of $I_{vac}$ are even smaller by almost a factor of two then those that we typically measure for backscattering. The pores

must be small and isolated (not interconnected) and this is typical of every polymer film we have analyzed.

### 6.2.3 Pristine JSR 6103 and aluminum capping

The PALS results for the pristine JSR 6103 and its Al-capped version are presented in Table 6.2. The first thing to note about this JSR film is that it has very high Ps formation in the 34-37% range with virtually all of the Ps escaping (∼93%) into vacuum. Almost all the Ps formed in this film decays with the vacuum lifetime of 140 ns having readily diffused through the interconnected mesopore network and escaping the film into vacuum. We do detect a low intensity "mesopore" lifetime in the 36-56 ns range characteristic of the small faction of Ps atoms that do decay before they can diffuse out of the film but this fitted lifetime is distorted by the effect of escape into vacuum and is a best a lower limit on the true mesopore lifetime. A capping layer is required to seal the surface so that Ps is actually corralled in the pores and hence probes the pore size. The Al-capping at RPI formed such a barrier and we get a clean measure of the Ps lifetime in the pristine JSR porous network of 59 ns. This lifetime corresponds to a mean cylindrical pore diameter of 3.3 nm. We use a cylindrical pore diameter to be consistent with absorption porosimetries and because the cross sectional diameter of a long tubular pore is also the mean free path, MFP. PALS should be sensitive to the MFP in the film where MFP=4V/S and V and S are the pore volume and surface area. In effect we are deducing that Ps has a mean distance of 3.3 nm between bounces in the pores of JSR. Since Ps can typically make a million bounces before annihilation it is not surprising that it can diffuse a long way (over 1000 nm) in interconnected pores of this size, rendering over 90% of the Ps in vacuum. We conclude that the JSR pores are percolated - i.e. they are totally interconnected. In MSQ films of lower porosity we can deduce

a finite pore interconnection length, but in JSR 6103 the pores are percolated. In this high porosity film we do not detect any short lifetime components characteristic of micropores, but this does not imply that micropores do not exist (contrary to JSR's contention that micropores are not present in 6103). It is very common in high porosity films for Ps in the micropores to "drain out" into the mesopores-they diffuse into the mesopores so quickly that they do not annihilate in the micropores. In chapter 4, the $N_2$ absorption data has confirmed the existence of micropores in 5109. Here, we would assume micropores are present in all these samples but PALS doesn't detect them in such a high porosity film – every MSQ matrix we have analyzed has robust Ps formation in micropores characterized by two Ps lifetimes, typically about 2.5 ns and 6-7 ns (these micropores are usually visible in low-to-modest mesoporosity versions of the MSQ). We will see evidence for these micropores in the Parylene-N deposited films.

Table 6.2: **PALS discrete fitting results of the pristine and Al-capped LKD-6103 sample. The vacuum intensity has been corrected by subtracting typical backscattered Ps intensities at different energies and divided by 1.2 to account for the differential detection efficiencies of $2\gamma/3\gamma$ events.**

| **Energy (keV)** | $\tau_{meso}$ **(ns)** | $\mathbf{I}_{meso}$ **(%)** | $\mathbf{I}_{vac}$ **(%)** | $\mathbf{I}_{Ps}$ **(%)** | $\mathbf{F}_{esc}$ **(%)** |
|---|---|---|---|---|---|
| 1.2 | 36 | 3.5 | 33.8 | 37.3 | 91 |
| 2.2 | 51 | 2.6 | 31.8 | 34.4 | 93 |
| 3.2 | 52 | 1.8 | 25.8 | 27.6 | 94 |
| 4.2 | 56 | 1.7 | 18.6 | 20.3 | 92 |
| 5.0 | 49 | 1.4 | 18.7 | 20.1 | 93 |
| 4.0 (capped) | 59 | 10.2 | 0 | N/A | 0 |

### 6.2.4 PALS results of the Parylene-N sealed samples

Two LKD-6103 films are sealed by Parylene-N deposition at different temperatures, one at -30°C and the other at RT. Similar depth-profiled experiments are done on these two samples and the discrete fitting results are shown in table 6.3 and table

6.4. Adequate fitting of the PALS spectra require 4 discrete Ps lifetimes plus the uninteresting positron lifetime. Three of the Ps lifetimes correspond to Ps annihilating in pores. Two correspond to micropores/free volume voids with lifetimes close 2 ns and 7 ns, while the third corresponds to mesopores (perhaps Parylene-N lined) in JSR. The first two short lifetimes about 2ns and 7ns stay quite constant at all energies and thus only their intensities are shown in the tables. The vacuum intensities in the last column are consistent with backscattering off a composite surface of MSQ and Parylene-N – the values scale as 1/E and have absolute values intermediate between the observed backscattering off pure Parylene-N in table 6.1 and those values typical of backscattering off MSQ films (typically about twice those for Parylene-N). For both Parylene-deposited JSR films we assert there is no evidence of Ps escape into vacuum-the highly interconnected JSR pores appear to be completely sealed at the surface.

Table 6.3: **Fitting results on (Parylene-N -30°C)-sealed JSR LKD-6103. $I_{vac}$ is the total vacuum intensity and is fully consistent with backscattered Ps.**

| **Energy (keV)** | **I at ∼2ns (%)** | **I at ∼7ns (%)** | $\tau_{meso}$ **(ns)** | $I_{meso}$ (%) | $I_{vac}$ (%) |
|---|---|---|---|---|---|
| 0.6 | 18.30 | 7.50 | 37 | 1.90 | 7.10 |
| 1.2 | 19.90 | 7.50 | 54 | 5.00 | 4.20 |
| 2.2 | 12.20 | 6.70 | 60 | 12.60 | 2.60 |
| 3.2 | 9.90 | 7.20 | 61 | 14.10 | 1.90 |
| 4.2 | 7.20 | 4.40 | 61 | 10.40 | 1.60 |
| 5.0* | 7.50 | 5.40 | 60 | 10.20 | 1.50 |

**Intensities acquired at 5.0keV should be reduced by 15% due to a systematic effect related to Ps formation*

The fitting results in Tables 6.3 and 6.4 are effectively identical and will be discussed interchangeably. Beside the fact that there is no Ps diffusive escape into vacuum (the pores are sealed by Parylene-N), the Ps mesopore lifetimes and intensities in both tables corresponding to the annihilation of Ps in the JSR mesopores is very revealing of Parylene-N penetration into the porous JSR. The mesopore in-

Table 6.4: **Fitting results on (Parylene-N RT)-sealed JSR LKD-6103. $I_{vac}$ is the total vacuum intensity and is fully consistent with backscattered Ps.**

| **Energy (keV)** | **I at ∼2ns (%)** | **I at ∼7ns (%)** | $\tau_{meso}$ **(ns)** | $I_{meso}$ **(%)** | $I_{vac}$ **(%)** |
|---|---|---|---|---|---|
| 0.6 | 18.20 | 6.80 | 36 | 1.60 | 6.30 |
| 1.2 | 18.80 | 7.30 | 55 | 5.40 | 3.80 |
| 2.2 | 13.00 | 5.60 | 60 | 12.20 | 2.60 |
| 3.2 | 9.40 | 3.40 | 59 | 13.30 | 2.20 |
| 4.2 | 8.00 | 2.30 | 60 | 10.00 | 1.70 |
| 5.0* | Bad fit | Bad fit | 60 | 9.90 | 1.60 |

**Intensities acquired at 5.0keV should be reduced by 15% due to a systematic effect related to Ps formation*

tensity at low implantation is almost reduced to zero and at the two lowest beam energies the fitted mesopore lifetime is lower than that for pristine JSR. Admittedly, the mesopore intensity, $I_{meso}$, is also so low that one might view the reduced lifetime with some degree of statistical and systematic skepticism, but it does suggest that there is some partial pore filling or lining (will be discussed in later sections). For both films we fit the pristine mesopore lifetime (59-60 ns) at deeper implantation where the mesopore intensity is largest indicating that the deeper-lying pores are free of Parylene-N effects - they are nominally pristine JSR pores.

The intensities of the two micropore components in Tables 6.3 and 6.4 are also interesting, especially at implantation energies of 0.6 and 1.2 keV. At 1.2 keV the intensities are 19-20% and 7.4% respectively, both being higher than pure Parylene-N values of ∼17 and 3%. Even if Parylene-N is filling 100% of the JSR near-surface pores over half the positrons must still be stopping in the JSR wall matrix. Thus, the primary source of these two short Ps lifetimes must be from Ps annihilation in the micropores of the JSR matrix – MSQ matrices always produce two micropore lifetimes around 2 ns and 6-7 ns. Now we can detect these micropores because Ps has no path to diffuse out of these micropores. The Parylene-N is either completely filling the mesopores or at least preventing Ps from entering the mesopores. The end result

is that at low implantation energy we are fitting the PALS spectrum of a nominally 50-50 composite by volume. Assuming the density of the matrix is about 1.5 g/cm$^3$ (literature values run from 1.3 to 1.8 g/cm$^3$) and the density of Parylene-N is 1.1 g/cm$^3$ then the Parylene-N concentration by weight is only about 40%. We would expect about 60% of the shallowly implanted positrons to stop in the JSR matrix. Thus, we have to conclude that the JSR matrix has copious micropores that can trap Ps. We would naturally have suspected this to be the case but the information from Argon DFT seemed to indicate that JSR 6103 does not have micropores in the wall. This contention appears to be simply wrong. We wanted to look for a micropore Ps signal because increased Ps annihilation from the micropores is a natural consequence of pore filling or pore lining that inhibits Ps from populating mesopores. If Ps does not appear in the mesopores it should be annihilating in JSR micropores or in the free volume voids of the Parylene-N. This seems to be the case.

## 6.3 Modeling of Parylene-N penetration

To understand the Parylene-N filling modes of these two samples and fit the two sets of Parylene-infused JSR data for the mesopore intensity, $I_{meso}$, two models are assumed. The simple one is that Parylene-N *completely* fills the pores at shallow depth and the deeper pores remains intact. Including the silicon substrate adds a third layer with a step function for Parylene-N penetration and the depth of this filled layer can be fitted as a free parameter. In order to reduce the mesopore intensity from that of JSR ($\sim$40%) to no more than 14% the filled layer depth must be a substantial fraction of the 300 nm film depth (well over 100 nm). As a result, for low beam implantation energies corresponding to mean implantation below 50 nm we expect no mesopore intensity at all. In figure 6.3, the fitting results of the three-layer

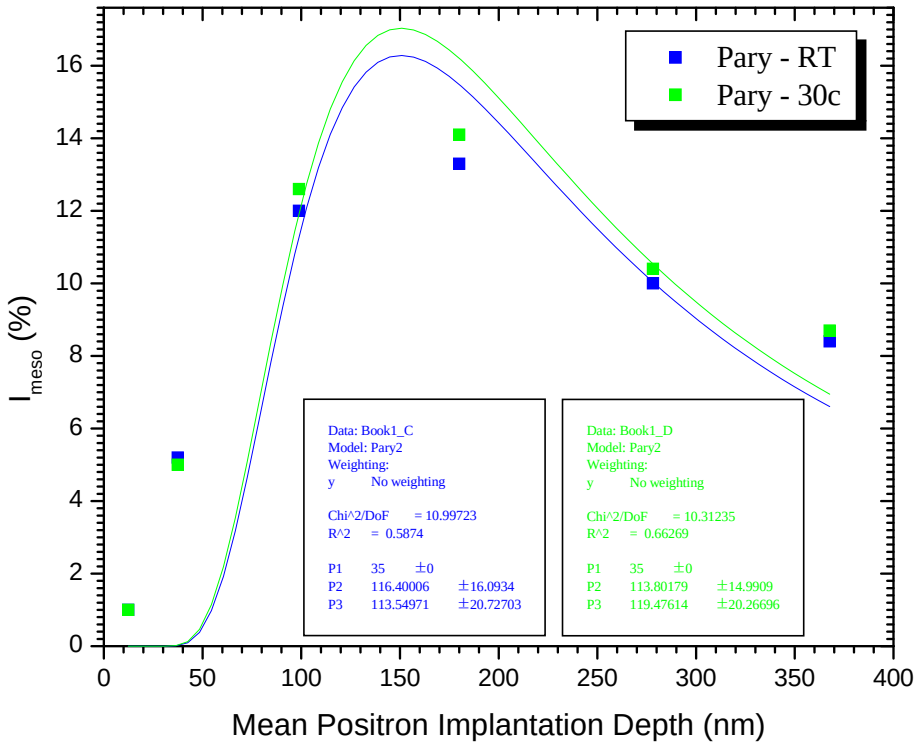


Figure 6.3: Mesopore intensities are plotted vs. mean implantation depth for the two Parylene-N sealed films. The curves correspond to overly simple models based on a three layer model: 100% Parylene-N filled JSR/pristine JSR/Si wafer.

model as well as the mesopore intensities of the two filled samples are shown. The Ps intensity from mesopores is fixed at 35%, which is consistent with the vacuum intensity in pristine JSR 6103 after corrected by $3\gamma/2\gamma$ efficiency difference. P1 presents the thickness of the fitted filled layer, and P2 is the thickness of the rest film. This step change penetration profile has no hope of accounting for the results. We need to get some open pores nearer to the surface.

The three layer model is obviously an over-simplified model. Much better fitting is obtained if we assume that the Parylene-N filling of the pores (or at least the Parylene-induced inhibition of Ps from populating the mesopores) is exponentially decreasing with depth. The exponential depth is characterized by the $\beta$ parameter and the Parylene-N profile can be expressed as $e^{-\beta z}$, where z is depth coordinate

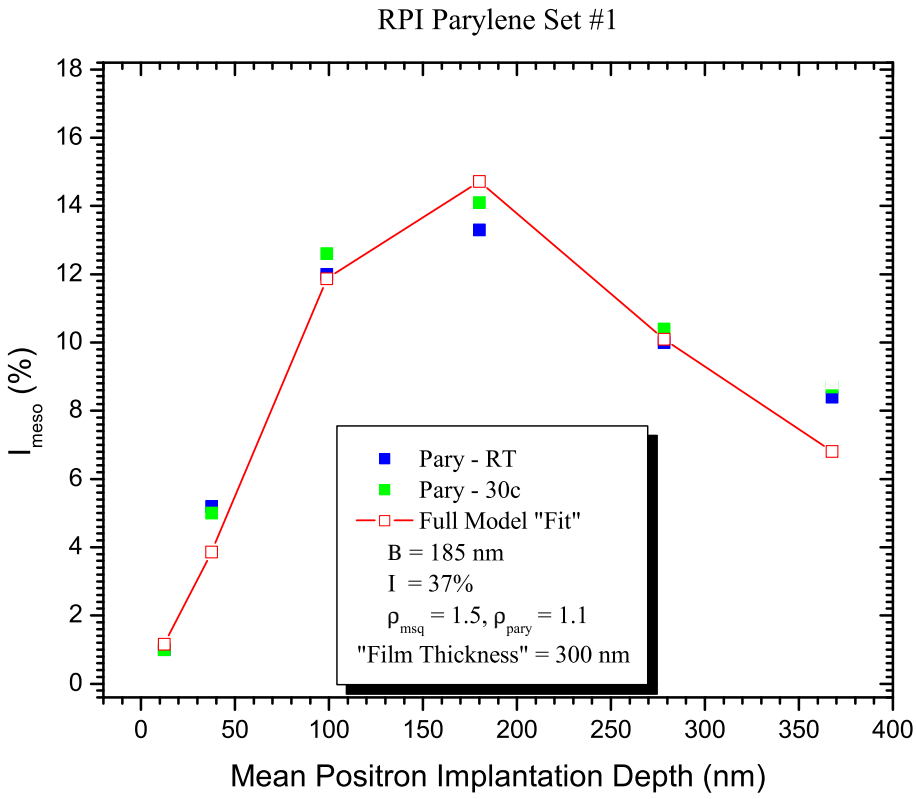


Figure 6.4: Improved fitting results of $I_{meso}$ vs. mean implantation results from assuming an exponential penetration of Parylene-N characterized by exponential depth $\beta$.

in the perpendicular direction of the sample surface. (The exponential penetration of Parylene-N is suggested in the earlier RPI work [105].) The red curve in figure 6.4 shows the fitting results from this exponential model and it agrees with the experimental data much better. In the fitting, the mesopore intensity is fixed at 37%, the densities of JSR 6103 wall material and Parylene-N are set at 1.5 g/cm$^3$ and 1.1 g/cm$^3$ respectively. The result shows that a layer with $\beta = 185$nm is required to produce the expected PALS data. When we change the input parameters we pretty consistently get near 180$\pm$20 nm. This is a little surprising since the film is only 300nm thick, thus almost two thirds of the film is penetrated by Parylene-N. The two samples that have been processed under different temperatures do not show significant difference in the mesopore intensities as well as the Parylene-N penetration

depths. There is only a tiny difference that may suggest at lower temperature (-30°C), the mesopore intensity is higher with less Parylene-N penetration.

In the Parylene-N filled/coated region, if there are regions of uncoated JSR pores then Ps formed in the surrounding JSR matrix would trap in these uncoated pores. At the lowest beam energy of 0.6 keV with mean implantation depth of 12 nm we are probing the top 25 nm of the film. Thus, to have $I_{meso}$ suppressed from 37% to 1.7% requires that 95% of every pore surface in this top 25 nm layer is either filled or at least lined with Parylene-N so as to inhibit Ps population of JSR mesopores. Moreover, whatever the actual degree of mesopore filling by Parylene-N it is sufficient to block all Ps formed and diffusing in the underlying JSR mesopores from escaping through the surface into vacuum. The film is sealed by Parylene-N.

The main question here is whether a complete pore filling is required to extinguish Ps trapping in mesopores of any size or only some critical thickness (1 nm?) of Parylene-N pore lining is sufficient to inhibit Ps trapping in the mesopores. There is no direct evidence from the experimental data to draw a definite conclusion on this issue, but the effective dielectric constant suggests a pore lining instead of a complete filling. The dielectric constant of the dense MSQ backbone in JSR 6103 can be reversely calculated using its effective dielectric constant 1.97 and its porosity 49%, which was found to be 2.9 [105]. The $k$ value of the pristine Parylene-N is 2.65. As we know that the composite dielectric constant can be calculated by

$$\frac{k_r - 1}{k_r + 2} = P \cdot \frac{k_1 - 1}{k_1 + 2} + (1 - P) \cdot \frac{k_2 - 1}{k_2 + 2}, \tag{6.1}$$

where $k_1$ is the dielectric constant of the material inside the pores, $k_2$ is the dielectric constant of the matrix skeleton, $P$ is the porosity of the film, and $k_r$ is the overall dielectric constant. If we assume that the mesopores of JSR 6103 are completely filled with 95% of the pores filled on the top 25 nm and an exponential filling profile

(and $\beta$ is 180±20 nm) extending down from the surface, the dielectric constant after filling would be about 2.4, which is much larger than the effective $k$ value estimated (2.13) for the filled film by the nuclear reaction analysis (NRA) [105]. Therefore, it is much likely that the Parylene-N just coats the inner surfaces of the mesopores. Figure 6.5 shows a probable illustration of the Parylene-N pore sealing mode.

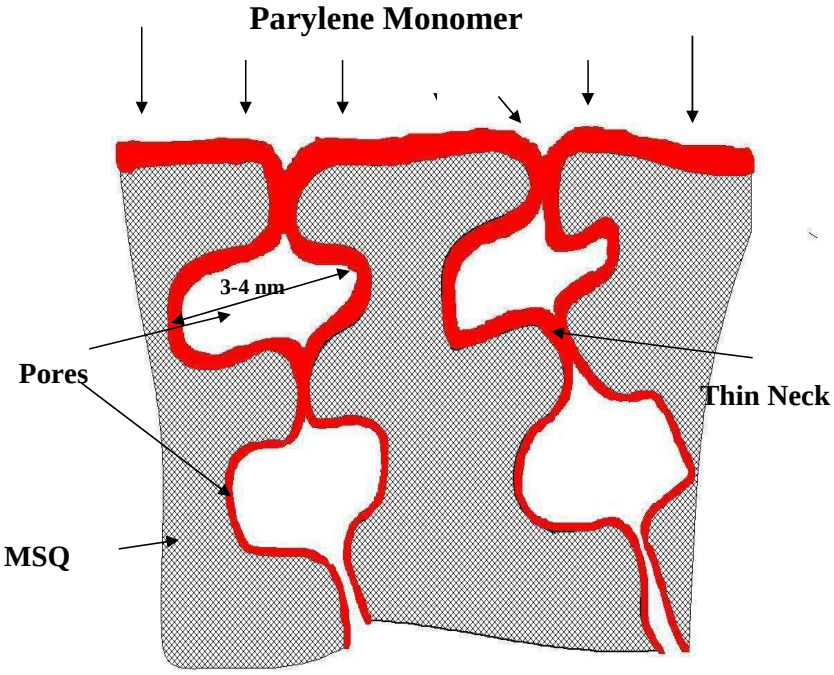


Figure 6.5: An illustration of the Parylene-N pore sealing/lining of the interconnected mesopores.

## 6.4 Deposition effects on Parylene-N pore sealing

Studies suggest that under different conditions, the depth profile of Parylene-N deposition may vary accordingly. The penetration depth could be affected by various factors, including Parylene-N thickness, pressure, temperature and the porous material itself. Samples with various Parylene-N deposition conditions and on different films are systematically studied. The samples we studied in the previous section are Parylene-N deposited at different temperatures, although we only see small effects on the filling layer thickness, which could due to the small temperature difference.

Those samples are all 5 nm of Parylene-N deposited by CVD at a pressure of 6 mTorr on JSR 6103. In this section, samples that have undergone 2 mTorr deposition pressure with different thicknesses of Parylene-N layer will be investigated and fitted by the exponential model. Two other JSR samples, namely 5109 and 5115, are also processed by 5 nm Parylene-N sealing layer under a deposition pressure of 2 mTorr.

A series of beam energies are used on these samples, from 0.6 keV, 1.2 keV and every 500 eV step up to 4.2 keV, which correspond to mean implantation depths of 12 nm, 38 nm, 66 nm, 100 nm, 139 nm, 182 nm, 229 nm and 281 nm. Four Ps lifetimes are fitted by discrete lifetime fitting, the results are shown in appendix D (table D.15 to table D.20). PALS results of different thicknesses of Parylene-N, including 1 nm, 2 nm, 5 nm and 30 nm, deposited at 2 mTorr on JSR 6103 are shown in table D.15 to table D.18. The PALS results of Parylene-N on other two JSR samples, JSR 5109 and JSR 5115, are shown in table D.19 and D.20.

To summarize the results, the first feature we note is that the Ps intensity annihilating in vacuum appears to be very consistent with solely backscattered Ps - i.e. there is no clear evidence of any Ps diffusing out into vacuum through the interconnected pores of JSR 6103. The pores are nominally sealed for all Parylene-N deposition depths even of 1 nm (although the Parylene-N also penetrates into the films). Figure 6.6 shows the fitted vacuum Ps intensities for Parylene-N deposited on JSR 6103 (linear fits are also shown in figure 6.6 for different series of Ps vacuum intensities of samples) and it is found that they follow the expected $E^{-1}$ dependence for backscattered Ps. Although there is no evidence of Ps diffusing out from the film into vacuum, we do see differences in the backscattered Ps intensities in different films. In the previous section, it has been shown that Ps backscattering off Parylene-N is about a factor of two lower than that off JSR/MSQ at each positron

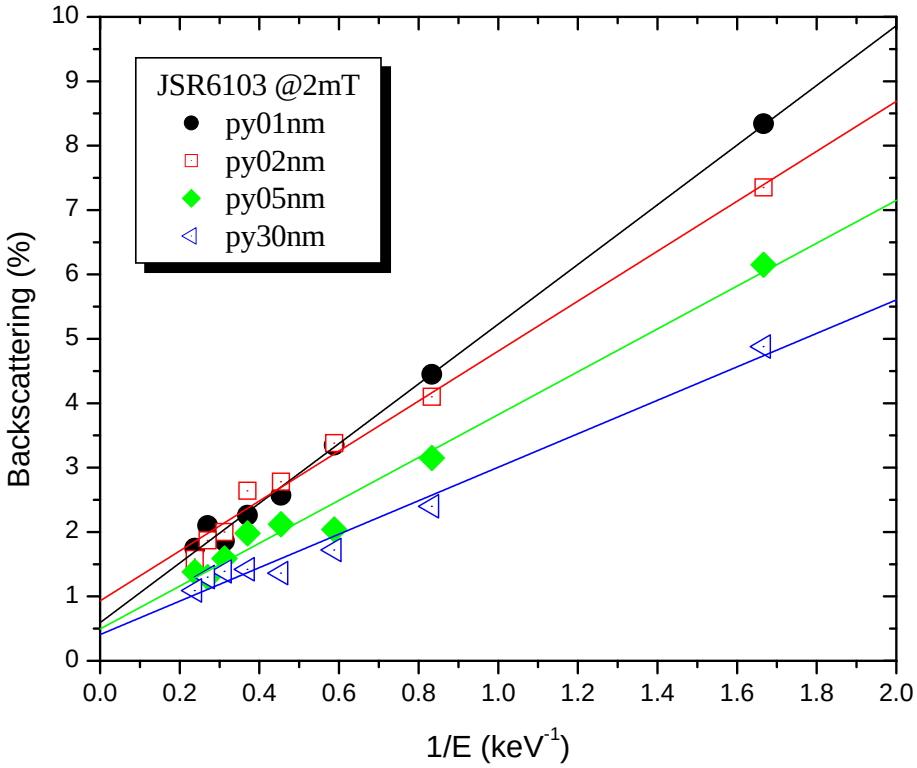


Figure 6.6: Total intensity of Ps in vacuum vs. the inverse of the positron beam energy. Four differential Parylene-N deposition thicknesses are used: 1, 2, 5, and 30 nm

implantation energy (Ps formation in Parylene-N overall is a factor of two less than MSQ). Backscattering is strongly surface sensitive and the downward trend in vacuum intensity with thicker parylene-N probably just reflects the changing relative contributions of the Parylene-N and the MSQ to the total backscattering. The crossing of 1 nm with the 2 nm line hints that this thin deposit may have a tiny fraction of escaping Ps, which will be discussed later.

For all practical purposes all four Parylene-N depositions seal the pores of the JSR. The intensity of Ps annihilating in the mesopores of the JSR (and its attendant lifetime which is ∼59 ns in pristine JSR 6103) are the critical parameters to indicate pore filling (or lining). The mesopore intensity is plotted in Figure 6.7 for the four different deposition depths. These depth profiles are generally similar in shape with a trend to lower mesopore intensity with increased Parylene-N thickness. Moreover, the

delayed onset for mesopore Ps intensity at low implantation (especially pronounced for the 30 nm deposition) suggests a solid Parylene-N layer has accumulated on the surface. Fitting for the micropores at 1.2 keV implantation on the 30 nm film yields results comparable to the 200 nm pure Parylene-N film - the surface is covered with at least 30 nm of Parylene-N. Hence we have upgraded our model of exponential Parylene-N penetration into the JSR 6103 to include a pure Parylene-N layer of adjustable thickness.

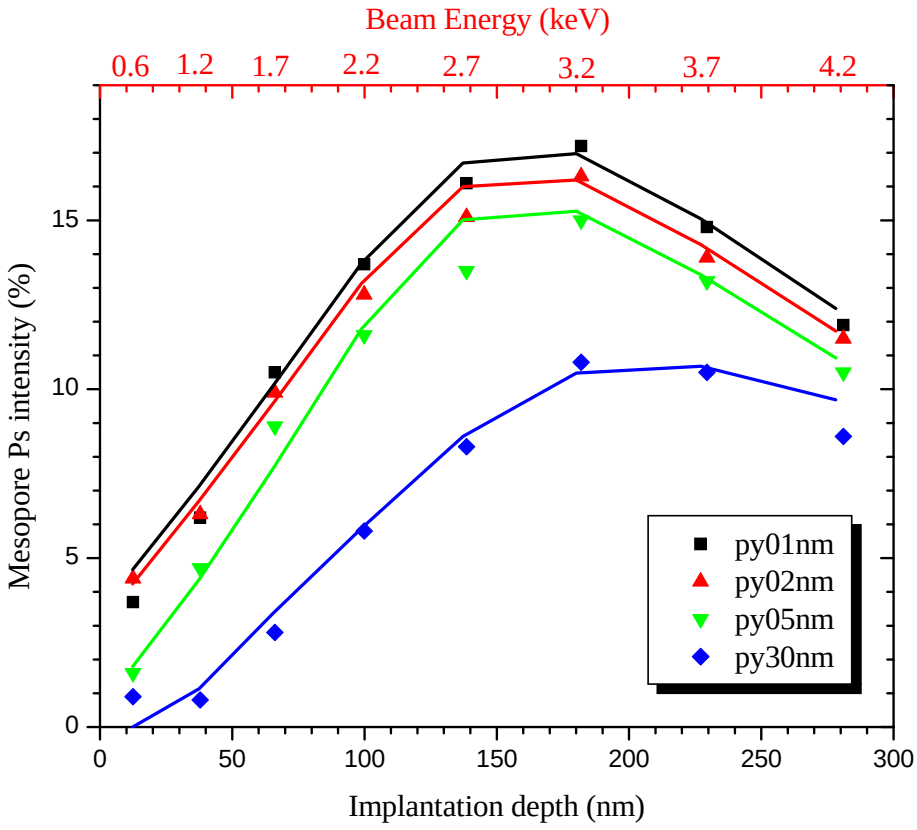


Figure 6.7: Total intensity of Ps in vacuum vs. the inverse of the positron beam energy and the fits from a modified exponential model.

Figure 6.7 also shows the model simulations superimposed on each data series. Some model parameters are constrained: the pristine JSR 6103 Ps mesopore intensity is set to 37%, which is measured on pure JSR 6103, the Parylene-N density is set to 1.1 g/cm$^3$ and the overlayer is set to be the deposition thickness of Parylene-N

(1, 2, 5, or 30 nm), the density of the JSR MSQ wall (matrix) is taken to be 1.6-1.7 g/cm$^3$, and the JSR film thickness is taken to be 300 nm (this thickness is strongly correlated with the MSQ wall density). The exponential penetration depth is taken to be $\beta$ and we do not require complete filling or extinction of the mesopore Ps at the surface. That is the role of the parameter $f(0)$, the filling/extinction fraction at the surface ($f(0)$=0 means no Parylene-N filling at all and $f(0)$=1.0 means that none of the JSR mesopores at the film surface are occupied with Ps. The fitting results are summarized in the table 6.5.

Table 6.5: **Modified exponential fitting results on different Parylene-sealed JSR samples at different Parylene-N thicknesses. The JSR mesopore intensity is fixed at 37%, the density of MSQ wall material is set as 1.65 g/cm$^3$ and the density of Parylene-N is set at 1.1 g/cm$^3$.**

| JSR sample | Parylene-N thickness | $\beta$ (nm) | $I_{meso}$ (%) | f(0) | t (nm) | $\rho_{MSQ}$ (cm/g$^3$) | $\rho_{Parylene-N}$ (cm/g$^3$) |
|---|---|---|---|---|---|---|---|
| LKD-6103 | 1nm | 189 | 37 | 0.85 | 1 | 1.65 | 1.1 |
| LKD-6103 | 2nm | 220 | 37 | 0.86 | 2 | 1.65 | 1.1 |
| LKD-6103 | 5nm | 221 | 37 | 0.92 | 5 | 1.65 | 1.1 |
| LKD-6103 | 30nm | 319 | 37 | 1 | 30 | 1.65 | 1.1 |
| LKD-5115 | 5nm | 233 | 37 | 0.85 | 5 | 1.65 | 1.1 |
| LKD-5109 | 5nm | 221 | 37 | 0.83 | 5 | 1.65 | 1.1 |

For 1 nm, 2 nm, and 5 nm of Parylene-N we typically fit $\beta$ close to 200 nm with slightly increasing $\beta$ (from 189 nm to 221 nm) and $f(0)$ (from 0.85 at 1 nm to about 0.92 at 5 nm). The effect of including the pure Parylene-N surface layer is insignificant — if this layer is fixed to be zero thickness (for the 30 nm Parylene-N deposited film) and the fitted value of $\beta$ drops only to 190 nm. This is the condition under which we fitted the 6 mTorr deposited 5 nm of Parylene-N film in the previous section (we determined $\beta$ = 180 nm). Hence, we see a moderate increase in $\beta$ when the deposition pressure is decreased from 6 mTorr to 2 mTorr. The RPI group also reports greater Parylene-N penetration at 2 mTorr as measured by NRA. For the 30 nm film we fit a higher value of $\beta$ = 319 nm and this increased penetration is

significant. The $f(0)$ is 1, which means not only the penetration depth is deeper but also almost no unfilled mesopores are left close to the sample surface. It might be surprising that additional penetration would occur after 5 nm Parylene-N deposition has effectively sealed and covered the film surface except that as long as $f(0)$ is less than 1, Parylene-N can still find routes to further diffuse deeper into the films.

In all four films we fit a mesopore Ps lifetime at low positron implantation energies that is markedly lower than the $\sim$59 ns measured for capped pristine JSR 6103. This is consistent with $f(0) < 1.0$ and, as the pore filling exponentially drops, the pores that do remain and can be populated with Ps have a pore size nominally reduced by Parylene-N lining/partial filling. For the 1 nm and 2 nm films the lifetimes are reduced at beam energies as high as 1.7 keV while for 5 nm and 30 nm only the 0.6 and 1.2 keV results are reduced. Hence, in the top 25-50 nm of the JSR film where there is heavy Parylene-N loading in the pores the few surviving pores are smaller and isolated/cutoff from the underlying pores. Once the Parylene-N loading with depth in the film falls below some critical concentration Ps is apparently able to diffuse through the interconnected pore network and access the pristine and interconnected JSR pores deeper in the film.

Is the 1 nm film really sealed? There is a hint that there might be 1-2% Ps escaping into vacuum since the mesopore intensity in figure 6.7 drops below the 2 nm curve at the lowest beam energy (whereas the 1 nm curve is everywhere else about 1% higher in intensity). This might be a sign that 1-2% Ps has escaped from the mesopores and disappeared into the vacuum component. We would see a 1-2% drop in mesopore Ps with a concomitant increase in the vacuum component. This is what we observe in figures 6.6 and 6.7. Hence the seal may not be perfect for the 1 nm deposition. The 1 nm sample has twice the backscattered Ps intensity as the 30 nm sample. This

could be due to the different relative contribution of backscattering from JSR 6103 and Parylene-N. The surface roughness is another factor that can also contribute to the overall differences since less Parylene-N can cause more uneven surfaces because of the really high porosity of 6103.

The above results for the 5 nm Parylene-N deposition on JSR 6103 can be compared with PALS results on two different JSR films with lower porosity and smaller pores. JSR 5109 has 39% porosity in pores of diameter around 3.3 nm while JSR 5115 has 33% porosity in pores of diameter of similar diameter. The mesopore lifetimes in both 5109 and 5115 at deep positron implantation are both fitted by PALS to be about 50 ns, which corresponds to an average cylindrical pore diameter of 2.8 nm compared with our value of 3.3 nm for 6103. In chapter 4, we have studied the 5109 and it is believed to be percolated, meaning that the pores are fully interconnected. Despite having smaller pores and less porosity the PALS results are very similar as can be seen in the table 6.5, where the fitted $\beta$ for these two films ranges from 200 nm - 225 nm. There is modest difference of $\beta$ observed for different JSR samples when comparing the first three 5nm Parylene-N sealed films. $\beta$ varies from 200nm to 225nm, when all the Ps intensity of JSR mesopores are set to be 37%. This number could be different for these three materials, although there is no drastic $\beta$ dependence on it within several percentages. At least from the Al capped versions of JSR 6103, 5109, and 5115, no dramatic Ps intensity difference was observed.

## 6.5 Conclusion and discussion

In conclusion, Parylene-N can effectively seal/fill the interconnected pores in the MSQ based ULK thin films, even with the thinnest (1 nm) Parylene-N deposition layer. However, it penetrates into the mesopore network quite deep and consequently

increases the effective $k$ value of the film. The PALS analysis results on the porous MSQ films are consistent with the Ar. DFT and EP results. As for micropores, the Ar. DFT shows no micropores at all within these porous MSQ samples, which is almost certainly wrong. The PALS results agree with the EP results on this issue.

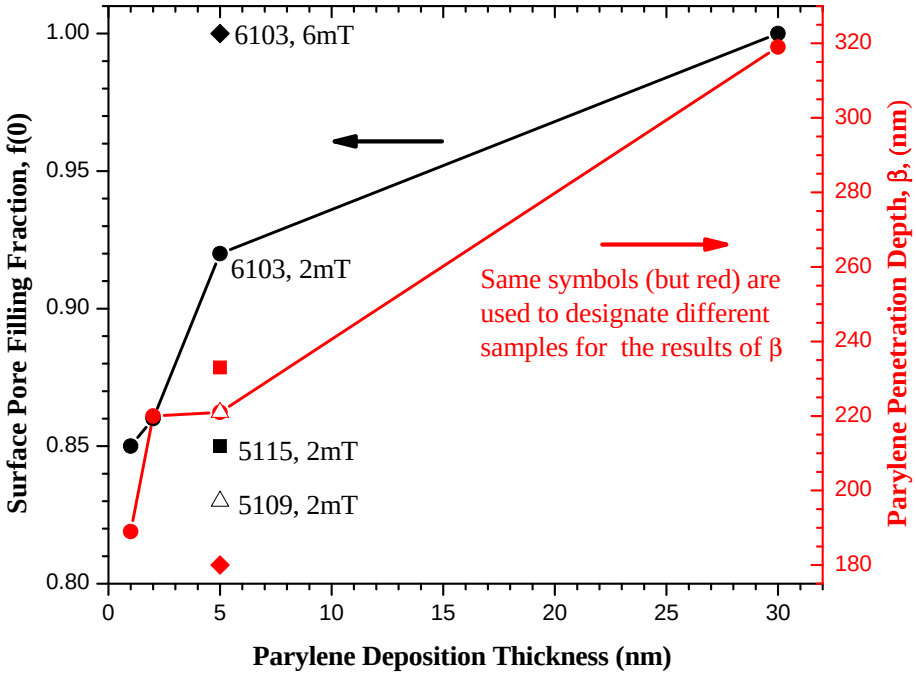


Figure 6.8: The Parylene-N surface filling fraction, $f(0)$ and penetration depth, $\beta$ vs. CVD Parylene-N deposition thickness. Fitting results for samples with Parylene-N deposited under different conditions are also shown.

It is inferred from the final $k$ value that the Parylene-N should be mainly lining/coating the mesopores, not completely filling the pores, which would give a much larger effective $k$ value with the long penetration depth of the Parylene-N. However, this is not conclusive and more experiments need to be conducted to understand this problem.

It has been shown by NRA experiments that the Parylene-N penetration depth also depends on various factors. We compared the fitting results based on the PALS experiments, and no huge effects on Parylene-N diffusion were observed by differen-

tiating the Parylene-N deposition conditions. As for the CVD Parylene-N deposition thickness, from 1 nm to 30 nm, the penetration depth only slightly increases from 189 nm at 1 nm to 221 nm at 5 nm; much bigger effect was observed at 30 nm, when the fitted penetration depth increases to 319 nm. Figure 6.8 shows composite results of both penetration depth and surface filling fractions by Parylene-N for different samples. The penetration depth, $\beta$, increases with deposition layer thickness. Meanwhile, the filling fraction, $f(0)$, also increases. Note that these are not strong correlations and might be significantly affected by the model and the choice of fitting parameters.

Fitting results for samples with Parylene-N deposited under different conditions are shown together in figure 6.8. Besides the deposition thickness effect, it seems that at higher deposition pressure (6 mT vs. 2 mT), the Parylene-N penetration depth is shorter (220 nm vs. 180 nm). This might be consistent with $\beta$ determined by competing effects of rapid Parylene-N deposition to seal the surface vs. Parylene-N diffusion rate into the films' interior. It is also conceivable that the porous MSQ samples themselves may change the fitted $\beta$. However, the three JSR samples we investigated are all highly interconnected and despite slightly different pore sizes, the Parylene-N is found to largely penetrate the entire film thicknesses. Samples with shorter pore interconnection length will be very useful in deducing this correlation in our future studies. It would be interesting to see if a host with significantly smaller PALS-deduced $L_{int}$ results in a correspondingly smaller value of $\beta$. If this is the case, then it would provide tangible evidence for the importance of keeping $L_{int}$ small in low-$k$ fabrication.

# CHAPTER VII

# Conclusions and future work

## 7.1 Summary of PALS studies on ULK thin films

With the exponential miniaturization [1] of integrated circuits the microelectronics industry will soon advance to the 30 nm generation and below where the reduction of resistive-capacitive (RC) delay will need to be predominated by the decrease of dielectric constant of the interlayer dielectric (ILD) materials. Porous ultralow-$k$ (ULK) materials with a $k$ value less than 2.5 [4] will be required to replace dense versions, while a high modulus/hardness, high stability, and a low coefficient of thermal expansion (CTE) should be retained. This scheduled transition into porous low-$k$ dielectrics in the next five years raises many integration and characterization challenges to the semiconductor industry. Specifically, novel nanopore characterization techniques, either for the pristine ULK thin films or for the process-induced pore structure changes, will become more and more important.

In this study, beam-based PALS with depth profiling capability has been demonstrated to be unique and advantageous in the nanopore characterization of very thin films. By linking the Ps annihilation lifetime directly to the size of the pore where the Ps annihilates using the extended Tao-Eldrup model, PALS can distinctly determine the nanopore size, which is also confirmed by other pore characterization

techniques. The implantation depth of the positrons is controllable by adjusting the beam energy, and thus the pore size at the corresponding depth can be deduced. By monitoring the Ps escape fraction using the various fitted Ps intensities at selected positron mean implantation depths, the pore interconnectivity can also be determined. In this work, we have systematically investigated the characteristics of a variety of nanoporous ULK thin films based on different pore forming mechanisms using beam-based PALS. The two important quantities, namely the the pore size (or MFP) and pore interconnection length, which together directly reflect the pore morphology, were deduced from the PALS analysis. This unique capability enables us to understand the key features of the pore structure and its evolution with porosity.

In chapter 3, the three distinct patterns of nanopore evolution are confirmed by the PALS results. Based on the same mCSSQ matrix, three types of porogens showed different self-assembly like behaviors due to their different porogen-porogen interactions. The combined determination of pore size and pore interconnection length successfully revealed the pore structure evolution.

The control of pore size and its interconnectivity in ULK thin films is a critical issue, especially in future technological nodes when the feature size scales down to 45 nm and less. It is believed that the final pore morphology is not only determined by porogen-porogen interactions, but also depends on specific porogen-matrix combinations. It was shown in chapter 4 that, utilizing the same porogen but different matrices, the porogen-induced pore sizes and interconnection lengths were quite different. These experiments were carried out in nucleation and growth systems (IBM's P12 as the pore generator), where the sequence and temperature of matrix condensation by cross-linking, matrix-porogen phase separation, and porogen degradation are crucial in determining the final pore size and its structure.

In order to examine this porogen/pore evolution according to the curing temperatures, *in-situ* heat treatments were carried out in our PALS apparatus. Hybrid (composite) samples with porogen molecules are studied and uniquely interesting results are found. In the thermal curing process, the condensation/cross-linking of the MSQ-based matrix and porogen degradation were observed, which were directly associated with the change of Ps intensities in different pore populations. Briefly, Ps tends to diffuse from smaller pores to larger pores; the specific micropore population (super micropore, or SMP) from the matrix material is observed with an increasing Ps intensity, which concomitantly "drains" the smaller micropores (UMP). The cross-linking process happens throughout the heating temperatures from 100°C to 450°C, notwithstanding the occurrence of the other important process - porogen degradation. At temperatures higher than 350°C, the long-lived Ps signal suddenly emerged, which is associated with mesopore formation. Severe Ps drainage effects were noticed from micropores to mesopores, and also from open interconnected mesopores to vacuum.

The porogen filling of the matrix intrinsic pores was also observed after spin-coating in the porogen-matrix composite film. Among the three matrix materials, OS1 was totally microporous, while OS2 and OS3 are mesoporous with different degrees of mesoporosity. In the slightly mesoporous matrix, OS2, the mesopores are totally filled by the P12 porogen at 17% porogen loading. In the highly mesoporous matrix, OS3, the P12 porogen can only partially fill the interconnected pore network at the same loading. Here the partial filling is distinguished by PALS as a complete filling of segments of the intrinsic pores, and not as a pore lining or pore size attenuation effect. Another interesting result is that the porogen molecules are not only filling/blocking the intrinsic mesopores in OS3, they also interact with the matrix

resins, optimized the packing of the resin particles at certain loadings; and the condensation of the matrix was observed after the porogen degradation. In the studies above, PALS is used as the primary characterization tool and its results were also compared with $N_2$ absorption data. These results are found to be very consistent.

In our studies, a variety of ULK nanoporous films have been investigated and certain similarities among these systems and their general properties were found to be interesting. The interconnection length in some systems can be fitted to a quadratic dependence on porosity with different fitting parameters. In an attempt to understand the percolation process associated with the porogen loading and aggregation in chapter 5, Monte Carlo simulations were carried out in a cubic lattice. The random generation of pores in a cubic lattice produced excellent agreement on MFP with the experimentally measured pore sizes (MFP) for the Samsung tCD system, which we expect to be a weakly interactive porogen. However, the porosity dependence of the geometrically-deduced average pore length from the simulation did not agree with the quadratic dependence of $L_{int}$ as determined by PALS. Porogen-porogen interactions that can enhance pore agglomeration play an important role in the early rise of the interconnection length in our experiments before percolation occurs. Although attractive forces were implemented in the simulations, it seemed that the percolation threshold can only be shifted, but the phase transition is still abrupt in a large enough lattice. This might be due to the quasi-dynamic feature of the simulation. A full dynamic simulation could be implemented, but is beyond the scope of this thesis.

A second conclusion from the simulation work has to do with the Ps diffusion length in the matrix material before it traps into the mesopores. It is found that, in several systems with varying pore sizes, this Ps diffusion length is quite consistent -

about 2 nm. The intensity of Ps annihilating in mesopores saturates with porosity much faster in systems with many smaller pores rather than that with fewer larger pores. This is a very reasonable result considering the wall thickness would be much thinner and the pore surface area higher in a system with small and scattered pores. Thus, the same 2 nm Ps diffusion length in the matrix would have much greater effect on the Ps intensity. The consistency of the Ps diffusion length in the chemically similar systems of varying pore structures indicates the possibility of an *absolute* porosity measure solely based on PALS parameters if the Ps diffusion length in the matrix is known *a priori* or can be determined experimentally. This is an exciting possibility since it has been a major drawback for PALS that a one-to-one projection cannot be drawn between the Ps intensity alone and porosity. Future experiments on Ps diffusion will be needed before we can come to a more definitive conclusion.

Investigations on the nanoporous ULK thin films with even lower $k$ values will increasingly rely on improved pore characterization techniques. Despite the continuing need for complementary absolute porosity calibration, PALS has been demonstrated to be a very useful and unique characterization technique in this particular field.

## 7.2 IC Integration processes that can accommodate low-$k$

It has been a persistent endeavor to fabricate an *integrable* ultra-low-$k$ ($k < 2.5$), or even extreme-low-$k$ ($k < 2.0$) material for the next several generations of microchips. The incorporation of nanopores unavoidably degrades the mechanical qualities of the ULK thin films. In spite of the optimization in pore size and its structure, more compromises and work-arounds must be carried out to accommodate these porous films. It has been mentioned in chapter 6, that pore sealing is one option to improve the film integrity at high porosities and it has been observed in

our experiments that the parylene-N deposition layer of only "1 nm" can effectively seal the interconnected pores. However, the penetration of parylene-N was found to be ∼200 nm deep and increased the effective $k$ value noticeably. Given the thickness of ILD thin films will be below 200 nm in the future sub-45nm generations, the depth of parylene-N penetration is quite significant. From the PALS analysis, the penetration depth of the deposition layer modestly depends on the initial conditions, such as the gas pressure and deposition thickness. Therefore, a critical issue for this type of pore sealing will be finding an effective way of controlling the intrusion depth of the sealing agent.

A number of approaches, in addition to the pore sealing approach, have been proposed to extend the downscaling to the 45 nm generation and beyond. UV curing and electron beam curing have been found to be effective methods to improve the mechanical properties of some ULK materials without increasing the effective $k$ values. Similar types of curing, e.g. energetic photon or electron bombardment, can also form better bonds in the low-$k$ material and enhance the cross-linking, consequently improving the mechanical prosperities of the ULK thin films.

In an effort to make ULK materials with less interconnectivity, porogen self-assembly and Di- or Tri-block copolymers are used to produce highly ordered nanopore structures. In the collaboration with SAIT, we have seen that the porogen template with hydrophilic/hydrophophobic domains can interact with the matrix precursor and solution to form ordered structures. These micellar domains are similar to the star-shaped porogen particles we have studied in chapter 4 (IBM PJB porogen). However, no dramatic lower pore connectivity has been observed in these films, and post fabrication treatments are still needed with these types of materials to remove shrinkage and increase strength.

Some novel integration modifications have been proposed by some researchers as well. Post integration porogen removal is a non-traditional approach to maintain the ULK integrity during the etching, ashing, copper deposition, and CMP processes. Before porogen degradation, the hybrid material is dense and compatible with the etching, ashing, and post treatment processes. There is no diffusion barrier needed for the copper deposition and the CMP process is also easier. However, to keep the porogen intact, the temperature during the integration must remain lower than the porogen degradation temperature, which is about 300°C to 350°C. Possibilities of residual porogen issues and film shrinkage after the porogen removal also need to be eliminated.

Nanoimprint lithography (NIL) has shown its potential to dramatically simplify the current integration processes and reduce the manufacturing costs. It uses a pre-trenched mold to transfer the desired pattern to the subject materials, which allows the replication of complex patterns and high patterning resolutions without photolithography, etching, and ashing. In recent years, many sub-10 nm feature sized devices have been successfully fabricated by NIL [107, 108]. The direct patterning of low-$k$ materials via NIL is also promising in the future technological generations. In an ongoing collaboration with NIST and Seoul National University, we have demonstrated using PALS and other complementary techniques that NIL can accommodate porous low-$k$ materials and preserve a high mode-replication fidelity [84]. We have also shown that this direct imprinting may also create self-sealing nanoporous low-$k$ patterns [86], which would be very advantageous in the future ULK applications.

## 7.3 Future work on ULK studies

*pore structure*

It has been demonstrated in chapter 3 and 4 that the interactions between porogens and matrix can dramatically affect the final pore morphology. PALS has shown its potential in characterizing certain dynamic features during the pore formation process, such as micropore formation and porogen degradation signaled by the Ps intensity changes corresponding to the specific Ps lifetimes. However, the detailed mechanism of nanopore formation is still not fully understood, specifically in the nucleation and growth system, where the nanopore size can be affected by a number of factors. PALS has shown the unique capability of probing the pore morphological evolution associated with porogen loading, porogen-porogen interactions, and curing temperature. In addition, variations in the matrix condensation/cross-linking process, the porogen-matrix microphase separation process, the matrix precursor molecular weight and chemistry, and the thermal curing ramping rate are all potentially critical factors in nanopore structural evolution that still need further investigation.

*absolute porosity*

Another important but unsolved question is: can PALS measure absolute porosity. The Ps formation intensity, which has been used as an important indicator of the relative porosity and its evolution, is still not fully understood. The Monte Carlo simulation of Ps diffusion in the matrix has shown some promising results. The fitting results from the simulations are more reliable in the samples with slowly rising Ps intensity as a function of porosity. When the Ps intensity saturates quickly, the diffusion length is largely determined by one single Ps intensity value at the lowest porosity. In order to obtain more reliable results, more ultra-low-*porosity* ($<5\%$) films are needed to study these fast-saturating samples. In this study, the MSQ-based films are only moderately different, in the sense that the matrix materials are chemically similar although the mesopores are formed by quite different porogens. A

wider range of samples may tell us more about Ps diffusion in various microporous materials. In cases when it is impractical to measure the Ps diffusion length, the absolute porosity calibration of Ps intensity using an independent technique is still useful as a future calibration of porosity using Ps intensity.

*pore interconnection length*

The Monte Carlo simulations of the pore interconnection length did not satisfactorily reproduce the PALS-deduced experimental results. Fully dynamic modeling with porogen-porogen interactions might obtain the desired consistency between the experiments and simulation. However, without complete knowledge of the porogen-porogen and porogen-matrix interactions, it is difficult to make any predictions on pore size and its structure of nanoporous materials. For Ps diffusion, only the Ps diffusion in the matrix has been considered. All the Ps that diffuse into open mesopores are assumed to consequently diffuse into vacuum, which is true for very thin films. It would be intriguing to simulate the whole Ps diffusion behavior, both in micropores and mesopores. From a simple 1-dimensional Monte Carlo simulation, the fraction of Ps that can escape a film surface depends on the Ps starting depth exponentially. The e-folding length of the exponential relation depends on the annihilation probability during each Ps collision with the wall material, the Ps lifetime, and its velocity. We would have a similar relationship between the Ps escape fraction into vacuum and its starting depth in the 3-D lattice. The pore structure will also affect the Ps escape fraction, as well as the deduced interconnection length, $L_{int}$ using $F_{esc}$. Simulations of this magnitude are beyond the scope of this experimental thesis.

*pore filling*

It has been observed by PALS that a pore filling agent, either from a deposition process (parylene-N) or from nanocomposite mixing at the solution phase (porogen),

can coat or fill the pores of the pristine porous materials and alter their characteristics. Actually, this pore-filling or pore-lining problem epitomizes a much more general topic, which indicates many possible applications of PALS. The broader significance of this particular application is twofold: 1) enhanced understanding of how pore structure directly impacts material performance; and 2) improved interpretation of the PALS-deduced pore characterization parameters under systematically controlled processing of a broad array of model systems. In the first case, we certainly expect pore structure to impact pore sealing performance. In a broader sense, for example, the P12 porogen filling of the intrinsic pores of the OS2 and OS3 matrices demonstrated more details of the porogen-matrix interaction and also affect the final pore structure via this interaction. Furthermore, this kind of characterization can also be applied to a wider range of permeable materials, such as the gas adsorption/desorption properties in selectable porous membranes [23], drug delivery from microporous drug-eluting materials, water absorption in polymer and nanocomposite materials, and selective molecule adsorption/desorption in highly porous metal-organic frameworks [109] or silica gels. Based on the characteristics of the specific adsorbates and the varying pristine porous materials, the "action" of pore filling and reappearance can be more thoroughly investigated by PALS and a deeper understanding of these materials may be obtained. As to the second point mentioned above, we note that there is no standardized method of thin film pore characterization. Any opportunity to sharpen one's interpretation of PALS results is very significant to our fundamental understanding of PALS. One example is the interpretation of $L_{int}$ (based on Ps diffusion) as a measure of pore interconnectivity. In chapter 6, PALS was used to characterize the parylene-N penetration (pore-lining) depth into different intrinsically porous ULK materials under different deposition

conditions. This is potentially useful to calibrate the PALS deduced pore interconnection length with the actual adsorbate penetration depth since the parylene-N diffusion should be directly related to the pore interconnectivity of the ULK thin films. The PALS-deduced $L_{int}$ depends on Ps diffusion and may not be one-to-one related with parylene-N penetration and diffusion. It would be very interesting to study parylene-N penetration and pore sealing in a porous film with $L_{int}$ $\sim$50-75 nm to see if parylene-N penetration is similarly curtailed. Furthermore, by altering only the surface chemistry of the pore walls, many fundamental issues can be addressed such as the Ps formation, Ps intensity, and Ps lifetime in identically shaped nanopores with different wall surface conditions.

*integration damage*

There has been a great deal of research done on ULK integration damage, including nanopore collapse and film shrinkage due to the etching, ashing, plasma treatment, and the subsequent cleaning processes. The vulnerability of nanoporous low-$k$ materials due to these treatments has been demonstrated by PALS more severe for higher porosity films [110]. The compatibility of specific cleaning mixtures with pore structures of ULK materials has also been investigated by PALS [111]. PALS has played and should continue to play an important role in these types of applications. Moreover, the application of PALS is not limited to the microelectronics industry; any material for which nanopore structure can influence its properties can be a potential application for PALS.

*PALS improvements*

Researchers have been continuously working to improve the PALS technique to deliver a broader impact in the development of nanoporous thin films, and from the beginning of the availability of low energy positron beams ($\sim$1980's), the need

for more intense positron beams has been universal. A new intense positron beam facility is under construction at the North Carolina State University Nuclear Reactor [112] through an NSF-funded collaboration between NCSU, the University of Michigan and Oak Ridge National Lab. It is based on pair production in the intense gamma flux near the reactor core and first measurements (fall 2007) of the slow positron beam rate emerging from the core are $5\times10^{8}$ $e^{+}$/s. After two-stages of moderation that improve the brightness of the beam at the expense of rate, the delivered rate at the end of the UM-designed spectrometer is expected to be several million positrons $s^{-1}$. This intense positron beam with depth-profiling PALS/PAS capability will shorten the nominal one hour runs to accumulate one million detected events in the typical lab-scale beam used in this thesis to less than one minute. It will provide fast, convenient, and inexpensive access to PALS characterization for academic and industrial research. With this *bright* future for PALS/PAS the many future applications left undone in this thesis should come to fruition.

# APPENDICES

# APPENDIX A

# Abbreviations

| | |
|---|---|
| ACAR | angular correlation of annihilation radiation |
| BET | Brunauer-Emmett-Teller |
| BMG | bulk metallic glass |
| CA | calix-arene |
| CD | cyclodextrin |
| CEMA | channel electron multiple array |
| CF | critical force |
| CMP | chemical mechanical polishing |
| CSSQ | cyclic silsesquioxane |
| CTE | coefficient of thermal expansion |
| CVD | chemical vapor deposition |
| DBS | Doppler broadening spectroscopy |
| DFT | density functional theory |
| ELK | extreme low-*k* |
| EP | ellipsometric porosimetry |
| FSG | fluorinated silicate glass |
| FWHM | full width at half-maximum |
| HSQ | Hydrogen Silsesquioxane |
| HSSQ | Hydrogen Silsesquioxane |
| IC | integrated circuit |
| ILD | interlayer dielectric |
| IMD | intermetal dielectric |
| ITRS | International Technology Roadmap for Semiconductors |
| IUPAC | International Union for Pure and Applied Chemistry |
| $L_{int}$ | interconnection length |
| LINAC | linear particle accelerator |
| L.L. | Lorentz-Lorenz |
| LSI | large scale integrated |
| mCSSQ | modified cyclic SSQ |
| MFP | mean free path |
| MSQ | methyl-silsesquioxane |
| MSSQ | methyl-silsesquioxane |
| MTMS | methyltrimethoxysilane |
| NIL | nanoimprint lithography |
| N&G | nucleation and growth |
| NP | neutron porosimetry |
| NRA | nuclear reaction analysis |
| o-Ps | ortho-positronium |
| OSG | organosilicate glass |
| PALS | positron/positronium annihilation lifetime spectroscopy |
| PAS | positron annihilation spectroscopy |
| PECVD | plasma enhanced chemical vapor deposition |
| PEO | polyethylene oxide |
| PGMEA | propylene glycol methyl ether acetate |
| p-Ps | para-positronium |
| Ps | positronium |
| PSD | pore size distribution |
| RC delay | resistive-capacitive delay |
| R.I. | refractive index |
| RT | room temperature |
| RTE model | rectangular Tao-Eldrup model |
| SAIT | Samsung advanced institute of technology |
| SANS | small angle neutron scattering |
| SAXS | small angle X-ray scattering |
| sCD | Heptakis(3-O-methyl-tetradecakis-2,5-di-O-[3-(trimethoxysilyl)propyl]-β-cyclodextrin |
| SOD | spin-on dielectric |
| SMP | super-micropore |
| SXR | specular X-ray reflectivity |
| SSQ | silsesquioxane |
| tCD | Heptakis(2,3,6-tri-O-methyl)-β-cyclodextrin |
| TDC | time-to-digital converter |
| TE model | Tao-Eldrup model |
| TEM | transmission electron microscopy |
| TEOS | Tetraethylorthosilicate |
| ULK | ultra low-*k* |
| ULSI | ultra-large-scale integration |
| UMP | ultra-micropore |
| VLSI | very large-scale integration |
| XRP | X-ray porosimetry |

# APPENDIX B

# $3\gamma/2\gamma$ detection efficiency

## B.1 Theory

Because $3\gamma$ events originating from intrinsic o-Ps annihilation have a higher probability to be detected than the $2\gamma$ events, we need to determine the efficiency ratio of these two types of events in order to meaningfully compare relative Ps intensities from different Ps lifetimes. The detection efficiency $\varepsilon$ is simply the fraction of detected annihilation radiation events out of the total number of events. We can define the detection efficiency of $3\gamma$ events, $\varepsilon_{3\gamma}$, as the fraction of detected $3\gamma$ events out of total $3\gamma$ events; the detection efficiency of $2\gamma$ events, $\varepsilon_{2\gamma}$ can be defined similarly. We can write $\overline{\varepsilon} = f \cdot \varepsilon_{3\gamma} + (1-f)\varepsilon_{2\gamma}$, where $\overline{\varepsilon}$ is the average detection efficiency. $f$ is the fraction of $3\gamma$ decay events; the $(1-f)$ is the fraction of $2\gamma$ decays. However, $f$ cannot be observed directly since the plastic scintillator cannot distinguish $3\gamma$ photons from $2\gamma$ events. What is actually observed is a mixture of $3\gamma$ and $2\gamma$ events. The $3\gamma$ intensity observed at its face value is $f_{obs}$, and it follows the relationship: $f_{obs} \cdot \overline{\varepsilon} = f \cdot \varepsilon_{3\gamma}$. The two equations above combined give the ratio $\varepsilon_{3\gamma}/\varepsilon_{2\gamma}$ as

$$\frac{\varepsilon_{3\gamma}}{\varepsilon_{2\gamma}} = \frac{f_{obs}}{f_{obs} - 1 + \varepsilon_{2\gamma}/\overline{\varepsilon}}. \tag{B.1}$$

## B.2 experiment and results

In order to measure the differential detection ratio, two types of thin film samples are used. The first kind is highly porous material that can form plenty of Ps (25-50%). With the high Ps formation fraction and highly interconnected pore structure, most of the Ps can diffuse into vacuum and annihilate solely in the $3\gamma$ mode. JSR, OS1/PJB, XLK and PNNL are all in this category. The other type is a dense material that only presents direct positron annihilation or p-Ps annihilation, which only produce $2\gamma$ decays. The silicon substrate and a SAIT matrix (a dense MSQ material) are used for this purpose. The two types (porous and dense) of materials are used in pairs to compare their rates difference, subsequently deducing the $3\gamma/2\gamma$ ratio. Several beam energies are used to see if there is any energy dependence for the $3\gamma/2\gamma$ ratio.

We define $R_{coin}$, $R_{start}$ and $R_{stop}$ as the coincident rate, start rate and stop rate respectively. Whenever the CEMA detects a signal that comes from the secondary electrons, the event is recorded as a start signal. Whenever a $\gamma$ decay is detected by one of the photo tubes, a stop signal is recorded. If the start and stop events are both observed (the time window is set to 1 $\mu$s), this start-stop pair is counted as a coincident event. If positrons in a specific material, such as silicon, only annihilate into $2\gamma$'s, it is straightforward to define the effective $\gamma$ detection efficiency as $\varepsilon_{2\gamma} = R_{coin}/R_{start}$, where the rates are all corrected by subtracting off the background noise. On the other hand, in porous materials, such as JSR, positrons annihilate into both $3\gamma$ and $2\gamma$ events, and from the $R_{coin}$ and $R_{start}$ we can only determine the combined detection efficiency, $\overline{\varepsilon} = R_{coin}/R_{start}$. By fitting the spectrum, we can deduce the Ps intensity from vacuum and mesopores. Note that the Ps vacuum

intensity is solely $3\gamma$ events, but the Ps mesopore intensity has some fraction of $3\gamma$ events. This fraction can be estimated by $\tau_{meso}/\tau_{vacuum}$. Then the total observed $3\gamma$ fraction $f_{obs}$ is the sum of the Ps vacuum intensity and the contribution from Ps mesopore intensity. From equation B.1, it is clear that by using the selected pair of samples, one measures $\varepsilon_{2\gamma}$ or $\overline{\varepsilon}$ directly from these two samples, which can determine the $3\gamma/2\gamma$ detection efficiency ratio.

Table B.1: **Rates and calculation summary of the uncapped films.**

| Energy (keV) | Sample | $R_{start}$ ($s^{-1}$)* | $R_{stop}$ ($s^{-1}$)* | $R_{coin}$ ($s^{-1}$)* | $\overline{\varepsilon}$(JSR) or $\varepsilon_{2\gamma}$(Si) (%) | $f_{obs}$ | $\varepsilon_{3\gamma}/\varepsilon_{2\gamma}$ | $\varepsilon_{3\gamma}/\varepsilon_{2\gamma}$‡ |
|---|---|---|---|---|---|---|---|---|
| 0.55 | JSR | 14625 | 2220 | 1246 | 8.517 | 44.5 | 1.209 | 1.168 |
| | Si | 8545 | 2078 | 672 | 7.863 | | | |
| 1.2 | JSR | 15630 | 2905 | 1334 | 8.538 | 48.5 | 1.228 | 1.229 |
| | Si | 7907 | 2642 | 614 | 7.762 | | | |
| 2.2 | JSR | 14888 | 3843 | 1245 | 8.362 | 42.0 | 1.225 | 1.245 |
| | Si | 7594 | 3525 | 586 | 7.717 | | | |
| 3.2 | JSR | 12491 | 4286 | 1020 | 8.166 | 35.4 | 1.169 | 1.217 |
| | Si | 6634 | 4015 | 514 | 7.748 | | | |
| 3.2 | JSR | 11639 | 3957 | 950 | 8.162 | 35.2 | 1.172 | 1.206 |
| | SAIT | 10115 | 3719 | 783 | 7.743 | | | |
| 3.2 (digi)† | JSR | 11670 | / | 950 | 8.141 | 35.1 | 1.174 | / |
| | SAIT | 10158 | / | 784 | 7.718 | | | |
| 4.2 | JSR | 10632 | 4481 | 858 | 8.073 | 30.4 | 1.126 | 1.205 |
| | Si | 5580 | 4249 | 435 | 7.792 | | | |
| 4.2 | JSR | 10115 | 4286 | 822 | 8.124 | 29.7 | 1.152 | 1.187 |
| | SAIT | 8799 | 4086 | 687 | 7.808 | | | |
| 4.2 (digi)† | JSR | 10138 | / | 822 | 8.108 | 29.7 | 1.171 | / |
| | SAIT | 8832 | / | 685 | 7.756 | | | |
| 4.2† (digi) | JSR | 10313 | / | 838 | 8.126 | 29.7 | 1.152 | / |
| | SAIT | 8953 | / | 699 | 7.808 | | | |

**The rates are converted from 100s continuous runs of the beam, and averaged for several runs.*
*‡These results are calculated directly from the ratio of stop rates.*
*†(digi) means the rate are read from the digitizer. The digitizer only shows the coincident rate.*

Table B.1 shows the beam rates, $R_{start}$,$R_{stop}$ and $R_{coin}$ at different beam energies of several sample pairs, and all the rates come from several consecutive 100 seconds runs. The background noise has been subtracted from the rates. $f_{obs}$ is the sum of

vacuum Ps intensity and the $3\gamma$ part of the mesopore intensity, which is deduced from discrete lifetime fitting. The ratio $\overline{\varepsilon}/\varepsilon_{2\gamma}$ can be determined through $R_{coin}/R_{start}$, or directly from the ratio of stop rates. The results of the detection efficiency ratio $\varepsilon_{3\gamma}/\varepsilon_{2\gamma}$ through both methods are listed in the table. This number varies from 1.13 to 1.23 in the method one and varies from 1.17 to 1.25 from the second method. It is found that the statistical error is small compared with the results variations and systematic errors. There might be a trend associated with beam energy is noticeable, however weakened by some fluctuations. One assumption is that at lower energies more Ps can escape backwards from the sample surface to the detectors because all the samples are uncapped. Those Ps finally annihilate inside the vacuum closer to the detectors, thus increase the $3\gamma$ detection efficiency even more.

Because the variations of $3\gamma/2\gamma$ ratio from the beam energy may come from the annihilation position, experiments of position dependence are carried out. It is found that the position dependence of the detection efficiency is important and should not be neglected. In Table B.2, $R_{start}$, $R_{stop}$ and $R_{coin}$ are recorded at different sample positions. It is shown that a one millimeter change in position can cause a 2%-6% difference in rates.

Table B.2: **Position dependence of the rate on sample SAIT matrix at 5.0 keV. The position in millimeters is the readings of one of the horizontal manipulators with the others fixed.**

| Sample Position (mm) | $R_{start}$ ($s^{-1}$) | $R_{stop}$ ($s^{-1}$) | $R_{coin}$ ($s^{-1}$)* |
|---|---|---|---|
| 11.04 | 7852 | 4101 | 643 |
| 10.54 | 7672 | 4061 | 623 |
| 10.04 | 7546 | 4024 | 606 |

**The coincident rates have not been corrected by subtracting the noise.*

Because we calculate the detection efficiencies directly using the data acquisition rates, it is important to examine how this sample position dependence may affect the $3\gamma/2\gamma$ results. From all the rates and positions, it is found that their relationship is

quite close to linear, and we can actually correct the rates to the same positions. At the same time, Ps may annihilate outside of the interconnected films. The effects are already shown in table B.1. Therefore, we use capped samples to confine all the Ps inside the film and can use the sample position to correct for the rates. In table B.3, for every sample pair, the rates of Silicon/Matrix are corrected by their positions, according to the other porous samples' position. The values of $3\gamma/2\gamma$ after correction are given in the table for closed samples.

Table B.3: $3\gamma/2\gamma$ **detection efficiency ratio of closed samples with sample positions adjusted to the same.**

| Sample | $R_{start}$ (/s) | $R_{stop}$ ($s^{-1}$) | $R_{coin}$ ($s^{-1}$) | $\bar{\varepsilon}/\varepsilon_{2\gamma}$ | $\varepsilon_{3\gamma}/\varepsilon_{2\gamma}$ |
|---|---|---|---|---|---|
| OS1/PJB | 6194 | 4107 | 482 | 1.018 | 1.18 |
| Matrix | 7585 | 4036 | 580 | | |
| XLK | 6337 | 4182 | 500 | 1.018 | 1.22 |
| Matrix | 7837 | 4098 | 609 | | |
| PNNL | 6110 | 4140 | 476 | 1.009 | 1.12 |
| Matrix | 7780 | 4085 | 603 | | |

The $3\gamma/2\gamma$ detection efficiency ratio shown in table B.3 varies from 1.12 to 1.22, which is a fairly large variation. It seems that there might still be some other systematic errors affecting the ratio, which may be related to the counting or timing system. The position variation and energy variation are larger than statistical uncertainties, although they may be at the same order with some other unknown uncertainties. We can use the overall average correction of Ps vacuum intensity, which would be around 1.2, to compensate the higher detection efficiency for vacuum Ps annihilation events. The energy and position dependence are small (<7% effect) and will be ignored in the routine analysis. The correction on Ps mesopore intensities can be estimated by the ratio of mesopore lifetime versus vacuum lifetime 142ns. They are normally small corrections and are not routinely done unless the mesopore lifetime is large and comparable to 142ns.

# APPENDIX C

# Bulk metallic glass

APPLIED PHYSICS LETTERS **91**, 261908 (2007)

# Characterization of fatigue-induced free volume changes in a bulk metallic glass using positron annihilation spectroscopy

R. S. Vallery, M. Liu, and D. W. Gidley
*Department of Physics, University of Michigan, Randall Laboratory, Ann Arbor, Michigan 48109, USA*

M. E. Launey[a] and J. J. Kruzic[b]
*Materials Science, School of Mechanical, Industrial, and Manufacturing Engineering, Oregon State University, Corvallis, Oregon 97331, USA*

(Received 23 August 2007; accepted 27 November 2007; published online 26 December 2007)

Depth-profiled Doppler broadening spectroscopy of positron annihilation on the cyclic fatigue-induced fracture surfaces of three amorphous $Zr_{44}Ti_{11}Ni_{10}Cu_{10}Be_{25}$ metallic glass specimens reveals the presence of a 30–50 nm layer of increased free volume that is generated by the propagating fatigue crack tip. The presence and character of this *fatigue transformation zone* is independent of the initial amount of bulk free volume, which was varied by structural relaxation via annealing, and the voids generated in the zone by intense cyclic deformation are distinct from those typical of the bulk. © *2007 American Institute of Physics*. [DOI: 10.1063/1.2825427]

Bulk metallic glasses (BMGs) have a wide array of attractive properties for structural applications, including high specific strength combined with good corrosion resistance, low damping, large elastic strain limits, and the ability to precisely process into complex geometries in a highly efficient manner.[1,2] Although metallic glasses do not have a traditional microstructure like their crystalline counterparts, other structural features can strongly affect their mechanical behavior. A review of the structural aspects of BMGs may be found in Ref. 3, and it is well known that the deformation of metallic glasses requires extra "free" volume relative to a fully dense glass that allows physical space for atomic movement under mechanical loading.[4] Accordingly, the amount of free volume affects the mechanical properties of bulk metallic glasses,[5–7] and recent studies have demonstrated a pronounced effect on the fatigue life.[8,9] Current research efforts are focused on understanding this latter effect by studying the fatigue crack growth properties, which surprisingly have been found to be largely *unaffected* by bulk free volume differences in the absence of hydrogen.[9]

Noting that the free volume increases in shear bands during inhomogeneous flow of metallic glasses,[4] it may be expected that the intense deformation near a fatigue crack tip will generate a *local* increase in free volume that determines the local flow properties, rendering fatigue crack growth behavior relatively insensitive to bulk free volume differences. Accordingly, spatially resolved characterization of free volume differences in BMGs is paramount if one wants to fundamentally understand the mechanisms controlling fatigue failure. Positron annihilation spectroscopy (PAS) has been used to qualitatively assess bulk (spatially unresolved) structural changes associated with sub-$T_g$ annealing,[10,11] plastic deformation,[12,13] and cooling rate variations.[14] In this work, we utilize depth-profiled PAS, which uses a focused beam of positrons to examine spatial variations in free volume on the scale needed to study the deformation associated with fatigue-induced cracks in BMGs.

Doppler broadening spectroscopy (DBS) of positron annihilation is a standard PAS technique to characterize open volume defects in materials (e.g., vacancies in crystals and packing defects in polymers).[15] Positron beams with variable low positron implantation energies are also widely used to depth profile near sample surfaces where significant deviations from bulk behavior occur.[15] In the present experiments, a focused positron beam spot of $<2$ mm diameter was used to depth profile and compare both the cyclically deformed fracture surfaces and the undeformed (polished) faces of three fully amorphous $Zr_{44}Ti_{11}Ni_{10}Cu_{10}Be_{25}$ compact tension $C(T)$ specimens (2.2 mm thick). In addition, positron annihilation lifetime spectroscopy (PALS) was performed on the undeformed bulk by depositing $^{22}$Na positron source between two identical samples. The three samples are discussed in detail elsewhere,[9] but briefly, one sample was isothermally relaxed at 610 K for $10\tau$, where $\tau$ represents the structural relaxation time ($\tau$=438 s at 610 K).[16] After annealing for $10\tau$, the BMG was confirmed to be fully amorphous by high resolution transmission electron microscopy and is assumed to be fully relaxed into its metastable equilibrium, or lowest free volume state with a normalized free volume difference relative to the original as cast state $\Delta\nu_f/\nu_m$ of 0.044%.[16] Here, $\Delta\nu_f$ is the average free volume difference per atom and $\nu_m$ is the atomic volume near the liquidus.[17] A residual stress relief annealing treatment (573 K for 2 min) was applied to the second sample [stress relieved (SR)] but, unlike the $10\tau$ sample, no free volume relaxation occurred at the low temperature and short time, as confirmed by differential scanning calorimetry (DSC) experiments.[9] A third sample was studied in its as-cast condition without stress relief or relaxation. Fatigue crack growth experiments were conducted in general accordance with ASTM standard E647 (Ref. 18) using a computer controlled servohydraulic test machine, 25 Hz sine wave cyclic loading, and a load ratio, the ratio of minimum to maximum applied load, of $R$=0.1. Using depth-profiled DBS, free volume was characterized on the cyclically deformed fracture surface where the

[a]Present address: Materials Sciences Division, Lawrence Berkeley National Laboratory, Berkeley, CA 94720, USA.
[b]Author to whom correspondence should be addressed. Tel.: +1-541-737-7027. FAX: +1-541-737-2600. Electronic mail: jamie.kruzic@oregonstate.edu.

 

applied stress intensity range was $\Delta K \approx 1.5$ MPa$\sqrt{m}$,[19] a value near the fatigue threshold.

A series of positron beam implantation energies ranging from 1.1 to 8.0 keV was used in the depth-profiled DBS experiments. The corresponding mean implantation depths of the positrons into the metallic glass (density ~6 g/cm$^3$) varied from less than 10 to 190 nm. The undeformed faces and the fracture surfaces of the three samples were all depth profiled. For each sample, the two fractured edges were stacked side by side with their corresponding surfaces aligned to give a total width of 4.4 mm, ensuring that no positrons missed the fracture surface. The 511 keV annihilation photopeak in the energy spectrum of a high purity Ge gamma detector was fitted to two Gaussian functions and a step-changing background, and the *S* parameter was defined as the fraction of all 511 keV events within a central region of ±0.88 keV from the peak.

The *S* parameter at deepest implantation on each undeformed face (0.522–0.526) is assumed to be the *bulk S* for each sample. For the fatigue fracture surface, the *S* parameter shows a significant depth-dependent deviation from the bulk *S* that is much stronger than the rather superficial effect on the polished (undeformed) surfaces (Fig. 1). All three samples, regardless of stress relief or structural relaxation, exhibit higher *S* parameters near the fatigue-cracked surface. At the lowest positron depth, an ubiquitous drop in *S* parameter is commonly attributed to positron diffusion back to and annihilation from a surface state. At the higher implantation depths up to 190 nm, *S* asymptotically approaches the bulk value. These *S* parameter profiles into the fracture surface are consistent with a thin surface layer of enhanced free volume generated by the intense deformation of the propagating crack.

Increased *S* parameter typically means that fewer positrons annihilate with high-momentum core electrons, suggesting that there are more open-volume (free volume) defects in the surface layer. However, all three samples have the same bulk *S* parameter despite the fact that the bulk free volume determined by DSC is distinctly lower for the long-relaxed $10\tau$ sample.[9,16] Thus, DBS is evidently not sensitive to the typical free volume changes from structural relaxation observed by DSC. This is also true for the bulk positron lifetime, a measure of the average void size. As shown in the insets of Fig. 1, PALS indicates no statistically significant difference in the positron lifetime between the $10\tau$ and the SR samples, while an increased positron lifetime (~1.5 ps) was found for the as-cast sample. Such results are similar to Nagel and co-workers,[10,11] who found a decrease of several picoseconds in the positron lifetime upon heating through the 100–200 °C range. In both cases, the decreased lifetime is not due to free volume reduction by structural relaxation (long time scale relaxation) since (1) DSC studies on the kinetics of the Zr–Ti–Cu–Ni–Be amorphous system have shown that free volume reduction by structural relaxation cannot occur at temperatures below 200 °C in readily achievable annealing times,[16,20] and (2) there is no free volume difference between the as-cast and SR samples with shorter positron lifetime.[9] All this implies that the definite increase in *S* within the fatigue fracture surface layers indicates that those regions have voids/defects that are different in nature to the free volume defects associated with structural relaxation in the undeformed bulk. This is consistent with recent PAS results that suggest that the size distribution of the free volume elements is bi- or trimodal, and that defects of a specific size range, denoted as flow defects, are predominantly produced during deformation.[13,21]

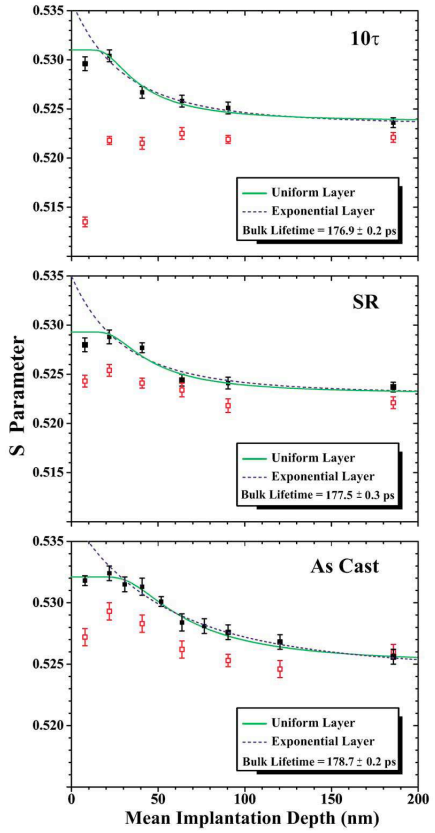


FIG. 1. (Color online) Depth-profiled Doppler broadening spectroscopy *S* parameter results for the $10\tau$, stress relieved (SR), and as cast samples. The *S*-parameter near the fatigue-fractured surface (solid symbols) is significantly larger than *S* for the undeformed face (open symbols) at equivalent depth. Fits of the depth profiles to simple models of *S* parameter depth dependence (uniform *S* layer—solid line and exponentially decreasing *S*—dashed line) are shown.

The fracture surface *S* profiles in Fig. 1 can be fitted using simple models of how the *S* parameter might depend on depth. The solid curve uses a two-layer model with a uniformly deformed surface layer of thickness *t* which has a constant *S* (~0.531) on top of an infinite layer with the bulk *S* value. The second model (dashed curve) has *S* decaying exponentially in depth from some high value at the surface to the bulk value. Both models give indistinguishably good fits with a layer thickness or exponential depth of 30–35 nm for both the $10\tau$ and SR samples, and 50 nm for the as-cast material.

The 30–50 nm depth of this layer corresponds well with the expected extent of plastic deformation due to the fatigue cycling. For plane strain conditions, the overall plastic zone extent normal to the crack plane (i.e., into the fracture surface) is three times the extent in the direction ahead of the crack tip, i.e.,[22]

$$r_p = \frac{1}{2\pi}\left(\frac{K}{\sigma_Y}\right)^2, \quad (1)$$

where $K$ is the maximum stress intensity of the loading cycle ($\sim 1.67$ MPa$\sqrt{m}$) and $\sigma_Y$ is the yield stress of the material ($\sim 1900$ MPa),[23] giving a value of 122 nm. Furthermore, during cyclic loading there is a smaller *cyclic* plastic zone where reversed plastic flow occurs each cycle. It is generally accepted that this cyclic plastic zone is roughly $\frac{1}{4}$ the total plastic zone size,[24] or in this case 31 nm, corresponding well with the depth-profiled DBS results. Thus, it appears that fatigue cycling induces a *fatigue transformation zone* ahead of the crack tip that has distinctly higher free volume than the bulk. The fatigue crack then propagates through this zone of higher free volume which appears to dominate the local flow behavior based on the insensitivity of fatigue crack growth rates to free volume reduction by structural relaxation.

In conclusion, depth-profiled DBS has been used to demonstrate the presence of a fatigue transformation zone of higher free volume that is generated by the propagating crack tip. All three samples, regardless of bulk free volume differences due to different structural relaxations, present similar surface layers of increased free volume that is qualitatively different from that of the bulk. Comparison of the measured transformation zone size to the deduced cyclic fatigue plastic zone size show these both occur on the same size scale. This localized transformation zone provides a structural basis to support the surprising findings[9] that fatigue crack growth propagation is largely unaffected by bulk free volume differences.

The Michigan Positron Group gratefully recognizes the assistance of Ross Smith and David Welch in this research. Furthermore, J.J.K. and M.E.L. would like to thank Dr. A. Peker and Dr. J. Schroers for supplying the BMGs and Dr. R. Busch for many useful discussions.

[1]M. F. Ashby and A. L. Greer, Scr. Mater. **54**, 321 (2006).
[2]J. Schroers, JOM **57**, 35 (2005).
[3]D. B. Miracle, T. Egami, K. M. Flores, and K. F. Kelton, MRS Bull. **32**, 629 (2007).
[4]F. Spaepen, Acta Metall. **25**, 407 (1977).
[5]R. Gerling, F. P. Schimansky, and R. Wagner, Acta Metall. **36**, 575 (1988).
[6]J. J. Lewandowski, W. H. Wang, and A. L. Greer, Philos. Mag. Lett. **85**, 77 (2005).
[7]P. Murali and U. Ramamurty, Acta Mater. **53**, 1467 (2005).
[8]M. E. Launey, R. Busch, and J. J. Kruzic, Scr. Mater. **54**, 483 (2006).
[9]M. E. Launey, R. Busch, and J. J. Kruzic, "Effects of free volume changes and residual stresses on the fatigue and fracture behavior of a ZrTiNiCuBe bulk metallic glass," Acta Mater. (in press).
[10]C. Nagel, K. Ratzke, E. Schmidtke, and F. Faupel, Phys. Rev. B **60**, 9212 (1999).
[11]C. Nagel, K. Ratzke, E. Schmidtke, J. Wolff, U. Geyer, and F. Faupel, Phys. Rev. B **57**, 10224 (1998).
[12]K. M. Flores, D. Suh, R. H. Dauskardt, P. Asoka-Kumar, P. A. Sterne, and R. H. Howell, J. Mater. Res. **17**, 1153 (2002).
[13]B. P. Kanungo, S. C. Glade, P. Asoka-Kumar, and K. M. Flores, Intermetallics **12**, 1073 (2004).
[14]A. Rehmet, K. Gunther-Schade, K. Ratzke, U. Geyer, and F. Faupel, Phys. Status Solidi A **201**, 467 (2004).
[15]*Positron Beams and Their Applications*, edited by Paul G. Coleman (World Scientific, Singapore, 2000), p. 191.
[16]M. E. Launey, J. J. Kruzic, C. Li, and R. Busch, Appl. Phys. Lett. **91**, 051913 (2007).
[17]K. Ohsaka, S. K. Chung, W. K. Rhim, A. Peker, D. Scruggs, and W. L. Johnson, Appl. Phys. Lett. **70**, 726 (1997).
[18]*Metals-Mechanical Testing; Elevated and Low-temperature Tests; Metallography*, Annual Book of ASTM Standards, Vol. 03.01 (ASTM International, West Conshohocken, Pennsylvania, 2004), p. 595.
[19]The stress-intensity factor $K$ is a global parameter which fully characterizes the local stress and deformation fields in the immediate vicinity of a crack tip in a linear-elastic solid, and thus can be used to correlate to the extent of crack advance. It is defined for a crack of length $a$ as $K = Y\sigma_{app}(\pi a)^{1/2}$, where $\sigma_{app}$ is the applied stress and $Y$ is a geometry factor of order unity. The stress intensity range is simply the difference between the maximum and minimum stress intensities applied to the specimen during each loading cycle.
[20]R. Busch and W. L. Johnson, Appl. Phys. Lett. **72**, 2695 (1998).
[21]K. M. Flores, E. Sherer, A. Bharathula, H. Chen, and Y. C. Jean, Acta Mater. **55**, 3403 (2007).
[22]T. L. Anderson, *Fracture Mechanics: Fundamentals and Applications*, 3rd ed. (Taylor & Francis, Boca Raton, FL, 2005), p. 66.
[23]H. A. Bruck, T. Christman, A. J. Rosakis, and W. L. Johnson, Scr. Metall. Mater. **30**, 429 (1994).
[24]J. R. Rice, *Fatigue Crack Propagation* (ASTM, Philadelphia, 1967), Vol. 415, p. 247.

# APPENDIX D

# PALS fitting results

## D.1 chapter 3: study of nanopore characteristics using PALS

Table D.1: **Detailed PALS results for sCD samples.**

| Sample | Energy (keV) | $\tau_{micro}$ (ns) | $I_{micro}$ (%) | $\tau_{meso}$ (ns) | $I_{meso}$ (%) | $I_{Ps,film}$ (%) | $F_{esc}$ (%) |
|---|---|---|---|---|---|---|---|
| mCSSQ matrix | 0.55 | --- | --- | --- | --- | 14.5 | --- |
| | 1.1 | 2.5, 7.0 | 35 | --- | --- | 7.3 | --- |
| | 2.1 | 2.8, 7.0 | 38 | --- | --- | 3.3 | --- |
| | 3.1 | 2.8, 6.9 | 38 | --- | --- | 2.1 | --- |
| | 4.1 | 2.5, 6.8 | 38 | --- | --- | 1.5 | --- |
| | 5.0 | 2.4, 6.8 | 43 | --- | --- | 1.7 | --- |
| T4Q4/sD 10% | 0.55 | --- | --- | 22.5 | 18.0 | 17.5 | 54.3 |
| | 1.1 | --- | --- | 21.0 | 13.3 | 18.6 | 28.5 |
| | 3.1 | 1.4, 6.1 | 14.0 | 19.0 | 13.6 | 15.1 | 9.9 |
| T4Q4/sCD 10% - C | 5.0 | --- | --- | 18.7±0.5 | 14.8 | 14.8 | N/A |
| T4Q4/sCD 20% | 1.1 | --- | --- | 20 | 10.3 | 24.0 | 57.0 |
| | 2.1 | --- | --- | 19.0 | 15.0 | 20.5 | 26.8 |
| | 3.1 | 1.5, 7.4 | 11.0 | 18.0 | 15.4 | 18.7 | 18.0 |
| | 5.0 | --- | --- | 18.9 | 15.8 | 18.3 | 13.7 |
| T4Q4/sCD 20% - C | 5.0 | --- | --- | 20.5±0.5 | 17.5 | 17.5 | N/A |
| T4Q4/sCD 30% | 2.1 | --- | --- | > 17 | 9.6 | 20.7 | 53.6 |
| | 3.1 | 1.6, 7.6 | 11.1 | > 16 | 10.9 | 17.4 | 37.4 |
| | 5.0 | --- | --- | 15-18 | 13.9 | 18.7 | 25.7 |
| T4Q4/sCD 30% - C | 5.0 | --- | --- | 21.0±0.5 | 17.8 | 17.8 | N/A |
| T4Q4/sCD 40% | 3.1 | 1, 2.3 | 8.9 | > 16 | 7.5 | 18.1 | 58.6 |
| | 4.1 | --- | --- | 15 | 11.1 | 18.2 | 39.0 |
| | 5.0 | --- | --- | 14 | 17.6 | 25.0 | 29.6 |
| T4Q4/sCD 40% - C | 5.0 | --- | --- | 20.5±0.5 | 21.4 | 21.4 | N/A |
| T4Q4sCD 50% | 3.1 | 1.2, 4.2 | 9.8 | > 14 | 7.8 | 19.7 | 59.9 |
| | 4.1 | --- | --- | > 15 | 6.5 | 14.6 | 55.5 |
| | 5.0 | --- | --- | > 13 | 12.6 | 20.8 | 39.4 |
| | 6.0 | --- | --- | >13 | 14.9 | 23.6 | 37.9 |
| T4Q4/sCD 50% - C | 5.0 | --- | --- | 20.5±0.5 | 19.5 | 19.5 | N/A |

Table D.2: **Detailed PALS results for CA samples.**

| Sample | E (keV) | $\tau_{meso}$ (ns) | $I_{meso}$ (%) | $I_{vac}$ (%) | $I_{Ps,film}$ (%) | $F_{esc}$ (%) |
|---|---|---|---|---|---|---|
| t100-ca6-10 | 1.10 | 22.8 | 5.3 | 1.3 | 6.5 | 19.3 |
| | 3.10 | 15.4 | 9.4 | 0.5 | 9.9 | 5.0 |
| | 5.00 | 12.6 | 16.8 | 0.8 | 17.7 | 4.8 |
| t100-ca6-20 | 1.10 | 25.8 | 4.8 | 20.6 | 25.3 | 81.2 |
| | 3.10 | 35.0 | 5.8 | 15.4 | 21.1 | 72.7 |
| | 4.10 | 35.1 | 8.3 | 13.1 | 21.5 | 61.2 |
| | 5.00 | 35.2 | 11.9 | 13.4 | 25.3 | 52.9 |
| capped | *3.00* | *56.1* | *7.0* | *0.4* | *7.4* | *5.2* |
| | *4.50* | *54.9* | *13.5* | *0.8* | *14.3* | *5.6* |
| | *7.00* | *48.0* | *16.6* | *1.0* | *17.6* | *5.9* |
| t100-ca6-30 | 1.10 | 22.1 | 4.3 | 25.8 | 30.0 | 85.7 |
| | 3.10 | 19.6 | 4.6 | 25.9 | 30.6 | 84.9 |
| | 4.10 | 37.6 | 3.0 | 26.0 | 29.0 | 89.7 |
| | 6.00 | 38.2 | 6.8 | 29.2 | 36.0 | 81.0 |
| capped | *3.00* | *37.1* | *2.9* | *2.3* | *5.3* | *44.7* |
| | *4.50* | *41.5* | *6.5* | *7.7* | *14.2* | *54.3* |
| | *7.00* | *44.0* | *10.9* | *9.9* | *20.8* | *47.7* |
| t100-ca6-40 | 1.10 | 32.5 | 4.4 | 17.8 | 22.2 | 80.0 |
| | 3.10 | 29.7 | 4.2 | 18.1 | 22.3 | 81.1 |
| | 4.10 | 34.7 | 5.0 | 19.8 | 24.8 | 80.0 |
| | 6.00 | 36.5 | 5.2 | 25.4 | 30.6 | 83.0 |
| capped | *3.00* | *37.1* | *2.7* | *3.6* | *6.3* | *57.5* |
| | *4.50* | *42.2* | *4.5* | *8.9* | *13.4* | *66.5* |
| | *7.00* | *44.1* | *4.8* | *12.5* | *17.3* | *72.3* |

## D.2 chapter 4: study of pore evolution including heat treatment

Table D.3: **Basic information of OS1-P12 samples**

| Sample ID | Film Thickness (nm) | Weight Fraction (%) | Est. Volume Fraction (%) | Ref. Index | Porosity from L.L. (%) |
|---|---|---|---|---|---|
| OS1-P12-3 | 630 | 3.59 | 4.6 | 1.3649 | 1.7 |
| OS1-P12-7 | 626.7 | 7.25 | 9.2 | 1.3469 | 6.1 |
| OS1-P12-10 | 652 | 11.04 | 13.8 | 1.3268 | 11 |
| OS1-P12-15 | 662.9 | 14.9 | 18.5 | 1.3147 | 14 |
| OS1-P12-20 | 682.8 | 19.24 | 23.6 | 1.2764 | 23.7 |
| OS1-P12-25 | 670.7 | 23.24 | 28.1 | 1.2782 | 23.2 |
| OS1-P12-30 | 716.8 | 32.1 | 38 | 1.2292 | 36 |

Table D.4: **Basic information of OS2-P12 samples**

| Sample ID | Film Thickness (nm) | Weight Fraction (%) | Est. Volume Fraction (%) | Ref. Index | Porosity from L.L. (%) |
|---|---|---|---|---|---|
| OS2-P12-2.5 | 586.6 | 1.85 | 2.6 | 1.3546 | 0.9 |
| OS2-P12-5.0 | 577.9 | 3.66 | 5.1 | 1.3482 | 2.5 |
| OS2-P12-7.5 | 588.3 | 5.26 | 7.2 | 1.3434 | 3.7 |
| OS2-P12-10 | 590.9 | 7.21 | 9.9 | 1.3384 | 5.0 |
| OS2-P12-10 | 502.4 | 7.3 | 10 | 1.3356 | 5.71 |
| OS2-P12-15 | 519.3 | 11.1 | 15 | 1.319 | 9.97 |
| OS2-P12-20 | 533.9 | 15 | 20 | 1.3009 | 14.66 |
| OS2-P12-25 | 541.5 | 19.1 | 25 | 1.2801 | 20.11 |
| OS2-P12-30 | 509.6 | 23.3 | 30 | 1.258 | 25.99 |
| OS2-P12-35 | 531.6 | 27.6 | 35 | 1.2364 | 31.81 |
| OS2-P12-40 | 548.5 | 32.1 | 40 | 1.2138 | 37.98 |

Table D.5: **OS3/P12 System (150°C/1hr)**

| Loading (%) | d | $\sigma$d | n | $\sigma$n | GOF |
|---|---|---|---|---|---|
| **17** | 439.1 | 3.1 | 1.3494 | 7.60E-04 | 0.9998 |
| **19** | 359.6 | 0.6 | 1.367 | 0.00125 | 0.99993 |
| **21** | 350 | 0.4 | 1.3818 | 2.60E-04 | 0.99996 |
| **23** | 343.7 | 0.4 | 1.3944 | 7.00E-04 | 0.99992 |
| **25** | 335.7 | 0.8 | 1.408 | 0.00102 | 0.99989 |
| **27.5** | 324.5 | 0.4 | 1.4285 | 3.50E-04 | 0.99988 |
| **30** | 321 | 0.4 | 1.4412 | 2.40E-04 | 0.99989 |

Table D.6: **Basic information of OS3-P12 samples. OS3 matrix is mesoporous intrinsically, which requires us taking into account its porosity even at 0% porogen loading. The absorption data is used (OS3 has intrinsically 37.35% mesoporosity) to calculate the other samples' porosity.**

| Sample ID | Film Thickness (nm) | Weight Fraction (%) | Ref. Index | Porosity from L.L. (%) |
|---|---|---|---|---|
| OS3-P12-0 | 504 | 0 | 1.248 | 37.4 |
| OS3-P12-13 | 378.1 | 13 | 1.2572 | 35.2 |
| OS3-P12-15 | 425.95 | 15 | 1.2584 | 34.9 |
| OS3-P12-17 | 360.77 | 16.9 | 1.2606 | 34.4 |
| OS3-P12-19 | 353.8 | 19 | 1.2616 | 34.1 |
| OS3-P12-21 | 343.5 | 21 | 1.2628 | 33.9 |
| OS3-P12-23 | 334.6 | 23 | 1.2646 | 33.4 |
| OS3-P12-25 | 333.16 | 24.9 | 1.2581 | 35.0 |
| OS3-P12-28 | 328.88 | 27.5 | 1.2514 | 36.5 |
| OS3-P12-30 | 330.87 | 30 | 1.2431 | 38.5 |
| OS3-P12-33 | 335.72 | 32.5 | 1.2324 | 41.1 |
| OS3-P12-35 | 341.49 | 35 | 1.2232 | 43.3 |
| OS3-P12-38 | 347 | 37.6 | 1.2119 | 46.0 |

Table D.7: **Fitted PALS data for the IBM P12-OS1 series with capped data in red.**

| Sample | Energy (keV) | $\tau_{meso}$ (ns) | $I_{meso}$ (%) | $I_{vac}$ (%) | $I_{Ps,film}$ (%) | $f_{esc}$ (%) |
|---|---|---|---|---|---|---|
| P12-OS1-3 | 0.55 | 19.6 | 12.5 | 4.9 | 17.4 | 28.1 |
| | 1.10 | 18.1 | 17.5 | 3.0 | 20.6 | 14.8 |
| | 3.10 | 16.7 | 18.9 | 0.3 | 19.2 | 1.4 |
| P12-OS1-7 | 0.55 | 20.6 | 17.3 | 12.0 | 29.2 | 40.9 |
| | 1.10 | 20.4 | 23.5 | 7.8 | 31.3 | 25.0 |
| | 3.10 | 19.7 | 26.7 | 1.4 | 28.1 | 4.9 |
| P12-OS1-10 | 0.55 | 25.7 | 13.8 | 18.0 | 31.8 | 56.6 |
| | 1.10 | 24.3 | 23.1 | 13.5 | 36.6 | 37.0 |
| | 2.10 | 24.2 | 28.1 | 5.0 | 33.1 | 15.0 |
| | 3.10 | 24.8 | 27.6 | 2.7 | 30.4 | 9.0 |
| P12-OS1-15 | 1.10 | 29.1 | 17.7 | 21.6 | 39.3 | 54.9 |
| | 2.10 | 27.2 | 26.6 | 10.2 | 36.7 | 27.6 |
| | 3.10 | 28.5 | 28.1 | 5.4 | 33.5 | 16.2 |
| | 5.10 | 28.7 | 27.7 | 2.7 | 30.3 | 8.7 |
| P12-OS1-20 | 1.10 | 34.8 | 9.8 | 34.5 | 44.4 | 77.8 |
| | 2.10 | 33.3 | 17.1 | 23.6 | 40.7 | 57.9 |
| | 3.10 | 35.4 | 22.9 | 14.5 | 37.4 | 38.8 |
| | 5.10 | 37.3 | 25.0 | 7.3 | 32.2 | 22.5 |
| P12-OS1-C | 4.5 | 38.6 | 16.7 | 0.0 | 16.7 | 0.0 |
| P12-OS1-25 | 2.10 | 36.0 | 12.9 | 28.6 | 41.5 | 68.9 |
| | 3.10 | 35.7 | 18.2 | 20.5 | 38.7 | 53.0 |
| | 5.10 | 37.5 | 23.1 | 10.5 | 33.5 | 31.3 |
| P12-OS1-C | 4.5 | 41.6 | 19.4 | 0.0 | 19.4 | 0.0 |
| P12-OS1-30 | 3.10 | 32.4 | 4.0 | 36.3 | 40.3 | 90.2 |
| | 5.10 | 30.0 | 5.6 | 27.6 | 33.2 | 83.1 |
| P12-OS1-C | 4.5 | 57.0 | 20.5 | 0.0 | 20.5 | 0.0 |

Table D.8: **Fitted PALS data for the IBM P12-OS2 series with capped data in red.**

| Sample | Energy (keV) | $\tau_{meso}$ (ns) | $I_{meso}$ (%) | $I_{vac}$ (%) | $I_{Ps,film}$ (%) | $F_{esc}$ (%) |
|---|---|---|---|---|---|---|
| P12-OS2-10 | 0.55 | 20.1 | 9.2 | 17.1 | 26.3 | 65.0 |
| | 1.10 | 17.4 | 13.4 | 13.8 | 27.2 | 50.8 |
| | 2.10 | 15.8 | 20.5 | 5.6 | 26.1 | 21.3 |
| | 3.10 | 14.6 | 26.1 | 3.0 | 29.1 | 10.2 |
| | 5.00 | 14.7 | 26.4 | 2.7 | 29.0 | 9.3 |
| P12-OS2-15 | 0.55 | 25.7 | 6.0 | 20.4 | 26.4 | 77.1 |
| | 1.10 | 15.0 | 17.3 | 19.2 | 36.5 | 52.6 |
| | 2.10 | 16.9 | 17.0 | 9.1 | 26.0 | 34.8 |
| | 3.10 | 15.4 | 25.1 | 5.0 | 30.1 | 16.5 |
| | 5.00 | 15.3 | 27.8 | 4.0 | 31.8 | 12.4 |
| P12-OS2-20 | 1.10 | 21.4 | 8.8 | 24.7 | 33.6 | 73.7 |
| | 2.10 | 19.4 | 14.7 | 14.2 | 29.0 | 49.1 |
| | 3.10 | 17.5 | 22.9 | 8.2 | 31.1 | 26.4 |
| | 5.00 | 17.8 | 25.2 | 6.0 | 31.2 | 19.3 |
| P12-OS2-25 | 2.10 | 20.9 | 13.1 | 20.3 | 33.5 | 60.8 |
| | 3.10 | 21.4 | 17.0 | 12.8 | 29.9 | 42.9 |
| | 5.00 | 20.4 | 23.1 | 9.2 | 32.4 | 28.5 |
| P12-OS2-25-c | 5.10 | 23.3 | 17.1 | 0.0 | 17.1 | 0.0 |
| P12-OS2-30 | 3.10 | 21.9 | 14.1 | 19.2 | 33.3 | 57.6 |
| | 4.10 | 22.8 | 16.3 | 14.6 | 30.9 | 47.1 |
| | 5.00 | 21.6 | 16.8 | 14.3 | 31.2 | 46.1 |
| P12-OS2-30-c | 5.10 | 27.6 | 19.2 | 0.0 | 19.2 | 0.0 |
| P12-OS2-35 | 3.10 | 21.5 | 8.9 | 24.5 | 33.4 | 73.3 |
| | 5.00 | 23.2 | 9.0 | 19.8 | 28.8 | 68.8 |
| P12-OS2-35-c | 5.10 | 34.5 | 19.5 | 0.0 | 19.5 | 0.0 |
| P12-OS2-40 | 3.10 | 25.6 | 2.5 | 29.1 | 31.6 | 92.1 |
| | 5.00 | 13.0 | 7.7 | 25.3 | 33.0 | 76.6 |
| P12-OS2-40-c | 5.10 | 42.7 | 18.6 | 0.0 | 18.6 | 0.0 |

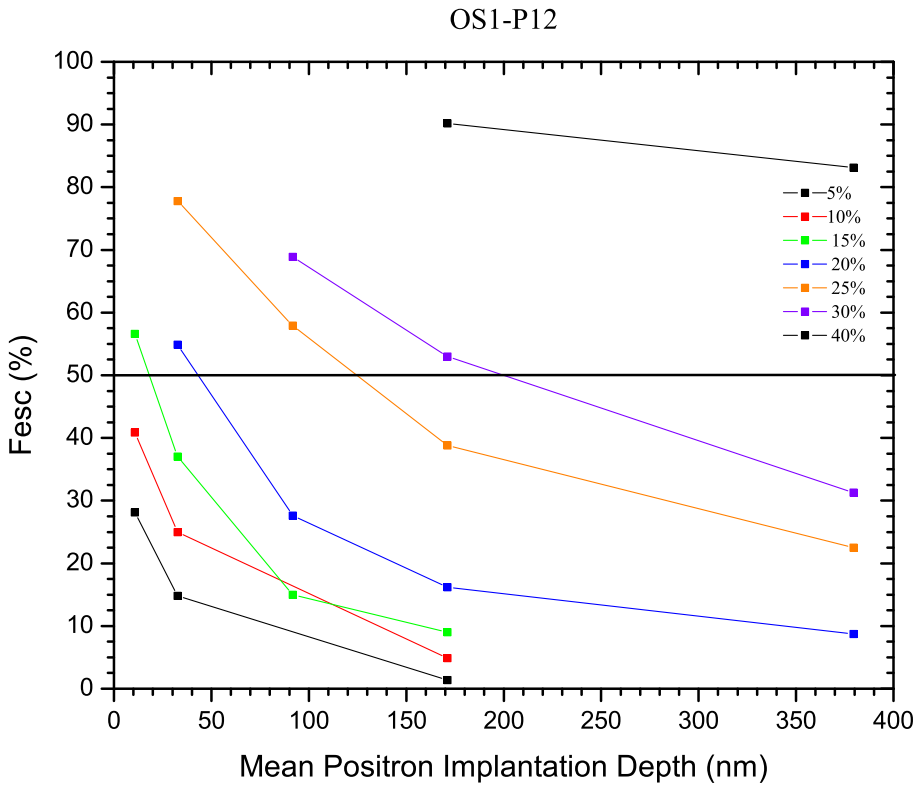


Figure D.1: Ps vacuum escape fractions vs. mean positron implantation depth for the various porosity films in the P12/OS1 series

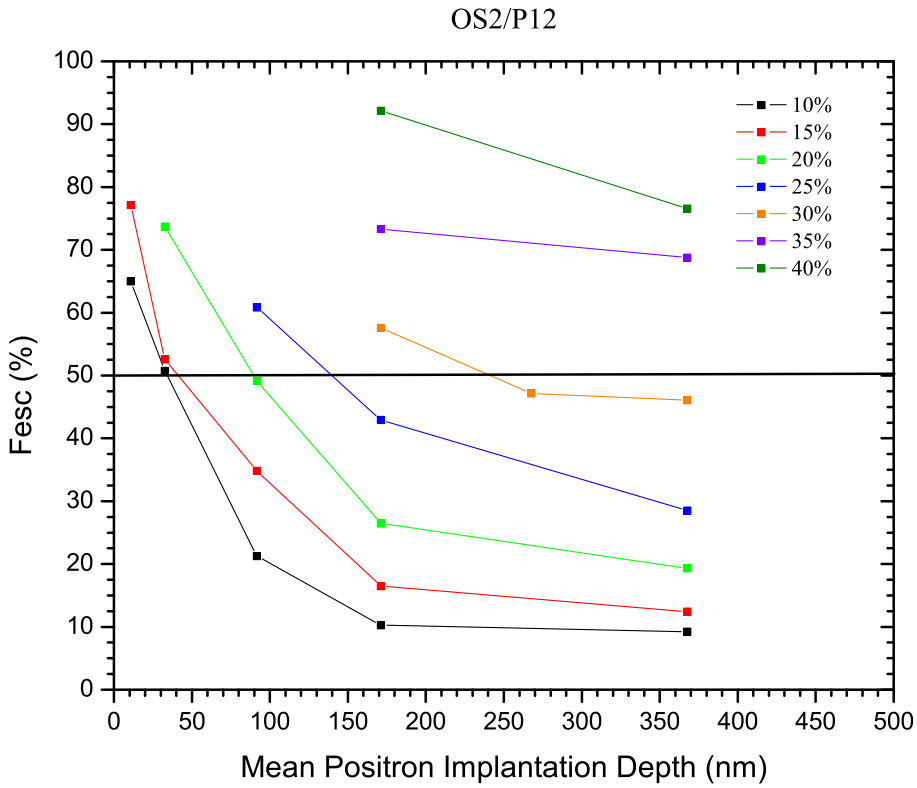


Figure D.2: Ps vacuum escape fractions vs. mean positron implantation depth for the various porosity films in the P12/OS2 series

Table D.9: **Summary of the OS1-PJB films. The estimated volume fraction was extrapolated from the weight fraction fractions supplied by IBM and the OS2-PJB data from the May 12, 2004 report.**

| Sample ID | Film Thickness (nm) | Weight Fraction (%) | Est. Volume Fraction (%) | Ref. Index | Porosity from L.L. (%) |
|---|---|---|---|---|---|
| PJB-OS1- 05 | 604.3 | 4.96 | 6.4 | 1.3495 | 5.4 |
| PJB-OS1-10 | 597.7 | 9.76 | 12.4 | 1.3342 | 9.2 |
| PJB-OS1-15 | 672.2 | 14.87 | 18.5 | 1.3116 | 14.8 |
| PJB-OS1-20 | 617.7 | 20.27 | 24.9 | 1.2905 | 20.1 |
| PJB-OS1-25 | 624.7 | 25.01 | 30.3 | 1.2677 | 25.9 |
| PJB-OS1-30 | 636.0 | 29.89 | 35.7 | 1.2467 | 31.4 |
| PJB-OS1-40 | 664.3 | 40.15 | 46.6 | 1.2059 | 42.1 |

Table D.10: **Summary of the PJB/OS2 films.**

| Sample ID | Film Thickness (nm) | Weight Fraction (%) | Est. Volume Fraction (%) | Ref. Index | Porosity from L.L. (%) |
|---|---|---|---|---|---|
| PJB-OS2-2.5 | 602.3 | 2.50 | 3.5 | 1.3481 | 2.5 |
| PJB-OS2-5.0 | 609.6 | 4.65 | 6.4 | 1.3402 | 4.5 |
| PJB-OS2-7.5 | 626.8 | 7.45 | 10.2 | 1.3301 | 7.1 |
| PJB-OS2-10 | 643.5 | 9.95 | 13.5 | 1.3201 | 9.7 |
| PJB-OS2-10 | 568.3 | 10 | 13.7 | 1.3182 | 10.17 |
| PJB-OS2-15 | 561.4 | 15 | 20.0 | 1.3021 | 14.34 |
| PJB-OS2-20 | 638.0 | 20 | 26.2 | 1.2749 | 21.49 |
| PJB-OS2-25 | 623.0 | 25 | 32.1 | 1.2568 | 26.31 |
| PJB-OS2-30 | 693.5 | 30 | 37.8 | 1.2324 | 32.89 |
| PJB-OS2-35 | 627.8 | 35 | 43.3 | 1.2131 | 38.17 |
| PJB-OS2-40 | 683.8 | 40 | 48.6 | 1.1918 | 44.06 |

Table D.11: **Summary of the PJB/OS3 films.**

| Sample ID | Film Thickness (nm) | Weight Fraction (%) | Est. Volume Fraction (%) | Ref. Index | Porosity from L.L. (%) |
|---|---|---|---|---|---|
| PJB-OS3-0 | 434.5 | 0.00 | 0.0 | 1.2473 | 37.4 |
| PJB-OS3-5 | 423.5 | 5.08 | 4.8 | 1.2465 | 37.6 |
| PJB-OS3-10 | 409.6 | 10.02 | 9.5 | 1.2451 | 37.9 |
| PJB-OS3-15 | 395.1 | 15.04 | 14.3 | 1.2440 | 38.2 |
| PJB-OS3-18 | 384.3 | 17.61 | 16.8 | 1.2427 | 38.5 |
| PJB-OS3-20 | 378.0 | 20.04 | 19.1 | 1.2412 | 38.8 |
| PJB-OS3-23 | 370.0 | 22.48 | 21.5 | 1.2403 | 39.0 |
| PJB-OS3-25 | 360.3 | 24.9 | 23.9 | 1.2398 | 39.2 |
| PJB-OS3-28 | 354.4 | 27.56 | 26.5 | 1.2359 | 40.1 |
| PJB-OS3-30 | 344.1 | 29.92 | 28.7 | 1.2326 | 40.9 |
| PJB-OS3-32 | 341.3 | 32.36 | 31.2 | 1.2273 | 42.2 |
| PJB-OS3-35 | 343.0 | 35.01 | 33.7 | 1.2170 | 44.6 |
| PJB-OS3-37 | 345.8 | 37.32 | 36.0 | 1.2100 | 46.3 |

Table D.12: **Fitted PALS data for the IBM PJB-OS1 series with capped data in red.**

| Sample | Energy (keV) | $\tau_{meso}$ (ns) | $I_{meso}$ (%) | $I_{vac}$ (%) | $I_{Ps,film}$ (%) | $f_{esc}$ (%) |
|---|---|---|---|---|---|---|
| PJB-OS1-05 | 0.55 | 56.5 | 9.1 | 1.0 | 10.1 | 9.9 |
| | 1.1 | 53.8 | 9.2 | 1.5 | 10.7 | 14.0 |
| | 2.1 | 53 | 9.4 | 1.0 | 10.4 | 9.6 |
| | 3.1 | 52.3 | 8.6 | 0.9 | 9.5 | 9.6 |
| PJB-OS10-05-C | 4.5 | 53.9 | 3.6 | 0.0 | 3.6 | 0.0 |
| PJB-OS1-10 | 0.55 | 59.9 | 14.5 | 5.3 | 19.8 | 26.9 |
| | 1.1 | 58.4 | 16.7 | 4.8 | 21.5 | 22.4 |
| | 2.1 | 57.9 | 16.3 | 2.7 | 19.0 | 14.1 |
| | 3.1 | 56.4 | 15 | 2.3 | 17.3 | 13.0 |
| PJB-OS1-10-C | 4.5 | 56.8 | 6.0 | 0.0 | 6.0 | 0.0 |
| PJB-OS1-15 | 0.55 | 62.8 | 15.6 | 11.1 | 26.7 | 41.5 |
| | 1.1 | 62.5 | 20.1 | 10.0 | 30.1 | 33.2 |
| | 2.1 | 60.5 | 22.2 | 5.5 | 27.7 | 19.9 |
| | 3.1 | 59.5 | 21.3 | 4.1 | 25.4 | 16.1 |
| | 5.1 | 59.3 | 18.7 | 3.0 | 21.7 | 13.8 |
| PJB-OS1-15-C | 4.5 | 59.8 | 10.8 | 0.0 | 10.8 | 0.0 |
| PJB-OS1-20 | 1.1 | 63.1 | 18.3 | 14.9 | 33.2 | 44.9 |
| | 2.1 | 63.7 | 23.5 | 8.0 | 31.5 | 25.4 |
| | 3.1 | 63.2 | 23.6 | 5.8 | 29.4 | 19.8 |
| | 5.1 | 62.3 | 20.5 | 4.1 | 24.6 | 16.6 |
| PJB-OS1-20-C | 4.5 | 64.0 | 12.7 | 0.0 | 12.7 | 0.0 |
| PJB-OS1-25 | 1.1 | 65.3 | 16 | 18.7 | 34.7 | 53.8 |
| | 2.1 | 66.5 | 21.6 | 10.8 | 32.4 | 33.4 |
| | 3.1 | 66.7 | 23.4 | 7.7 | 31.1 | 24.7 |
| | 5.1 | 66.9 | 20.8 | 4.7 | 25.5 | 18.3 |
| PJB-OS1-25-C | 4.5 | 66.9 | 13.6 | 0.0 | 13.6 | 0.0 |
| PJB-OS1-30 | 2.1 | 67.6 | 19 | 14.3 | 33.3 | 43.0 |
| | 3.1 | 68.5 | 21.8 | 10.5 | 32.3 | 32.5 |
| | 5.1 | 70.3 | 19.6 | 5.9 | 25.5 | 23.2 |
| PJB-OS1-30-C | 4.5 | 70.2 | 12.6 | 0.0 | 12.6 | 0.0 |
| PJB-OS1-40 | 3.1 | 71.7 | 14.1 | 18.8 | 32.9 | 57.1 |
| | 5.1 | 75.6 | 13.8 | 10.0 | 23.8 | 42.0 |
| PJB-OS1-40-C | 4.5 | 85.2 | 16.5 | 0.0 | 16.5 | 0.0 |

Table D.13: **Fitted PALS data for the IBM PJB-OS2 series with capped data in red.**

| Sample | Energy (keV) | $\tau_{meso}$ (ns) | $I_{meso}$ (%) | $I_{vac}$ (%) | $I_{Ps,film}$ (%) | $F_{esc}$ (%) |
|---|---|---|---|---|---|---|
| PJB-OS2-2 | 0.55 | 24.6 | 7.4 | 4.5 | 11.9 | 37.8 |
| | 1.1 | 24.0 | 9.2 | 3.6 | 12.8 | 27.9 |
| | 2.1 | 22.1 | 9.7 | 3.2 | 12.9 | 24.8 |
| | 3.1 | 24.6 | 9.1 | 2.9 | 12.1 | 24.4 |
| | 5.1 | 25.7 | 8.2 | 2.9 | 11.1 | 25.7 |
| PJB-OS2-2-C | 4.5 | 55 - 57 | 1.7 | 0 | 1.7 | 0 |
| PJB-OS2-5 | 0.55 | 34.6 | 7.2 | 8.9 | 16.1 | 55.3 |
| | 1.1 | 34.4 | 9.6 | 6.8 | 16.4 | 41.5 |
| | 2.1 | 32.5 | 10.0 | 5.3 | 15.3 | 34.7 |
| | 3.1 | 39.0 | 10.5 | 3.4 | 14.0 | 24.7 |
| | 5.1 | 32.8 | 9.1 | 5.1 | 14.2 | 35.9 |
| PJB-OS2-5 | 4.5 | 55 - 57 | 2.3 | 0 | 2.3 | 0 |
| PJB-OS2-7 | 1.1 | 41.4 | 11.0 | 11.7 | 22.7 | 51.5 |
| | 2.1 | 41.6 | 12.8 | 7.3 | 20.2 | 36.3 |
| | 3.1 | 41.4 | 13.1 | 6.4 | 19.4 | 32.8 |
| | 4.1 | 41.1 | 12.7 | 6.1 | 18.8 | 32.2 |
| | 5.1 | 42.9 | 12.4 | 5.3 | 17.7 | 30.1 |
| PJB-OS2-7 | 4.5 | 55 - 57 | 3.7 | 0 | 3.7 | 0 |
| PJB-OS2-10 | 1.1 | 45.6 | 11.8 | 16.1 | 27.9 | 57.8 |
| | 2.1 | 50.9 | 16.9 | 7.4 | 24.3 | 30.6 |
| | 3.1 | 48.2 | 16.4 | 6.8 | 23.2 | 29.3 |
| | 5.1 | 46.1 | 15.0 | 6.5 | 21.5 | 30.3 |
| PJB-OS2-10 | 4.5 | 55 – 57 | 5.6 | 0 | 5.6 | 0 |
| PJB-OS2-13.7 | 1.10 | 49.4 | 13.3 | 16.2 | 29.5 | 54.8 |
| | 2.10 | 52.6 | 18.5 | 7.2 | 25.7 | 28.0 |
| | 3.10 | 51.9 | 19.4 | 4.6 | 24.0 | 19.2 |
| | 5.10 | 50.9 | 11.5 | 1.6 | 13.1 | 12.2 |
| PJB-OS2-20 | 1.10 | 48.0 | 11.2 | 20.9 | 32.1 | 65.1 |
| | 2.10 | 56.1 | 18.3 | 10.3 | 28.5 | 36.0 |
| | 3.10 | 55.6 | 20.7 | 6.4 | 27.1 | 23.6 |
| | 5.00 | 56.0 | 20.8 | 4.4 | 25.2 | 17.4 |
| | 6.00 | 55.4 | 18.6 | 4.7 | 23.2 | 20.0 |
| PJB-OS2-20-c | 5.10 | 56.1 | 7.9 | 0.0 | 7.9 | 0.0 |
| PJB-OS2-26.2 | 2.10 | 52.5 | 13.8 | 19.5 | 33.2 | 58.6 |
| | 3.10 | 55.1 | 18.5 | 12.2 | 30.7 | 39.7 |
| | 4.10 | 57.3 | 21.2 | 8.8 | 30.0 | 29.4 |
| | 6.00 | 57.7 | 20.0 | 8.3 | 28.3 | 29.4 |
| PJB-OS2-26.2-c | 5.10 | 62.4 | 15.5 | 0.0 | 15.5 | 0.0 |
| PJB-OS2-32.1 | 2.10 | 48.2 | 9.8 | 25.5 | 35.4 | 72.2 |
| | 3.10 | 49.6 | 15.2 | 17.0 | 32.2 | 52.7 |
| | 4.10 | 58.8 | 18.9 | 12.1 | 30.9 | 39.1 |
| | 6.00 | 56.4 | 16.7 | 12.6 | 29.3 | 43.0 |
| PJB-OS2-32.1-c | 5.10 | 66.7 | 16.1 | 0.0 | 16.1 | 0.0 |
| PJB-OS2-37.8 | 3.10 | 45.9 | 10.8 | 21.1 | 32.0 | 66.1 |
| | 4.10 | 55.8 | 13.8 | 18.2 | 32.0 | 56.8 |
| | 5.00 | 55.3 | 15.2 | 18.1 | 33.2 | 54.4 |
| PJB-OS2-37.8-c | 5.10 | 69.8 | 18.7 | 0.0 | 18.7 | 0.0 |
| PJB-OS2-43.3 | 3.10 | 39.3 | 7.7 | 24.0 | 31.6 | 75.7 |
| | 4.10 | 43.8 | 7.7 | 23.9 | 31.6 | 75.6 |
| | 5.00 | 44.8 | 7.3 | 23.2 | 30.5 | 76.1 |
| | 6.00 | 45.9 | 6.4 | 21.1 | 27.5 | 76.7 |
| PJB-OS2-43.3-c | 5.10 | 76.5 | 15.9 | 0.0 | 15.9 | 0.0 |
| PJB-OS2-48.6 | 3.10 | 20.8 | 4.8 | 28.0 | 32.8 | 85.3 |
| | 5.00 | 16.4 | 4.8 | 28.7 | 33.5 | 85.8 |
| | 6.00 | 19.2 | 3.6 | 25.5 | 29.1 | 87.7 |
| PJB-OS2-48.6-c | 5.10 | 77.1 | 17.0 | 0.0 | 17.0 | 0.0 |

Table D.14: **Summary of the PJB/OS3 uncured films (150°C/1hr)**

| Loading (%) | D (nm) | σd | n | σn | GOF |
|---|---|---|---|---|---|
| **0** | 438.5 | 1.2 | 1.26 | 9.4E-4 | 0.99994 |
| **15.04** | 389.5 | 0.6 | 1.308 | 0.00217 | 0.99986 |
| **17.6** | 370.5 | 0.7 | 1.308 | 7.9E-4 | 0.99988 |
| **20** | 368.3 | 0.06 | 1.332 | 6.4E-4 | 0.99995 |
| **22.5** | 361.2 | 0.7 | 1.35 | 8.4E-4 | 0.9999 |
| **25** | 361.8 | 1.7 | 1.389 | 0.00572 | 0.99992 |
| **27.6** | 351.4 | 3 | 1.408 | 0.00837 | 0.99989 |

## D.3 chapter 6: parylene pore sealing of ultra low-k materials

Table D.15: **1 nm parylene at 2 mT on JSR6103**

| Energy (keV) | $\tau_{meso}$ (ns) | $I_{meso}$ (%) | $I_{vac}$* (%) | $I_{Ps}$ (%) |
|---|---|---|---|---|
| 0.6 | 30.5 | 3.7 | 8.3 | 12 |
| 1.2 | 40.8 | 6.2 | 4.5 | 10.7 |
| 1.7 | 52.7 | 10.5 | 3.4 | 13.9 |
| 2.2 | 56.5 | 13.7 | 2.6 | 16.3 |
| 2.7 | 57.8 | 16.1 | 2.3 | 18.4 |
| 3.2 | 59.3 | 17.2 | 1.9 | 19.1 |
| 3.7 | 57.9 | 14.8 | 2.1 | 16.9 |
| 4.2 | 58.4 | 11.9 | 1.8 | 13.7 |

Table D.16: **2 nm parylene at 2 mT on JSR6103**

| Energy (keV) | $\tau_{meso}$ (ns) | $I_{meso}$ (%) | $I_{vac}$* (%) | $I_{Ps}$ (%) |
|---|---|---|---|---|
| 0.6 | 26.3 | 4.4 | 7.4 | 11.8 |
| 1.2 | 33.5 | 6.3 | 4.1 | 10.4 |
| 1.7 | 49.9 | 9.7 | 3.4 | 13.1 |
| 2.2 | 52.8 | 12.8 | 2.8 | 15.6 |
| 2.7 | 55.3 | 15.1 | 2.6 | 17.7 |
| 3.2 | 57.5 | 16.3 | 2 | 18.3 |
| 3.7 | 57.2 | 13.9 | 1.9 | 15.8 |
| 4.2 | 57.9 | 11.5 | 1.6 | 13.1 |

Table D.17: **5 nm parylene at 2 mT on JSR6103**

| **Energy (keV)** | $\tau_{meso}$ **(ns)** | $\mathbf{I}_{meso}$ **(%)** | $\mathbf{I}_{vac}$*** (%)** | $\mathbf{I}_{Ps}$ **(%)** |
|---|---|---|---|---|
| 0.6 | 38.5 | 1.6 | 6.2 | 7.8 |
| 1.2 | 56.1 | 4.7 | 3.2 | 7.9 |
| 1.7 | 63.2 | 8.9 | 2 | 10.9 |
| 2.2 | 59.3 | 11.6 | 2.1 | 13.7 |
| 2.7 | 60.5 | 13.5 | 2 | 15.5 |
| 3.2 | 61.2 | 15 | 1.6 | 16.6 |
| 3.7 | 61.4 | 13.2 | 1.3 | 14.5 |
| 4.2 | 59.9 | 10.5 | 1.4 | 11.9 |

Table D.18: **30 nm parylene at 2 mT on JSR6103**

| **Energy (keV)** | $\tau_{meso}$ **(ns)** | $\mathbf{I}_{meso}$ **(%)** | $\mathbf{I}_{vac}$*** (%)** | $\mathbf{I}_{Ps}$ **(%)** |
|---|---|---|---|---|
| 0.6 | 33.9 | 0.9 | 4.9 | 5.8 |
| 1.2 | 41.3 | 0.8 | 2.4 | 3.2 |
| 1.7 | 65.6 | 2.8 | 1.7 | 4.5 |
| 2.2 | 62.3 | 5.8 | 1.4 | 7.2 |
| 2.7 | 61.9 | 8.3 | 1.4 | 9.7 |
| 3.2 | 61.6 | 10.8 | 1.4 | 12.2 |
| 3.7 | 61.3 | 10.5 | 1.3 | 11.8 |
| 4.2 | 62.5 | 8.6 | 1.1 | 9.7 |

Table D.19: **5 nm parylene at 2 mT on JSR5109**

| **Energy (keV)** | $\tau_{meso}$ **(ns)** | $\mathbf{I}_{meso}$ **(%)** | $\mathbf{I}_{vac}$*** (%)** | $\mathbf{I}_{Ps}$ **(%)** |
|---|---|---|---|---|
| 0.6 | 25.2 | 4.1 | 6.4 | 10.5 |
| 1.2 | 34.4 | 7.0 | 3.7 | 10.7 |
| 1.7 | 43.1 | 10.3 | 2.9 | 13.2 |
| 2.2 | 47.7 | 13.3 | 2.3 | 15.6 |
| 2.7 | 49.4 | 15.5 | 2.0 | 17.5 |
| 3.2 | 50.7 | 16.0 | 1.6 | 17.6 |
| 3.7 | 48.9 | 15.1 | 1.9 | 17.0 |
| 4.2 | 51.1 | 12.2 | 1.2 | 13.4 |

Table D.20: **5 nm parylene at 2 mT on JSR5115**

| **Energy (keV)** | $\tau_{meso}$ **(ns)** | $\mathbf{I}_{meso}$ **(%)** | $\mathbf{I}_{vac}$*** (%)** | $\mathbf{I}_{Ps}$ **(%)** |
|---|---|---|---|---|
| 0.6 | 25.8 | 3 | 6.4 | 9.4 |
| 1.2 | 36.8 | 6 | 3.7 | 9.7 |
| 1.7 | 44.6 | 9.7 | 2.9 | 12.6 |
| 2.2 | 48 | 12.3 | 2.5 | 14.8 |
| 2.7 | 50.5 | 14.9 | 1.9 | 16.8 |
| 3.2 | 51.3 | 14.7 | 1.7 | 16.4 |
| 3.7 | 50.4 | 14 | 1.6 | 15.6 |
| 4.2 | 51.7 | 10.7 | 1.4 | 12.1 |

# APPENDIX E

# C++ codes of the simulation programs

## E.1 Monte Carlo simulation in a cubic lattice

```
// cubic lattice with L=200 with periodic boundary
conditions in x, y directions
//mean free path, z average and positron
implantation simulation
// At different depth, the weight is the distribution
// diffusion of positrons is modeled as the skin layer
around mesopores and vacuum
// every positron/Ps has probability of diffusing into
mesopores and vacuum,
// added the f_esc fraction function, using the Monte
Carlo function to calculate f_esc
// From the one dimensional random walk model,
the probability for a Ps to escape from the surface is
exponentially decreasing versus its original
implantation depth
// the probability of diffusing into different pores are
also correlated with their sizes.

#include <iostream>
#include <time.h>
#include <stdlib.h>
#include <iomanip>
#include <fstream>
#include <math.h>
#include <vector>
#include "randomc.h"
#include <string>

using namespace std;

const double PI = 3.1415926536;

const int size = 200;
const int size3 = size * size * size;
double pmax;
double pstep;
double Beamenergy = 3.0;//default beam energy is
3.0keV
const double poresize = 2.0; //unit cell/pore size
const double walldensity = 2.0; // material density,
the total film thickness is size * poresize * walldensity
const double diffulgth =1.3;//difusion length in unit
of cells
double ptrap = 0; //the probability of Ps diffusing
into a mesopore or vacuum
int32 seed = (int32) time(0);     // random seed
TRandomMersenne rg(seed);

template <class T>
inline void Intialize2DArray(T **&xxx, long rows,
long cols){
        long i, j;
        for (i=0; i<rows; i++){
                for (j=0; j<cols; j++){
                        xxx[i][j] = T(0);}
        }
}

template <class T>
void Create2DArray(T **&xxx, long rows, long cols)
{
        xxx = new T *[rows];
        for (long i=0; i<rows; i++){
                xxx[i]=new T[cols];}
        Intialize2DArray(xxx, rows, cols);
}

template <class T>
void Delete2DArray(T **&xxx, long rows)
{
        for(long i=0; i<rows; i++){
                delete []xxx[i];}
```

```
	delete []xxx;
	xxx=0;
}

template <class T>
void Create3DArray(T ***&xxx, long n1, long n2, long
n3)
{
	xxx = new T **[n1];
	for (long i=0; i<n1; i++){
		Create2DArray(xxx[i], n2, n3);
		Intialize2DArray(xxx[i], n2, n3);
	}
}

template <class T>
void Delete3DArray(T ***&xxx, long n1, long n2)
{
	for (long i=0; i<n1; i++){
		Delete2DArray(xxx[i], n2);}
	delete []xxx;
	xxx=0;
}

void initialize( int ***);
void GenPores ( int ***, double );
void MarkCluster ( int *** );
void clustersize (int***, int*);
double mean_freepath ( int ***, const double& );
double PosImplant ( int ***, double, double );
double PosImplant2 (int ***, double, double );
void Statistical ( int ***, double );
string diffusion(int***, int, int, int);
double MonteCarlo(int***, double, double, int* );
string diffusion2(int***, double, double, double, int*);
double interlgth(int***, double, int*);
bool escape(int, int, int);
bool PsRandWalk(double);
double PsEscP (double);
void PsEscCalibration ();
double distance(int, int, int, double, double, double);

void main ()
{
	ofstream outResultsFile( "results.dat",
ios::app );// generate results.dat file that has porosity,
MFP and Lint results
	ofstream outFescFile( "fesc.dat", ios::app );
				// generate fesc.dat file to
monitor the fesc change according to depth at
different energies
	ofstream outIntensityFile( "intensity.dat",
ios::app );// generate intensity.dat file to see the
intensities of mesopore, micropore and vacuum
change to porosity
	outResultsFile << "Lsize=" << size  << "
Psize=" << poresize << "  density=" << walldensity

	<< " diffusion=" << diffulgth << endl;
	outFescFile << "Lsize=" << size  << "  Psize="
<< poresize << "  density=" << walldensity
	<< " diffusion=" << diffulgth << endl;
	outIntensityFile << "Lsize=" << size  << "
Psize=" << poresize << "  density=" << walldensity

	<< " diffusion=" << diffulgth << endl;
	cout << "maximum porosity? " << endl;
	cin >> pmax;
	cout << "porosity step?" << endl;
	cin >> pstep;
	int ***lattice;
	Create3DArray(lattice, size, size, size);
	int* cluster = new int[size3];
	int count = int (pmax*size3);
	int stepcount = int (pstep*size3);
	vector<double> results[3];		//array to
store the results: porosity, MFP, Lint
	double P = 0;
	for (int i = stepcount; i <= count ;
i+=stepcount)
	{
		P = double (i)/double(size3);
		cout << "porosity=" << P << "
" << endl;
		GenPores ( lattice, pstep );
		MarkCluster ( lattice );
		clustersize(lattice, cluster);
//		MonteCarlo (lattice, P, Beamenergy,
cluster); // optional. output the intensities of
mesopores, micropores and vacuum into file
"intensity.dat"
		double MFP = mean_freepath
( lattice, P );
		double Lint = interlgth (lattice, P,
cluster); //  return the interconnection length by
Monte Carlo implantation of positrons
		cout << MFP << "		" << endl;
		cout << Lint << "		" << endl;
		results[0].push_back(P);
		results[1].push_back(MFP);
		results[2].push_back(Lint);
	}
	outResultsFile << setw(8) << "porosity" <<
setw(8) << "MFP" << setw(8) << "Lint" << endl;
	for (int i=0; i<results[0].size(); i++)
		outResultsFile << setw (8) <<
results[0][i] << setw (8) << results[1][i]    << setw(8)
<< results[2][i] << endl;
	Delete3DArray(lattice, size, size);
	delete [] cluster;
}
void GenPores ( int ***lattice, double const pstep )
{
	int VoidAmount = int (pstep*size3);
	for (int i=1; i<=VoidAmount; i++ ){
		int x = (int) (rg.Random()*size);
		int y = (int) (rg.Random()*size);
		int z = (int) (rg.Random()*size);
//generate randomized coordinates x, y, and z of
pores
		if ( lattice[x][y][z] == 0 )
```

```
                                lattice[x][y][z] = x * size *
size + y * size + z + 1;
                        else{ i--;}
                }
}

void MarkCluster ( int ***lattice )
{
        int i = 0;
        int j = 0;
        int k = 0;
        int iteration = 0;
        int Mark = 0;
        int mini = 0;

        do
        {Mark = 0;
        iteration++;
        for ( i=0; i<size; i++ ){
                for ( j=0; j<size; j++ ){
                        for ( k=0; k<size; k++ ){
                                if ( lattice[i][j][k] ==
0 )
        continue;
        else if ( lattice [i][j][(k+1)%size] > lattice
[i][j][k]){
                lattice [i][j][(k+1)%size] = lattice
        [i][j][k];
                Mark = 1;}
        else if (lattice [i][j][(k+size-1)%size] > lattice
[i][j][k]){
                lattice [i][j][(k+size-1)%size] =
        lattice [i][j][k];
                Mark = 1;}
        else if ( lattice [i][(j+1)%size][k] > lattice
[i][j][k]){
                lattice [i][(j+1)%size][k] = lattice
[i][j][k];                              Mark = 1;}
        else if ( lattice [i][(j+size-1)%size][k] >
lattice [i][j][k] ){
                lattice [i][(j+size-1)%size][k] =
lattice [i][j][k];
                Mark = 1;}
        else if (( i < size-1 ) && ( lattice [i+1][j][k] >
lattice [i][j][k] )){
                lattice [i+1][j][k] = lattice [i][j][k];
                Mark = 1;}
        else if (( i > 0 ) && ( lattice [i-1][j][k] > lattice
[i][j][k] )){
                lattice [i-1][j][k] = lattice [i][j][k];
                Mark = 1;}
                        }
                }
        }
}
        while ( Mark );
}

void clustersize (int ***lattice, int* cluster)
{
        for (int i=0; i<size3; i++)
                cluster[i] = 0;
        for (int i=0; i<size; i++){
                for (int j=0; j<size; j++){
                        for (int k=0; k<size; k++){
                                if (lattice[i][j][k] !=
0)                              cluster[lattice[i][j][k]-
1]++;}//the cluster size corresponds to (i,j,k), starts
from 0, to size*size*size-1
                        }
        }
}

double mean_freepath ( int ***lattice, const double&
P )
{
        int i = 0;
        int j = 0;
        int k = 0;
        int total_surface = 0;
        for ( i=0; i<size; i++ ){
                for ( j=0; j<size; j++ ){
                        for ( k=0; k<size; k++ ){
                                if ( lattice[i][j][k] ==
0 )
        continue;
                                if (( k < size-1 ) &&
( lattice [i][j][k+1] == 0 ))
        total_surface++;
                                if (( k > 0 ) &&
( lattice [i][j][k-1] == 0 ))
        total_surface++;
                                if (( j < size-1 ) &&
( lattice [i][j+1][k] == 0 ))
        total_surface++;
                                if (( j > 0 ) &&
( lattice [i][j-1][k] == 0 ))
        total_surface++;
                                if (( i < size-1 ) &&
( lattice [i+1][j][k] == 0 ))
        total_surface++;
                                if (( i > 0 ) &&
( lattice [i-1][j][k] == 0 ))
        total_surface++;
                                }
                        }
        }
        double mean_free = 4*double
(size3)*P/double ( total_surface );
        return mean_free*poresize;
}

void Statistical ( int ***lattice, double P )
{
        int i = 0;
        int j = 0;
        int k = 0;
        int l = 0;
        int index_number = 0;
        int LatticeVol = size*size*size;
        int totalpore = int (P * LatticeVol);
        int escape_volum = 0;
        double sum_z = 0.0;
        int cluster_number = 0;
```

```
	int *clustervolum;
	int *clusterZdepth;
	double escape =0.0;
	double average_z = 0.0;
	double surface_average_z = 0.0;
	int surfacesumZ = 0;
	int percolate=0;

	clustervolum = new int[LatticeVol];
	clusterZdepth = new int [LatticeVol];
	for (i=0; i<LatticeVol; i++){
		clustervolum [i] = 0;
		clusterZdepth [i] =0;}

	for ( i=0; i<size; i++ ){
		for ( j=0; j<size; j++ ){
			for ( k=0; k<size; k++ )    {
				if ( lattice[i][j][k] !=
0 ){
	index_number = lattice[i][j][k] -1;
	clustervolum[index_number]++;
	if ( lattice[i][j][k] <= i * size * size + j * size +
k + 1 )
	clusterZdepth [index_number] = i -
index_number / (size * size) + 1;}
				}
		}
	}

	for ( i=0; i<size*size*size; i++ ){
		if ( clustervolum[i] == 0 )
			continue;
		else{
	clusterZdepth[i] = clusterZdepth[i] *
clustervolum[i];
			cluster_number++;
			sum_z += clusterZdepth [i];}
	}
	for ( i=0; i<size*size; i++ ){
		escape_volum += clustervolum[i];
		surfacesumZ += clusterZdepth[i];}
	for ( j=0; j<size; j++ ){
		for ( k=0; k<size; k++ ){
			if ( lattice[size-1][j][k] < size
* size && lattice[size-1][j][k] != 0 ){
				percolate = 1;
				break;
			}
		}
	}
	if ( percolate == 1 ){
		ofstream outPercoFile( "perco.dat",
ios::app );
		if ( !outPercoFile ){
			cerr << "File could not be
opened" << endl;
			exit (1);}
		outPercoFile << setw (4) << P <<
setw (4) << 1 << ' ';
	}
	else{
		ofstream outPercoFile( "perco.dat",
ios::app );
		if ( !outPercoFile ){
			cerr << "File could not be
opened" << endl;
			exit (1);}
		outPercoFile << setw (4) << P <<
setw (4) << 0 << ' ';}
	escape = double (escape_volum)/
double( totalpore );
	surface_average_z = double (surfacesumZ) /
double ( escape_volum );
	average_z = double (sum_z) / (double
( totalpore ));
	ofstream outResultsFile( "results.dat",
ios::app );

	if ( !outResultsFile ) {
		cerr << "File could not be opened"
<< endl;
		exit (1);
	}

	outResultsFile << setw (4) << P
	<< setw (12) << escape
	<< setw (12) << average_z
	<< setw (12) << surface_average_z
	<< setw (10) << cluster_number << endl;
	delete [] clustervolum;
	delete [] clusterZdepth;
}

double PosImplant ( int ***lattice, double P, double
energy ) //intensity is weight just by marhkovian
distribution, no Ps diffusion length is considered
{
	double T[size+1] = {1}; // transmitted
positrons
	double weight[size+1] = {0}; //weight at
every layer which is decided by beam energy and
Marhkovian distribution
	double filmthickness = (double)size*poresize;
	double z_bar =
40.0/sqrt(2.0)/walldensity*pow(energy,1.6); //z_bar
is 164 at energy 3.0keV
	double z0=2.0/sqrt(PI)*z_bar; //z0=185 at
3.0keV
	for (int z=1; z<=size; z++ )
	{
		T[z] =(double) exp(-(double
(z*poresize)/double
(z0))*(double(z*poresize)/double(z0)));
		weight[z] =T[z-1] - T[z]; //the
fraction of positron stop at layer z
	}
	double microporeweight = 0.0;
	double vacuumweight = 0.0;
	double mesoporeweight = 0.0;
	double totalweight = 0.0;
	for (int i=0; i<size; i++ ){
		for (int j=0; j<size; j++ ){
			for (int k=0; k<size; k++ ){
```

```
                                        if ( lattice[i][j][k] ==
0 )                                     microporeweight
+= weight[i+1];
                                    else if (lattice[i][j][k]
<= size*size)
            vacuumweight += weight[i+1];
                                        else
            mesoporeweight += weight[i+1];}
                    }
            }
            double absimicro =
microporeweight/double(size*size);
            double absimeso =
mesoporeweight/double(size*size);
            double absivac =
vacuumweight/double(size*size);
            return absivac/(absimeso+absivac);
}

//second version of function posimplant, diffusion
length is considered, used incombination with
function diffusion(int***, int, int, int);
double PosImplant2 ( int ***lattice, double P, double
energy )
{
//          cout << " Positron Implantation Simulation
Results " << endl;
            double T[size+1] = {1}; //
            double weight[size+1] = {0}; //weight at
every layer which is decided by beam energy and
Marhkovian distribution
            double z_bar =
40.0/sqrt(2.0)/walldensity*pow(energy,1.6); //z_bar
is 164 at energy 3.0keV
            double z0=2.0/sqrt(PI)*z_bar; //z0=185 at
3.0keV
            for (int z=1; z<=size; z++ )
            {
                    T[z] =(double) exp(-(double
(z*poresize)/double
(z0))*(double(z*poresize)/double(z0)));
                    weight[z] =T[z-1] - T[z]; //the
fraction of positron stop at layer z
            }
            double microporeweight = 0.0;
            double vacuumweight = 0.0;
            double mesoporeweight = 0.0;
            for (int i=0; i<size; i++ ){
                    for (int j=0; j<size; j++ ){
                            for (int k=0; k<size; k++ ){
                                    if ( lattice[i][j][k] ==
0  ){
            string diff = diffusion(lattice, i, j, k);
            if (diff == "vacuum")
                    vacuumweight += weight[i+1];
                            else if (diff == "meso")
            mesoporeweight += weight[i+1];
                            else
            microporeweight += weight[i+1];}
                            else if (lattice[i][j][k] <=
size*size)
            vacuumweight += weight[i+1];
                                    else
            mesoporeweight += weight[i+1];}
                            }
                    }
            }
            double absimicro =
microporeweight/double(size*size);
            double absimeso =
mesoporeweight/double(size*size);
            double absivac =
vacuumweight/double(size*size);
            return absivac/(absivac+absimeso);
}

string diffusion (int*** lattice, int i, int j, int k)
{
            int diffulgth = 1;
            if (i<diffulgth)
                    return "vacuum";
            bool meso = false;
            bool vacuum = false;
            for ( int ii=-diffulgth; ii<= diffulgth; ii++){
                    for (int jj=-diffulgth; jj<= diffulgth;
jj++){
                            for (int kk=-diffulgth;
kk<=diffulgth; kk++){
                                    if (lattice[min(size-
1,(i+ii))][(j+jj+size)%size][(k+kk+size)%size] >difful
gth*size*size)
                                            meso =
true;
                                    else if
(lattice[min(size-
1,(i+ii))][(j+jj+size)%size][(k+kk+size)%size] >0)
                                            vacuum =
true;}
                    }
            }
            if (vacuum) return "vacuum";
            if (meso) return "meso";
            return "micro";
}

double MonteCarlo (int *** lattice, double P,  double
Beamenergy, int* cluster)// Positrons are implanted
by Monte Carlo method, the stopping positron is
distributed as Marhkovian distribution
//and evenly distributed over the x-y plane
{
            int totalpos = 10000;
            double z_bar =
40.0/pow(2.0,0.5)/walldensity*pow(Beamenergy,1.6
); //z_bar is 164 at energy 3.0keV
            double z0=2.0/sqrt(PI)*z_bar; //z0=185 at
3.0keV
            int vacuumcount = 0;
            int mesoporecount = 0;
            int microporecount = 0;
            int ps = totalpos;
            for (int i=0; i<totalpos; i++){
                    cout << i << " positrons generated
\r";
```

```
                double x = rg.Random()*size; //
generate a positron at x, y cooridnate
                double y = rg.Random()*size;
                double z = z0*sqrt(-log(1.0-
rg.Random()))/poresize; //reverse of the cumulative
probability function 1-exp(z/z0)^2.
                int count = 0; //number of cells that
positron can penetrate
                while(z>0.0){
                        if
(lattice[count][(int)y][(int)x] ==0) // if that position
is wall material, then it is counted as the penetration
depth
                                z-=1.0;
                        count++; // count the total
length it traveled, including wall and voids
                        if (count==size) break;}//if
it can penetrate the whole lattice depth, it will end
into the substrate and won't be counted
                z = z + (double)count;
                if (z>size) continue;
                string diff =
diffusion2(lattice,x,y,z,cluster); //return if the Ps
diffuse into closed mesopores or open pores.
                if (diff == "vacuum")
                        vacuumcount ++;
                else if (diff == "meso")
                        mesoporecount ++;
                else
                        microporecount ++;
        }
        double ivac =
(double)vacuumcount/(double)ps;
        double imeso =
(double)mesoporecount/(double)ps;
        double imicro =
(double)microporecount/(double)ps;
        ofstream outIntensityFile( "intensity.dat",
ios::app );
       outIntensityFile << setw (6) << P << setw(10)
<< ivac << setw(10) << imeso << setw(10) << imicro
<< endl;
        return ivac/(ivac+imeso); //return fesc
}

string diffusion2(int*** lattice, double x, double y,
double z, int* cluster)// diffusion from any position
(x,y,z) with controllable diffusion length. x,y,z will
finally be rounded to integers.
{// the probability of diffusing into mesopores and
vacuum is different
        if (z<=diffulgth) return "vacuum";
        int xmin = int((x-diffulgth)+size)%size;
        int xmax = int((x+diffulgth)+size)%size;
        int ymin = int((y-diffulgth)+size)%size;
        int ymax = int((y+diffulgth)+size)%size;
        int zmin = min(size-1, (int)(z-diffulgth));
        int zmax = min(size-1, (int)(z+diffulgth));
        int i=abs(zmax-zmin+size)%size;//max
could be smaller than min because of the periodic
boundary condition
        int j=abs(ymax-ymin+size)%size;
        int k=abs(xmax-xmin+size)%size;
        vector <int> traps;
        int index = -1;
        for ( int ii=0; ii<=i; ii++){
                for (int jj=0; jj<=j ; jj++){
                        for (int kk=0; kk<=k; kk++){
        int xxx=(xmin+kk+size)%size;// the index of
lattice that the Ps can diffuse into
        int yyy=(ymin+jj+size)%size;
        int zzz=(zmin+ii+size)%size;
        index = lattice[zzz][yyy][xxx];
        if (index == 0) continue; // index is zero-
>wall material
        if (distance(xxx,yyy,zzz,x,y,z)>diffulgth)
continue;
        bool exist = false; //if the mesopore with the
same index has not appeared before within the
diffusion length range, exist=false
        for (int a=0; a<traps.size(); a++){ // how
many available traps/mesopores exist, for the first
trap, traps.size()=0, skip to (!exist)
        if (traps[a] == index)// if has the same index,
count as one big cluster, and not count as one new
trap
        exist = true;}
                if (!exist)
        traps.push_back(index);  // traps keeps track
of the available pores around with their index
numbers.
                                }
                        }
        }// traps[] records the distinct mesopores
indices that are not connected with each other and all
within the diffusion length range (different indices)
        double total = 0;
        vector <double> cumu;
        for (int i=0; i<traps.size(); i++){ // iterate
through all the distinct traps around within the
diffusion length
//              if (traps[i]>size*size)
                        total += 1.0;//(1.0+
(diffulgth *diffulgth) / pow((double)cluster[traps[i]-
1], 2.0/3.0)); //total weight of probability of diffusing
into these pores
//              else
//                      total += 1.0;
                cumu.push_back(total);}//store the
accumulative weight in elements of traps.
        double prand =
rg.Random()*(max(total,1.0));     //generate a
random number in the range from 0 to max(total,1)
        index = -1; // reset the index;
        for (int i=0; i<cumu.size(); i++){
                if (prand < cumu[i]){
                        index = traps[i]; //index
starts from 1 to size*size*size
                        break;}}
        if (index > size*size)
                return "meso";
        else if (index >0)//{
//              if (escape(xxx, yyy, zzz))
                        return "vacuum";
```

```
//                      else
//                              meso = true;}
        return "micro";
}

//using the Monte Carlo function to calculate the 50% escape depth as the interconnection length
double interlgth(int *** lattice, double P, int* cluster)
{
        double fesc =0.0;
        double i=0.0;
        double Lint = 0.0;
        for (i=0.1; i<6.0; i+=0.1){
                fesc = PosImplant (lattice, P, i ); // use the no diffusion version of the fesc
//                      fesc = PosImplant2 (lattice, P, i); // use the round diffusion length
//                      fesc = MonteCarlo (lattice, P, i, cluster ); // use the real diffusion length calculated between the site and the position of the Ps
                cout << "energy " << i << "   fesc=  " << fesc << "          " << endl;
                ofstream outFescFile( "fesc.dat", ios::app );
                if ( !outFescFile ) {
                        cerr << "File could not be opened" << endl;
                        exit (1);}
        outFescFile << setw (8) << fesc << endl;
        if (fesc >0.5) Lint = i;
        }
        return 40.0/sqrt(2.0)/walldensity*pow(Lint,1.6);
}

bool escape (int x, int y, int z) //given the x,y,z of the Ps diffusion starting point, check if that Ps can diffuse out of the film through open pores.
{
//phenomilogically we assume this probability of escaping is proportionally decreasing according to the depth of Ps.
        double esc = 0.01;
        double pesc = exp(-z*esc);
        if (rg.Random()<pesc)
                return true;
        else
                return false;
}

double distance(int xxx, int yyy, int zzz, double x, double y, double z)
{
// the actual range of xxx, yyy, zzz is xxx->(xxx+1)%size, yyy->(yyy+1)%size, zzz->(zzz+1)%size
// we need to find the minimum distance from x to either xxx or (xxx+1)%size in x component, and similarly other components
// xd should also consider the boundary condition
        double xd = max(min(abs(double(x-xxx-0.5)),(double)size-abs(double(x-xxx-0.5)))-0.5,0.0);
        double yd = max(min(abs(double(y-yyy-0.5)),(double)size-abs(double(y-yyy-0.5)))-0.5,0.0);
        double zd = max(min(abs(double(z-zzz-0.5)),(double)size-abs(double(z-zzz-0.5)))-0.5,0.0);
        double d = sqrt(xd*xd + yd*yd + zd*zd);
        return d;
}

bool PsRandWalk(double depth)// give the  Ps diffusing out probability from a certain depth using 1 dimensional random walk
{
        double step = 1; // step length
        double Pdecay = 0.0001;
        double L = 0.0;
        for (;;)
        {
                if (rg.Random() < Pdecay)
                        return false;                   // if the random generator generates a number less than the decay probability, Ps annihilates and function returns false

                                                        // which means the Ps won't escape the film
                switch(int(rg.Random()*2.0)%2){
                case 0:
                        L += step;
                        break;
                case 1:
                        L -= step;}
                if (L> depth)
                        return true;                    // Once the random walk displacement is larger than the depth, return true; Ps can escape;
        }
}

double PsEscP (double depth) // given the implantation depth, return the escape probability solely decided by the 1-d Monte Carlo random walk model
// no pore structure is considered
{
        int success = 0;
        int total = 1000;
        for (int i=0; i<total; i++)
                success += (int)PsRandWalk(depth);
        double EscP = (double) success/(double)total;
        return EscP;
}

void PsEscCalibration ()
{
        const int Maxdepth = 100;
        vector <double> cali;
        for (int i=0; i< Maxdepth; i++){
                cali.push_back(PsEscP(i));
                cout << cali[i] << endl;}
}
```

## E.2 Monte Carlo simulation of spherical pores in a continuum space

```
#include "point.h"
#include "Rt.h"
#include "randomc.h"
#include <stdio.h>
#include <math.h>
#include <time.h>
#include <iostream>
#include <fstream>
#include <iomanip>
#include <vector>
#include <string>

using namespace std;

#define sq(x) ((x)*(x))
#define cube(x) ((x)*(x)*(x))
#define PI 3.14159265359
#define EMPTY (-N)

const int size = 200;
const int N = size*size*size;
const int pslimit = (int)(N * 0.5);
const double rMax = 1.0;
const double rMin = sqrt(3.0)/2.0; //rMin has to be
larger than or equal this number, then the real space
is size/rMin if we normalize the spheres
int big = 1;
// for each index, there is only one pore corresponds
to it. In every lattice cell, there is at most one pore
exists.
const double E = 2.0;
// the implantation energy
const double walldensity = 2.0;
// the film density
const double poresize = 2.0;
const double diffulgth = 1.0;
int32 seed = (int32) time(0);
// random seed
point pore[N] = {0};        //Generate an array of
pores contain N elements
int cluster[pslimit] = {0};
int order[N];
Rt lrt[N] = {0};
TRandomMersenne rg(seed);

inline double v(double r)
{ return PI * cube(2*r) / 6.0;}
int GeneratePore(point*);
int PlacePore (int n, point* npt);
void move();
double distance(double, double, double, int);
double CalcDistance (int nn, point* npt);
int FindAndConnect (int n, int nn);
int FindRoot (int i);
int CalcControl (int i);
bool Percolation ();
void RandomCheck ();
void PoreStats (double p);
void MeanPoreVol (int n);
void MeanPoreLength (int n);
string diffusion(point pore[], double x, double y,
double z);
double MonteCarlo (point pore[], double P,  double
Beamenergy);
void LengthDistribution (int n);

void main ()
{
        for (int i=0; i<N; i++)//initilization
        {
                pore[i].x = 0;
                pore[i].y = 0;
                pore[i].z = 0;
                pore[i].root = -N; //root record the
pore it points to in a cluster, if -N, it's isolated
        }
        double phiC = 0;
        double phiTC = 0;
        int pMax = 0;
        //placing pore iteration
        for (int i=0; i<N; i++)      {
                point* npt = new point;
                int index = GeneratePore (npt); //
generate the x,y,z coordinates of the pore
                int nn = PlacePore (index, npt);
                if ( nn == -1 )
                        i--;
                else{
                        double phi = 100*
(double)(i + 1) * v(rMin) / (double)N;
//cout << setw(3) << (int) phi << " % porosity\r";
                        if (!Percolation ()){
                                phiC = phi/100;
                                phiTC = (double)(i
+ 1) * v(rMax) / (double)N;}
                        if
(i%(int(size*size*0.3))==0){
        cout << "P is " << phi << "                    "
<< endl;
//MonteCarlo(pore, phiTC*100.0, E); // generate
positrons and simulate the diffusion
                PoreStats (phi);
                MeanPoreVol (i+1);
                MeanPoreLength (i+1);
                LengthDistribution (i+1);}
                }
                delete npt;
        }
```

```
	cout << "pMax is " << pMax << endl;
	cout << "phic is " << phiC << endl;
	cout << "phiTC is " << phiTC << endl;
}

int GeneratePore(point* pt)
{
	pt->x = rg.Random() * size;
// any position within the space size^3
	pt->y = rg.Random() * size;
	do{
		pt->z = -log(1-rg.Random()) *
(double)size/5.0;}
	while (pt->z >size);
	int index = (int)pt->z * sq(size) + (int)pt->y *
size + (int)pt->x;
// index is unique for a certian position
	return index;
}

int PlacePore (int n, point* npt) //given the index n
and the new *npt points to a new pore. return -1 if
the new pore can not be located, and return 1 if
successful.
{
	if(pore[n].root!=EMPTY)
// for each 1x1x1 space, it can only contain at most
one sphere with rMin = sqrt(3)/2.
		return -1;
// so if a new generated sphere has the same index, it
can not fit into that space, no need to check their
distance
	int i0 = n/(size*size);
// convert the index back to coordinates
	int j0 = (n-i0*size*size)/size;
	int k0 = n-i0*size*size-j0*size;
	const int range = int(ceil(2.0*rMax));	//
range from one side, when rMax =1, range = 2.
	static const int range3 =
125;//(2*range+1)*(2*range+1)*(2*range+1); // the
total 3d range needs to be searched
//	double (*d)[2]=new double [range3][2];

//search through occupied list, nerest 125 cells
(when rMax =1). it is decided by the outer radius how
many neighbor space needs to be searched
	double d[125][2] ={0};
	for (int i=0; i<2; i++){
		for (int j=0; j<range3; j++){
			d[j][i] = 0;}}
	for (int i=-range; i<=range; i++)
// search range is (2*range+1)^3 when rMax is
integer
	{
		for (int j=-range; j<=range; j++)
		{
			for (int k=-range; k<=range;
k++){
			int neighbor =
((i0+i+size)%size)*size*size+((j0+j+size)%size)*size
+(k0+k+size)%size; //index of the neighboring pore
			int di =
(i+range)*(2*range+1)*(2*range+1)+(j+range)*(2*ra
nge+1)+k+range; // the count of its connected
neighbor
			if (pore[neighbor].root !=
EMPTY){
d[di][0] = CalcDistance(neighbor, npt);
// distance to its neighbor
d[di][1] = neighbor;
if (d[di][0] <= 2*rMin)
	return -1;}
			}
		}
	}
	pore[n].x = npt->x;// if pass the check, the
new pore is located at x, y, z
	pore[n].y = npt->y;
	pore[n].z = npt->z;
	pore[n].root = -1; // itself is the root , with
size 1 before connected to any other pores. -x means
it's the root, with the cluster size x.
	int r1 = n;
	// .root positive means pointing to another
pore index
	for(int i=0; i<range3; i++){
if (d[i][0] != 0 && d[i][0] < 2*rMax)
	r1 = FindAndConnect(r1,(int)d[i][1]);
	}
	return 1;
}

double CalcDistance (int nn, point* npt)
{
	return distance(npt->x,npt->y,npt->z,nn);
}

int FindAndConnect (int n, int nn)
{
	int r1 = n;
	int r2 = FindRoot (nn);
	if (r2!=r1){
	if(pore[r1].z>pore[r2].z){ // if the r1 depth is
deeper than r2, use r2 as the root. (so root is always
the closest to the surface in a certian cluster)
		pore[r2].root += pore[r1].root;
		pore[r1].root = r2;
		r1 = r2;}
	else{
		pore[r1].root += pore[r2].root;
		pore[r2].root = r1;}
	if (-pore[r1].root > big)
		big = -pore[r1].root;}
	return r1;
}

int FindRoot (int i)
{
	if (pore[i].root<0)
		return i;
	return pore[i].root = FindRoot(pore[i].root);
}
```

```
bool Percolation ()
{
	for (int i=N-size*size; i<N; i++){
		if (pore[i].root != EMPTY &&
pore[FindRoot(i)].root == -big){
			for (int j=0; j<size; j++){
	if (pore[j].root != EMPTY &&
pore[FindRoot(j)].root == -big){
	return true;}
		}
	}
	}
	return false;
}

void RandomCheck()
{
	cout << "Checking the randomness of the
pores..." << endl;
//pore number distribution over layer
	for (int i=0; i<size; i++){
		int counter = 0;
		for (int j=0; j<size*size; j++){
			if
(pore[i*size*size+j].root != EMPTY)
	counter ++;}
cout << "layer [" << i << "] " << counter << endl;}
}

void PoreStats (double p)
{
	for (int i=0; i<pslimit; i++){
		cluster[i] = 0;}
	for (int i=0; i<N; i++){
		if (pore[i].root != EMPTY &&
pore[i].root < 0)
		cluster[-pore[i].root-1] ++;}
	cout << endl;
}

void MeanPoreVol (int n)
//weighted by volumes
{
	int sigmaNV = 0;
	int sigmaV = n;
	for (int i=0; i<pslimit; i++){
		if (cluster[i] != 0)
			sigmaNV += cluster[i] * sq(i
+ 1);}
	double mpv = (double)sigmaNV /
(double)sigmaV;
	cout << mpv << endl;
}

void MeanPoreLength (int V)
{
	for (int i=0; i<N; i++){
		lrt[i].zmax = -N-1;
		lrt[i].zmin = -N-1;
	}
	for (int i=0; i<N; i++)	{
		if (pore[i].root == EMPTY)
			continue;
		else if (pore[i].root < 0){
if (lrt[i].zmax < -N)
	lrt[i].zmax = min((pore[i].z + rMax),
(double)size);
if (lrt[i].zmin < -N)
	lrt[i].zmin = max((pore[i].z - rMax), 0.0);
}
else{
	int r = FindRoot (i);
	if (lrt[r].zmax < -N)
	lrt[r].zmax = min(pore[i].z + rMax,
(double)size);
	else if (pore[i].z > lrt[r].zmax)
		lrt[r].zmax = min(pore[i].z + rMax,
(double)size);
	if (lrt[r].zmin < -N)
	lrt[r].zmin = max(pore[i].z - rMin, 0.0);
	else if (pore[i].z < lrt[r].zmin)
	lrt[r].zmin = max(pore[i].z - rMin, 0.0);}
}
double lengthV = 0;
for (int i=0; i<N; i++){
	if (pore[i].root < 0 && pore[i].root != EMPTY)
		lengthV += (lrt[i].zmax - lrt[i].zmin)
* (double)(-pore[i].root);}
double mlength = lengthV / (double)V;
cout << mlength << endl;
ofstream outlength ("meanlength.txt", ios::app);
outlength << setw(12) << (double)V * 100 * 8.0 * PI /
6.0 / (double)cube(size) << setw(16) << mlength <<
endl;
}

void LengthDistribution (int n)
{
	int lnum[size+1];
	int lv[size+1];
	for (int i=0; i<size+1; i++){
		lnum[i] = 0;
		lv[i] = 0;
	}
	for (int i=0; i<N; i++){
		if (lrt[i].zmax != lrt[i].zmin){
			lnum[(int)(lrt[i].zmax -
lrt[i].zmin)] ++;
			lv[(int)(lrt[i].zmax -
lrt[i].zmin)] += -(double)pore[i].root * PI * 8.0 / 6.0;}
	}
	ofstream outl ("lengthndistribution.txt",
ios::app);
	for (int i=1; i<size+1; i++)
		outl << setw(12) << (double)n * 100
* 8.0 * PI / 6.0 / (double)cube(size)
		<< setw(8) << i << setw(10) <<
lnum[i] << setw(10) << lv[i] << endl;
}

double MonteCarlo (point pore[], double P,  double
Beamenergy)// Positrons are implanted by Monte
Carlo method, the stopping positron is distributed as
Marhkovian distribution
```

```
//and evenly distributed over the x-y plane
{
	int totalpos = 10000;
	double z_bar =
40.0/pow(2.0,0.5)/walldensity*pow(Beamenergy,1.6
); //z_bar is 164 at energy 3.0keV
	double z0=2.0/sqrt(PI)*z_bar; //z0=185 at
3.0keV
	int vacuumcount = 0;
	int mesoporecount = 0;
	int microporecount = 0;
	int ps = totalpos;
	for (int i=0; i<totalpos; i++){
		cout << i << " positrons generated
\r";
		double x = rg.Random()*size; //
generate a positron at x, y cooridnate
		double y = rg.Random()*size;
		double z = z0*sqrt(-log(1.0-
rg.Random()))/poresize; //reverse of the cumulative
probability function 1-exp(z/z0)^2.
		int index = (int)x * sq(size) + (int)y *
size + (int)z; // index is unique for a certian position
		int count = 0; //number of cells that
positron can penetrate
		while(z>0.0){
			if (pore[index].root ==
EMPTY) // if that position is wall material, then it is
counted as the penetration depth
				z-=1.0;
			count++; // count the total
length it traveled, including wall and voids
			if (count==size) break;}//if
it can penetrate the whole lattice depth, it will end
into the substrate and won't be counted
		z = z + (double)count;
		if (z>size) continue;
		string diff = diffusion(pore,x,y,z);
//return if the Ps diffuse into closed mesopores or
open pores.
		if (diff == "vacuum")
			vacuumcount ++;
		else if (diff == "meso")
			mesoporecount ++;
		else
			microporecount ++;
	}
	double ivac =
(double)vacuumcount/(double)ps;
	double imeso =
(double)mesoporecount/(double)ps;
	double imicro =
(double)microporecount/(double)ps;
	ofstream outIntensityFile( "intensity.dat",
ios::app );
	outIntensityFile << setw (6) << P << setw(10)
<< ivac << setw(10) << imeso << setw(10) << imicro
<< endl;
	return ivac/(ivac+imeso); //return fesc
}

string diffusion(point pore[], double x, double y,
double z)// diffusion from any position (x,y,z) with
controllable diffusion length. x,y,z will finally be
rounded to integers.
{// the probability of diffusing into mesopores and
vacuum is different
	if (z<=diffulgth) return "vacuum";
	int xmin = int((x-diffulgth-rMin)+size)%size;
	int xmax =
int((x+diffulgth+rMin)+size)%size;
	int ymin = int((y-diffulgth-rMin)+size)%size;
	int ymax =
int((y+diffulgth+rMin)+size)%size;
	int zmin = min(size-1, (int)(z-diffulgth-
rMin));
	int zmax = min(size-1,
(int)(z+diffulgth+rMin));
	int i=abs(zmax-zmin+size)%size;//max
could be smaller than min because of the periodic
boundary condition
	int j=abs(ymax-ymin+size)%size;
	int k=abs(xmax-xmin+size)%size;
	vector <int> traps;
	int index = -1;
	for ( int ii=0; ii<=i; ii++){
		for (int jj=0; jj<=j ; jj++){
			for (int kk=0; kk<=k; kk++){
	int xxx=(xmin+kk+size)%size;// the index of
lattice that the Ps can diffuse into
	int yyy=(ymin+jj+size)%size;
	int zzz=(zmin+ii+size)%size;
	index = zzz * sq(size) + yyy * size + xxx; //
index is unique for a certian cell position;
if (pore[index].root == EMPTY)
	 continue; // If not occupied, continue
if (distance(x,y,z,index) > diffulgth+rMin)
	 continue; // if the distance from the
positron to the pore is larger than the diffusion length,
continue
bool exist = false; //if the mesopore with the same
index has not appeared before within the diffusion
length range, exist=false
for (int a=0; a<traps.size(); a++){ // how many
available traps/mesopores exist, for the first trap,
traps.size()=0, skip to (!exist)
	if (FindRoot(traps[a]) == FindRoot(index))//
FindRoot() returns the index of the root, if has the
same root, count as one big cluster, and not count as
one new trap
			exist = true;}
	if (!exist)
	traps.push_back(FindRoot(index));  // traps
keeps track of the available pores around with their
root index numbers.
				}
			}
	}// traps[] records the distinct mesopores
indices that are not connected with each other and all
within the diffusion length range (different indices)
	double total = 0;
	index = -1;
	vector <double> cumu;
```

```
	for (int i=0; i<traps.size(); i++){
		if (traps[i]>size*size)
			total += 1.0;
//2.0/PI*atan((double)(-pore[traps[i]].root)); //total
weight of probability of diffusing into these pores is
proportional to the cluster size
		else			//the cluster size is
stored in the heat cell with its index
FindRoot(traps[i]), ->root and take the negative
			total += 1.0; // if it is an
open cluster, then the Ps has 100% probability of
diffusing into this cluster
		cumu.push_back(total);}//store the
accumulative weight in elements of traps.
	double prand = rg.Random()*total;
	//generate a random number in the range
from 0 to total
	for (int i=0; i<cumu.size(); i++){
		if (prand < cumu[i]){
			index = traps[i]; //index
starts from 1 to size*size*size
			break;}}
	if (index > size*size)
		return "meso";
	else if (index >0)
//	{
//		if (escape(xxx, yyy, zzz))
			return "vacuum";
//		else
//			meso = true;}
	return "micro";
}

double distance(double x, double y, double z, int nn){
	double dd = sq(min(abs(pore[nn].x-x),(size-
abs(pore[nn].x-x))))	+sq(min(abs(pore[nn].y-
y),(size-abs(pore[nn].y-y))))+sq(pore[nn].z-z);
	// no periodic boundary conditions on z
direction
	return sqrt (dd);
}
```

## E.3 Attractive porogen simulation

```
#include "randomc.h"
#include <iostream>
#include <time.h>
#include <cstdlib>
#include <iomanip>
#include <fstream>
#include <math.h>
#include <stdio.h>

using namespace std;
const int size = 100;
const int size3 = size*size*size;
int32 seed = (int32) time(0); TRandomMersenne
rg(seed);

class site
{
public:
        double potential;
        int label;
};

inline void Intialize2DArray(site **&xxx, long rows,
long cols)
{
        long i, j;
        for (i=0; i<rows; i++){
                for (j=0; j<cols; j++){
                        xxx[i][j].label = 0;
                        xxx[i][j].potential = 0;}
        }
}

template <class T>
void Create2DArray(T **&xxx, long rows, long cols)
{
        xxx = new T *[rows];
        for (long i=0; i<rows; i++){
                xxx[i]=new T[cols];}
        Intialize2DArray(xxx, rows, cols);
}

template <class T>
void Delete2DArray(T **&xxx, long rows)
{
        for(long i=0; i<rows; i++){
                delete []xxx[i];}
        delete []xxx;
        xxx=0;
}

template <class T>
void Create3DArray(T ***&xxx, long n1, long n2, long
n3){
        xxx = new T **[n1];
        for (long i=0; i<n1; i++){
                Create2DArray(xxx[i], n2, n3);
                Intialize2DArray(xxx[i], n2, n3);}
}

template <class T>
void Delete3DArray(T ***&xxx, long n1, long n2)
{
        for (long i=0; i<n1; i++){
                Delete2DArray(xxx[i], n2);}
        delete []xxx;
        xxx=0;
}

void GenPores ( site ***, double );
void MarkCluster ( site *** );
void Statistical ( site ***, double );
void mean_freepath ( site ***, double );
void PosImplant ( site ***, double );
void Potential ( site ***, int, int, int );
void MovePore ( site ***, int, int, int, double );
int MoveDirect ( site***, int, int, int, double );
double CalcForce( site*** , int, int, int, int );
double U ( site***, int, int, int );

double absx ( double x )
{
        if ( x>= 0 )
                return x;
        else
                return -x;
}

int sign ( double x )
{
        if ( x> 0 )
                return 1;
        if ( x == 0 )
                return 0;
        else
                return -1;
}

void main ()
{
        site ***lattice;
        int i = 0;
        int j = 0;
        int k = 0;
        double CriticalForce = 0;

        Create3DArray(lattice, size, size, size);
        for ( i =0; i < size; i++ ){
```

```
                for ( j = 0; j < size; j++ ){
                        for ( k = 0; k < size; k++ ){
        lattice[i][j][k].label = 0;
        lattice[i][j][k].potential = 0;}}}
        cout << "Input the critical force...>=0" <<
endl;
        cin >> CriticalForce;
        ofstream outResultsFile( "results.dat",
ios::app );
        if ( !outResultsFile ){
                cerr << "File could not be opened"
<< endl;
                exit (1);}
        outResultsFile << "size" << size << "CForce"
<< CriticalForce << endl
        << setw (12)  << 'P'
        << setw (12) << "Escape"
        << setw (12) << "Averz"
        << setw (12) << "Surfz"
        << setw (12) << "mfp"
        << endl;
        GenPores ( lattice, CriticalForce );
        Delete3DArray(lattice, size, size);
}

void GenPores ( site ***lattice, double CriticalForce )
{
        double P = 0;
        double P_start = 0;
        double P_stop = 0;
        double step = 0;
        int Start_number = 0;
        int Stop_number = 0;
        int step_number = 0;
int x,y,z = 0;
int i = 0;
cout << "Input the start porosity..." << endl;
cin >> P_start;
cout << "Input the stop porosity..." << endl;
cin >> P_stop;
cout << "Input the porosity step..." << endl;
cin >> step;
Start_number = int (P_start*size3);
Stop_number = int (P_stop*size3);
step_number = int (step*size3);
for ( i=1; i<=Stop_number; i++ ){
        x = rg.Random() *(double) size;
        y = rg.Random() *(double) size;
        z = rg.Random() *(double) size;
//generate randomized coordinates x, y, and z of
pores
if ( lattice[x][y][z].label !=0 ){
        i--;
        continue;}
else
MovePore ( lattice, x, y, z, CriticalForce );
cout << i << "\r";
if ( i >= Start_number && i%step_number == 0 ){
        P = double (i) / double (size3);
        MarkCluster ( lattice );
        Statistical ( lattice, P );
        mean_freepath ( lattice, P );}
        }
}

void Potential ( site *** lattice, int x, int y, int z )
{
        int xx, yy, zz = 0;
        double const k = -0.0001;
        int ii,jj,kk = 0;
        int xtrans, ytrans, ztrans = 0;
        double rrc = 9;
        double rc = 0;
        double rr = 0;

        lattice[x][y][z].potential += -2.5;
        rc= sqrt(rrc);
        for ( xx=x-rc; xx<=x+rc; xx++ ){
                if ( xx < 0 || xx >= size )
                        xtrans = xx - size*
abs(xx)/xx;
                else
                        xtrans = xx;
                for ( yy=y-rc; yy<=y+rc; yy++ )
{
if ( yy < 0 || yy >= size )
        ytrans = yy - size * abs(yy)/yy;
else
        ytrans = yy;
for ( zz=z-rc; zz<=z+rc; zz++ ){
        if ( zz < 0 || zz >= size )
                ztrans = zz - size * abs(zz)/zz;
        else
                ztrans = zz;
rr = (x-xx)*(x-xx)+(y-yy)*(y-yy)+(z-zz)*(z-zz);
        if ( rr > 0 && rr <= rrc )
        lattice[xtrans][ytrans][ztrans].potential +=
k*((rrc/rr)*(rrc/rr)-rrc/rr);
        else
                continue;}
                }
        }
}

void MovePore ( site *** lattice, int x, int y, int z,
double CriticalForce )
{
        int d = 0;
        int step = 0;
        do{
                step++;
                d = MoveDirect ( lattice, x, y, z,
CriticalForce );
                switch (d){
                        case 0:
                                break;
                        case 1:
                                x = x+1;
                                break;
                        case 2:
                                y = y+1;
                                break;
                        case 3:
                                z = z+1;
```

```
                        break;
                case -1:
                        x = x-1;
                        break;
                case -2:
                        y = y-1;
                        break;
                case -3:
                        z = z-1;
                        break;}
        if ( x < 0 || x >= size )
                x = x - size* abs(x)/x;
        else
                x = x;
        if ( y < 0 || y >= size )
                y = y - size* abs(y)/y;
        else
                y = y;
        if ( z < 0 || z >= size )
                z = z - size* abs(z)/z;
        else
                z = z;
    }
    while ( d!=0 && step <=3*size &&
lattice[x][y][z].label == 0 );
    switch (d){
        case 1:
                x = x-1;
                break;
        case 2:
                y = y-1;
                break;
        case 3:
                z = z-1;
                break;
        case -1:
                x = x+1;
                break;
        case -2:
                y = y+1;
                break;
        case -3:
                z = z+1;
                break;}
    if ( x < 0 || x >= size )
        x = x - size* abs(x)/x;
    else
        x = x;
    if ( y < 0 || y >= size )
        y = y - size* abs(y)/y;
    else
        y = y;
    if ( z < 0 || z >= size )
        z = z - size* abs(z)/z;
    else
        z = z;
    lattice[x][y][z].label = x*size*size + y*size + z
+ 1;
    Potential ( lattice, x, y, z );}

int MoveDirect ( site*** lattice, int x, int y, int z,
double CriticalForce ){
    int direct = 0;
    int d = 0;
    double Force, maxF = 0;
    for ( direct = 1; direct <=3; direct++ ){
        Force = CalcForce ( lattice, x, y, z,
direct);
        if ( CriticalForce > absx(Force) ){
            continue;}
        else if ( absx(Force) > maxF ){
            maxF = absx(Force);
            d = direct* sign(Force);}
    }
    return d;
}

double CalcForce( site*** lattice, int x, int y, int z , int
direct ){
    switch ( direct ){
    case 1:
        return (U( lattice, x-1, y, z ) -
U(lattice, x+1, y, z))/2;
    case 2:
        return (U( lattice, x, y-1, z ) -
U(lattice, x, y+1, z ))/2;
    case 3:
        return (U( lattice, x, y, z-1 ) -
U(lattice, x, y, z+1 ))/2;}

}

double U ( site*** lattice, int x, int y, int z )
{
    if ( x < 0 || x >= size )
        x = x - size* abs(x)/x;
    else
        x = x;
    if ( y < 0 || y >= size )
        y = y - size* abs(y)/y;
    else
        y = y;
    if ( z < 0 || z >= size )
        z = z - size* abs(z)/z;
    else
        z = z;
    return lattice[x][y][z].potential;
}

void MarkCluster ( site ***lattice ){
int i = 0;
int j = 0;
int k = 0;
int iteration = 0;
int Mark = 0;
do{
    Mark = 0;
    iteration++;
    for ( i=0; i<size; i++ ){
        for ( j=0; j<size; j++ ){
            for ( k=0; k<size; k++ ){
if ( lattice[i][j][k].label ==0 )
    continue;
```

```
else if ( lattice [i][j][(k+1)%size].label > lattice
[i][j][k].label){
        lattice [i][j][(k+1)%size].label = lattice
[i][j][k].label;
        Mark = 1;}
else if (lattice [i][j][(k+size-1)%size].label > lattice
[i][j][k].label){
        lattice [i][j][(k+size-1)%size].label = lattice
[i][j][k].label;
        Mark = 1;}
else if ( lattice [i][(j+1)%size][k].label > lattice
[i][j][k].label){
        lattice [i][(j+1)%size][k].label = lattice
[i][j][k].label;
        Mark = 1;}
else if ( lattice [i][(j+size-1)%size][k].label > lattice
[i][j][k].label ){
        lattice [i][(j+size-1)%size][k].label = lattice
[i][j][k].label;
        Mark = 1;}
else if (( i < size-1 ) && ( lattice [i+1][j][k].label >
lattice [i][j][k].label )){
        lattice [i+1][j][k].label = lattice [i][j][k].label;
        Mark = 1;}
else if (( i > 0 ) && ( lattice [i-1][j][k].label > lattice
[i][j][k].label )){
        lattice [i-1][j][k].label = lattice [i][j][k].label;
        Mark = 1;}}}
                }
        }
        while ( Mark );
}

void Statistical ( site ***lattice, double P )
{
        int i = 0;
        int j = 0;
        int k = 0;
        int l = 0;
        int index_number = 0;
        int LatticeVol = size*size*size;
        int totalpore = int (P * LatticeVol);
        int escape_volum = 0;
        double sum_z = 0.0;
        int cluster_number = 0;
        int *clustervolum;
        int *clusterZdepth;
        double escape =0.0;
        double average_z = 0.0;
        double surface_average_z = 0.0;
        int surfacesumZ = 0;
        int percolate=0;

        cout <<"P is " << P << "        " << endl;
        clustervolum = new int[LatticeVol];
        clusterZdepth = new int [LatticeVol];
        for (i=0; i<LatticeVol; i++){
                clustervolum [i] = 0;
                clusterZdepth [i] =0;}

        for ( i=0; i<size; i++ ){
                for ( j=0; j<size; j++ ){
                        for ( k=0; k<size; k++ ){
                                if
( lattice[i][j][k].label != 0 ){
        index_number = lattice[i][j][k].label -1;
        clustervolum[index_number]++;

if ( lattice[i][j][k].label <= i * size * size + j * size + k +
1 )
        clusterZdepth [index_number] = i -
index_number / (size * size) + 1;}
                                }
                        }
        }
        for ( i=0; i<size*size*size; i++ ){
                if ( clustervolum[i] == 0 )
                        continue;
else{
        clusterZdepth[i] = clusterZdepth[i] *
clustervolum[i];
        cluster_number++;
        sum_z += clusterZdepth [i];}
}
for ( i=0; i<size*size; i++ ){
        escape_volum += clustervolum[i];
        surfacesumZ += clusterZdepth[i];}
escape = double (escape_volum)/ double( totalpore );
if ( escape_volum == 0 )
        surface_average_z = 0;
else
        surface_average_z  = double (surfacesumZ) /
double ( escape_volum );
average_z = double (sum_z) / (double ( totalpore ));

ofstream outResultsFile( "results.dat", ios::app );
        if ( !outResultsFile ) {
                cerr << "File could not be opened"
<< endl;
                exit (1);}
        outResultsFile  << setw (12) << P
        << setw (12) << escape
        << setw (12) << average_z
        << setw (12) << surface_average_z;
        for ( j=0; j<size; j++ ){
                for ( k=0; k<size; k++ ){
                        if ( lattice[size-1][j][k].label
< size * size && lattice[size-1][j][k].label != 0 ){
                        percolate = 1;
                        break;}
                }
        }
        delete [] clustervolum;
        delete [] clusterZdepth;
}

void mean_freepath ( site ***lattice, double P ){
        int i = 0;
        int j = 0;
        int k = 0;
        int total_surface = 0;
        double mean_free = 0.0;

        for ( i=0; i<size; i++ ){
```

```
for ( j=0; j<size; j++ ){
        for ( k=0; k<size; k++ ){
                if ( lattice[i][j][k].label == 0 )
                        continue;
                if (( k < size-1 ) && ( lattice
[i][j][k+1].label == 0 ))
                        total_surface++;
                if (( k > 0 ) && ( lattice [i][j][k-
1].label == 0 ))
                        total_surface++;
                if ( k==0 || k==size-1 )
                        total_surface++;
                if (( j < size-1 ) && ( lattice
[i][j+1][k].label == 0 ))
                        total_surface++;
                if (( j > 0 ) && ( lattice [i][j-
1][k].label == 0 ))
                        total_surface++;
                if ( j == 0 || j==size-1 )
                        total_surface++;
                if (( i < size-1 ) && ( lattice
[i+1][j][k].label == 0 ))
                        total_surface++;
                if (( i > 0 ) && ( lattice [i-
1][j][k].label == 0 ))
                        total_surface++;
                if ( i == size-1 )
        total_surface++;}
        }
}
mean_free = 4 * double (size3 ) * P / double
( total_surface );
ofstream outResultsFile( "results.dat", ios::app );

if ( !outResultsFile ) {
        cerr << "File could not be opened" << endl;
        exit (1);}
        outResultsFile << setw(12) << mean_free <<
endl;
}

void PosImplant ( site ***lattice, double P )
{
        int z = 0;
        double z0 = 0;
        int i = 0;
        int j = 0;
        int k = 0;
        double openvol = 0;
        double closevol = 0;
        double *clustervol = 0;
        double T[size+1] = {0};
        double weight[size+1] = {0};
        double z_bar = 0;
        double escape_frac = 0;
        double z_045 = 0;
        double z_055 = 0;
double z_05  = 0;

clustervol = new double[size*size*size];
T[0]=1;
for ( z_bar=1.0; z_bar<=size; z_bar+=0.1 ){
        for (i=0; i<size*size*size; i++)
                clustervol [i] = 0;
        z0 = z_bar/0.886226925452758;
        openvol = 0;
        closevol = 0;
        for ( z=1; z<=size; z++ ){
                T[z] = exp(-(double (z)/z0)*(double
(z)/z0));
                weight[z] = T[z-1] - T[z];}
                for ( i=0; i<size; i++ ){
                        for ( j=0; j<size; j++ ){
                                for ( k=0; k<size;
k++ ){
if ( lattice[i][j][k].label  == 0 )
        continue;
else
        clustervol[lattice[i][j][k].label -1] +=
weight[i+1];}
        }
}
for ( i=0; i<size*size; i++ )
        openvol += clustervol[i];
for ( i=size*size; i<size*size*size; i++ )
        closevol += clustervol[i];
escape_frac = double (openvol)/ double
(closevol+openvol);
if ( escape_frac > 0.5 ){
        z_055 = z_bar;}
if ( escape_frac < 0.4 )
        break;
ofstream outResultsFile( "results.dat", ios::app );
if ( !outResultsFile ) {
        cerr << "File could not be opened" << endl;
        exit (1);}
outResultsFile << setw (12) << z_055 << endl;
cout << "  z_bar is " << z_055 << "   escape is " <<
escape_frac << endl;
if ( z_bar > size ){
cout << " 50% escape depth cannot be found " <<
endl;
ofstream outResultsFile( "results.dat", ios::app );
if ( !outResultsFile ){
        cerr << "File could not be opened" << endl;
        exit (1);}
outResultsFile << setw (12) << size << endl;}
        delete [] clustervol;
}
```

## E.4 Random walk simulation

```
#include "stdafx.h"
#include <vector>
#include <fstream>
using namespace std;

const int size = 100;

const int r = 3;
const int size3 = size * size * size;
int *lattice = new int[size3];
bool (*bond)[3] = new bool[size3][3];
double pmax = 0;
double pstep = 0;
double pgrow = 0;
double pdirect = 0.01;
int32 seed = (int32) time(0);
TRandomMersenne rg(seed);
vector <double> *result = new vector<double> [5];
void initial();
void outputl();
void generate();
int putnew(int&, int&, int&);
int grow(int&, int&, int&, int);
void walk(int&, int&, int&, int);
void MarkCluster();
void CalcCluster(double);
void mfp(int);
void outputf();
inline int xyzn(int x, int y, int z){
return x*size*size + y*size + z;}

int main()
{
        initial();
        generate();
        outputf();
        delete [] lattice;
        return 0;
}

void initial()
{
        for (int i=0; i<size3; i++){
                lattice[i] = 0;
                for (int j=0; j<3; j++)
                        bond[i][j] = false;
        }
        cout << "Stop porosity:";
        cin >> pmax;
        cout << "Porosity step:";
        cin >> pstep;
        cout << "Grow probability:";
        cin >> pgrow;
}

void outputl()
{
        for (int i=0; i<size; i++){
                for (int j=0; j<size; j++){
                        for (int k=0; k<size; k++){
cout << setw(3) << lattice[xyzn(i,j,k)];
if(bond[xyzn(i,j,k)][2])
        cout << "-";
else
        cout << " ";}
cout << endl;
for(int k=0; k<size; k++){
        if(bond[xyzn(i,j,k)][1])
                cout <<"  | ";
        else
                cout << "    ";}
        cout << endl;}
cout << endl;}
}

void generate()
{
        int count = 0;
        double p = 0;
        int x = 0;
        int y = 0;
        int z = 0;
        int olddirection = -1;
        cout << " Porosity " << " escape frac "
         << "surface z " << "average z " << "     mfp"
         << endl;
        for (;;){
        double r = rg.Random();
if (pgrow < r || count == 0 || olddirection == -1)
        olddirection = putnew(x, y, z);
else
        olddirection = grow(x, y, z, olddirection);
if (olddirection >= 0){
        count++;
        p = (double)count/(double)size3;
        cout << pmax*size3 - count << " pores to be
generated... \r";}
else
        continue;
if (pstep != 0 && count%int(pstep*size3) == 0){
        MarkCluster();
        CalcCluster(p);
        outputl();
        mfp(count);}
if (count >= int(pmax*size3))
        break;
        }
}
```

```
int putnew(int& x, int& y, int& z)
{
	x = rg.IRandom(0,size-1);
	y = rg.IRandom(0,size-1);
	z = rg.IRandom(0,size-1);
	if(lattice[xyzn(x,y,z)] != 0)
		return -2;
	int end = 0;
	for(int d=0; d<6; d++){
		int x1 = x;
		int y1 = y;
		int z1 = z;
		walk(x1, y1, z1, d);
if(lattice[xyzn(x1,y1,z1)] != 0){
	end ++;
	x1 = x;
	y1 = y;
	z1 = z;
	switch (d){
	case 3:
		x1 = (x+size-1)%size;
		break;
	case 4:
		y1 = (y+size-1)%size;
		break;
	case 5:
		z1 = (z+size-1)%size;
		break;
	}
	bond[xyzn(x1,y1,z1)][d%3] = true;}
}
if (end >0){
	lattice[xyzn(x,y,z)] = xyzn(x,y,z) + 1;
	return rg.IRandom(0,5);}
	else{
		bool nn = false;
		for(int i=-r; i<r+1; i++){
			for(int j=-r; j<r+1; j++){
				for(int k=-r; k<r+1;
k++){
	if(lattice[xyzn((x+i+size)%size,(y+j+size)%si
ze,(z+k+size)%size)] != 0){
					x = (x+i+size)%size;
					y = (y+j+size)%size;
					z = (z+k+size)%size;
					 nn = true;}
					 }
				}
			}
			if(nn)
				return -2;
			else{
				lattice[xyzn(x,y,z)] =
xyzn(x,y,z) + 1;
				return rg.IRandom(0,5);}
	}
}

int grow(int& x, int& y, int& z, int d)
{
	int direction = -1;
	if (d<0)
		d = rg.IRandom(0,5);
	int olddirection = d;
	vector<int> check;
	for(int i=0; i<6; i++){
		int x1 = x;
		int y1 = y;
		int z1 = z;
		walk (x1, y1, z1, i);
		if(lattice[xyzn(x1,y1,z1)] == 0)
			check.push_back(i);
	}
	if(check.size() > 0)
		direction =
check[(int)rg.IRandom(0,check.size()-1)];
	else{
	for(;;){
		direction = rg.IRandom(0, 5);
		if (abs(direction - olddirection) != 3)
			break;}
	}
	int x1 = x;
	int y1 = y;
	int z1 = z;
	switch (direction){
	case 3:
		x1 = (x+size-1)%size;
		break;
	case 4:
		y1 = (y+size-1)%size;
		break;
	case 5:
		z1 = (z+size-1)%size;
		break;
	}
	bond[xyzn(x1,y1,z1)][direction%3] = true;
	walk(x,y,z,direction);
	if (lattice[xyzn(x,y,z)] !=0)
		return -1;
	else{
		lattice[xyzn(x,y,z)] = xyzn(x,y,z) + 1;
		return direction;
	}
}

void walk (int& x, int& y, int& z, int d)
{
	switch (d){
	case 0:
		x = (x + 1) % size;
		break;
	case 3:
		x = (x + size - 1) % size;
		break;
	case 1:
		y = (y + 1) % size;
		break;
	case 4:
		y = (y + size - 1) % size;
		break;
	case 2:
		z = (z + 1) % size;
		break;
```

```
		case 5:
			z = (z + size - 1) % size;
			break;
		}
}

void MarkCluster ()
{
		int iteration = 0;
		int Mark = 0;
		int n = 0;
		int n1 = 0;
		int n2 = 0;
		int n3 = 0;
		int n4 = 0;
		int n5 = 0;
		int n6 = 0;
		do{
		Mark = 0;
		iteration++;
		cout << setw (4) << iteration << "th scan\r";
		for (int i=0; i<size; i++ ){
			for (int j=0; j<size; j++ ){
				for (int k=0; k<size; k++ ){
n = xyzn(i,j,k);
if (lattice[n] == 0)
		continue;
else{
		n1 = xyzn(i,j,(k+1)%size);
		n2 = xyzn(i,j,(k+size-1)%size);
		n3 = xyzn(i,(j+1)%size,k);
		n4 = xyzn(i,(j+size-1)%size,k);
		n5 = xyzn((i+1),j,k);
		n6 = xyzn((i-1),j,k);
		if (lattice[n1] > lattice[n] && bond[n][2]){
			lattice[n1] = lattice[n];
			Mark = 1;}
		if (lattice[n2] > lattice[n] && bond[n2][2]){
			lattice[n2] =  lattice[n];
			Mark = 1;}
		if (lattice[n3] > lattice[n] && bond[n][1]){
			lattice[n3] = lattice[n];
			Mark = 1;}
		if (lattice[n4] > lattice[n] && bond[n4][1]){
			lattice[n4] = lattice[n];
			Mark = 1;}
		if (i<size-1 && lattice[n5] > lattice[n] &&
bond[n][0]){
			lattice[n5] = lattice[n];
			Mark = 1;}
		if (i>0 && lattice[n6] > lattice[n] &&
bond[n6][0]){
			lattice[n6] = lattice[n];
			Mark = 1;}}}}
			}
		}
		while ( Mark );
}

void CalcCluster (double P)
{
		int l = 0;
		int index_number = 0;
		int totalpore = int (P * size3);
		int escape_volum = 0;
		double sum_z = 0.0;
		int cluster_number = 0;
		int *clustervolum;
		int *clusterZdepth;
		double escape =0.0;
		double average_z = 0.0;
		double surface_average_z = 0.0;
		int surfacesumZ = 0;
		int percolate=0;

		clustervolum = new int[size3];
		clusterZdepth = new int [size3];
		for (int i=0; i<size3; i++){
			clustervolum [i] = 0;
			clusterZdepth [i] =0;
		}
		for (int i=0; i<size; i++ ){
			for (int j=0; j<size; j++ ){
				for (int k=0; k<size; k++ ){
					if
( lattice[xyzn(i,j,k)] != 0 ) {
		index_number = lattice[xyzn(i,j,k)] -1;
		clustervolum[index_number]++;
					if
( lattice[xyzn(i,j,k)] <= xyzn(i,j,k))
		clusterZdepth [index_number] = i -
index_number / (size * size) + 1;}
				}
			}
		}
		for (int i=0; i<size3; i++ ){
			if ( clustervolum[i] == 0 )
				continue;
			else{
				clusterZdepth[i] =
clusterZdepth[i] * clustervolum[i];
				cluster_number++;
				sum_z += clusterZdepth [i];
			}
		}
		for (int i=0; i<size*size; i++ ){
			escape_volum += clustervolum[i];
			surfacesumZ += clusterZdepth[i];
		}
		escape = double (escape_volum)/
double( totalpore );
		if (escape_volum)
			surface_average_z = double
(surfacesumZ) / double ( escape_volum );
		else
			surface_average_z = 0;
		if (totalpore)
			average_z = double (sum_z) /
(double ( totalpore ));
		else
			average_z = 0;
		result[0].push_back(P);
		result[1].push_back(escape);
		result[2].push_back(surface_average_z);
```

```
	result[3].push_back(average_z);
	cout << setw(10) << P
		<< setw(12) << escape
		<< setw(10) << surface_average_z
		<< setw(10) << average_z;
	delete [] clustervolum;
	delete [] clusterZdepth;
}

void mfp(int count)
{
	int total_surface = count*6;
	for (int i=0; i<size3; i++ ) {
		for(int j=0; j<3; j++)
			if(bond[i][j])
				total_surface -= 2;
	}
	double mean_free = 4 * double(count) /
double(total_surface);
	cout << setw(10) << mean_free << endl;
	result[4].push_back(mean_free);
}

void outputf()
{
	ofstream outResultsFile( "sitebond.dat",
ios::app );
	outResultsFile << "size " << size
	<< " grow" << pgrow << " r" << r << endl;
	outResultsFile << setw(12) << "Porosity"
	<< setw(12) << "Escape"
	<< setw(12) << "SurfZ"
	<< setw(12) << "AveZ"
	<< setw(12) << "MeanFreeP" << endl;
	for(int j=0; j<(int)result[0].size(); j++){
		for(int i=0; i<5; i++){
			outResultsFile << setw(12)
<< result[i][j];}
		outResultsFile << endl;
	}
}
```

# BIBLIOGRAPHY

# BIBLIOGRAPHY


[1] G. E. Moore, Microelectronics **38**, 8 (1965).

[2] G. E. Moore, IEEE IEDM Tech. Dig. page 11 (1975).

[3] L. Peters, Semicond. Int. **21**, 9 (1998).

[4] Semiconductor Industry Association, International Technology Roadmap for Semiconductors (2007).

[5] J. Davis and J. Meindl, *Interconnect Technology and Design for Gigascale Integration*, Kluwer Academic Publishers (2003).

[6] K. Maex, M. R. Baklanov, D. Shamiryan, F. Iacopi, S. H. Brongersma, and Z. S. Yanovitskaya, J. Appl. Phys. **93**, 8793 (2003).

[7] M. Morgen, E. Todd Ryan, J.-H. Zhao, C. Hu, T. Cho, and P. S. Ho, Annu. Rev. Mater. Sci. **30**, 645 (2000).

[8] N. Hayasaka *et al*, in "*Proc. 15th Dry Process Symp.*", Tokyo, Japan (1993), p. 31.

[9] S. W. Lim, Y. Shimogaki, Y. Nakano, K. Tada, and H. Komiyama, Appl. Phys. Lett. **68**, 832 (1996).

[10] G. Maier, Prog. Polym. Sci. **26**, 3 (2001).

[11] D. W. Gidley, H.-G. Peng, and R. S. Vallery, Annu. Rev. Mater. Res. **36**, 49 (2006).

[12] Y. Kobayashi, K. Ito, T. Oka, and K. Hirata, Radiat. Phys. Chem. **76**, 224 (2007).

[13] M. Van Bavel, F. Iacopi, M. Baklanov, and K. Maex, Future FAB Intl. Issue **17** (Jun. 21st, 2004).

[14] S. J. Gregg and S. W. Sing, *Adsorption, surface area and porosity,* 2$^{nd}$ ed, Academic press, NY (1982).

[15] M. R. Baklanov, L. L. Vasilyeva, T. A. Gavrilova, F. N. Dultsev, K. P. Mogilnikov, and L. A. Nenasheva, Thin Solid Films **171**, 43 (1989).

[16] M.R. Baklanov, K.P. Mogilnikov, V.G. Polovinkin, and F.N. Dultsev, J. Vac. Sci. Technol. B **18**, 1385 (2000).

[17] H. A. Lorentz, Ann. Phys. **9**, 641 (1880).

[18] L. Lorenz, Ann. Phys. **11**, 70 (1880).

[19] E. Huang, M. F. Toney, W. Volksen, D. Mecerreyes, P. Brock, H.-C. Kim, C. J. Hawker, J. L. Hedrick, V. Y. Lee, T. Magbitang, R. D. Miller, and L. B. Lurio, Appl. Phys. Lett. **81**, 2232 (2002).

[20] W. Wu, W. E. Wallace, E. Lin, G. W. Lynn, C. J. Glinka, R. T. Ryan, and H. Ho, J. Appl. Phys. **87**, 1193 (2000).

[21] P. J. Schultz and K. G. Lynn, Rev. Mod. Phys. **60**(3), 701 (1988).

[22] E. M. B. de Sousa, W. F. de Magalhaes, and N. D. S. Mohallem, J. Phys. Chem. Solids **60**, 211 (1999).

[23] T. C. Merkel, B. D. Freeman, R. J. Spontak, Z. He, and I. Pinnau, Science **296**, 519 (2002).

[24] R. G. Rajendran, MRS Bull. **30**, 587 (2005).

[25] K. G. Lynn, J. R. MacDonald, R. A. Boie, L. C. Feldman, J. D. Gabbe, M. F. Robbins, E. Bonderup, and J. Golovchenko, Phys. Rev. Lett. **38**, 241 (1977).

[26] P. A. M. Dirac, Proc. Roy. Soc. Lond. A **126**, 360 (1930).

[27] C. D. Anderson, Phys. Rev. **43**, 491 (1933).

[28] G. Carboni and W. Dahme, Phys. Lett. **123B**, 349 (1983).

[29] S. Orito, K. Yoshimura, T. Haga, M. Minowa, and M. Tsuchiaki, Phys. Rev. Lett. **63**, 597 (1989).

[30] G. S. Atoyan, S. N. Gninenko, V. I. Razin, and Yu. V. Ryabov, Phys. Rev. B **220**, 317 (1989).

[31] A. P. Mills, Jr. and D. M. Zuckerman, Phys. Rev. Lett. **64**, 2637 (1990).

[32] D. W. Gidley, J. S. Nico, and M. Skalsey, Phys. Rev. Lett. **66**, 1302 (1990).

[33] D. W. Gidley, K. A. Marko, and A. Rich, Phys. Rev. Lett. **36**, 395 (1976).

[34] R. S. Vallery, P. W. Zitzewitz, and D. W. Gidley, Phys. Rev. Lett. **90**, 203402 (2005).

[35] M. J. Puska and R. M. Nieminen, Rev. Mod. Phys. **66**(3), 841 (1994).

[36] E. Bellotti, M. Corti, E. Fiorini, C. Liguori, A. Pullia, A. Sarracino, P. Sverzellati, and L. Zanotti, Phys. Lett. B **124**, 435 (1983).

[37] M. Charlton and J. W. Humberston, *Positron Physics*, Cambridge University Press (2001).

[38] O. E. Mogensen, Appl. Phys. **6**, 315 (1975).

[39] O. E. Mogensen, "proceedings of the 6th ICPA, Fort Worth, Texas," in P. G. Coleman, S. C. Sharma, and L. M. Diana, editors, "Positron Annihilation," North-Holland, New York (1982), p. 763.

[40] H. J. Ache, "proceedings of the 5th ICPA, Japan, 1979," in R. R. Hasiguti and K. Fujiwara, editors, "Positron Annihilation," Japanese Institute of Metals, Sendai, Japan (1979), p. 31.

[41] W. Brandt, Lett. Nuovo Cimento **33**, 499 (1982).

[42] A. Dupasquier, "proceedings of the "Enrico Fermi" School summer course on "Positrons in Solids," Varenna, Italy, 1981," in W. Brandt and A. Dupasquier, editors, "Positron Solid-State Physics," NorthHolland, Amsterdam (1983), p. 510.

[43] O. E. Mogensen, J. Chem. Phys. **60**, 998 (1974).

[44] L. Onsager, Phys. Rev. **54**, 554 (1938).

[45] F. M. Jacobson, Chem. Phys. **109**, 455 (1986).

[46] C. Dauwe, B. Van Waeyenberge, and J. De Baerdemaeker, Acta Phys. Pol. A **107**, 623 (2005).

[47] V. M. Byakov and S. V. Stepanov, J. Radioanal. Nucl. Chem. **210**, 371 (1996).

[48] W. Brandt and R. Paulin, Phys. Rev. Lett. **21**, 193 (1968).

[49] M. Eldrup, A. Vehanen, P. J. Schultz, and K. G. Lynn, Phys. Rev. B **32**, 7048 (1985).

[50] J. Serna, Physica Status Solidi A **122**, 489 (1990).

[51] K. Ito and Y. Kobayashi, Mater. Sci. Forum **445-446**, 307 (2004).

[52] P. G. Coleman, editor, *Positron Beams and Their Applications, Chpater 2*, World Scientific (2000).

[53] L. Madanski and F. Rasetti, Positron Annihilation **79**, 397 (1950).

[54] W. Puff, Comput. Phys. Commun. **30**, 359 (1983).

[55] S. W. Provencher, Comput. Phys. Commun. **27**, 229 (1982).

[56] R. B. Gregory, Nucl. Instrum. Methods Phys. Res., Sect. A **302**, 496 (1991).

[57] S. J. Tao, J. Chem. Phys. **56**, 5499 (1972).

[58] M. Eldrup, D. Lightbody, and J. N. Sherwood, Chem. Phys. **63**, 51 (1981).

[59] D. W. Gidley, W. E. Frieze, T. L. Dull, A. F. Yee, E. T. Ryan, and H.-M. Ho, Phys. Rev. B **60**, 8 (1999).

[60] T. L. Dull, W. E. Frieze, D. W. Gidley, J. N. Sun, and A. F. Yee, J. Phys. Chem. B **105**, 4657 (2001).

[61] B. Jasinska, A. L. Dawidowicz, T. Goworek, and J. Wawryszczuk, Opt. Appl. **33**, 7 (2003).

[62] J. N. Sun, *Probing porous low-dielectric constant thin films using positronium annihilation lifetime spectroscopy*, Ph.D. Thesis, The University of Michigan (2002).

[63] D. W. Gidley, T. L. Dull, W. E. Frieze, J. N. Sun, and A. F. Yee, Materials Research Society Symposium Proceeding **612**, D4.3.1 (2000).

[64] D. W. Gidley, W. E. Frieze, T. L. Dull, J. N. Sun, A. F. Yee, C. V. Nguyen, and D. Y. Yoon, Appl. Phys. Lett. **76**, 1282 (2000).

[65] C. He, T. Oka, Y. Kobayashi, N. Oshima, T. Ohdaira, A. Kinomura, and R. Suzuki, Appl. Phys. Lett. **91**, 024102 (2007).

[66] J. Algers, P. Sperr, W. Egger, G. Kögel, and F. H. J. Maurer, Phys. Rev. B **67**, 125404 (2003).

[67] S. Valkealahti and R. M. Nieminen, Appl. Phys. A (Solids and Surfaces) **32**, 95 (1983).

[68] S. Valkealahti and R. M. Nieminen, Appl. Phys. A (Solids and Surfaces) **35**, 51 (1984).

[69] C. T. Kresge, M. E. Leonowicz, W. J. Roth, J. C. Vartuli, and J. S. Beck, Nature **359**, 710 (1992).

[70] R. A. Pai, R. Humayun, M. T. Schulberg, A. Sengupta, J. N. Sun, and J. J. Watkins, Science **303**, 507 (2004).

[71] H. W. Ro, K. Char, E. Jeon, H.-J. Kim, D. Kwon, H.-J. Lee, J.-K. Lee, H.-W. Rhee, C. Soles, and D. Y. Yoon, Adv. Mater. **19**, 705 (2007).

[72] H.-G. Peng, R. S. Vallery, M. Liu, W. E. Frieze, D. W. Gidley, J.-H. Yim, H.-D. Jeong, and J. Kim, Appl. Phys. Lett. **87**, 161903 (2005).

[73] J. H. Yim, J. B. Seon, T. D. Jeong, L. Y. S. Pu, M. R. Baklanov, and D. W. Gidley, Adv. Funct. Mater. **14**, 277 (2004).

[74] J. H. Yim, Y. Y. Lyu, H. D. Jeong, S. K. Mah, J. Hyeon-Lee, J. H. Hahn, G. S. Kim, S. Chang, and J. G. Park, J. Appl. Polym. Sci. **90**, 626 (2003).

[75] C. D. Gutsche, B. Dhawan, K. H. No, and R. Muthukrishnan, J. Am. Chem. Soc. **103**, 3782 (1981).

[76] J. J. P. Stewart, Comput. Chem. **10**, 209 (1989).

[77] S. Polarz, B. Smarsly, L. Bronstein, and M. Antonietti, Angew. Chem. Int. Ed. **40**, 4417 (2001).

[78] C. T. Chua, G. Sarkar, and X. Hu, J. Electrochem. Soc. **145**, 4007 (1998).

[79] A. Zenasni, F. Ciaramella, V. Jousseaume, Ch. Le Cornec, and G. Passemard, J. Electrochem. Soc **154**, G6 (2007).

[80] M. Baklanov, M. Green, and K. Maex, editors, *Dielectric Films for Advanced Microelectronics*, John Wkley & Sons, Ltd (2007).

[81] Q. R. Huang, H.-C. Kim, E. Huang, D. Mecerreyes, J.L. Hedrick, W. Volksen, C. W. Frank, and R. D. Miller, Macromolecules **36**, 7661 (2003).

[82] E. F. Connor, L. K. Sundberg, H.-C. Kim, J. J. Cornelissen, T. Magbitang, P. M. Rice, V. Y. Lee, C. J. Hawker, W. Volksen, J. L. Hedrick, and R. D. Miller, Angew. Chem. **115**, 3915 (2003).

[83] D. Zhao, J. Feng, Q. Huo, N. Melosh, G. H. Fredrickson, B. F. Chmelka, and G. D. Stucky, Science **279**, 548 (1998).

[84] H. W. Ro, R. L. Jones, H. Peng, D. R. Hines, H. J. Lee, E. K. Lin, A. Karim, D. Y. Yoon, D. W. Gidley, and C. L. Soles, Adv. mater. **19**, 2919 (2007).

[85] H. W. Ro, R. L. Jones, H. Peng, H.-J. Lee, E. K. Lin, A. Karim, D. Y. Yoon, D. W. Gidley, and C. L. Soles, volume 6921, page 69211M (2008).

[86] H. W. Ro, H. Peng, K. Niihara, H. J. Lee, E. K. Lin, A. Karim, D. W. Gidley, H. Jinnai, D. Y. Yoon, and C. L. Soles, Adv. mater. **20**, 1934 (2008).

[87] H.-G. Peng, *Probing polymeric thin films using beam-based positronium annihilation lifetime spectroscopty*, Ph.D. Thesis, The University of Michigan (2004).

[88] D. Stauffer and A. Aharony, editors, *Introduction to Percolation Theory*, Taylor & Francis, London (1994).

[89] M. L. O'Neill, M. K. Haas, B. K. Peterson, R. N. Vrtis, S. J. Weigel, D. Wu, M. D. Bitner, and E. J. Karwacki, Mater. Res. Sco. Symp. Proc. **914**, 3 (2007).

[90] J. W. Essam and M. F. Sykes, J. Math. Phys. **5**, 1117 (1964).

[91] S. Wilke, Phys. Lett. A **96A**, 344 (1983).

[92] R. M. Ziff, Phys. Rev. Lett. **69**, 2670 (1992).

[93] P. N. Suding and R. M. Ziff, Phys. Rev. E **60**, 275 (1999).

[94] D. R. Baker, G. Paul, S. Sreenivasan, and H. E. Stanley, Phys. Rev. E **66**, 046136 (2002).

[95] M. Matsumoto and T. Nishimura, ACM Transactions on Modeling and Computer Simulation **8**, 3 (1998).

[96] J. Hoshen and R. Kopelman, Phys. Rev. B **14**, 3438 (1976).

[97] M. Rottereau, J.C. Gimel, T. Nicolai, and D. Durand, Euro. Phys. J. E **11**, 61 (2003).

[98] M. E. J. Newman and R. M. Ziff, Phys. Rev. Lett. **85**, 4104 (2000).

[99] P. A. Rikvold and G. Stell, J. Chem. Phys. **82**, 1014 (1985).

[100] R. Suzuki, T. Ohdaira, Y. Kobayashi, K. Ito, R.S. Yu, Y. Shioya, H. Ichikawa, H. Hosomi, K. Ishikiriyama, H. Shirataki, S.Matsuno, and J. Xu, Materials Science Forum **445-446**, 224 (2004).

[101] J. S. Nico, *Precision measurement of the orthopositronium decay rate using the vacuum technique*, Ph.D. Thesis, The University of Michigan (1991).

[102] A. L. R. Bug, S. A. Safran, Gray S. Grest, and Itzhak Webman, Phys. Rev. Lett. **55**, 1896 (1985).

[103] C. Jezewski, W. A. Lanford, C. J. Wiegand, J. J. Senkevich, and T.-M. Lu, Semicond. Int. **27**, 56 (2003).

[104] J. J. Senkevich, C. J. Wiegand, G.-R. Yang, and T.-M. Lu, Chem. Vap. Deposition **10**, 247 (2004).

[105] J. S. Juneja, G. A. Ten Eyck, H. Bakhru, and T.-M. Lu, J. Vac. Sci. Technol. B **23**, 2232 (2005).

[106] W. Gorham, J. Polym. Sci., Part A-1 **4**, 3027 (1966).

[107] S. Y. Chou and P. R. Krauss, Microelect. Eng. **35**, 237 (1997).

[108] M. D. Austin, H. Ge, W. Wu, M. Li, Z. Yu, D. Wasserman, S. A. Lyon, and S. Y. Chou, Appl. Phys. Lett. **84**, 5299 (2004).

[109] O. M. Yaghi, M. O'Keeffe, N. Ockwig, H. K. Chae, M. Eddaoudi, and J. Kim, Nature **423**, 705 (2003).

[110] D. Moore, R. Carter, H. Cui, P. Burke, P. McGrath, S. Q. Gu, D. W. Gidley, and H. Peng, J. Vac. Sci. Technol. B **23**, 332 (2005).

[111] S. Myneni, H.-G. Peng, D. W. Gidley, and D. W. Hess, J. Vac. Sci. Technol. B **23**, 1463 (2005).

[112] A. G. Hathaway, *Design and testing of a prototype slow positron beam at the NC State University PULSTAR reactor*, Masters thesis, North Carol. State Univ. (2005), 90 pp.